

TECHNISCHE UNIVERSITÄT MÜNCHEN  
MAX-PLANCK-INSTITUT FÜR ASTROPHYSIK

# Hydrodynamic simulations of combustion processes at high densities in compact stars

Matthias Herzog

Vollständiger Abdruck der von der Fakultät für Physik der Technischen Universität München zur Erlangung des akademischen Grades eines

*Doktors der Naturwissenschaften*

genehmigten Dissertation.

Vorsitzender: Univ.-Prof. Dr. L. Oberauer

Prüfer der Dissertation:

1. Univ.-Prof. Dr. F. K. Röpke,  
Julius-Maximilians-Universität Würzburg
2. Univ.-Prof. Dr. A. Ibarra

Die Dissertation wurde am 27.09.2012 bei der Technischen Universität München eingereicht und durch die Fakultät für Physik am 13.12.2012 angenommen.



# Contents

<b>Contents</b>	<b>3</b>
<b>1. Prologue</b>	<b>7</b>
1.1. Compact stars . . . . .	7
1.2. Formation of compact stars . . . . .	9
1.3. Supernovae of Type Ia . . . . .	11
1.3.1. Observations of Type Ia supernovae . . . . .	12
1.3.2. Type Ia supernova progenitor systems . . . . .	12
1.3.3. Modeling of thermonuclear supernovae . . . . .	14
1.4. Neutron stars and the equation of state of dense matter . . . . .	15
1.5. Organization of this thesis . . . . .	17
<b>2. Fundamental considerations</b>	<b>19</b>
2.1. Equation of state of compact stars . . . . .	19
2.1.1. White dwarf matter . . . . .	19
2.1.2. Hadronic nuclear matter . . . . .	20
2.1.3. Strange quark matter . . . . .	20
2.2. Hydrostatic configurations of compact stars . . . . .	22
2.2.1. Equations of hydrostatic equilibrium . . . . .	22
2.2.2. Limiting mass and stability of compact stars . . . . .	23
2.2.3. Examples of hydrostatic configurations of compact stars . . . . .	24
2.3. Fluid dynamics . . . . .	29
2.4. Combustion . . . . .	31
2.4.1. Basic concepts of combustion theory . . . . .	31
2.4.2. Turbulent combustion . . . . .	33
2.4.3. Estimation of relevant length scales . . . . .	35
2.4.4. Conditions for exothermic combustion . . . . .	35
2.5. Gravitational waves . . . . .	36
2.5.1. Theory of gravitational waves . . . . .	36
2.5.2. Detection of gravitational waves . . . . .	39
2.6. Weak interactions . . . . .	40
2.7. Neutrino emission during thermonuclear burning in white dwarfs . . . . .	41
2.7.1. Weak neutrinos . . . . .	42

2.7.2. Thermal neutrinos . . . . .	42
<b>3. Numerical methods</b>	<b>43</b>
3.1. The LEAFS-code – general overview . . . . .	43
3.1.1. Solving the Euler equations . . . . .	43
3.1.2. Gravitational potential . . . . .	46
3.1.3. Moving hybrid grid . . . . .	47
3.1.4. Burning velocity in white dwarf matter and level-set method . . . . .	47
3.1.5. Modeling the thermonuclear burning . . . . .	48
3.1.6. Subgrid scale turbulence model . . . . .	49
3.1.7. Tracer particle method . . . . .	50
3.2. Modifications to the code I: Neutron star simulations . . . . .	50
3.2.1. Equation of state . . . . .	51
3.2.2. Conversion from hadronic matter into strange quark matter . . . . .	51
3.2.3. Effective relativistic gravitational potential . . . . .	52
3.2.4. Relaxation of initial neutron star setup . . . . .	53
3.2.5. Moving hybrid grid with fixed outer boundary . . . . .	55
3.3. Modifications to the code II: Simulations of high-density white dwarfs . . . . .	55
3.3.1. Weak interaction rates . . . . .	55
3.3.2. Neutrino energy . . . . .	58
3.3.3. Inclusion of neutron-rich nuclides in post-processing code . . . . .	59
3.4. Calculation of gravitational wave signal . . . . .	59
<b>4. Combustion of a hadronic neutron star into a quark star</b>	<b>63</b>
4.1. Introduction . . . . .	63
4.2. Modeling the conversion process as a combustion . . . . .	65
4.3. Conditions for exothermic combustion . . . . .	67
4.4. Simulations . . . . .	69
4.4.1. Neutron star setup . . . . .	70
4.4.2. Onset of turbulence . . . . .	73
4.4.3. Intermediate case: $B^{1/4} = 150 \text{ MeV}$ . . . . .	75
4.4.4. Lower limit: $B_{\text{low}}^{1/4} = 147 \text{ MeV}$ . . . . .	78
4.4.5. Upper limit: $B_{\text{high}}^{1/4} = 155 \text{ MeV}$ . . . . .	79
4.4.6. Lattimer-Swesty EoS: different incompressibility moduli $K$ . . . . .	79
4.4.7. Different subgrid scale models . . . . .	81
4.4.8. Neutron stars with different masses . . . . .	81
4.5. Gravitational wave signal . . . . .	83
4.5.1. Simulations . . . . .	83
4.5.2. Order-of-magnitude estimation . . . . .	87
4.5.3. Energy spectra . . . . .	89
4.5.4. Detectability . . . . .	90

---

4.5.5. Comparison of numerical methods . . . . .	90
4.6. Conclusions . . . . .	92
<b>5. Deflagrations in high-density carbon-oxygen white dwarfs</b>	<b>95</b>
5.1. Introduction . . . . .	95
5.1.1. The fate of high-density white dwarfs . . . . .	95
5.1.2. Current state of research . . . . .	97
5.1.3. Objectives of this part of the thesis . . . . .	101
5.2. Hydrodynamic simulations . . . . .	102
5.2.1. Initial configurations . . . . .	102
5.2.2. Resolution . . . . .	103
5.2.3. Discussion of standard model Cc3 . . . . .	111
5.2.4. Central density . . . . .	114
5.2.5. Burning velocity . . . . .	114
5.2.6. Chemical composition . . . . .	117
5.2.7. Comparison with calculations of Bravo and García-Senz (1999) . . . . .	120
5.2.8. General relativistic corrections . . . . .	123
5.2.9. Subgrid scale turbulence model . . . . .	124
5.2.10. Energy loss due to neutrinos . . . . .	126
5.3. Nucleosynthesis . . . . .	131
5.3.1. Numerical specifications . . . . .	131
5.3.2. General results . . . . .	133
5.3.3. Neutron-rich isotopes . . . . .	135
5.4. Conclusions . . . . .	140
<b>6. Epilogue</b>	<b>143</b>
<b>A. Gravitational wave signal of a typical thermonuclear supernova</b>	<b>147</b>
A.1. Introduction . . . . .	147
A.2. Delayed-detonation model N0100 . . . . .	148
A.3. Results . . . . .	149
A.3.1. Gravitational wave amplitudes . . . . .	149
A.3.2. Gravitational wave energy . . . . .	150
A.4. Discussion and outlook . . . . .	152
<b>Bibliography</b>	<b>155</b>



# 1. Prologue

## 1.1. Compact stars

*Compact stars* are stellar objects that are supported against gravitational collapse by nuclear forces, in particular the degeneracy pressure of subatomic particles; in contrast to ordinary main sequence or giant stars, in which thermal pressure balances the gravitational forces. If we include the exotic siblings of compact stars, black holes, we refer to them as *compact objects*. Compact stars form the end stages in the life of ordinary stars after they have depleted their nuclear fuel and expelled their outer layers. The masses of compact stars are on the order of one solar mass ( $M_{\odot}$ ), but the radii are small,  $10^{-5}$  to  $10^{-2}$  of the solar radius ( $R_{\odot}$ ); hence the term *compact*. Consequently, the densities and pressures in their interiors are extremely high – the central densities cover a wide range from  $10^6$  to  $10^{15}$   $\text{g cm}^{-3}$ . These properties indicate that compact stars are unique laboratories of dense matter that cannot be imitated in terrestrial experiments. In this respect, research on compact stars connects astrophysics and nuclear physics to a new research field known as *nuclear astrophysics*.

We divide compact stars into two distinct *families*. The first family comprises *white dwarfs* (*WDs*), which are supported by the electron degeneracy pressure against gravitational collapse. There are different types of white dwarfs with different chemical composition; their properties are in general quite well understood.

Much less is known about the interior of compact stars belonging to the second family, *neutron stars* (*NSs*). In the simplest picture, their supporting pressure is due to the degeneracy of neutrons. Their radii,  $\sim 10$  km, are about a factor of  $10^2$  smaller than the radii of white dwarfs. Since they have similar masses, the densities in neutron stars are higher by a factor of  $\sim 10^6$  compared to white dwarfs. We will discuss the various possible compositions of neutron stars in Section 1.4.

The degeneracy pressure of any kind of subatomic particle cannot support arbitrarily high masses. Consequently, both the masses of white dwarfs and of neutron stars have a definite upper limit – a property that is not shared by, for example, main sequence stars or black holes, and is of great importance regarding many aspects, as we will see later. We know the maximum mass of white dwarfs, the *Chandrasekhar limit*, quite well; whereas our knowledge of the maximum mass of neutron stars is rather vague (cf. Section 2.2).

In the history of astronomy, which reaches back to ancient civilizations, the study of compact stars is a very young part of the field. Only the substantial progress in observational methods at the beginning of the 20th century allowed astronomers to discover more than the closest of these faint objects; and only the development of the theory of quantum physics 90

years ago made it possible to develop theoretical models to describe compact stars.

Systematic research on white dwarfs started when Adams (1915) measured the spectrum of a very faint companion of Sirius and found that its color is similar to that of Sirius itself, which appears white to the human eye. That means that the companion, Sirius B, has to be a hot, very small star. The nature of Sirius B cannot be explained by means of classical physics. Based on work of Eddington (1924, 1926), the puzzle was solved by Fowler (1926), who applied the newly established theory of quantum physics and found that a white dwarf can be seen as a cold, degenerate electron gas; consequently, the electron degeneracy pressure prevents a gravitational collapse.

The field of neutron star research is even younger than that of white dwarfs. As described above, white dwarfs were discovered observationally before a theoretical explanation had been available. The discovery of neutron stars happened the other way round: Soon after Chadwick (1932) discovered the neutron, Baade and Zwicky (1934a,b) proposed that, during a *supernova* (SN), normal stars collapse into stars consisting mostly of neutrons. Such stars “may possess a very small radius and an extremely high density” (Baade and Zwicky, 1934b). Naturally, Baade and Zwicky called them *neutron stars*. A few years later, Tolman (1939) and Oppenheimer and Volkoff (1939) found the equations that allowed for the first general relativistic description of neutron stars.<sup>1</sup>

Neutron stars have long been believed to be unobservable, until in 1967 Jocelyn Bell discovered a periodic pulsating radio source (Hewish et al., 1968), which was called *pulsar* and soon identified as a rotating neutron star. In the following decades, a large number of pulsars has been discovered; most of them as radio pulsars, but also various pulsars emitting in optical, X-ray, or gamma wavelengths. For example, the *ATNF pulsar catalogue* (Australia Telescope National Facility, 2012) now lists more than 2000 radio pulsars.

The mass of neutron stars can only be measured in binaries. A special case is the binary *Hulse-Taylor-Pulsar* B1913+16, which was named after Russell Hulse und Joseph Taylor, who discovered it in 1974. The simultaneous measurement of Keplerian as well as relativistic parameters lead to an unprecedented and still unmatched accuracy of the mass measurement that results in a mass of the pulsar of  $M_{\text{primary}} = (1.4398 \pm 0.0002) M_{\odot}$ , while the mass of the secondary, an invisible neutron star, is  $M_{\text{secondary}} = (1.3886 \pm 0.0002) M_{\odot}$ , according to the most recent analysis (Weisberg et al., 2010). For a long time the primary was the neutron star with the highest mass measured with high confidence, until Demorest et al. (2010) set a new milestone in the history of neutron star observations: They measured the Shapiro-delay of the binary millisecond pulsar J1614-2230 and calculated a mass of the neutron star of  $M = (1.97 \pm 0.04) M_{\odot}$ , which is up to now the highest neutron star mass determined with high precision and reliability.

Furthermore, we know from observations that the radii of neutron stars are in the range of 8

---

<sup>1</sup>Because Oppenheimer and Volkoff (1939) assumed the star to consist of a pure degenerate neutron Fermi gas, they found a maximum mass of  $0.7 M_{\odot}$  of a nonrotating neutron star and therefore concluded: “It seems unlikely that static neutron stars can play any great part in stellar evolution.”

to 18 km, but those measurements are very difficult and often model dependent and thus suffer from a high degree of uncertainty (Steiner et al., 2010; Heinke et al., 2006).

## 1.2. Formation of compact stars

In this section we give an overview on how compact stars – neutron stars and the different types of white dwarfs – form as final stage of their respective main sequence progenitor. This section is based on stellar evolution theory according to the recent review article by Siess (2008), see there and the references therein for further information.

When a protostar, a collapsed gas cloud that is massive enough to enable future hydrogen burning ( $M \gtrsim 0.07 M_{\odot}$ ), enters the main sequence of the Hertzsprung-Russell diagram, hydrogen burning starts – from now on we call such an object *main sequence star* or simply *star*. In its core, protons are fused (“burned”) into  ${}^4\text{He}$  via the *proton-proton (pp) chain* and, except for low mass stars and stars of zero metallicity, via the *CNO cycle*. After the hydrogen fuel has been exhausted completely in the core, the star contracts and heats up. If the contraction process stops before the temperature in the core reaches  $\sim 10^8$  K, no helium burning is ignited, the star ends as a *helium (He) white dwarf*. This is the case for stars with a mass of less than  $\sim 0.5 M_{\odot}$ . (The masses that are stated here and in the following, which are required to reach the respective next nuclear burning stage, are only guidelines; the actual mass limits depend on the metallicity of the star, because the relevant physical parameter is the maximal temperature reached in the core. In addition, theoretical ambiguities such as different treatments of convection processes in stellar evolution modeling contribute to the uncertainties.) However, no isolated He white dwarf exists in today’s Universe, because the burning processes in low mass stars are slow and it takes longer than the current age of the Universe to exhaust the nuclear fuel of stars with masses  $< 0.5 M_{\odot}$ .

In more massive stars, the alpha particles (denoted as  ${}^4\text{He}$  or  $\alpha$ ) are burned into  ${}^{12}\text{C}$  by means of the *triple-alpha process*



In later stages of helium burning, a competition for the remaining alpha particles arises between the triple-alpha process and the reaction



The rate of the first process is proportional to the third power of the abundance of alpha particles, while for the second reaction this dependence is linear. Therefore, when the alpha particles become less and less abundant, the second reaction dominates: As soon as the helium abundance decreases to about 10%, more carbon is destroyed than produced. By the time all alpha particles are used up, both the triple-alpha process and the reaction (1.3) cease

and the  $^{12}\text{C}/^{16}\text{O}$  ratio remains constant and of order unity. The exact ratio depends on the respective modeling, in particular on the treatment of convection processes in stellar evolution theory and on the rates of the aforementioned reactions, especially of the relatively uncertain  $^{12}\text{C}(\alpha, \gamma)^{16}\text{O}$  reaction.<sup>2</sup> For a detailed discussion of this topic, which is important for modeling Type Ia supernova progenitors, see Straniero et al. (2003). According to them, the central carbon fraction is in the range of 0.1 to 0.7, whereas in the model of Siess (2008) the carbon fraction is between 0.24 and 0.34.

At the end of the hydrogen burning, when no more protons are available, all catalyzing elements involved in the CNO-cycle have been burned into  $^{14}\text{N}$ . Now, during the helium burning phase, the  $^{14}\text{N}$  is burned into  $^{22}\text{Ne}$  via the reaction chain



Therefore, all catalyzing elements of the CNO-cycle end up as  $^{22}\text{Ne}$  after helium burning is complete, and the core of the star consists mainly of  $^{12}\text{C}$ ,  $^{16}\text{O}$ , and  $^{22}\text{Ne}$ . In stars with initial masses lower than 7 to  $9M_{\odot}$  the temperatures in the core do not reach  $\sim 7 \times 10^8$  K and thus no carbon burning is possible. In this case, the star ends its life as a *carbon-oxygen (C+O) white dwarf* after expelling its outer layers. C+O white dwarfs constitute the majority of all white dwarfs in the present-day Universe. Some of them are progenitors of Type Ia supernovae, as we will discuss in Section 1.3.2.

After the helium burning is complete, the star contracts and heats up again. If the temperature in the core reaches  $\sim 7 \times 10^8$  K, the conditions for carbon burning<sup>3</sup> are fulfilled and the carbon and oxygen in the core burn to oxygen, neon, and smaller fractions of magnesium and sodium. If the mass of the initial star does not exceed 10 to  $11M_{\odot}$ , the temperature in the core is too low for the next burning phase, neon burning, and an oxygen-neon core remains. The fate of the star depends now on whether the mass of the core exceeds the limiting mass with respect to gravitational collapse, which is similar to the Chandrasekhar mass. If the core does not exceed this limit, the star becomes an *oxygen neon (O+Ne) white dwarf* after the expulsion of its outer layers. If the core mass is higher, the core collapses, initiated by a pressure reduction due to electron captures on oxygen and neon nuclei. The outer layers of the star fall onto the compact core, until the infalling matter bounces off the surface of the core; subsequently, a mechanism that is not yet fully understood leads to the explosion of the star as an *electron-capture supernova*, a special kind of *core-collapse supernova* (for details and recent reviews of core-collapse supernovae see Janka et al. (2007) and Janka (2012)). After the outer layers of the star have been ejected, the core remains and forms a low-mass neutron star. The maximum initial mass that a star is allowed to have to form an O+Ne white dwarf instead of collapsing into a neutron star is poorly known, since it depends on uncertain parameters such

---

<sup>2</sup>When we discuss nuclear reactions, we sometimes use the notation  $A(a, b)B$  for a reaction of the form  $A + a \rightarrow B + b$ .

<sup>3</sup>In this case the carbon-rich matter is not or only partially degenerate (*nondegenerate carbon burning*), in contrast to the explosive *degenerate carbon burning* during a thermonuclear supernova.

as the core mass growth rate. According to Siess (2008), this limit is between 9 and  $10.5 M_{\odot}$ , depending on the metallicity.

In stars with masses larger than 10 to  $11 M_{\odot}$ , the oxygen-neon core passes through all subsequent burning stages, starting with neon burning, until its core consists entirely of degenerate iron. The core accretes mass until it exceeds its limiting mass; afterward it collapses and the star explodes, forming a core-collapse supernova by a similar mechanism like the one that causes electron-capture supernovae, see above. If the stellar progenitor has been very massive, larger than  $\sim 25 M_{\odot}$ , the core exceeds the limiting mass for neutron stars as well and collapses further into a black hole. Otherwise, the compact remnant is a neutron star.

This brief overview of stellar evolution treats only single stars. In binaries the interaction of the two component stars leads to complicated processes, some resulting in forms of compact stars that cannot be explained by single star evolution. For example, the evolution of a single, very low-mass star into a He white dwarf takes longer than the present age of the Universe, as discussed before, but in binaries mass loss processes give rise to a much faster formation of He white dwarfs (e.g. Benvenuto and De Vito, 2005).

Binaries provide also an additional way to form neutron stars: Accreting white dwarfs may collapse when they approach the Chandrasekhar limit because electron capture processes lower the pressure in the star, similar to what happens in the core of a star during an electron-capture supernova. We will discuss this particular formation channel, called *accretion induced collapse (AIC)*, in detail in Section 5.

We have seen that compact stars are the final stages in the evolution of most stars. They are in general inert objects; and to many of them nothing is happening except that they are cooling and spinning down, while they are emitting less and less radiation. However, in some cases interesting and sometimes spectacular events occur in connection with compact stars. The dense matter inside neutron stars might undergo a phase transition or a sudden conversion to a more stable form of matter. Binary neutron stars eventually merge, giving rise to extremely luminous gamma-ray bursts. Also white dwarfs become very interesting objects in case they are accreting matter in binaries – they may collapse, show luminous and sometimes recurrent events such as novae, or even explode in a supernova. We introduce the latter occurrence in our next section.

### 1.3. Supernovae of Type Ia

Compact stars are tightly connected to supernovae. As mentioned in Section 1.2, most neutron stars are assumed to be compact remnants of core-collapse supernovae that are visible to us as supernovae of Type Ib, Ic, or II; whereas some white dwarfs in binaries are believed to be torn apart by a thermonuclear explosion (*thermonuclear supernova*) that is believed to be the physical mechanism responsible for Type Ia supernovae. In the following sections we aim to give a brief overview of observational and theoretical aspects of these events; and we will introduce some modeling approaches.

### 1.3.1. Observations of Type Ia supernovae

*Stella nova* – this is how Tycho Brahe called the “new star” that suddenly appeared on the sky in the year 1572 (Brahe, 1573). Subsequently, all transient star-like occurrences were referred to as *novae* – until Baade and Zwicky (1927) called the very brightest of them *supernovae*, those that “emit nearly as much light as the whole nebula in which they originate,” at the time of their maximum brightness. Rudolph Minkowski (1939, 1941) studied the spectra of supernovae in great detail and classified them into two groups, which he “provisionally” called Type I and Type II. The first group contains all supernovae whose spectra show no signs of hydrogen, whereas in the spectra of Type II supernovae hydrogen lines are visible. In the following decades this spectral classification was refined, Elias et al. (1985) introduced the differentiation between the types Ia and Ib. Afterward, all supernovae were classified as Type Ia if their spectra lack hydrogen lines but show strong silicon lines near maximum light.

What Brahe observed in 1572 was actually a Type Ia supernova, as we know now because no compact remnant was found (cf. Section 1.3.2, for an overview of historical supernovae see Green and Stephenson, 2003, and references therein). Moreover, the recent measurement of the light echo provided spectroscopic evidence for Brahe’s supernova being of Type Ia (Krause et al., 2008). Also the first recorded supernova, observed in the year 185 AD by Chinese astronomers, was likely a Type Ia supernova, as well as last year’s SN 2011fe, which appeared in the relatively nearby *Pinwheel Galaxy* (M101) and was visible in small telescopes around maximum light (e.g. Röpke et al., 2012; Nugent et al., 2011).

The observation of Type Ia supernova light curves (luminosity as a function of time) is a valuable tool that helps to measure cosmological distances, because Type Ia supernovae have two properties that qualify them as useful distance indicators: They are extremely bright, and we can determine how bright they are. Although not all Type Ia supernovae have the same intrinsic brightness, the majority of them obey the *Phillips relation*, or *width-luminosity relation*, which says that supernovae that are dimmer at maximum luminosity show a faster decline rate of their brightness (Phillips, 1993). Thus Type Ia supernovae are *standardizable candles*. At the end of the 1990s, observations of distant Type Ia supernovae lead to the at that time surprising result that the expansion of the Universe is accelerating (Riess et al., 1998; Perlmutter et al., 1999). In 2011, Saul Perlmutter, Brian Schmidt and Adam Riess were awarded the Nobel Prize in physics for their discovery.

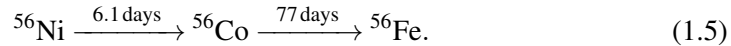
### 1.3.2. Type Ia supernova progenitor systems

The scientific community agrees in general on three important aspects concerning the physical nature of the progenitor systems of Type Ia supernovae:

- The observational nondetection of any compact object in remnants of Type Ia supernovae, the homogeneity of observational properties, and the good agreement with simple model calculations – in particular regarding the abundances of elements seen in the spectra – lead to the general consensus that Type Ia supernovae are best explained by the

thermonuclear combustion of C+O white dwarfs. This line of argument was recently strengthened by a detailed analysis of SN 2011fe (e.g. Nugent et al., 2011).

- Truran et al. (1967), Colgate and McKee (1969), and Arnett (1979) developed the now established theory that the light curve of supernovae is powered by the radioactive decay chain of  $^{56}\text{Ni}$ ,



$^{56}\text{Ni}$  can be produced abundantly by nuclear burning of isospin-symmetric matter at high temperatures and densities; such matter is sufficiently available in white dwarfs consisting of  $^{12}\text{C}$  and  $^{16}\text{O}$ .

- Because single white dwarfs are inert objects, thermonuclear supernovae can only occur in binary systems, in which interaction with a companion star causes the explosion.

But the exact nature of the progenitor binary system and the explosion mechanism is not clear and subject to current research. Supernovae of Type Ia can be divided into several subclasses. One important defining observational property of this sub-classification is the brightness of the supernova – in addition to *normal* Type Ia supernovae also *sub-luminous* or *super-luminous* examples are observed, and such that are in some regard *peculiar* (e.g. Li et al., 2011, and references therein). It is likely, but not necessary, that the different subclasses originate from different progenitor systems. We will now describe the main thermonuclear supernova scenarios that are suggested to explain Type Ia supernovae. For an elaborate review of the topics touched on in the following and further references see Hillebrandt and Niemeyer (2000); see also the references in Section 1.3.3.

In the *single-degenerate scenario*, the companion of the C+O white dwarf is a main sequence star, a giant star, or a helium star, that transfers mass onto the white dwarf. This scenario can be further divided into *Chandrasekhar-mass models* and *sub-Chandrasekhar-mass models*. In the former, the white dwarf accretes matter from the donor star until its mass approaches the Chandrasekhar limit, when the pressure and the temperature in the center rise until carbon ignites. The explosion happens due to the following mechanism, on which all thermonuclear supernova models are based: Because of the degeneracy of the white dwarf matter, the temperature increase caused by the carbon burning does not immediately lead to an expansion of the star; however, the nuclear reaction rates are a strong function of temperature. Consequently, once the energy released by the carbon burning is too high to be redistributed convectively, the burning leads to a thermonuclear runaway and, after the degeneracy of the matter has been lifted, to the explosion of the white dwarf. The white dwarf matter is entirely ejected into space, leaving no compact remnant.

Many questions remain in this classical model, which was long thought to describe the majority of Type Ia supernovae: Is the combustion mode (cf. Section 2.4) a subsonic deflagration, a supersonic detonation, or does the burning start as a deflagration and eventually turn into a

detonation (*delayed-detonation model* – Khokhlov, 1991)? Is the ignition point in the center or off-center; are there multiple ignition points? Does the deflagration front wrap around the star, before an inwards-directed detonation is triggered (*gravitationally-confined detonation (GCD)* – Plewa et al., 2004)?

In the most common sub-Chandrasekhar-mass model, a C+O white dwarf with significantly less mass than the Chandrasekhar mass accretes helium from a companion. The helium forms a shell around the C+O core. In this shell the helium ignites at one – or many nearby – points; the resulting helium-burning detonation wraps around the C+O core, which is subsequently compressed by the detonation shocks propagating towards the center. Triggered by the compression, the carbon ignites near the center and a second detonation leads to the explosion of the white dwarf, as the energy release due to the thermonuclear burning lifts the degeneracy of the matter and causes a rapid expansion of the hot ashes.

In the *double-degenerate scenario* the companion is a C+O white dwarf itself. The two white dwarfs eventually merge and in one or several hot spots in the interior of the metastable merger remnant a detonation is ignited. In this scenario the total amount of burnt matter can be larger than the Chandrasekhar mass.

All of the above mentioned scenarios have advantages and disadvantages, some match certain observational aspects better and some worse, but currently there is no model, or set of models, that provides a self-consistent picture to explain the observed properties satisfactorily. Therefore, great effort is made to improve the models. In the next section we will give some examples of recent attempts regarding thermonuclear supernova modeling.

### 1.3.3. Modeling of thermonuclear supernovae

The modeling of thermonuclear supernovae using numerical methods made great progress over the last four decades. It started with simple parametrized one-dimensional hydrodynamic models (e.g. Nomoto et al., 1976). Some of those early results matched the observed light curves and spectra astonishingly well, such as the now famous W7 model of Nomoto et al. (1984). However, these early models lack a consistent description of the physical processes. Until today, significant improvement has been achieved in many areas. We will now give a nonexhaustive list of some recent state-of-the-art computations of the different progenitor scenarios, focusing on the results obtained by the research collaboration that is based in Garching and Würzburg.

The Chandrasekhar-mass scenario was examined in two-dimensional hydrodynamic simulations of delayed-detonation models by Kasen et al. (2009); the results show a good agreement with the Philipps relation. Three-dimensional simulations were carried out either assuming deflagration scenarios (Röpke et al., 2006a) or delayed-detonation scenarios (Seitenzahl et al., 2011). The latter introduced a new, physical, way to determine the points in time and space where the detonation ignites (Ciaraldi-Schoolmann et al., in prep., Ciaraldi-Schoolmann, 2012). Fink et al. (2007, 2010) conducted two-dimensional hydrodynamic simulations of the detonation of sub-Chandrasekhar-mass white dwarfs that are surrounded by a

helium shell. Highly resolved simulations of the merger of two white dwarfs were performed by Pakmor et al. (2010, 2012) by means of a *smoothed-particle hydrodynamics (SPH)* computation and subsequent mapping into a grid code.

In order to make reliable assertions of the nature of Type Ia supernovae, it is necessary to compare the results of the hydrodynamic simulations to observational data. In particular, light curves and spectra from observations of Type Ia supernovae are available. These can be compared to *synthetic* light curves and spectra. It is now possible to conduct detailed, multi-dimensional radiative transfer calculations that are based on the results of the hydrodynamic simulations to obtain those synthetic observables (e.g. Sim, 2007; Kromer and Sim, 2009; Kromer et al., 2010; Kasen et al., 2009).

Data about the solar isotopical abundances provide additional information. In *nucleosynthesis* calculations, the abundances of all nuclides synthesized during the supernova are calculated by post-processing the results of the above mentioned hydrodynamic computations. This is frequently achieved by using a tracer particle method (cf. Section 3.1.7). Comparing the nucleosynthesis results to the solar abundances provides useful constraints for several model parameters, as we will discuss in Section 5.3.

Binary population synthesis studies provide information about the frequency of the different progenitor binary systems (Ruiter et al., 2010, 2011). By this way it is possible to make statements on whether the population of a specific progenitor system is large enough to explain the majority of Type Ia supernovae.

Despite all efforts, no particular progenitor model could be confirmed or excluded by these methods so far. Further improvements in the modeling of thermonuclear supernovae together with more advanced observations will certainly shed more light on this interesting topic in the near future.

## 1.4. Neutron stars and the equation of state of dense matter

In the last section we discussed thermonuclear supernovae, which are tightly connected to white dwarfs. Now we turn to neutron stars and give a brief overview of the current status of research, and concentrate on recent insights into the question about the nature of cold dense matter.

We model compact stars as fluids, as is commonly done. Essential for the understanding of compact stars is therefore the *equation of state (EoS)*, which describes the relation between the state variables of a fluid. In our work we understand  $P_X(e, T)$ , the functional dependency of the pressure  $P$  on the total energy density  $e$  (or mass density  $\rho$  in the nonrelativistic case) and temperature  $T$ , for a given composition  $X$ , as “the” equation of state of a particular fluid. A given density corresponds to a low pressure in the case of a *soft* equation of state, whereas for the same density a *stiff* equation of state yields a high pressure. We will discuss several aspects of the respective EoS of compact stars in different parts of this work.

The composition of neutron stars – described by the EoS – is very uncertain, because it is

very challenging to describe cold dense matter, regardless of whether the chosen approach is theoretical, experimental, or observational. From a theoretical point of view, the properties of cold dense matter are well understood up to the neutron drip density  $e_{\text{drip}} \sim 4 \times 10^{11} \text{ g cm}^{-3}$  (Shapiro and Teukolsky, 1983; Camenzind, 2007), at which neutrons start to drip out of nuclei. At higher densities, in particular above the nuclear saturation density  $e_{\text{nuc}} = 2.8 \times 10^{14} \text{ g cm}^{-3}$ , we enter the realm of many-body quantum field theory, in which no analytic solutions exist. Also a numerical approach is difficult and only possible in approximative ways. Depending on the chosen approach and assumptions, several models for the high-density regime exist. We divide them into three groups: hadronic neutron star models, hybrid star models, and strange quark star models. Hadronic neutron stars are neutron stars without deconfined quarks in their interior. In this case, theoretical models (e.g. Weber, 2005) predict a thin atmosphere of hydrogen and helium above a crust consisting of a lattice of heavy nuclei surrounded by free electrons and probably superfluid neutrons. The area at which the density reaches values that inhibit the existence of nuclei defines the boundary to the core, which consists mostly of neutrons, with smaller fractions of protons, electrons, and muons. Some models predict an inner core in which transitions to more exotic phases occur, such as Bose-Einstein condensates of kaons or pions. In other models hyperons appear in the inner core. We will discuss examples of hadronic EoS in Section 2.1.2.

Hybrid stars, the second group, have a crust and an outer core much like hadronic neutron stars, but at some point in the core a phase transition to deconfined quark matter occurs, either with or without a zone of coexisting quark and hadronic matter (*mixed phase*). The quarks in the inner core might be in a color-superconducting phase involving two or three flavors (*two-flavor superconducting (2SC)* or *color-flavor locked (CFL)*, respectively, cf. Madsen (1999) and Weber (2005)).

The third group of neutron star models comprises strange quark stars, which consist entirely of deconfined quarks of the three flavors u, d, and s. Unlike in hybrid star models, the quark matter (called *strange quark matter* because of the defining strangeness content) may be stable also at vanishing pressure. The quark phase can thus extend to the surface of the star. We will discuss strange quark stars in detail in Section 4.1, and again refer to Madsen (1999) and Weber (2005) for further information.

In Section 4 we encounter neutron stars that feature a core of strange quark matter surrounded by a hadronic outer layer – a possibly metastable intermediate state that is not included in the models discussed here. We will refer to these unusual configurations simply as *quark stars*.

Various attempts are made to probe the EoS of dense matter in laboratory experiments, in particular by means of heavy-ion collisions. However, in some large experiments, such as those at the RHIC in Brookhaven and the LHC at CERN, the matter is predominantly “hot”, contrary to the “cold” matter in neutron stars. Furthermore, extreme densities comparable to those at the center of neutron stars are impossible to reach in the laboratory; and the probed matter is necessarily more isospin-symmetric than the neutron-rich matter in neutron stars. Therefore, attempts to experimentally constrain the dense matter EoS are currently restricted

to density ranges found in the crust of neutron stars (e.g. Li et al., 2009).

The EoS can also be constrained by observations of neutron stars. The most important way to achieve this is to measure the mass-radius relation (Lattimer and Prakash, 2004, 2007). The influence of different EoS on the mass-radius relation is explained and visualized in detail in Section 2.2. Unfortunately, until now nobody succeeded in measuring the mass and the radius of one neutron star simultaneously to acceptable accuracy. The currently available simultaneous determinations of mass and radius are inaccurate and highly model dependent. Steiner et al. (2010) applied statistical methods to get useful information from the data, but it was not possible to put conclusive constraints on the EoS.

Precise mass measurements alone can be used to exclude some soft EoS, if very high masses are measured. The observation of a pulsar with  $M = 1.97 M_{\odot}$  (Demorest et al., 2010) that we mentioned in Section 1.1 is therefore an important discovery. Based on that measurement some authors excluded the existence of quark matter in neutron stars; however, Weissenborn et al. (2011) presented models of quark stars with maximum masses above  $2 M_{\odot}$  and could thereby reject this conclusion. Hence, the observation of a  $1.97 M_{\odot}$ -pulsar excluded some specific soft EoS but not an entire group of neutron star models. A discovery of an even more massive neutron star might change that picture; for this reason astronomers continue the look for the most massive pulsars.

Another possible way to constrain the EoS is to observe the decrease in temperature of young neutron stars and compare the data with calculated cooling curves, which depend on the EoS. A prominent example is the neutron star in the supernova remnant Cassiopeia A, which is approximately 300 years old (Blaschke et al., 2012). But due to the theoretical uncertainties and the rareness of suitable objects the results obtained with this method are not yet conclusive either.

## 1.5. Organization of this thesis

We have now introduced several important general aspects concerning compact stars. In the following Chapter 2 we will explain the fundamental concepts on which the main parts of this work are based. These concepts are integrated into our numerical methods that we will present in Chapter 3. The main part of this thesis contains two distinct topics: In Chapter 4 we will discuss the combustion of a hadronic neutron star into a quark star, and in Chapter 5 we treat deflagrations in high-density carbon-oxygen white dwarfs. Concluding remarks in Chapter 6 will close this thesis.

The fundamental considerations of Chapter 2 as well as the numerical methods introduced in Chapter 3 are relevant for both of our main topics: They both cover turbulent deflagration processes in a compact star, and we treat both topics using the same numerical methods with only minor modifications. Even the initial conditions are similar. This large overlap justifies the incorporation of the two topics into one thesis. However, the respective questions approached in Chapter 4 and 5 are obviously too specific to be combined in a natural fashion

into one Introduction and one Motivation. Therefore, we choose to organize this work in a way uncommon for a thesis, as we will introduce and motivate each part separately at the beginning of the respective chapters.

### **Nomenclature and Conventions**

As explained in the previous section, we refer to all compact stars with central densities above nuclear saturation density, namely hadronic neutron stars, hybrid stars, and (strange) quark stars, by the generic term *neutron star*, regardless of the nature of the respective equation of state of the matter comprising the star. The term *quark star* describes compact stars that are partially or entirely made of quark matter, whereas *strange quark stars* consist exclusively of self-bound strange quark matter.

The total energy density, that is the sum of internal energy density and rest mass density, is denoted as  $e$ . This quantity is required for a general relativistic treatment of fluids. In the nonrelativistic case,  $e$  is replaced by the mass density  $\rho$ . The nonrelativistic internal energy is  $E$ , the corresponding specific internal energy is  $\varepsilon$ . Number densities are denoted with  $n$ , for example  $n_B$  for the baryon number density. Other quantities have their usual meaning or are explained when introduced.

We apply the Einstein summation convention, that is summation over all possible values of every index that appears twice in a product is implied. In doing so, Greek indices range from 0 to 3, Latin indices from 1 to 3, if not stated otherwise.

Derivatives with respect to time are, as usual, indicated by a dot above the respective variable.

## 2. Fundamental considerations

In this chapter we describe the fundamental concepts on which this thesis is based. At first we describe the equations of state relevant for white dwarfs, hadronic neutron stars, and strange stars; we will continue with a discussion of hydrostatic configurations of compact stars, explain the concepts of fluid dynamics and combustion, and end with an introduction to the theory of gravitational waves, weak interactions in white dwarf matter, and the emission of neutrinos during thermonuclear burning in white dwarfs.

### 2.1. Equation of state of compact stars

The equation of state (EoS), the pressure as a function of density, temperature, and composition, describes the fluid that constitutes compact stars. An important aspect of the composition is the *electron fraction*  $Y_e$ , which quantifies the degree of neutronization in stellar matter. It is defined as the ratio of the number density of electrons with respect to the number density of baryons ( $Y_e = n_e/n_B$ ), or equivalently as the ratio of the charge number with respect to the mass number ( $Y_e = Z/A$ ) in nuclei.

An EoS is needed to close the system of differential equations in the hydrostatic (Section 2.2.1) as well as the hydrodynamic case (Section 2.3).

#### 2.1.1. White dwarf matter

Degenerate electrons provide the most important contribution to the EoS of white dwarf matter. Their degeneracy pressure supports the white dwarf against gravitational collapse. Contrary to the ongoing debate on the neutron star EoS, there is general agreement on the physical constituents of white dwarf matter. We follow the prescription of the *Timmes EoS* by Timmes and Arnett (1999), see also Röpke (2003) for a more detailed discussion.

In the picture of the Timmes EoS, both energy and pressure are the sum of contributions from electrons, positrons, totally ionized nuclei, and photons,

$$E_{\text{tot}} = E_{e^-} + E_{e^+} + E_{\text{ion}} + E_{\text{rad}}, \quad (2.1)$$

$$P_{\text{tot}} = P_{e^-} + P_{e^+} + P_{\text{ion}} + P_{\text{rad}}. \quad (2.2)$$

The electrons and positrons are described as Fermi gases with variable degree of degeneracy and relativity. The prevalent density and temperature conditions permit the description of the ionized nuclei as an ideal, nonrelativistic Boltzmann gas. The last contribution, energy and

pressure due to radiation, is described by means of the Stefan-Boltzmann law as a local black body.

### 2.1.2. Hadronic nuclear matter

As mentioned several times before, the form of the EoS of matter above nuclear saturation density ( $\rho_{\text{nuc}} = 2.8 \times 10^{14} \text{ g cm}^{-3}$ ) is uncertain and model dependent, because this field eludes exact calculation (cf. Section 1.4).

Various authors computed EoS based on their particular models of high-density matter and provided it to the community for further use. Those EoS have to meet two requirements to be usable in our simulations. Firstly, for reasons of numerical efficiency, the EoS has to be available in tabulated form (cf. Section 3.2.1). Secondly, because we deal with combustion processes which release large amounts of energy, the EoS must have been calculated for finite temperatures. Many calculations of neutron star EoS assume zero temperature, which is an excellent approximation for inert neutron stars but is not suitable in our case.

For our numerical simulations we need both a hadronic EoS, which we introduce in this section, and a quark matter EoS, which we will present in the next section. From the limited choice of hadronic EoS in the literature that fulfill both above stated requirements, we consider the two micro-physical, finite-temperature EoS that are most frequently used in simulations of astrophysical events such as core collapse supernovae and neutron star mergers: the EoS by Lattimer and Swesty (1991) (*LS EoS*) and by Shen et al. (1998) (*Shen EoS*). The LS EoS is based on a nonrelativistic liquid drop model. Lattimer and Swesty (1991) published two versions of their EoS, a softer version (*LS180*) with an incompressibility modulus of  $K = 180 \text{ MeV}$ , and a stiffer version (*LS220*) with  $K = 220 \text{ MeV}$ . For calculating the Shen EoS relativistic mean field theory was applied, here  $K = 280 \text{ MeV}$  is adopted.

The recent measurement of the Shapiro delay of the binary millisecond pulsar J1614-2230 (Demorest et al., 2010) yields a gravitational mass of the pulsar of  $M = (1.97 \pm 0.04) M_{\odot}$  (cf. Section 1.4). In contrast to the Shen EoS, the LS EoS, in particular LS180, is rather soft. Consequently it leads to a maximum mass for a hadronic non-rotating neutron star of only  $M_{\text{max}}^{\text{LS180}} \sim 1.8 M_{\odot}$  and is therefore in conflict with the observations of pulsar J1614-2230, whereas LS220 EoS and Shen EoS are compatible with this observation (see also Section 2.2.3, where we present our calculations of maximum masses for different EoS).

### 2.1.3. Strange quark matter

We describe strange quark matter (SQM) by a simple bag model for finite temperatures (Cleymans et al., 1986) based on the MIT bag model (Chodos et al., 1974). This model treats strange quark matter as three noninteracting, ideal Fermi gases of massless u-, d-, and s-quarks, respectively, inside a confining bag. This bag is described by a constant pressure  $B$  that acts contrary to the individual Fermi pressures of the quark gases. In this approximation the chemical potential of all quark flavors is equal and hence the system can be described by

a single chemical potential  $\mu$ . Consequently, the number density of all quark flavors is equal as well, and the quark charges balance each other – the matter contains no electrons. The total pressure is

$$P = \sum_{i=u,d,s} P_i - B. \quad (2.3)$$

Now we take finite temperatures into account. Following Madsen (1999), we get contributions to the thermodynamic potential  $\Omega$  from the quarks,

$$\Omega_q = - \left( \frac{7\pi^2}{60} T^4 + \frac{\mu^2 T^2}{2} + \frac{\mu^4}{4\pi^2} \right) V, \quad (2.4)$$

and the gluons

$$\Omega_g = - \frac{8\pi^2}{45} T^4 V, \quad (2.5)$$

where  $T$  is the temperature and  $V$  the volume of the system. We now obtain the total pressure,

$$P = - \frac{\partial (\Omega_q + \Omega_g)}{\partial V} - B \quad (2.6)$$

$$= \frac{19}{36} \pi^2 T^4 + \frac{3}{2} T^2 \mu^2 + \frac{3}{4\pi^2} \mu^4 - B. \quad (2.7)$$

By inserting the EoS for an ideal gas of massless particles,  $e_i = 3P_i$ , we get an expression for the total energy  $e$ ,

$$e = \sum_{i=u,d,s} e_i + B \quad (2.8)$$

$$= \frac{19}{12} \pi^2 T^4 + \frac{9}{2} T^2 \mu^2 + \frac{9}{4\pi^2} \mu^4 + B. \quad (2.9)$$

For the baryon number density  $n$  we obtain

$$n = T^2 \mu + \frac{1}{\pi^2} \mu^3. \quad (2.10)$$

Equations (2.7) and (2.9) can be combined to the simple pressure-density relation

$$P = \frac{1}{3} (e - 4B). \quad (2.11)$$

The value of the bag constant  $B$  is not known; however, some constraints can be derived. We can specify a lower limit of  $B$  due to the fact that nucleons do not decay spontaneously

into two-flavor quark matter. Madsen (1999) shows that this lower limit is  $B^{1/4} \geq 145 \text{ MeV}$  and gives an expression for the energy per baryon,  $E/A$ , as function of  $B$ ,

$$E/A = 829 \text{ MeV} \frac{B^{1/4}}{145 \text{ MeV}}. \quad (2.12)$$

Because nuclear matter has an energy per baryon of  $E/A \sim 930 \text{ MeV}$ , according to (2.12) bag constants lower than  $B^{1/4} = 160 \text{ MeV}$  correspond to strange quark matter that is stable at zero pressure (*absolutely stable strange quark matter*).

The next step to a more realistic EoS would be to include the masses of the quarks. Although the current masses of u- and d-quarks are at most  $10 \text{ MeV}$  and are therefore negligible, the mass of the s-quark is of the order of  $100 \text{ MeV}$ . However, in this case an analytic expression for  $P$ ,  $e$  and  $n$  is no longer possible for finite temperatures. Including quark masses as well as QCD interactions (Farhi and Jaffe, 1984) leads, for example, at a given  $B$  to an energy per baryon which is about  $20 \text{ MeV}$  higher than given by equation (2.12) (Bauswein et al., 2010) and thus shifts the range of bag constants in which strange quark matter is absolutely stable.

## 2.2. Hydrostatic configurations of compact stars

In this section we will discuss hydrostatic configurations of compact stars. We will first introduce the equations of hydrostatic equilibrium and then present various examples. The calculation of those configurations serves several purposes. They help to get a general picture about some properties of the different families of compact stars, and they enable us to compare characteristic features of different equations of state. Furthermore, we use some of the hydrostatic solutions presented here as initial models for our hydrodynamic simulations (cf. Sections 4.4.1 and 5.2.1).

### 2.2.1. Equations of hydrostatic equilibrium

Based on a static and spherically symmetric metric, the solution of the Einstein equations are two coupled partial differential equations,

$$\frac{dM(r)}{dr} = 4\pi e(r) r^2 \quad (2.13)$$

$$\frac{dP(r)}{dr} = -\frac{GM(r)e(r)}{r^2} \left(1 + \frac{P(r)}{e(r)c^2}\right) \left(1 + \frac{4\pi r^3 P(r)}{M(r)c^2}\right) \left(1 - \frac{2GM(r)}{rc^2}\right)^{-1}. \quad (2.14)$$

$G$  is Newton's gravitational constant,  $P(r)$  is the pressure,  $e(r)$  is the total energy density including the rest mass density, and  $M(r)$  is the gravitational mass inside the radial coordinate  $r$ ,

$$M(r) = 4\pi \int_0^r e(r') r'^2 dr'. \quad (2.15)$$

Equations (2.13–2.14) are commonly called *Tolman-Oppenheimer-Volkov (TOV) equations* (Tolman, 1939; Oppenheimer and Volkoff, 1939), for a derivation using a modern formalism see e.g. Camenzind (2007).

To obtain the much simpler Newtonian equations of hydrostatic equilibrium, we set  $c \rightarrow \infty$  and replace the total energy density  $e$  by the mass density  $\rho$ , and get

$$\frac{dM(r)}{dr} = 4\pi\rho(r)r^2 \quad (2.16)$$

$$\frac{dP(r)}{dr} = -\frac{GM(r)\rho(r)}{r^2}. \quad (2.17)$$

Equation (2.17) can also be derived by simply balancing pressure and gravitational forces. Equations (2.13–2.14) or (2.16–2.17) can not be solved without defining a relation between the pressure and the density, the equation of state. After having chosen an EoS, we can pick an initial value, for instance the density in the center  $\rho_c$ , and integrate equations (2.13–2.14) or (2.16–2.17) using a simple numerical integration scheme (e.g. Runge-Kutta methods). As a result we obtain the mass and the radius of the star, and density and pressure profiles.

We choose the central density as an initial value, and by varying it we get for a given EoS mass-radius and mass-central density relations. These relations are a valuable tool to examine the influence of different EoS on the properties of compact stars. Examples using different EoS, both for white dwarfs and neutron stars, are presented in Section 2.2.3.

### 2.2.2. Limiting mass and stability of compact stars

With the help of several examples we will see in the next section that we do not obtain arbitrarily high masses when we solve the equations of hydrostatic equilibrium (2.13–2.14). Instead, an upper limit of the resulting masses exists. This limiting mass is characteristic for the employed EoS. A physical explanation for this behavior is that the degeneracy pressure cannot support arbitrarily high masses – if a compact star exceeds its maximum mass, the degeneracy pressure can no longer compensate the gravitational forces and the star will collapse to a more compact object. In such a case, a carbon-oxygen white dwarf will collapse to a neutron star, whereas a neutron star will collapse to a black hole. Because the limiting mass is tightly connected to the EoS, it is not surprising that the value is well known for white dwarfs but uncertain for neutron stars.

Chandrasekhar (1931) derived an approximation to the limiting mass of white dwarfs, which is now called *Chandrasekhar limit*. In terms of the electron fraction  $Y_e$  it can be expressed as

$$M_{\text{ch}} = 1.457 \left( \frac{Y_e}{0.5} \right)^2 M_{\odot}. \quad (2.18)$$

Its derivation is exclusively based on Fermi-Dirac statistics. A more realistic treatment, including contributions from ions and photons in the EoS, as well as accounting for general

## 2. Fundamental considerations

---

relativistic effects, yields a slightly lower limiting mass, as we will see in Section 2.2. Chandrasekhar (1931) assumed  $Y_e = 0.4$  and consequently obtained a limiting mass below  $1 M_\odot$ . Today, the electron fraction of white dwarfs is believed to be slightly below 0.5; therefore, a value of  $1.4 M_\odot$  is often adopted as the Chandrasekhar limit.

The limiting mass of neutron stars is sometimes called *Tolman-Oppenheimer-Volkoff (TOV) limit*. As said before, it depends strongly on the EoS, but there are some model-independent constraints on the limiting mass. A lower limit is set by neutron star observations to  $\sim 2 M_\odot$ , as discussed in Section 1.1. It is possible to estimate a firm upper limit based on the fundamental conditions that any EoS has to meet, such as causality (the speed of sound must not exceed the speed of light) and a monotonously increasing density with increasing pressure ( $\partial P / \partial \rho \geq 0$ ). These two conditions lead to a theoretical upper limit of  $3.2 M_\odot$  (Rhoades and Ruffini, 1974).

Not all solutions of the equations of hydrostatic equilibrium (2.13–2.14) are hydrostatically stable. A criterion for hydrostatic stability of compact stars can be written as<sup>1</sup> (Friedman et al., 1988; Cook et al., 1992)

$$\frac{\partial M}{\partial \rho_c} \geq 0. \quad (2.19)$$

If this condition is not fulfilled, small radial perturbations will grow and lead to a collapse of the star, with the same consequences as in the case in which the maximum mass is exceeded. In the next section we will use this condition to calculate the maximum central density for compact stars of a given EoS.

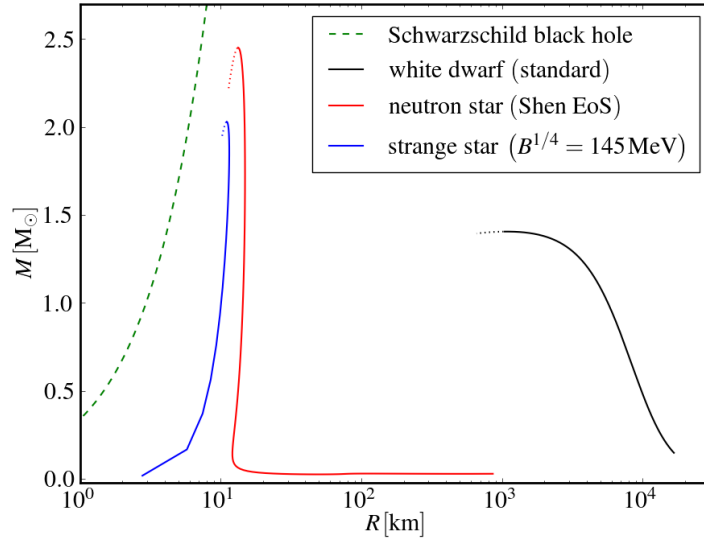
### 2.2.3. Examples of hydrostatic configurations of compact stars

In the following we calculate examples of hydrostatic configurations of compact stars, using the equations of state that we introduced in Section 2.1. Most examples shown in this section are solutions of the relativistic equations (2.13–2.14), only a few solutions of the Newtonian equations (2.16–2.17) are presented. Both variants of the equations of hydrostatic equilibrium are solved by simple numerical integration. As mentioned above, by varying the initial value of the integration, we get, for each EoS, a mass-radius and mass-central density relation. With the help of these relations we will discuss and put some constraints on the properties of compact stars with different EoS.

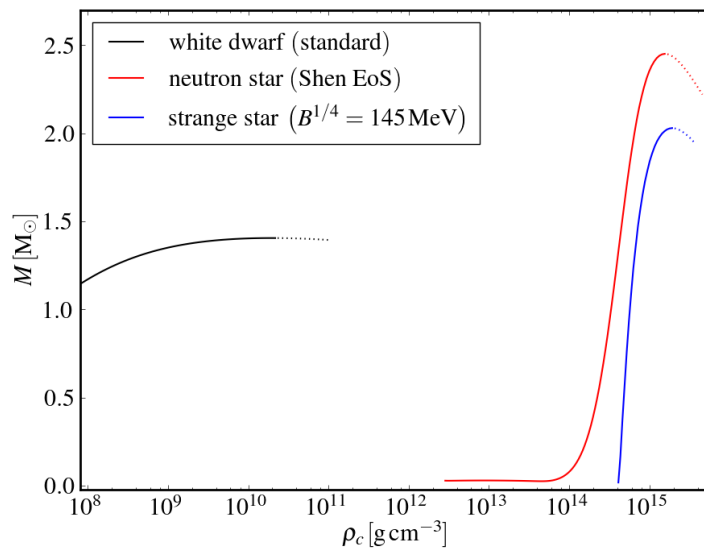
We start with an overview of the mass-radius relations of all compact stars discussed in this work, shown in Figure 2.1 (a). The dashed curve in the upper left corresponds to the Schwarzschild radius of a black hole of mass  $M$ , as a way to quantify the mass-radius relation of black holes. It is displayed to complete the three families of compact objects. The maximum mass of neutron stars is very close to that line, illustrating the high compactness of neutron stars. Remarkable is the gap between  $\sim 20$  km and  $\sim 1000$  km; no massive compact

---

<sup>1</sup>This criterion has to be evaluated along curves of constant angular momentum. We are considering only nonrotating stars; in that case, the angular momentum is always zero.



(a)



(b)

**Figure 2.1.** Mass-radius (a) and mass-central density (b) relation for typical strange stars, neutron stars, and white dwarfs. In both panels, the dotted parts of the curves resemble hydrostatically unstable configurations. The dashed line in (a) indicates the radius of a Schwarzschild black hole of mass  $M$ .

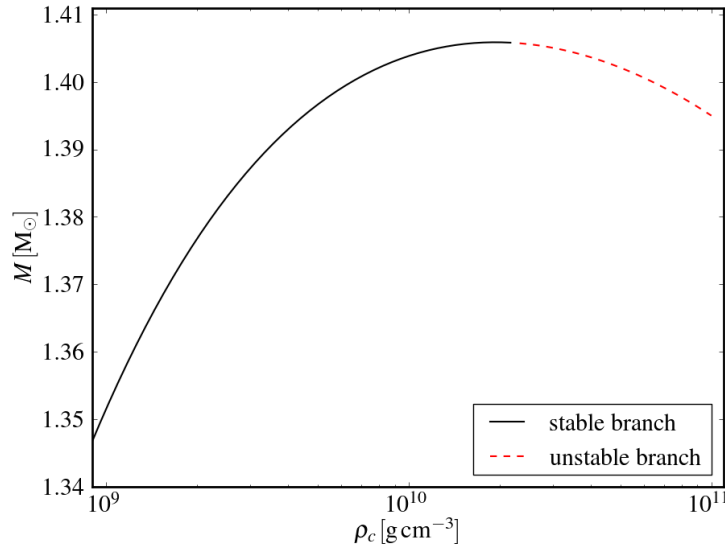
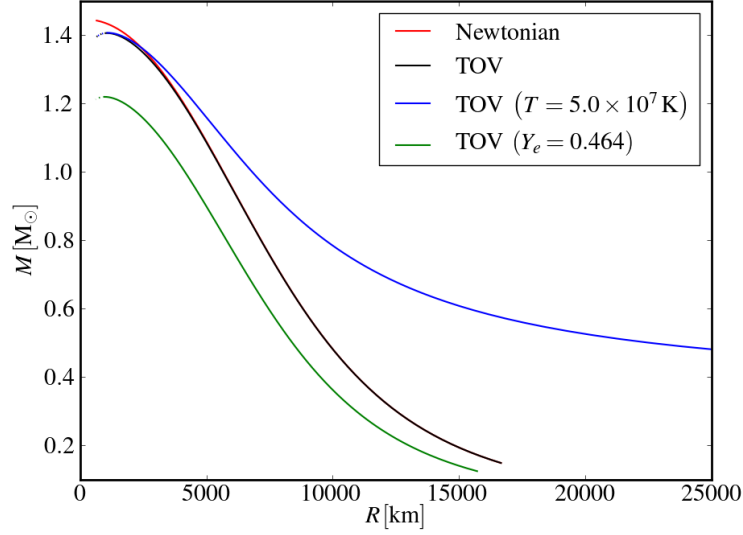


**Figure 2.2.:** Mass-central density relation for white dwarfs near maximum mass. The red dashed part represents the hydrostatically unstable branch.

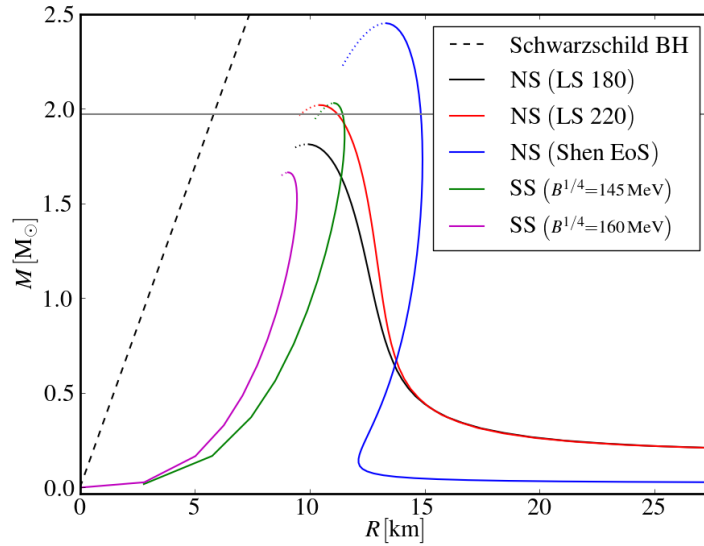
stars exist in this range. This makes it possible to distinguish observationally between neutron stars and white dwarfs by estimating the radius of the compact star.

Figure 2.1 (b) is a plot of the relation between mass and central density for the same configurations that are shown in Figure 2.1 (a). Just like the gap between neutron star and white dwarf radii, a large gap exists between the typical central densities of neutron stars and white dwarfs in the central density range  $\rho_c = 5 \times 10^{10}$  to  $1 \times 10^{14} \text{ g cm}^{-3}$ . We again present the mass-central density relation in Figure 2.2, this time a close-up of the region near the limiting mass of white dwarfs is shown. By using condition (2.19) we can divide the curve into hydrostatically stable and unstable branches. We apply this method to all EoS, the dotted part of each curve in Figures 2.1 and 2.3 represents the branch of configurations which do not fulfill the stability condition (2.19) and are consequently unstable.

It is visible in Figure 2.2 that here the configuration of maximum mass is also the configuration of maximum central density, and we obtain from our calculations an EoS-dependent upper limit for the central density of white dwarfs. Knowledge of this quantity will be important for us in the discussion of high-density white dwarfs in Section 5. From Figure 2.2 we can derive a maximum central density of C+O white dwarfs with solar metallicity of  $\rho_c^{\text{max}} \sim 2 \times 10^{10} \text{ g cm}^{-3}$ . An analytical investigation on general relativistic instabilities in ideal Fermi gases yields a similar result, Camenzind (2007) obtains  $\rho_c^{\text{max,th}} = 2.65 \times 10^{10} \text{ g cm}^{-3}$ . The maximum central density of neutron stars is, like the limiting mass, uncertain because it depends on the EoS. The hadronic as well as quark EoS we use in this work lead to a maximum



(a)



(b)

**Figure 2.3.:** (a) Mass-radius relation for white dwarfs, using the EoS described in Section 2.1.1.  $T = 5 \times 10^5$  K and  $Y_e = 0.498864$  except for the blue ( $T = 5 \times 10^7$  K,  $Y_e$  unchanged) and green ( $Y_e = 0.464$ ,  $T$  unchanged) curve. The red curve results from a purely Newtonian calculation without a general relativistic potential. (b) Mass-radius relation for different strange stars and hadronic neutron stars. The dashed line indicates the Schwarzschild radius of a black hole of mass  $M$ . The gray horizontal line corresponds to the mass of pulsar J1614-2230. In both panels, the dotted parts of the curves resemble hydrostatically unstable configurations.

## 2. Fundamental considerations

---

central densities in the range  $1 \times 10^{15}$  to  $2 \times 10^{15} \text{ g cm}^{-3}$  (cf. Figure 2.1 b).

The mass-radius relation for white dwarfs with different properties is presented in Figure 2.3 (a). Here we use the same EoS (cf. Section 2.1.1) for all calculations. As standard values we choose a low temperature of  $T = 5 \times 10^5 \text{ K}$  and a solar electron fraction of  $Y_e = 0.498864$ ; variations of these values lead to the blue and green curve. Our calculations yield a limiting mass of  $M_{\text{lim}} = 1.406 M_{\odot}$ , which is 3.5 % lower than the one derived by Chandrasekhar, according to equation (2.18). This equation predicts that lowering the  $Y_e$  leads to a strongly decreased limiting mass. This is confirmed by the numerical results, clearly visible in the green curve in Figure 2.3 (a). We calculated this curve by setting the electron fraction to  $Y_e = 0.464$ , which corresponds to the  $Y_e$  of hypothetical iron white dwarfs<sup>2</sup> made of  $^{56}\text{Fe}$ . In this case the maximum mass drops to  $M_{\text{lim}}^{\text{Fe-WD}} = 1.22 M_{\odot}$ .

The blue curve in Figure 2.3 (a) shows the mass-radius relation of hot white dwarfs. Here we increased the temperature by a factor of 100 to  $T = 5 \times 10^7 \text{ K}$ . High temperatures lead to extremely inflated radii of low-mass configurations, up to  $10^5 \text{ km}$ . At high masses no difference to the cold configurations is visible, because the high degeneracy of the dense matter reduces the influence of the temperature on the EoS.

In addition, we calculated one curve without general relativistic corrections by solving equations (2.16–2.17). This curve is distinguishable from the one including relativistic corrections only at high masses (see Figure 2.3 a). We calculated the hydrostatic solutions up to  $\rho_c = 1 \times 10^{11} \text{ g cm}^{-3}$ , where the validity of our implementation of the white dwarf EoS becomes doubtful. Condition (2.19) is fulfilled everywhere, no unstable branch can be identified. Consequently, it is impossible to determine a maximum central density with these data; therefore, it is important to include general relativistic corrections when the maximum central density and maximum mass are determined, although the compactness of a configuration near the limiting mass is still lower, by nearly two orders of magnitude, than that of a typical neutron star.

Figure 2.3 (b) shows the mass-radius relation for different hadronic neutron stars and strange stars. Also here the event horizon of a Schwarzschild black hole is indicated. The differences between the curves result only in changes of the EoS, the temperature and electron fraction are kept constant. The figure shows the vast differences between the various EoS. Also between the different hadronic EoS the discrepancies are huge. As mentioned before, the mass-radius relation is a common way to constrain the EoS, especially for neutron stars. Already one accurate simultaneous measurement of the radius and the mass of a neutron star would most likely exclude a number of EoS, as can be imagined from Figure 2.3 (b). But this figure also makes it clear that there exist degeneracies, for example the mass-radius relations of hadronic neutron stars with the LS180 EoS and strange stars with  $B^{1/4} = 145 \text{ MeV}$  intersect near their respective maximum masses, although they show completely different behavior at lower masses. This degeneracy explains why it is so difficult to distinguish observationally between

---

<sup>2</sup>According to current stellar evolution theory no iron white dwarfs exist, because the iron cores of massive stars collapse instead of surviving as white dwarfs.

hadronic neutron stars and strange stars.

## 2.3. Fluid dynamics

Up to now, we only discussed *static* configurations of the fluids that constitute compact stars in our models. In this section, however, we explain how to describe the *dynamic*, time-dependent behavior of the fluid. The field that treats the flow of fluids is accordingly called *fluid dynamics*; in this work, and in astrophysics in general, it is also frequently called *hydrodynamics*. To reduce the complexity of the governing equations and make their solution computationally less expensive, we make two important simplifications. Firstly, we consider only Newtonian dynamics and neglect the influence of relativistic effects on the fluid flow<sup>3</sup>. These effects are negligible in the case of white dwarfs because of their low compactness (e.g. Röpke, 2003), whereas in the case of neutron stars the error originating from the uncertain EoS dominates the total error.

Secondly, we neglect the viscosity of the fluid and treat the fluid as an inviscid, *ideal* fluid, a common approximation in numerical astrophysics. Viscosity becomes important only on very small scales that we cannot resolve in our simulations, whereas on resolved scales the discretization error is considerably larger than the error introduced by neglecting viscosity (e.g. Röpke, 2003; Reinecke, 2001). For the same reasons it is justified to neglect other *dissipative processes* such as diffusion and heat conduction.

The following is based on the classical textbook of Landau and Lifshitz (1987), and on Toro (1997) and LeVeque (1998), who focus more on numerical aspects. See also Röpke (2003) and Reinecke (2001).

Ideal flows are governed by the Euler equations, each expressing one conservation law, together forming a set of hyperbolic partial differential equations. Conservation of mass is expressed by the *equation of continuity*,

$$\frac{\partial \rho}{\partial t} + \nabla \cdot (\rho \mathbf{v}) = 0, \quad (2.20)$$

with the mass density  $\rho$  and the three-dimensional velocity vector of the fluid  $\mathbf{v}$ . Momentum conservation leads to

$$\frac{\partial \rho \mathbf{v}}{\partial t} + \nabla \cdot (\rho \mathbf{v} \otimes \mathbf{v}) + \nabla P = 0, \quad (2.21)$$

where an external-force term  $\rho \mathbf{f}$  might be added on the right-hand side.  $P$  is the pressure. The third equation expresses conservation of energy,

$$\frac{\partial}{\partial t} \left( \frac{\rho v^2}{2} + \rho \varepsilon \right) + \nabla \cdot \left( \rho \mathbf{v} \left( \frac{v^2}{2} + w \right) \right) = 0, \quad (2.22)$$

---

<sup>3</sup>However, we take some effects of general relativity into account by applying an effective relativistic gravitational potential, see Section 3.2.3.

## 2. Fundamental considerations

---

with the internal energy density  $\varepsilon$  and the enthalpy density  $w = \varepsilon + P/\rho$ . Again, an external-force term  $\rho \mathbf{v} \cdot \mathbf{f}$  might be added on the right-hand side. Furthermore, if the energy is changed because of energy release in chemical or nuclear reactions, an additional source term  $\rho S$  appears on the right-hand side.

Analogous to the hydrostatic case, an equation of state is needed to close this system of partial differential equations.

Decomposing the Euler equations into components allows us to write them in a vectorial *flux form*, which we will later use to solve them numerically. To this end we define the *state vector*  $\mathbf{U}$ , which contains the conserved quantities, as

$$\mathbf{U} = \begin{pmatrix} \rho \\ \rho v_x \\ \rho v_y \\ \rho v_z \\ \rho \varepsilon \end{pmatrix}, \quad (2.23)$$

and the *flux vectors*  $\mathbf{F}_i$

$$\mathbf{F}_x = \begin{pmatrix} \rho v_x \\ P + \rho v_x^2 \\ \rho v_x v_y \\ \rho v_y v_z \\ \rho v_x w \end{pmatrix}, \quad \mathbf{F}_y = \begin{pmatrix} \rho v_y \\ \rho v_x v_y \\ P + \rho v_y^2 \\ \rho v_y v_z \\ \rho v_y w \end{pmatrix}, \quad \mathbf{F}_z = \begin{pmatrix} \rho v_z \\ \rho v_x v_z \\ \rho v_y v_z \\ P + \rho v_z^2 \\ \rho v_z w \end{pmatrix}. \quad (2.24)$$

We can now write equations (2.20–2.22) as

$$\frac{\partial \mathbf{U}}{\partial t} + \frac{\partial \mathbf{F}_x}{\partial x} + \frac{\partial \mathbf{F}_y}{\partial y} + \frac{\partial \mathbf{F}_z}{\partial z} = 0. \quad (2.25)$$

This way to write the Euler equations shows clearly that a change of the conserved quantities with time is only caused by gradients of the fluxes.

The concept of conservation laws becomes even clearer in the *integral form* of the Euler equations. In order to derive them, we consider a conserved quantity  $Q$  and its density  $q(x, t)$  that could be any of the components of the state vector  $\mathbf{U}$  as defined in equation (2.23). For simplicity, we restrict ourselves to one dimension, generalization to three dimensions is straightforward. We consider an interval  $[x_1, x_2]$ ; anticipating our numerical method described in Section 3.1.1, we may call this interval a *grid cell*. At a time  $t$ , the total amount of a conserved quantity  $Q$  in this grid cell is

$$Q(t) = \int_{x_1}^{x_2} q(x, t) dx. \quad (2.26)$$

The *flux*  $f(x, t)$  of the fluid is given by

$$f(x, t) = q(x, t)v(x, t), \quad (2.27)$$

with the fluid velocity  $v(x, t)$ . The grid cell  $[x_1, x_2]$  can only lose or gain some amount of  $Q$  due to fluxes at its boundaries  $x_1$  and  $x_2$ ; therefore, the difference in fluxes at  $x_1$  and  $x_2$  has to be the rate of change of  $Q$  in the cell,

$$\frac{d}{dt} \int_{x_1}^{x_2} q(x, t) dx = q(x_1, t) v(x_1, t) - q(x_2, t) v(x_2, t). \quad (2.28)$$

This form of the conservation laws is usually called the *integral form*. When we conduct a time integration of equation (2.28) in the interval  $[t_1, t_2]$ , we obtain:

$$\int_{x_1}^{x_2} q(x, t_2) dx - \int_{x_1}^{x_2} q(x, t_1) dx + \int_{t_1}^{t_2} q(x_2, t) v(x_2, t) dt - \int_{t_1}^{t_2} q(x_1, t) v(x_1, t) dt = 0 \quad (2.29)$$

If  $q(x, t)$  and  $v(x, t)$  are differentiable, we can use

$$q(x, t_2) - q(x, t_1) = \int_{t_1}^{t_2} \frac{\partial}{\partial t} q(x, t) dt \quad (2.30)$$

and

$$q(x_2, t) v(x_2, t) - q(x_1, t) v(x_1, t) = \int_{x_1}^{x_2} \frac{\partial}{\partial x} (q(x, t) v(x, t)) dx \quad (2.31)$$

to obtain

$$\int_{t_1}^{t_2} \int_{x_1}^{x_2} \left( \frac{\partial}{\partial t} q(x, t) + \frac{\partial}{\partial x} (q(x, t) v(x, t)) \right) dx dt = 0. \quad (2.32)$$

This has to hold for any space interval  $[x_1, x_2]$  and any time interval  $[t_1, t_2]$ . Hence the integrand has to vanish, and we recover the Euler equations in the differential form of the conservations laws:

$$\frac{\partial}{\partial t} q(x, t) + \frac{\partial}{\partial x} (q(x, t) v(x, t)) = 0. \quad (2.33)$$

In Section 3.1.1 we will describe our numerical method to solve the Euler equations. It is based on the integral form shown in equation (2.28).

## 2.4. Combustion

### 2.4.1. Basic concepts of combustion theory

A central concept in this work is *combustion*, also known as *burning*. Combustion may be defined as a series of exothermic reactions that release energy as heat. It is usually introduced in the context of chemical burning, where a *fuel* changes its composition after reacting with an *oxidant*. This concept is well-known and we encounter it regularly in everyday life, be it in car

## 2. Fundamental considerations

---

and jet engines, candles and campfires, or power plants and steel mills. In this work, however, we will apply it to two different, astrophysical, contexts far from chemical flames. In white dwarfs we treat *thermonuclear burning*, where nuclear fusion reactions conceptually replace the chemical reactions. In this case it is straightforward to transfer the concepts of combustion to the new environment. Furthermore, we will model the *conversion of hadronic matter into strange quark matter* in neutron stars as a combustion process. Although less intuitive than in the case of thermonuclear burning, it is possible and useful to apply the concept of combustion here as well. We will now briefly introduce basic concepts of combustion theory. For a detailed discussion see Peters (2000), Reinecke (2001) and Röpke (2003).

Combustion processes occur in various different modes and regimes. Burning can take place simultaneously in a large volume, or it may happen in a thin reaction layer, forming a *flame*. Flames can propagate supersonically as shock-driven *detonations*, or subsonically and diffusion-driven as *deflagrations*. In both topics that we will discuss in this thesis, the fuel does not need any other agent (“oxidant”) for burning and energy release. The analogous case in chemical combustion theory is called *premixed combustion*, where the fuel and an oxidizing agent are already mixed at low temperatures and the flame propagates, in the deflagration case, by conduction of heat (Peters, 2000).

In the following we will only discuss the concepts of premixed combustion that propagates subsonically in a thin reaction layer. We will motivate this decision in Section 4 for the conversion of hadronic matter into strange quark matter, and in Section 5 for thermonuclear burning in high-density carbon-oxygen white dwarfs. In the latter case, as in chemical flames, the flame propagates by conduction of heat; in the former case, the abundance of s-quarks plays the role of temperature, accordingly the diffusion of s-quarks leads to the propagation of the flame front.

The most consistent approach to model the combustion processes in compact stars would be to solve the *reactive Euler equations* after having inserted adequate reaction terms into the Euler equations (2.20–2.22). However, the flame physics happens on very small scales compared to the scales that we can resolve in our simulations; therefore, we have to treat the burning in an approximative way. In this work, we apply the *discontinuity approximation*. In this picture, the flame is modeled as a discontinuity in the *state variables* such as density, pressure, and energy density. The discontinuity, or *flame front*, separates the unburnt fuel from the burnt ashes; all information about the internal structure of the flame is lost. The flame front propagates at the *laminar burning velocity*  $v_{\text{lam}}$  relative to the surrounding fluid into the unburnt material. Because we neglect all internal flame physics in the discontinuity approximation,  $v_{\text{lam}}$  cannot be determined directly in our computations but acts as an external parameter that has to be determined by detailed small-scale calculations (e.g. Timmes and Woosley, 1992). In the respective Sections 4 and 5 we will describe which burning velocity we prescribe in our simulations.

### 2.4.2. Turbulent combustion

Under certain conditions the laminar propagation of the combustion front can be distorted by Rayleigh-Taylor (buoyancy) instabilities (see Timmes and Woosley (1992) and references therein). A necessary condition for unstable burning is that the gradient of the gravitational potential and the gradient of the total energy density point in opposite directions (*inverse density stratification*).

Rayleigh-Taylor instabilities can only grow and lead to turbulent motion if the perturbations of the front exceed some minimal length scale,  $\lambda_{\min}$ , which depends on the burning velocity  $v_{\text{lam}}$ , the gravitational acceleration  $g$ , and the density contrast between the total energy density of the unburnt phase  $e_{\text{unburnt}}$  and the total energy density of the burnt phase  $e_{\text{burnt}}$  (Timmes and Woosley, 1992),

$$\lambda_{\min} = 2\pi v_{\text{lam}}^2 \left( g \frac{e_{\text{unburnt}} - e_{\text{burnt}}}{e_{\text{unburnt}} + e_{\text{burnt}}} \right)^{-1}. \quad (2.34)$$

We calculate  $\lambda_{\min}$  in the case of the conversion of hadronic matter into strange quark matter for different setups in Section 4.4.2.

In the established heuristic turbulence model (Richardson, 1922; Kolmogorov, 1941) instabilities such as the Rayleigh-Taylor instability (and secondary shear instabilities) lead to turbulent eddies on large scales, which decay successively into ever smaller eddies until, at the Kolmogorov length scale  $l_K$ , viscosity effects dissipate the smallest eddies into thermal energy. In this *turbulent cascade* kinetic energy is transported from the largest to the smallest scales and is finally dissipated. Or, as Lewis Fry Richardson (1922) famously wrote:

Big whirls have little whirls  
that feed to their velocity  
and little whirls have lesser whirls  
and so on to viscosity.

This picture assumes that magnetic fields do not significantly affect the dynamics. For the velocity fluctuation  $v(l)$  on a given scale  $l$ , which can be interpreted as the turnover velocity of an eddy of size  $l$ , this model yields the *Kolmogorov scaling* (Landau and Lifshitz, 1987),

$$v(l) = v(L) \left( \frac{l}{L} \right)^{1/3}, \quad (2.35)$$

where  $L$  is the integral scale, the size of the largest eddies.

An important quantity to describe turbulent flows is the dimensionless *Reynolds number*  $Re = vl\rho/\mu$ , which quantifies the ratio between inertial and viscous forces;  $l$  is a characteristic length scale,  $v$  is a characteristic velocity and  $\mu$  the dynamic viscosity of the fluid.

## 2. Fundamental considerations

---

According to equation (2.35), the Reynolds number on different scales is

$$Re(l) = Re(L) \left( \frac{l}{L} \right)^{4/3}, \quad (2.36)$$

since  $Re(l) \propto v(l)l$ .

At the Kolmogorov scale  $l_K$  holds, by definition,  $Re(l_K) = 1$ , so if we know the Reynolds number on the integral scale  $L$  we can estimate  $l_K$  by

$$l_K = L \left( \frac{1}{Re(L)} \right)^{3/4}. \quad (2.37)$$

The scale on which the eddy turnover velocity is equal to the laminar burning velocity is defined as the Gibson scale  $l_G$  (e.g. Peters, 2000),

$$v(l_G) = v_{\text{lam}}. \quad (2.38)$$

Turbulence cannot distort the flame front on scales smaller than  $l_G$  because according to equation (2.35) on these scales the eddy turnover velocity is smaller than the laminar burning velocity, whereas on scales larger than  $l_G$ , the turbulent eddies alter the shape of the flame front.

A special case arises if

$$l_{\text{burn}} < l_G < l_{\text{resolved}} \quad (2.39)$$

holds. Relation (2.39) leads to two important consequences:  $l_{\text{burn}} < l_G$  means that the turbulent eddies cannot disturb the flame front. Thus, it can still be described as a well-defined discontinuity. The burning is said to take place in the *flamelet regime* (Peters, 2000): Although the internal flame structure is not disturbed, the total burning rate is enhanced as turbulence alters the geometry and thus enlarges the surface of the front. Because  $l_G < l_{\text{resolved}}$  the surface of the flame front is also enhanced on unresolved scales, leading to an increase in the effective front propagation velocity on these scales. This effective velocity is described by the *turbulent burning velocity*  $v_{\text{turb}}$ , which is defined as the mean propagation velocity of the flame front at the marginally resolved scale. For strong turbulence, the turbulent burning velocity becomes independent of the laminar burning velocity.

Simulations in which the relevant length scales follow condition (2.39), and in which the turbulent motions on smaller, unresolved scales are described by some physical model, are called *large eddy simulations (LES)*. Also in our simulations we resolve the largest scales of the turbulent fluid motion, but rely on a *subgrid scale (SGS) model* to take the turbulence on unresolved scales into account. We will describe our numerical approach to conduct LES in Section 3.1.6.

### 2.4.3. Estimation of relevant length scales

We will now use the concepts introduced in the preceding section to estimate the length scales concerning turbulent burning in the physical environments that we will encounter in the subsequent chapters.

The combustion theory was developed for chemical flames and adapted to thermonuclear supernovae (Niemeyer and Woosley, 1997; Niemeyer and Kerstein, 1997). The Kolmogorov scaling was found to fit quite well in the case of burning in white dwarfs (Ciaraldi-Schoolmann et al., 2009; Zingale et al., 2005). Hence we can use the expressions introduced in the preceding section to estimate the length scales concerning turbulent combustion in white dwarfs. This estimation was already done several times, we will now show the results of Röpke (2003). In flows around a Rayleigh-Taylor bubble of size  $L \approx 10^7$  cm in burning white dwarf matter he obtained Reynolds numbers of  $Re(L) \sim 10^{14}$ . Applying equation (2.37) yields a corresponding Kolmogorov scale of  $l_K = 10^{-3}$  cm. Depending on the density and composition of the fuel, the Gibson length  $l_G$  varies in a wide range between  $10^1$  and  $10^7$  cm.

Until now, the concepts of turbulent combustion were never applied to model the conversion of hadronic matter into strange quark matter in neutron stars, although this approach was suggested several times (e.g. Horvath and Benvenuto, 1988; Horvath, 2010). As mentioned above, the Kolmogorov scaling provides a good fit to the thermonuclear burning in white dwarfs. Based on these results and in the absence of exact calculations we draw an analogy and assume that also the conversion of hadronic matter into strange quark matter, modeled as a combustion, follows the Kolmogorov scaling. We are therefore able to estimate the corresponding length scales of turbulent burning as follows.

To this end, we consider a rising Rayleigh-Taylor unstable bubble of typical size  $L \approx 10^5$  cm. Horvath and Benvenuto (1988) estimate the Reynolds number of large scale flows in both neutron and strange stars to be  $Re(L) \sim 10^{10}$ . Again applying equation (2.37) leads to a Kolmogorov scale of  $l_K = 10^{-8}$  cm. If we assume the above Kolmogorov scaling law and typical macroscopic velocity variations  $v(L) \approx 10^9$  cm s<sup>-1</sup>, we find a Gibson scale of  $l_G = 10^2$  cm. In this estimation we adopted the laminar burning velocity determined by Niebergal et al. (2010), as we do in our numerical simulations. This approach is discussed in detail in Section 4.2.

### 2.4.4. Conditions for exothermic combustion

By definition, combustion has to be exothermic. Following Anile (1989), this implies that the total energy density of the burnt phase (ashes),  $e_{\text{burnt}}$ , in a fixed thermodynamic state  $(P, X)$  has to be lower than the energy for the unburnt phase (fuel),  $e_{\text{unburnt}}$ , in the same state,

$$e_{\text{unburnt}}(P, X) > e_{\text{burnt}}(P, X), \quad (2.40)$$

where  $P$  is the pressure,  $X$  is the generalized volume,  $X = (e + P)/n_B^2$ , and  $n_B$  is the baryon number density. In the nonrelativistic case condition (2.40) reduces to (Anile, 1989)

$$\varepsilon_{\text{unburnt}}(P, v) > \varepsilon_{\text{burnt}}(P, v). \quad (2.41)$$

Here  $v = 1/\rho$  is the specific volume, and  $\varepsilon$  is the specific internal energy. In our simulations of thermonuclear burning in white dwarfs we assume that condition (2.41) is always fulfilled above a certain threshold density (cf. Section 3.1.5) and the burning thus proceeds in an exothermic fashion at high enough densities. This assumption is justified because the nuclear fusion reactions in the considered environment are in general exothermic. Numerically, we add the difference in binding energy between the fuel and the ashes to the internal energy while all other thermodynamic quantities and the equation of state are kept constant.

However, it turned out that in the case of the conversion of hadronic matter into strange quark matter condition (2.40) is not automatically fulfilled, because the release of binding energy is due to a change of the phase of the matter, represented by a change of the EoS. Therefore, the question if the combustion is exothermic for a given thermodynamic state becomes very important for the outcome of our computations. We present a detailed discussion of this topic in Section 4.3.

## 2.5. Gravitational waves

Gravitational waves are distortions in spacetime, emitted by accelerating masses and propagating as waves with the speed of light. They are a prediction of Einstein's theory of general relativity and have no equivalent in Newton's theory of gravitation. Although no direct detection of gravitational waves succeeded yet, next-generation detectors have promising prospects, as we will discuss briefly in Section 2.5.2. If successful detections become routine, the gravitational wave signal will be a valuable addition to the electromagnetic and neutrino signal and an important component of a true "multi-messenger astronomy".

### 2.5.1. Theory of gravitational waves

In this section we will discuss gravitational waves as a solution of the Einstein equations. These solutions can only be calculated in the limit of weak gravitational fields, but this is certainly a good approximation in the case of gravitational waves, which are only very tiny distortions of space-time. The Einstein equations can be linearized in the weak field limit. In this case, the space-time metric  $\mathbf{g}$  can be decomposed into the Minkowski metric of flat space-time  $\eta$  as a background metric and a small perturbation  $\mathbf{h}$ ,

$$g_{\mu\nu} = \eta_{\mu\nu} + h_{\mu\nu} \quad |h_{\mu\nu}| \ll 1. \quad (2.42)$$

The equations of motion that govern the behavior of the perturbation  $\mathbf{h}$  can be found by inserting the metric (2.42) into Einstein's equations and evaluating them to first order. We skip the

lengthy calculations and refer to the introductory texts of Camenzind (2007) and Chakrabarty (1999).

The decomposition (2.42) of  $\mathbf{g}$  is not unique, it does not determine the coordinate system. Hence we have the freedom to fix it by choosing a suitable gauge. Due to this gauge invariance, gauge transformations between different gauges exist which do not change the curvature and therefore the physical space-time remains unaltered, in analogy to the gauge invariance of electromagnetism. A good choice in our case is the *harmonic gauge*. To express it we introduce the *trace-reversed* perturbation

$$\bar{h}_{\mu\nu} = h_{\mu\nu} - \frac{1}{2}\eta_{\mu\nu}h, \quad (2.43)$$

where  $h$  is the trace of the perturbation  $\mathbf{h}$ ,  $h = h_{\alpha}^{\alpha}$ . Now the harmonic gauge condition in the weak field limit is

$$\partial_{\mu}\bar{h}^{\mu}_{\nu} = 0. \quad (2.44)$$

Applying this gauge condition (2.44) to the equation of motion leads to the linearized Einstein equations in the harmonic gauge (Chakrabarty, 1999),

$$\square\bar{h}_{\mu\nu} = -16\pi GT^{\mu\nu}, \quad (2.45)$$

where  $G$  is Newton's gravitational constant,  $T^{\mu\nu}$  is the stress-energy tensor, and  $\square$  is the flat space-time d'Alembert operator,  $\square = \eta^{\alpha\beta}\partial_{\alpha}\partial_{\beta}$ .

In the following we discuss at first vacuum solutions in full linearized general relativity to gain insight into the propagation of the gravitational waves. After that, we move to the generation of gravitational waves in post-Newtonian approximations.

In the vacuum case, that is in the case of vanishing stress-energy tensor ( $T^{\mu\nu} = 0$ ), the linearized field equations simplify to

$$\square\bar{h}_{\mu\nu} = 0. \quad (2.46)$$

Equation (2.46) resembles the wave equation in electromagnetism. Also in our case, plane waves are solutions to equation (2.46). They can be written as

$$\bar{h}_{\mu\nu} = A_{\mu\nu}\exp(ik_{\alpha}x^{\alpha}), \quad (2.47)$$

where the rank-2 tensor  $\mathbf{A}$  is constant and symmetric. The four-vector  $\mathbf{k}$  is also constant and acts as a wave vector. By inserting equation (2.47) into the Einstein equation (2.46), we get

$$k^{\mu}k_{\mu} = 0. \quad (2.48)$$

It follows from this relation that gravitational waves propagate with the speed of light, because the wave vector is a null vector. If we take equation (2.47) again and insert it into the gauge condition (2.44), we get

$$k_{\mu}A^{\mu\nu} = 0. \quad (2.49)$$

## 2. Fundamental considerations

---

This shows that  $\mathbf{A}$  is orthogonal or *transverse* to  $\mathbf{k}$  in the chosen gauge. The harmonic gauge condition (2.44) still leaves an additional freedom to choose a suitable coordinate system (Chakrabarty, 1999). We can apply a gauge transformation such that

$$A^\mu{}_\mu = 0 \quad (2.50)$$

holds – the trace of  $\mathbf{A}$  vanishes. Therefore the gauge used in the following is called the *transverse traceless (TT)* gauge due to equations (2.49) and (2.50). Equation (2.50) also means that

$$\bar{h}_{\mu\nu}^{\text{TT}} = h_{\mu\nu}^{\text{TT}}. \quad (2.51)$$

Furthermore, it can be shown (e.g. Camenzind, 2007; Chakrabarty, 1999) that we can write  $\mathbf{A}$  in matrix form with only two independent components:

$$A_{\mu\nu} = \begin{pmatrix} 0 & 0 & 0 & 0 \\ 0 & A_{11} & A_{12} & 0 \\ 0 & A_{12} & -A_{11} & 0 \\ 0 & 0 & 0 & 0 \end{pmatrix}. \quad (2.52)$$

These two independent components represent the only two different polarization states of the gravitational wave. Due to the shape of the deformation of an initially ring-shaped arrangement of test particles, these two polarization states are usually denoted by “+” and “×”, respectively (see e.g. Camenzind, 2007).

At this point we will leave the discussion of the propagation of gravitational waves and switch to the question of how to describe the generation of gravitation waves. As mentioned above, we will now change into a post-Newtonian framework to simplify matters.

Gravitational waves are caused by temporal variations of the quadrupole or higher moments of the stress-energy tensor. In the post-Newtonian approximation only the variation of the quadrupole is considered, hence the gravitational wave emission described in this way is often called *quadrupole radiation*. The signal generated by variations of the quadrupole moment is much higher than the signal originating from variations of higher moments and dominates the total signal (Davis et al., 1971). Therefore the quadrupole radiation is a fairly good approximation to the total signal.

From now on our metric will always be Euclidean and we keep the orthonormal basis fixed. Therefore we do not discriminate between co- and contravariant vectors in the following. We define the trace-free part of the mass quadrupole tensor, the common Newtonian quadrupole moment, as

$$Q_{ij}(t) = \int d^3x \rho(\mathbf{x}, t) \left( x_i x_j - \frac{1}{3} \delta_{ij} \mathbf{x}^2 \right), \quad (2.53)$$

where  $\rho$  is the mass density, and the transverse-traceless projection operator  $\mathbf{P}$  as

$$P_{ijkl}(\mathbf{n}) = (\delta_{ik} - n_i n_k) (\delta_{jl} - n_j n_l) - \frac{1}{2} (\delta_{ij} - n_i n_j) (\delta_{kl} - n_k n_l), \quad (2.54)$$

with the normalized position vector  $\mathbf{n} = \mathbf{x}/R$  and the distance to the source  $R = |\mathbf{x}|$ . Using these expressions, the gravitational quadrupole radiation field in the transverse-traceless gauge  $\mathbf{h}^{\text{TT}}$  is, neglecting all higher-order correction terms (e.g. Camenzind, 2007),

$$h_{ij}^{\text{TT}}(\mathbf{x}, t) = \frac{2G}{c^4 R} P_{ijkl}(\mathbf{n}) \frac{\partial^2}{\partial t^2} Q_{kl} \left( t - \frac{R}{c} \right). \quad (2.55)$$

In Section 3.4 we will describe how we implemented the calculation of  $\mathbf{h}^{\text{TT}}$  in our numerical code.

### 2.5.2. Detection of gravitational waves

The detection of gravitational waves on a regular basis would be a great complement to the classical astronomical observational methods. In principle, it is possible to measure the amplitude of gravitational waves directly. Equation (2.55) shows that the amplitude is proportional to  $1/R$ . In contrast, only the intensity, the square of the amplitude, of electromagnetic waves is measurable, leading to a  $1/R^2$ -dependence. This may lead to an advantage of large-distance gravitational wave observations compared to the corresponding observations of electromagnetic waves.

Indirect evidence of the existence of gravitational waves was already found in the decrease of the orbital period of the Hulse-Taylor pulsar (cf. Section 1.1), which follows exactly the predictions of general relativity; but a direct detection was not yet achieved. Gravitational waves, being distortions in spacetime, lead to changes in the distances between test masses. These changes can be measured by extremely high-precision laser interferometry. In the last decade, large ground-based two-armed interferometers were built; the most important existing instruments are the *Large Interferometer Gravitational-Wave Observatory (LIGO)* in the USA and the *Virgo Interferometer* in Italy. Both experiments are currently updated, “bringing these instruments to sensitivities that should make gravitational wave detections a routine occurrence” (LIGO Scientific Collaboration, 2012). The sensitivity of *Advanced LIGO* and *Advanced Virgo* is anticipated to be a factor of ten higher compared to their predecessors (Waldman, 2011). The frequency range of highest sensitivity of both LIGO and Virgo is  $\sim 10^2$  to  $10^3$  Hz (The LIGO Scientific Collaboration and The Virgo Collaboration, 2012). Gravitational wave sources such as core-collapse supernovae, rapidly-rotating deformed neutron stars, or the coalescence of neutron star or black hole binaries are expected to emit in this frequency range.

Third generation ground-based telescopes such as the proposed *Einstein Telescope (ET)* will push the sensitivity range towards lower frequencies, down to  $\sim 5$  Hz (Hild et al., 2011). Measurements of lower frequencies are not possible on earth due to atmospheric and seismic noise; therefore, several space-based gravitational wave instruments are proposed. The prospects of the realization of the *Laser Interferometer Space Antenna (LISA)* recently deteriorated after NASA left the project. But a new proposal for a similar, European, space interferometer, the *evolved Laser Interferometer Space Antenna/ New Gravitational Wave*

*Observatory (eLISA/NGO)*, was made (Amaro-Seoane et al., 2012). This instrument would probe the frequency range from  $10^{-4}$  to  $10^{-1}$  Hz. Sources in this range are coalescing supermassive black holes or binaries of compact objects long before coalescence. In the even more distant future, the proposed space-based missions *DECi-Hertz Interferometer Gravitational wave Observatory (DECIGO)* (Sato et al., 2009) and *Big Bang Observer (BBO)* might measure the primordial gravitational wave background at frequencies around 10 Hz.

Another possibility to detect gravitational waves is provided by *pulsar timing arrays*, in which variations of the arrival time of pulses emitted by radio pulsars can be used to detect gravitational waves. For high-precision measurements of the pulsar signals large arrays of radio telescopes are needed; several suitable instruments are currently in the construction phase. This method will be useful to detect sources that emit in very low frequencies,  $10^{-9}$  to  $10^{-8}$  Hz, such as supermassive binary black holes in the center of merging galaxies (Hobbs et al., 2010).

## 2.6. Weak interactions

The weak interactions relevant for matter in the interior of compact stars are electron capture processes,



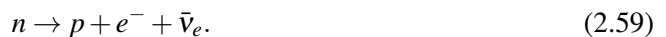
positron capture processes,



$\beta^+$  decays,



and  $\beta^-$  decays,



All reactions, which can also occur inside nuclei, change the electron fraction  $Y_e$  (cf. Section 2.1) of the matter.

We will discuss old, cool neutron stars in Section 4. In those objects, reactions (2.56–2.59) are in equilibrium ( $\beta$ -*equilibrium*). Therefore we can assume a  $Y_e$  that is constant in time as a good approximation in our neutron star simulations. Treating weak interactions in neutron star simulations would be numerically challenging because of the complicated neutrino physics, as we will explain in Section 2.7.1.

In particular, electron capture reactions (2.56) play an important role in high-density white dwarfs, as we will see in Section 5, where we will discuss deflagrations in high-density carbon-oxygen white dwarfs. Electron captures lead to neutronization, expressed as decreasing  $Y_e$ , leading to lower electron degeneracy pressure and thereby affecting the dynamics of the fluid.

Electron captures on the constituent parts of C+O white dwarfs,  $^{12}\text{C}$  and  $^{16}\text{O}$ , occur via the following reactions (Shapiro and Teukolsky, 1983):



The threshold energy for the first reaction chain is 13.37 MeV, for the second reaction chain 10.42 MeV. The Fermi energies of the electrons match these values at densities of  $\rho_{\text{ec,C}} = 3.9 \times 10^{10} \text{ g cm}^{-3}$  and  $\rho_{\text{ec,O}} = 1.9 \times 10^{10} \text{ g cm}^{-3}$ , respectively (Shapiro and Teukolsky, 1983). As we will discuss in Section 5.1.2, central densities of accreting C+O white dwarfs are not expected to exceed  $\rho_c \sim 1 \times 10^{10} \text{ g cm}^{-3}$ , well below  $\rho_{\text{ec,C}}$  and  $\rho_{\text{ec,O}}$ , before thermonuclear burning starts in the central region. Therefore, for densities appearing in C+O white dwarfs, no electron captures on the unburnt material occur. They are only possible after the start of thermonuclear burning, in the hot “ashes”.

## 2.7. Neutrino emission during thermonuclear burning in white dwarfs

Neutrinos play a great role in the physics of compact stars. The dynamics of core-collapse supernovae are substantially affected by neutrino transport processes, and the lion’s share of the released explosion energy is carried away by neutrinos. Protoneutron stars cool by neutrino emission; also young, hot white dwarfs emit plenty of neutrinos while they cool down. The aspect that we will discuss in the following is neutrino emission during thermonuclear burning in white dwarfs, which is rarely treated in the literature but will be important concerning our topic of Section 5, deflagrations in high-density carbon-oxygen white dwarfs. The neutrino emission in the event of thermonuclear supernovae was discussed by Nomoto et al. (1984), Kunugise and Iwamoto (2007), and recently by Odrzywolek and Plewa (2011).

In the hot ashes of burnt C+O matter, the thermodynamic conditions are such that a large amount of neutrinos can be emitted. We have seen in Section 2.2.3 that the maximum central density of white dwarfs is  $\rho_c^{\text{max}} \sim 2 \times 10^{10} \text{ g cm}^{-3}$ . Neutrino trapping starts only at densities of  $\sim 10^{11}$  to  $10^{12} \text{ g cm}^{-3}$  (Bethe, 1990), white dwarf matter is therefore always transparent to neutrinos; in good approximation, they leave the star without any interaction. This simplifies the neutrino physics greatly, because we can assume that the energy that the neutrinos get when they are created is immediately lost to the star. Following Odrzywolek and Plewa (2011) and others, we will distinguish between *weak* and *thermal* neutrinos. In the following two sections we will briefly introduce the physical processes that generate the neutrinos during thermonuclear burning in white dwarfs; we will describe our numerical methods for the calculation of the emitted neutrino energies in Section 3.3.2.

### 2.7.1. Weak neutrinos

*Weak neutrinos* are emitted in nuclear reactions involving the weak interaction<sup>4</sup>; the amount of emitted energy depends on specific reaction rates and therefore on the composition of the matter. The reaction rates themselves depend strongly on temperature and density. Weak neutrinos and antineutrinos are produced in electron and proton captures, and  $\beta^+$  and  $\beta^-$  decays, as specified in equations (2.56–2.59) in Section 2.6.

Neutrinos from electron captures (reaction 2.56) are abundantly produced in the neutronization processes that take place during the thermonuclear burning. As we will see, the energy released in reactions (2.56–2.59) will dominate the energy released in all other neutrino generating processes in the physical environment discussed in Section 5.

### 2.7.2. Thermal neutrinos

In the hot plasmas of stellar interiors, neutrinos are also emitted due to processes that are independent of nuclear reactions; the amount of emitted energy depends only on the density and temperature of the matter. Most important are neutrinos originating from electron-positron pair annihilation, photoemission, plasmon decay, bremsstrahlung, and recombination processes (for a brief description and summary of the individual contributions of these processes see Itoh et al. (1996)). Neutrinos from these processes are often combined as *thermal neutrinos*, they comprise neutrinos and antineutrinos of all flavors, whereas in reactions (2.56–2.59) only electron and antielectron neutrinos are produced.

---

<sup>4</sup>Of course, also “thermal” neutrinos are created due to the weak interaction.

## 3. Numerical methods

We introduced the fundamental concepts of our work in the preceding section; we will now present our numerical methods and tools based on these concepts. While keeping the review of the established computer code that is the basis of our work rather compact, we will focus on some aspects of high relevance to our work and describe the modifications we made to the code to adapt it to the specific physical problems discussed in Sections 4 and 5.

### 3.1. The LEAFS-code – general overview

The forefather of the simulation code used in this work is PROMETHEUS, written by Fryxell et al. (1989). Central parts of the current version of our code, especially the hydrodynamics solver, are still similar to its original form. The code was developed further and adapted to Type Ia supernova simulations; Niemeyer and Hillebrandt (1995) introduced a subgrid scale model to conduct simulations of turbulent flames in thermonuclear supernovae. Reinecke (2001) modernized the code and implemented the level-set method. It was further improved by Röpke (2003) and many other collaborators and is now used regularly in various Type Ia supernovae simulations for more than one decade (e.g. Reinecke et al., 2002b; Röpke and Hillebrandt, 2005; Röpke et al., 2006a; Fink et al., 2007; Ciaraldi-Schoolmann et al., 2009; Kasen et al., 2009; Pakmor et al., 2010; Fink et al., 2010; Pakmor et al., 2012; Röpke et al., 2012). Its present official name is LEAFS (*LEvel-set based Astrophysical Flame Simulations*). Central aspects of it are described in the following paragraphs. This section is based on Toro (1997) and LeVeque (1998) for general aspects of numerical fluid dynamics, and on Reinecke (2001), Reinecke et al. (2002a), and Röpke (2003) for the specifications of the LEAFS-code.

Our code treats the fluid dynamics and the flame propagation separately using an operator splitting scheme that divides each time step in a hydrodynamics part and a flame propagation part. In the next section we will discuss the hydrodynamics part of the code.

#### 3.1.1. Solving the Euler equations

To solve the Euler equations (2.20–2.22) numerically, we have to discretize them in time and space. The obvious approach appears to be a *finite-difference method*, in which the computational domain is discretized into grid points on which the conserved quantities are defined; the derivatives in the partial differential equations (2.20–2.22) are substituted by finite differences. Also time is discretized into *time steps*; the calculation of the solution at the next time step can be done either implicitly or explicitly. However, this method has a number of profound

disadvantages that prohibit their application to the topics of this work. Firstly, the error of the spatial discretization leads to nonconservation of quantities that are physically conserved. Secondly, the solutions of the Euler equations in differential form have to be continuous; the resolution of discontinuities such as shocks is not possible. This behavior is particularly unfortunate because we model flames as discontinuities.

*Finite-volume methods* do not have these shortcomings. Here, differential equations such as the Euler equations are solved in their integral form (cf. Section 2.3). The physical domain is discretized into finite volumes or *grid cells*; the corresponding values of each conserved quantity are defined as the integral average over the volume of each cell. Time is discretized into finite time steps, comparable to the finite-difference method, and either implicit or explicit time-stepping is possible here as well. At each time step, the fluxes over the cell interfaces are calculated and the averaged values in the cells updated accordingly; thus, this scheme is conservative by construction. Higher-order methods are able to capture shocks very well, as we will discuss later. Finite-volume methods need considerably more computing time than finite-difference methods of comparable order, but this is compensated by the lower requirements on the resolution of the former.

Finite-volume methods are thus clearly preferred in the context of this work. Consequently, such schemes are implemented in the LEAFS-code, where the physical domain is discretized into a Cartesian grid of rectangular (in two dimensions) or rectangular-box shaped (in three dimensions) cells. Some properties of the specific implementation of our grid are described in Section 3.1.3.

As mentioned above, in finite-volume methods the spatially discretized conserved quantities are defined in each cell. The idea is now to calculate from the initial value of the conserved quantities  $\mathbf{U}(t_0)$  (cf. equation 2.23) the state  $\mathbf{U}(t)$  at time  $t$ , sequentially in  $n$  steps, as

$$\mathbf{U}(t_0) \rightarrow \mathbf{U}(t_0 + (\Delta t)_1) \rightarrow \mathbf{U}(t_0 + (\Delta t)_1 + (\Delta t)_2) \rightarrow \cdots \rightarrow \mathbf{U}(t_0 + (\Delta t)_1 + (\Delta t)_2 + \cdots + (\Delta t)_n).$$

For  $t - t_0 = \sum_{i=1}^n (\Delta t)_i$  we have

$$\mathbf{U}(t_0 + (\Delta t)_1 + (\Delta t)_2 + \cdots + (\Delta t)_n) = \mathbf{U}(t) + \Delta \mathbf{U}, \quad (3.1)$$

where we denote the *discretization error* as  $\Delta \mathbf{U}$ . The size of the time step  $\Delta t$ , which is in general different in each step, depends on the numerical scheme and will be discussed later. All methods described in the following are explicit in the sense that the solution  $\mathbf{U}(t + \Delta t)$  at a time  $t + \Delta t$  depends only on the solution  $\mathbf{U}(t)$  of the preceding time step. A prescription to calculate  $\mathbf{U}(t + \Delta t)$  for a given  $\mathbf{U}(t)$  is now required. We will sketch the three-step algorithm suggested by Godunov (1959) that is the simplest realization of the class of *Godunov's schemes*.

The fluxes across the cell interfaces depend on the gradients of the conserved quantities that are defined at the center of each cell; hence, the first step, the *reconstruction step*, is to determine the values of the conserved quantities at the cell interfaces. The simplest way to do this is the *piecewise constant method*, in which the cell-centered values are just assigned to

the cell boundaries. At the interface between two cells the values of the conserved quantities, which are in general distinct, meet at one point and thus form a discontinuity. This is called a *Riemann problem* or *shock tube problem*. Its solution, which can be achieved either with an exact or an approximative *Riemann solver* (cf. Toro, 1997), comprises the second step of the algorithm. The solution of the Riemann problem consists of a superposition of different *waves* such as shock waves, rarefaction waves and contact discontinuities. The wave solutions are then used to calculate fluxes of each conserved variable across the interfaces. In the third step, the cell-centered conserved variables are updated accordingly, which completes the cycle.

The original Godunov’s scheme as described above is of first order in space and therefore quite diffusive (cf. LeVeque, 1998), which leads to unwanted smearing out of shocks. Much better results can be achieved using higher-order Godunov’s schemes. The improvements arise from a more sophisticated treatment of the reconstruction step. Instead of the piecewise constant method explained above, in PROMETHEUS as well as in our code the *piecewise parabolic method (PPM)* of Colella and Woodward (1984) is implemented. As the name implies, PPM interpolates the conserved variables at the cell interfaces by local parabolae instead of constant values. The reconstructed values of the conserved variables are used as input for the Riemann solver. By means of the resulting fluxes the values of the conserved variables are updated in each cell.

An *dimensional operator splitting* scheme is applied in our code. The general problem is splitted in one-dimensional subproblems that are solved separately and consecutively for each of the directions parallel to the coordinate axes. After each one-dimensional *sweep* the values of the conserved variables are updated in all cells; the order of the sweeps is reversed in every other time step to guarantee second-order accuracy in time. The operator splitting avoids the computationally more expensive and conceptually more difficult solution of multi-dimensional Riemann problems at the cost of introducing an additional *splitting error* in every time step; this error vanishes only in linear problems. It is negligible in standard applications of our code, but can cause problems in quasi-stationary flows (see below). The one-dimensional Riemann problems are solved using the accurate and fast approximative Riemann solver of Colella and Glaz (1985).

Our code features explicit time-stepping. To get a stable solution, it has to be guaranteed that the waves from Riemann problems of neighboring cells do not interact with each other. Therefore, an upper limit of the time step size has to be enforced. It is determined by applying the *Courant-Friedrichs-Lewy (CFL) condition* (Courant et al., 1928),

$$\Delta t \leq C_{\text{CFL}} \frac{\Delta x}{v_{\text{max}}}, \quad (3.2)$$

where  $v_{\text{max}}$  is the largest velocity of all waves and  $\Delta x$  is the grid cell size. A necessary condition for a numerical method to converge is that  $C_{\text{CFL}}$  is not larger than unity; numerical stability usually requires  $C_{\text{CFL}} \lesssim 0.8$ .

In our code,  $v_{\max}$  is calculated in each time step as

$$v_{\max} = \max(v_i, c_{s,i}), \quad i = x, y, z, \quad (3.3)$$

with the sound speed  $c_{s,i}$ . Usually,  $C_{\text{CFL}} = 0.8$  is adopted. However, we are confronted with initially very slow fluid motions in both of the main subjects of this thesis. In these cases, simulations adopting  $C_{\text{CFL}} = 0.8$  show numerical errors that appear as artifacts such as unnatural fluid flow, predominantly at the coordinate axes. These errors are likely due to our dimensional operator splitting scheme. Because the fluid stays in a quasi-stationary state for a large number of time steps, the errors introduced by the operator splitting in each time step add up until they become nonnegligible. The larger the time steps, the larger are the splitting errors; therefore, reducing the time step alleviates this problem. Consequently, we decreased the factor  $C_{\text{CFL}}$  until the artifacts vanished and we obtained valid and stable numerical solutions. In the neutron star simulations of Section 4 the value is decreased to values as low as  $C_{\text{CFL}} = 0.08$ . Most of the high-density white dwarf simulations of Section 5 are conducted with  $C_{\text{CFL}} = 0.4$ . A different possibility to tackle this problem would be to implement *unsplit* approaches such as those proposed by Colella (1990) for two dimensions and Saltzman (1994) for three dimensions. These methods are based on the solution of one-dimensional Riemann problems as well, but an intermediate step is introduced in which values of the conserved variables at each interface are updated by fluxes that are perpendicular to the sweep direction of the split scheme. In three dimensions, this method requires the solution of 12 instead of 3 one-dimensional Riemann problems per grid cell and time step.

#### 3.1.2. Gravitational potential

The gravitational force  $\mathbf{g}$  is included as an external force into the hydrodynamics solving routine. It is calculated via the gradient of the gravitational potential  $\Phi$ ,

$$\mathbf{g} = -\nabla\Phi. \quad (3.4)$$

In white dwarf simulations, gravitation is usually treated in a Newtonian, nonrelativistic approach, because the compactness of a typical white dwarf is low,  $GM/Rc^2 \sim 10^{-4}$ , and relativistic effects are therefore negligible. Furthermore, a Newtonian potential is consistent with Newtonian hydrodynamics and thus preferable. In our neutron star simulations we apply an effective relativistic gravitational potential that we present in Section 3.2.3. The case of the more compact high-density white dwarfs, topic of Section 5, will be discussed in Section 5.2.8.

In the nonrelativistic case the gravitational potential  $\Phi$  is determined by solving Poisson's equation

$$\Delta\Phi = 4\pi G\rho, \quad (3.5)$$

with Newton's gravitational constant  $G$  and the mass density  $\rho$ . We solve this equation by applying the multipole method presented by Müller and Steinmetz (1995) but restrict ourselves to the monopole,  $l = 0$ . This is justified because we model nonrotating stars, where the gravitational field is approximately spherically symmetric.

### 3.1.3. Moving hybrid grid

To ensure that in our simulations the regions of highest interest are optimally resolved for a given fixed number of grid cells and no computational resources are wasted on regions of subordinate importance, the computational domain is separated into two grids (Röpke, 2005; Röpke et al., 2006b), an outer coarser grid, where the cell size increases outwards, and an uniformly spaced inner grid intended to resolve the flame in an optimal way. Both grids are *moving grids*, the size of their physical domain can be expanded or compressed. The outer grid tracks the expansion of the whole star, while the inner grid tracks the flame front and expands with it into the outer grid.

We set *outflow boundary conditions* at the outer boundaries of the computational domain. When our domain is restricted to a quadrant (in two dimensions) or octant (in three dimensions) of the star, *reflecting boundary conditions* are applied at the inner boundaries to enforce the respective symmetries. For a detailed discussions of the different types of boundary conditions see LeVeque (1998).

### 3.1.4. Burning velocity in white dwarf matter and level-set method

As discussed in Section 2.4, we model combustion flames as discontinuities in the state variables. We have to include the burning velocity as an external parameter because we do not resolve the flame physics. The laminar burning velocity  $v_{\text{lam}}$  in white dwarf matter was determined by Timmes and Woosley (1992). They used different one-dimensional, small-scale flame models, included a nuclear network, and calculated the burning velocity for different carbon fractions  $X(^{12}\text{C})$  and fuel densities  $\rho$ . In our code, we use their analytical fit to their results,

$$v_{\text{lam}} = 9.2 \times 10^6 \left( \frac{\rho}{2 \times 10^9 \text{ g cm}^{-3}} \right)^{0.805} \left( \frac{X(^{12}\text{C})}{0.5} \right)^{0.889} \text{ cm s}^{-1}. \quad (3.6)$$

According to Timmes and Woosley (1992), this fit is accurate at a 10%-level<sup>1</sup> for densities  $\rho \geq 10^7 \text{ g cm}^{-3}$  and  $\rho \leq 10^{10} \text{ g cm}^{-3}$ .

To track the flame front we use the *level-set method* which was introduced by Osher and Sethian (1988) and implemented in the code by Reinecke et al. (1999b), see also Reinecke (2001) and Röpke (2003). In this scheme, a signed distance function  $G$ , which is positive in the burnt material and negative in the unburnt material, is assigned to each point in the computational domain. The zero level set of  $G$  thus separates the burnt from the unburnt matter and marks the location of the flame front. The level set is propagated with the burning velocity perpendicular to the flame surface and advected as a passive scalar without fundamental modifications of the hydrodynamics solver. Because the zero level set marks the position of

---

<sup>1</sup>Röpke (2003) pointed out that the deviation can be higher at low densities and carbon fractions different from  $X(^{12}\text{C}) = 0.5$ .

the flame, it can be used to calculate the volume fraction of the burnt and unburnt matter in each cell.

### 3.1.5. Modeling the thermonuclear burning

A correct treatment of the energy released by thermonuclear burning is important for a correct modeling of the fluid dynamics. However, including a full nuclear reaction network (cf. Section 3.1.7) is computationally expensive, and also unnecessary, because only a few representative species are needed for a good approximation of the energy release of the combustion process (see Reinecke et al. (2002a) for a detailed description of the method outlined in the following, cf. also Fink (2010)). Our code includes five species: carbon and oxygen, which comprise the fuel, alpha particles, a representative of intermediate mass elements (IME) with atomic number of  $A^{\text{IME}} = 30$  that we call “magnesium”, and a representative of iron group elements (IGE) with atomic number of  $A^{\text{IGE}} = 56$  that we call “nickel”. The nuclear binding energy of these species is included into the code; in the case of “magnesium” and “nickel” an appropriate average is taken. Not only the burning velocity and the energy release of the thermonuclear burning, but also the chemical composition of the burnt matter have to be taken as external parameters due to our flame model. In the following we describe our model of thermonuclear burning and how it is integrated in one time step cycle of our code.

If the fuel, consisting of carbon and oxygen, has a density lower than  $\rho_{\text{burn}}^{\text{min}}$ , no burning takes place and the fuel stays unchanged. We assume that the fuel burns instantly into ash if  $\rho_{\text{fuel}} \geq \rho_{\text{burn}}^{\text{min}}$ . The composition of the burnt matter in terms of the five representative species depends on the density of the fuel. For  $\rho_{\text{fuel}} \geq \rho_{\text{NSE}}$  we assume that the burnt matter consists of matter in equilibrium with respect to the strong interaction (*nuclear statistical equilibrium*, *NSE*), we will justify this assumption by comparing relevant timescales in Section 3.3.1.

In our model, NSE matter is a mixture of alpha particles and “nickel”. The ratio of alpha particles to “nickel” depends on the temperature and density of the burnt matter. Based on solutions of the NSE-equations (see e.g. Seitenzahl et al., 2009), this ratio was calculated to achieve the correct *Q-values*, the differences in the binding energies between fuel and ash. Based on these tabulated results the composition of NSE matter is adjusted in an iteration process.

The intermediate density regime,  $\rho_{\text{burn}}^{\text{min}} \leq \rho_{\text{fuel}} < \rho_{\text{NSE}}$ , is called *incomplete burning regime*. Here, the (partially) burnt matter consists of unburnt carbon and oxygen, “magnesium”, and NSE matter consisting of alpha particles and “nickel”. The abundances of those four components as a function of fuel density were determined and tabulated in detailed calculations; the tables were calibrated to get a correct energy release in the hydrodynamic simulations. The composition of NSE matter is adjusted as described above.

In our code, we adopt  $\rho_{\text{burn}}^{\text{min}} = 2.9 \times 10^6 \text{ g cm}^{-3}$  and  $\rho_{\text{NSE}} = 9.0 \times 10^7 \text{ g cm}^{-3}$ . Those values are the results of detailed calculations of nuclear burning as well.

The flame propagation is decoupled from the hydrodynamics; because of this operator splitting scheme each time step is split into a hydrodynamics part and a flame propagation part.

A complete time step proceeds now as follows: In the hydrodynamics part, the conserved variables are updated after the Riemann problems are solved (cf. Section 3.1.1). After that, in the flame propagation part, the level set is propagated with the calculated burning velocity and the burnt volume fraction of each cell is determined (cf. Section 3.1.4). A table lookup provides the abundances of the burnt matter, depending on the fuel density. The released energy is calculated by the respective  $Q$ -values, and is added to the internal energy of the fluid in the respective cell. Subsequently, the equation of state routine is called to update the state variables. With the help of the NSE-table, an iteration scheme provides the ratio of alpha particles to “nickel” in NSE matter, depending on the temperature and density of the burnt matter. After that the released energy is adjusted to the NSE composition and the abundances of the five representative species are updated accordingly. A second call to the EoS routine provides the final update of the state variables, which completes the cycle.

The conversion from hadronic matter into strange quark matter is treated in an analogous but inherently simpler manner; we will present our corresponding implementation in Section 3.2.2.

### 3.1.6. Subgrid scale turbulence model

As described in Section 2.4.2, we cannot resolve the turbulent motion down to the Gibson scale. Therefore, we perform *large eddy simulations*: Only the largest scales of the system are resolved, while the turbulent motion on smaller scales is modeled by a *subgrid scale (SGS) model*. The SGS model determines the turbulent energy, from which the turbulent burning velocity can be inferred. Schmidt et al. (2006a,b) introduced a sophisticated SGS turbulence model and implemented it into the code. Usually it is applied using a localized closure, but for the purpose of comparison it can be applied using a simpler, statistical closure. We will compare the results obtained with both models in Section 4.4.7. In either case, the model determines the subgrid scale turbulence velocity  $q_{\text{SGS}}$ . The turbulent burning velocity  $v_{\text{turb}}$  is then obtained by setting (Schmidt et al., 2006b)

$$v_{\text{turb}} = v_{\text{lam}} \sqrt{1 + \frac{4}{3} \left( \frac{q_{\text{SGS}}}{v_{\text{lam}}} \right)^2}, \quad (3.7)$$

with the laminar burning velocity  $v_{\text{lam}}$  as a lower limit.

Since this description of the turbulent motions is currently only implemented in three dimensions, we use a different SGS model in our two-dimensional simulations, which was implemented by Niemeyer and Hillebrandt (1995). Here, the turbulent kinetic subgrid scale energy  $E_q$  is determined, and the turbulent burning velocity is calculated by

$$v_{\text{turb}} = \max(v_{\text{lam}}, 2\sqrt{E_q}). \quad (3.8)$$

The laminar burning is the inherent lower limit also in this case.

### 3.1.7. Tracer particle method

To avoid the large computational costs of the inclusion of a full nuclear reaction network into the hydrodynamics code, we use a simplified scheme consisting of only five representative species in our simulations, as described in Section 3.1.5. By this approximation the energy release and the composition, expressed by the molecular weight, are captured to sufficient accuracy for a correct treatment of the fluid dynamics, but no useful information about the elemental and isotopic abundances of the nuclei synthesized in the burning processes is provided. Instead of including a larger nuclear network to get more accurate nucleosynthesis results, we use a *tracer particle method* (Iwamoto et al., 1999; Travaglio et al., 2004; Seitenzahl et al., 2010). To this end we include a large number of Lagrangian *tracer particles* into the hydrodynamics code which are passively advected with the flow. The thermodynamic history of each particle is recorded. After the completion of the hydrodynamic simulation, the recorded temperature and density evolution is evaluated using a large nuclear network in a subsequent *post-processing* step (see also Fink, 2010).

The post-processing code we use is described by Thielemann et al. (1990), Thielemann et al. (1996), Iwamoto et al. (1999), and Travaglio et al. (2004). For each nuclide  $i$  it determines the specific nuclear abundance  $Y_i$  that is defined as the ratio of the number density  $n_i$  to the baryon number density  $n_B$ ,

$$Y_i = \frac{n_i}{n_B} = \frac{n_i}{\sum_j A_j n_j} = \frac{n_i}{\rho N_A}, \quad (3.9)$$

where  $A_i$  is the mass number and  $N_A$  Avogadro's constant. The time rate of change of the specific abundances is governed by a system of coupled differential equations (e.g. Thielemann et al., 1990),

$$\dot{Y}_i = \sum_j c_j^i Y_j + \sum_{j,k} c_{j,k}^i Y_j Y_k + \sum_{j,k,l} c_{j,k,l}^i Y_j Y_k Y_l. \quad (3.10)$$

The coefficients  $c_k^i$ ,  $c_{j,k}^i$ , and  $c_{j,k,l}^i$  describe the rates of one-nuclei, two-nuclei and three-nuclei reactions, respectively. One-nuclei reactions are electron/positron captures,  $\beta$ -decays, or photodisintegrations. We included the reaction rate library REACLIB (Rauscher and Thielemann, 2000, updated 2009) and the weak reaction rates from Langanke and Martínez-Pinedo (2001) into the code.

## 3.2. Modifications to the code I:

### Simulations of neutron stars and conversions from hadronic into strange quark matter

In Section 4 we will discuss the conversion of a hadronic neutron star into a quark star. Although the LEAFS-code as described above was written to simulate the thermonuclear burning

in white dwarfs, we used the same code for our simulations of neutron stars, taking advantage of the methodical similarities of combustion in white dwarfs and in neutron stars. Since the code was never before used to simulate neutron stars, we had to adapt it to the new problem; in this section we will describe the changes made to the code that are relevant for the subject of Section 4.

### 3.2.1. Equation of state

We included several different super-nuclear-density equations of state into the code, for hadronic matter the Shen EoS, LS180 EoS, and LS220 EoS, as described in Section 2.1.2. The tables of these EoS are freely available and can be obtained from <http://user.numazu-ct.ac.jp/~sumi/eos/> and <http://www.astro.sunysb.edu/dswesty/lseos.html>, respectively.

The hydrodynamics code works with nonrelativistic quantities such as rest mass density  $\rho$  and internal energy density  $\varepsilon$ , whereas the above mentioned EoS are given in quantities of a relativistic fluid, in particular the total energy density  $e$  and the baryon number density  $n_B$ . To guarantee compatibility of code and EoS we have to define a rest mass density  $\rho$  by

$$\rho := n_B m_B, \quad (3.11)$$

where  $m_B$  is the average mass of a baryon in nuclear matter; we adopted  $m_B c^2 = 930 \text{ MeV}$  (e.g. Madsen, 1999). Consequently, we obtain an internal energy density of

$$\varepsilon := (e - \rho) c^2 = (e - n_B m_B) c^2, \quad (3.12)$$

if we express  $e$  in mass units,  $[e] = \text{g cm}^{-3}$ , as we usually do in this work. Using these definitions we can convert the EoS tables into quantities required by the hydrodynamics code and use the existing EoS routines without major modifications.

We added strange quark EoS for various bag constants in the range  $B^{1/4} = 145$  to  $160 \text{ MeV}$ ; here we applied the analytical expressions presented in Section 2.1.3 to construct tables. Also for strange quark matter we have to define  $\rho$  and  $\varepsilon$ , which is more difficult in this case because no equivalent to the baryon mass exists for quark matter. The closest analog is probably the total energy per baryon  $E/A$  at zero pressure. We therefore define  $\rho$  and  $\varepsilon$  for strange quark matter by substituting  $m_B$  in equations (3.11) and (3.12) by  $E/A$  as given by equation (2.12). Hence,  $\rho$  and  $\varepsilon$  depend on the bag constant  $B$  for given  $e$ . With these definitions we are also able to adapt the strange quark matter EoS to the existing EoS routines.

### 3.2.2. Conversion from hadronic matter into strange quark matter

To model the conversion from hadronic matter into strange quark matter we need some prescription for an analog to the burning routine described in Section 3.1.5. Conceptually this is simpler than in the case of thermonuclear burning, because now we do not have different

species, but have one homogeneous fuel – hadronic nuclear matter – which is converted into homogeneous ash, strange quark matter.

Analogous to what was described in Section 3.1.5, after the hydrodynamics part of each time step, the level set is propagated into the hadronic matter with the conversion velocity, which is an external parameter just like the thermonuclear burning velocity. We will describe how we determine the conversion velocity in Section 4.2. After the level set propagation, the converted volume in each cell is determined. If the condition for exothermic burning is fulfilled (cf. Sections 2.4.4 and 4.3), the matter in this volume is switched from hadronic to strange quark matter; in doing so the total energy density  $e = \rho + \varepsilon/c^2$  and the baryon number density  $n_B$  is kept constant while the internal energy density  $\varepsilon$  and the mass density  $\rho$  are adjusted accordingly. Hence, the total energy and the baryon number is conserved during the conversion process, as should be the case. After this, the time step is completed by calling the EoS routine to update the state variables, in particular the pressure and temperature. Here a problem of this scheme arises in *mixed cells* that are only partly converted – which EoS routine should be called? Our approach is to call both the hadronic and the strange quark matter EoS routine and determine the volume-weighted average from the two values of pressure and temperature, respectively. We then assign the averaged values to the whole cells. This approach gives satisfactory results but is certainly not completely consistent, and there is room for improvement in future work.

### 3.2.3. Effective relativistic gravitational potential

In contrast to the case of white dwarfs (compactness  $(GM/Rc^2)_{\text{WD}} \lesssim 0.001$ ), in neutron stars (compactness  $(GM/Rc^2)_{\text{NS}} \sim 0.1$ ) general relativistic effects cannot be neglected. Computations in full general relativity are, however, beyond our scope. Given the overall uncertainties, particularly in the EoS, we consider the error introduced by the use of Newtonian dynamics to be not critical, however a comparison of our results with general relativistic simulations would be interesting. But a modification of the gravitational potential cannot be avoided, otherwise the results would be completely beside the point. For example for a given mass of the neutron star the central density would be much lower and thus exothermic combustion would not be possible at all, as we will see in Section 4.3. Therefore an effective relativistic gravitational potential (Marek et al., 2006) based on the Tolman-Oppenheimer-Volkov (TOV) equations (2.13–2.14) was implemented (cf. Section 2.2.1).

Because the TOV equations assume spherical symmetry, the TOV potential is used to determine a one-dimensional relativistic correction to a potentially multi-dimensional Newtonian potential  $\Phi$  (Marek et al., 2006). Therefore, we obtain from equations (2.13–2.14) the one-dimensional relativistic potential  $\Phi_{\text{TOV}}^{\text{1D}}$ . Without relativistic corrections we get, for instance from equations (2.16–2.17), a one-dimensional nonrelativistic potential  $\Phi^{\text{1D}}$ . The corrected, effective potential is now

$$\Phi_{\text{eff}} = \Phi + \Phi_{\text{TOV}}^{\text{1D}} - \Phi^{\text{1D}}. \quad (3.13)$$

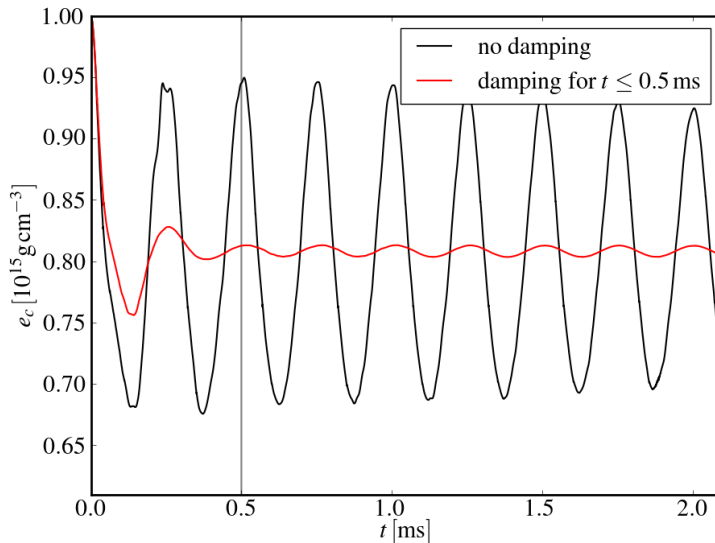


**Figure 3.1.:** Temporal evolution of central density in two neutron star simulations without conversion processes. In the run including relaxation (red line) the damping was switched off at  $t = 0.5$  ms (gray vertical line).

In our code we determine  $\Phi$  as explained in Section 3.1.2. Because it is calculated assuming spherical symmetry, we could just set  $\Phi_{\text{eff}} = \Phi_{\text{TOV}}^{\text{ID}}$ , but for reasons of comparability and possible future improvements in the calculation of  $\Phi$  we use the above stated method.

In our neutron star simulations, we replace the mass density  $\rho$  in Poisson’s equation (3.5) by the total energy density  $e$ . In the case of white dwarfs, the difference between  $\rho$  and  $e$  is negligible.

### 3.2.4. Relaxation of initial neutron star setup

When we run our simulation code with our initial neutron star configuration for some time without any changes to the fluid and all conversion or burning processes switched off, the star does not stay in hydrostatic equilibrium as it should ideally do; instead, we see strong oscillations of the fluid on the grid, visible as oscillations of the central density  $e_c$  as a function of time  $t$  in Figure 3.1 (black line). Because the conversion processes discussed in Section 4 start slowly and the neutron star stays in hydrostatic quasi-equilibrium for a long time, the conditions are similar to the case without conversion processes shown here, and hence the same oscillations are visible in simulations including the conversion process. Since the oscillation period,  $p \sim 0.2$  ms, is of the same order as the relevant timescales of our computations, the oscillations may lead to incorrect results. It is thus preferable to find a method to reduce the

oscillations. To this end, it is possible to include an additional external force, an artificial *friction force* proportional to the fluid velocity, to damp the oscillations. Instead of implementing an external friction force it is simpler and more effective to multiply all fluid velocities  $v_i$  at each time step with a damping factor  $D$  that is slightly smaller than unity,

$$v'_i = D v_i = \left(\frac{1}{10}\right)^a v_i; \quad i = x, y, z; \quad a \ll 1. \quad (3.14)$$

We applied this procedure for a given damping time  $t_{\text{damp}}$ . After  $t = 0.8t_{\text{damp}}$  the damping factor  $D$  is increased linearly up to unity at  $t = t_{\text{damp}}$ ; in this way the damping is gradually reduced to ease a smooth transition to the subsequent simulation without damping.

We achieve good results with  $a = 10^{-4}$ , corresponding to  $D \approx 1 - 2 \times 10^{-4}$ , and  $t_{\text{damp}} = 0.5$  ms, as can be seen in the red line in Figure 3.1. The oscillations are reduced to a negligible level of  $\lesssim 1\%$  and stay at this level after the damping is switched off (gray vertical line in Figure 3.1; we stopped the simulations at  $t = 5$  ms). However, the central density of the relaxed configuration is substantially lower than the initial density; the mass is redistributed slightly<sup>2</sup>, as is the case in the simulation without damping (black line in Figure 3.1). This is most likely due to the adaption of the fluid, governed by Newtonian dynamics, to the effective relativistic gravitational potential (cf. Section 3.2.3). We do not deem this decrease of central density as a problem concerning our simulations. We use the above stated values,  $a = 10^{-4}$  and  $t_{\text{damp}} = 0.5$  ms, in all our simulations presented in Section 4. The conversion process is started when the relaxation of the star is complete at  $t = t_{\text{damp}} = 0.5$  ms.

Due to this relaxation method a fraction of the kinetic energy is “dissipated” and energy conservation is violated; in addition, the redistribution of the mass changes the potential energy of the system. This has no effect on the interpretation of our simulations, because we compare our results to the relaxed configuration at  $t = t_{\text{damp}}$  which we consider as our initial condition.

In our simulations of white dwarfs an application of this relaxation method is not necessary. The oscillations here are much weaker, and the periods considerably larger than the timescales relevant for most problems (Reinecke, 2001). In standard simulations of thermonuclear supernovae this issue is irrelevant anyway due to the rapid expansion of the white dwarf after ignition. Also in our simulations with high-density white dwarfs (cf. Section 5), which are somehow comparable to the neutron star simulations because they stay in hydrostatic quasi-equilibrium for a relatively long time, we observe no oscillations or mass redistribution on the simulated time scales. The likely reason for this different behavior is that the initial white dwarf models that we use in our hydrodynamic simulations are purely Newtonian hydrostatic configurations (solutions of equations (2.16–2.17); cf. Section 2.2.1 and 2.2.3), whereas the neutron star initial models are general relativistic configurations (solutions of equations (2.13–2.14)). Although we use an effective relativistic gravitational potential in the neutron star

---

<sup>2</sup>Due to the conservative schemes we used, the total mass is conserved at a  $\sim 10^{-7}$ -level during the relaxation process.

simulations, the match between gravitational potential and fluid dynamics seems to be much better in the nonrelativistic case. A similar mismatch between Newtonian fluid dynamics and relativistic gravitational potentials is also repeatedly observed in core-collapse supernovae, see Marek et al. (2006).

Purely Newtonian neutron star configurations, however, cannot be used as neutron star initial models because they would have completely unrealistic properties such as extremely low central densities or masses well above  $3M_{\odot}$ .

#### 3.2.5. Moving hybrid grid with fixed outer boundary

Contrary to simulations of thermonuclear supernovae, in which the star explodes and the radius of the objects grows by many orders of magnitude, the radius of a neutron star changes in our simulations by less than 20% during the conversion of hadronic matter into strange quark matter in its interior. To prevent these slight changes in radius from triggering an expansion of the outer grid (cf. Section 3.1.3), which would lead to an unnecessary reduction of the resolution in the interesting regions inside of the star, we fixed the outer boundaries of the outer grid to their initial physical size. Thus, the inner grid can still track the conversion front, while no resolution is lost on regions of less importance.

### 3.3. Modifications to the code II: Simulations of high-density white dwarfs

In this section we will describe the modifications of the code relevant to the simulation of deflagrations in high-density carbon-oxygen white dwarfs, the second main topic of this thesis that we will discuss in Section 5. Because this subject is much closer to the purposes the code was written for, the modifications are only minor. However, one major addition was made: we can now take account of the energy loss due to neutrinos during the burning process, and thereby calculate neutrino luminosities. This will be discussed in Section 3.3.2. In the next section we will motivate our choice of weak interaction rates, an important aspect regarding thermonuclear burning in high-density white dwarfs.

#### 3.3.1. Weak interaction rates

The *weak interaction rates* comprehend the reaction rates of the neutrino-producing reactions (2.56–2.59):  $\beta^-$  and  $\beta^+$  decays, and electron and positron captures, as discussed in Section 2.6. All reactions can take place involving both nuclei and free nucleons. In standard Type Ia supernova simulations, which involve low-density white dwarfs, weak reactions are mainly interesting because of their influence on the nucleosynthesis yields, while the explosion dynamics are practically unaffected by those reactions. However, in deflagrations of high-density white dwarfs – the topic of Section 5 – electron capture processes, whose

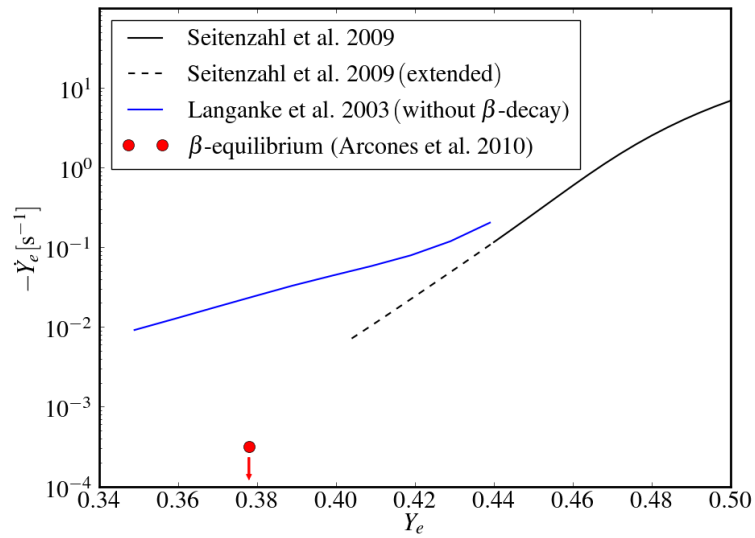


**Figure 3.2.:** The time rate of change of the electron fraction,  $\dot{Y}_e$ , is plotted vs. the electron fraction  $Y_e$  at fixed temperature  $T = 1.0 \times 10^{10}$  K and density  $\rho = 1.0 \times 10^{10}$  g cm<sup>-3</sup>. Shown are the extended rates by Seitenzahl et al. (2009) and the rates without  $\beta$ -decays given by Langanke et al. (2003) plus electron capture rates on free protons. The position of the  $\beta$ -equilibrium is taken from Arcones et al. (2010).

strength is a strong function of density, have a profound influence on the fluid dynamics; they are an important factor that co-decides if the white dwarf collapses or explodes, as discussed in Section 5.1.

For a long time, the standard weak interaction rates used in astrophysical simulations have been the rates calculated by Fuller et al. (1985). They used shell model calculations for nuclei in the mass number range  $A = 16$  to 40 (*sd*-shell nuclei), but had to rely on approximative approaches for nuclei with higher mass numbers up to  $A = 60$ . Many simulations of thermonuclear burning processes in white dwarfs were done using these rates; we will give a summary on the respective literature in Section 5.1. Later, new weak interaction rates were calculated by Langanke and Martínez-Pinedo (2000, 2001). They were able to conduct accurate shell model calculations also for nuclei in the *pf*-shell and provided weak interaction data for more than 100 nuclei with mass numbers  $A = 45$  to 65. The new data resulted in, on average, significantly lower electron capture rates compared to the earlier work by Fuller et al. (1985).

In our code we do not apply the weak interaction rate data directly, because we do not include a full nuclear reaction network. Instead, we calculate the influence of the weak interaction rates on two important quantities, the electron fraction  $Y_e$  and the energy released by the emission of neutrinos and antineutrinos,  $E_\nu$ .

At high densities and temperatures, the hot ashes of thermonuclear burning evolve rapidly into an equilibrium with respect to the strong interaction (nuclear statistical equilibrium, NSE). The timescale until NSE is reached is estimated by Khokhlov (1991) as

$$\tau_{\text{NSE}} = \left( \frac{\rho}{\text{g cm}^{-3}} \right)^{0.2} \exp \left( \frac{1.797 \times 10^{11} \text{ K}}{T} - 40.5 \right) \text{ s}. \quad (3.15)$$

In the relevant density and temperature range this timescale is small compared to the dynamical timescale and the time to reach  $\beta$ -equilibrium: Equation (3.15) gives, for example,  $\tau_{\text{NSE}} = 1.6 \times 10^{-8} \text{ s}$  for  $\rho = 10^{10} \text{ g cm}^{-3}$  and  $T = 10^{10} \text{ K}$ ; whereas  $\tau_{\text{dynamical}} \sim 0.1 \text{ s}$  and  $\tau_{\text{weak}} \sim 10^{-8} \text{ s}$  for one weak reaction, but it takes much longer to achieve  $\beta$ -equilibrium. Therefore we can assume that the matter at sufficiently high densities and temperatures burns instantly into NSE and weak interactions occur only when the material is already in NSE.

The elemental and isotopical abundances of NSE matter depend only on the three quantities temperature  $T$ , density  $\rho$ , and electron fraction  $Y_e$ . Therefore, it is possible to calculate – for given  $T$ ,  $\rho$ , and  $Y_e$  – the NSE abundances of all nuclei, apply weak interaction rates to determine the changes in their abundances, and subsequently calculate the time rate of change of the electron fraction,  $\dot{Y}_e$ , and the energy released due to neutrinos,  $\dot{E}_\nu$ . After that, the calculated values of  $\dot{Y}_e$  and  $\dot{E}_\nu$ , as a function of  $T$ ,  $\rho$ , and  $Y_e$ , are tabulated for further use. In the hydrodynamic simulations, the tabulated results are then used in each time step to update the values of  $Y_e$  and  $E_\nu$ <sup>3</sup>. This approach is not suitable for non-NSE matter, because in this

---

<sup>3</sup>The calculation of  $Y_e$  was already implemented in the code; we extended the tables (see below) and included the calculation of  $E_\nu$ .

case it is not possible to determine the nuclear abundances if exclusively the quantities  $T$ ,  $\rho$ , and  $Y_e$  are known; however, the rates of weak reactions in the material burned at lower densities are very small and can be neglected to good approximation. In the unburnt material (carbon and oxygen) no weak interactions occur, as we investigated in Section 2.6.

The tables in our code are based on the rates determined by Langanke and Martínez-Pinedo (2001). Based on these rates, Seitzzahl et al. (2009) calculated and tabulated values for  $\dot{Y}_e$  and  $\dot{E}_\nu$  as functions of  $T$ ,  $\rho$ , and  $Y_e$ . They take all four physical processes, reactions (2.56–2.59) in nuclei and free nucleons, into account. Furthermore, Coulomb corrections and temperature dependent nuclear partition functions are included.

For this work we use an extended version of their tables with minimum values of  $Y_e^{\min} = 0.404$ . These rates are accurate down to  $Y_e \sim 0.44$ , for lower  $Y_e$  the reliability is limited due to the lack of nuclei with according proton-to-neutron ratios in the underlying rate tables (I. Seitzzahl, private communication). In Figure 3.2 these rates are shown for a fixed density and temperature value at the upper limit occurring in the simulations presented in Section 5 ( $T = 1.0 \times 10^{10}$  K,  $\rho = 1.0 \times 10^{10}$  g cm<sup>-3</sup>). These rates are compared to the rates used in core-collapse supernovae computations which do not include  $\beta$ -decay rates<sup>45</sup> (Langanke et al., 2003). Further indicated is the position of the  $\beta$ -equilibrium in NSE matter, where the matter is in equilibrium with respect to the strong and the weak interaction, according to Arcones et al. (2010). In the physical environment considered in Section 5, matter should approach  $\beta$ -equilibrium asymptotically (e.g. Woosley, 1997; Arcones et al., 2010). Therefore, judging from Figure 3.2, we consider it justified to use the extended rates after Seitzzahl et al. (2009), which seem to reach the  $\beta$ -equilibrium asymptotically. The rates used in core-collapse supernovae are clearly too high for our case, since in the timescales relevant for this work ( $\tau \sim 1$  s),  $\beta$ -decay reactions are important; they decelerate the neutronization and finally lead to  $\beta$ -equilibrium. Hence, we are confident that the described approach is the most consistent way to treat this subject possible at the moment, but if complete weak interaction data for  $Y_e \lesssim 0.44$  become available in the future, we will adjust our tables.

#### 3.3.2. Neutrino energy

We will now explain how we calculate the energy per time  $\dot{E}_\nu$  that is released as kinetic energy of neutrinos. This is done for each grid cell; the energy is subtracted from the internal energy of the cell in each time step. We will present the resulting neutrino luminosities in Section 5.2.10.

Concerning the *weak neutrinos* introduced in Section 2.7.1: We discussed in the preceding section how the time rate of change of the specific energy  $\dot{E}_\nu$ , along with the time rate of change of the electron fraction  $\dot{Y}_e$ , was calculated by Seitzzahl et al. (2009) based on the

---

<sup>4</sup>Due to the considerably shorter timescales in core-collapse supernova simulations compared to Type Ia supernova simulations, the (slow)  $\beta$ -decays can be neglected in such simulations.

<sup>5</sup>The rates of Langanke et al. (2003) do not include electron captures on free protons. We added those rates, calculated by the use of an analytical expression.

weak interactions rates by Langanke and Martínez-Pinedo (2001). We use their results to determine the amount of energy carried away by weak neutrinos.

We calculate the energy that is released from the white dwarf due to the emission of *thermal neutrinos* using a freely accessible code provided by Timmes, F. X. (2011), in which analytic fitting formulas from Itoh et al. (1996) are implemented. This code differentiates between neutrinos created in five different plasma processes as mentioned in Section 2.7.2 (electron-positron pair annihilation, photoemission, plasmon decay, bremsstrahlung, recombination). With the help of this code we constructed tables of the time rate of change of the specific energy due to thermal neutrinos as a function of temperature and density, and use them as described above.

Both methods can only be applied to simulations of thermonuclear burning in white dwarfs. Neutrino physics of neutron stars are much more complicated because in this case the matter is not transparent to neutrinos; due to scatterings the energy of a neutrino when it is created in a weak reaction and the energy of this neutrino when it leaves the star are in general not the same. Hence, including neutrino physics in neutron star simulations requires more elaborated numerical schemes such as Boltzmann neutrino transport calculations or approximative methods (see Janka et al. (2007) and Liebendörfer et al. (2006), and references therein).

#### 3.3.3. Inclusion of neutron-rich nuclides in post-processing code

A minor modification was done to the nuclear reaction network in the post-processing code (cf. Section 3.1.7): To the standard network that contains 384 nuclides, used for instance by Seitenzahl et al. (2010), we added various neutron-rich isotopes to get correct results regarding the neutron-rich nucleosynthesis that is important in the context of Section 5. Now, our network consists of 458 nuclides up to  $^{98}\text{Zr}$ , including protons, neutrons, and alpha particles. The network is similar to the *alternate n-rich network* employed by Woosley (1997); hence, we can compare our results of nucleosynthesis during deflagrations in high-density white dwarfs more easily to his work. This we will do in Section 5.3.

## 3.4. Calculation of gravitational wave signal

After having discussed modifications to the LEAFS-code that we have done to adapt it to either of the two main subjects of this thesis in the preceding sections, we now introduce the implementation of our approach to calculate gravitational wave signals. This can be applied to both neutron star and white dwarf simulations – in Section 4.5 we will present our attempts to compute the gravitational wave signal of the conversion of a neutron star into a quark star, and in Appendix A we will show the gravitational wave signal of a typical thermonuclear supernova. Our numerical approach for the computation of the gravitational wave signal follows Blanchet et al. (1990) and Müller and Janka (1997). As described in Section 2.5, we calculate only the approximate *quadrupole radiation* because of the Newtonian nature of our simulations.

### 3. Numerical methods

---

The most straightforward way to determine the amplitude of gravitational quadrupole waves is by calculating the second derivative of the quadrupole moment  $\mathbf{Q}$ . The gravitational quadrupole radiation field in the transverse-traceless gauge  $\mathbf{h}^{\text{TT}}$  is, as discussed in Section 2.5,

$$h_{ij}^{\text{TT}}(\mathbf{x}, t) = \frac{2G}{c^4 R} P_{ijkl}(\mathbf{n}) \frac{\partial^2}{\partial t^2} Q_{kl} \left( t - \frac{R}{c} \right). \quad (3.16)$$

$\mathbf{P}$  is the transverse-traceless projection operator as defined in equation (2.54). However, the calculation of the second time derivative gives rise to numerical instabilities, the resulting signal is quite noisy. Therefore, to avoid this unfavorable method, Nakamura and Oohara (1989) and Blanchet et al. (1990) introduced a different way to compute the amplitude. With this new method, which was applied successfully to core-collapse supernovae by Mönchmeyer et al. (1991) and Müller and Janka (1997), the gravitational quadrupole radiation field  $\mathbf{h}^{\text{TT}}$  is calculated by

$$h_{ij}^{\text{TT}}(\mathbf{x}, t) = \frac{2G}{c^4 R} P_{ijkl}(\mathbf{n}) \int d^3x \rho (2v_k v_l - x_k \partial_l \Phi - x_l \partial_k \Phi). \quad (3.17)$$

Here  $\mathbf{v}$  is the velocity and  $\Phi$  is the usual Newtonian gravitational potential or an effective relativistic gravitational potential (cf. Section 3.2.3). Blanchet et al. (1990) showed that equation (3.17) is equivalent to equation (3.16), while Mönchmeyer et al. (1991) demonstrated the numerical superiority of the method that implements equation (3.17). See also Müller et al. (2012) for a recent application.

Since gravitational waves have two polarization states (“+” and “×”, cf. Section 2.5), the amplitude can be written in terms of the two *unit linear-polarization tensors*  $\mathbf{e}_+$  and  $\mathbf{e}_\times$  (Misner et al., 1973) as

$$h_{ij}^{\text{TT}}(\mathbf{x}, t) = \frac{1}{R} (A_+ \mathbf{e}_+ + A_\times \mathbf{e}_\times). \quad (3.18)$$

In the case of a plane wave propagating in  $z$ -direction, the unit linear-polarization tensors are

$$\mathbf{e}_+ = \mathbf{e}_x \otimes \mathbf{e}_x - \mathbf{e}_y \otimes \mathbf{e}_y \quad (3.19)$$

$$\mathbf{e}_\times = \mathbf{e}_x \otimes \mathbf{e}_y + \mathbf{e}_y \otimes \mathbf{e}_x, \quad (3.20)$$

where  $\mathbf{e}_x$  and  $\mathbf{e}_y$  are the unit vectors parallel to the  $x$ - and  $y$ -axis, respectively. We calculate the amplitudes  $A_+$  and  $A_\times$  considering two different lines of sight, as was suggested in Müller and Janka (1997). Since they use preferentially spherical coordinates, they speak of the polar ( $\vartheta = 0$ ,  $\varphi = 0$ ) and equatorial ( $\vartheta = \pi/2$ ,  $\varphi = 0$ ) direction. In our case, as we use exclusively Cartesian coordinates, it is more appropriate to call it the  $z$ -direction and  $x$ -direction, as we will do in the following. With the definition

$$A_{ij} = \frac{G}{c^4} \int d^3x \rho (2v_i v_j - x_i \partial_j \Phi - x_j \partial_i \Phi), \quad (3.21)$$

the amplitudes  $A_+$  and  $A_\times$  in the  $z$ -direction can be expressed as

$$A_+^z = A_{xx} - A_{yy} \quad (3.22)$$

$$A_\times^z = 2A_{xy}, \quad (3.23)$$

while in the  $x$ -direction one obtains

$$A_+^x = A_{zz} - A_{yy} \quad (3.24)$$

$$A_\times^x = -2A_{yz}. \quad (3.25)$$

When we show results of our calculations of the gravitational wave signal in Section 4.5 and Appendix A, we will always present the four amplitudes (3.22–3.25). We implemented the calculation of these amplitudes according to equation (3.21) in the code. For comparison and to check our results, we also calculate the signal directly by using equation (3.16). As we will show in the respective sections, the results from the two methods agree, in general, very well. However, when calculating the signal using equation (3.16), the results are very noisy, as expected.

Beyond the amplitudes, another interesting quantity is the total amount of energy radiated away by gravitational waves,  $E_{\text{gw}}$ . It can be expressed as (Müller and Janka, 1997)

$$E_{\text{gw}} = \frac{2c^3}{5G} \int_{-\infty}^{+\infty} \left( \frac{d}{dt} \left( A_{ij} - \frac{1}{3} \delta_{ij} A_{kk} \right) \right)^2 dt \quad (3.26)$$

$$= \frac{2c^3}{15G} \int_{-\infty}^{+\infty} \left( \dot{A}_{xx}^2 + \dot{A}_{yy}^2 + \dot{A}_{zz}^2 - \dot{A}_{xx}\dot{A}_{yy} - \dot{A}_{xx}\dot{A}_{zz} - \dot{A}_{yy}\dot{A}_{zz} + \right. \\ \left. + 3(\dot{A}_{xy}^2 + \dot{A}_{xz}^2 + \dot{A}_{yz}^2) \right) dt. \quad (3.27)$$

All values of  $E_{\text{gw}}$  stated in the following chapters are calculated by means of equation (3.27). As it turns out (see Section 4.5.2 and Appendix A), the gravitational wave energy in the systems considered in this work (isolated neutron stars and exploding white dwarfs) is many orders of magnitudes lower than the kinetic, potential, or internal energy and is therefore dynamically unimportant. Hence, the error caused by the fact that we did not couple the gravitational waves part of the code to the hydrodynamics part is negligible.

Also the *frequency*  $f$  of a gravitational wave signal is an important quantity to determine, because detectors are only sensitive in a confined frequency range. We adopt the approach of Müller (1982) and Müller et al. (2012) and conduct Fourier analyses of the calculated gravitational wave amplitudes and determine by this means the energy spectrum  $\partial E_{\text{gw}} / \partial f$ . The Fourier transforms of the  $A_{ij}(t)$  are

$$\tilde{A}_{ij}(f) = \int_{-\infty}^{\infty} A_{ij}(t) e^{2\pi i f t} dt. \quad (3.28)$$

### 3. Numerical methods

---

According to Müller et al. (2012) we obtain the energy spectrum by

$$\frac{\partial E_{gw}}{\partial f} = \frac{2c^3}{15G} (2\pi f)^2 \left( |\tilde{A}_{xx} - \tilde{A}_{yy}|^2 + |\tilde{A}_{xx} - \tilde{A}_{zz}|^2 + |\tilde{A}_{yy} - \tilde{A}_{zz}|^2 + \right. \quad (3.29)$$

$$\left. + 6 \left( |\tilde{A}_{xy}|^2 + |\tilde{A}_{xz}|^2 + |\tilde{A}_{yz}|^2 \right) \right). \quad (3.30)$$

## 4. Combustion of a hadronic neutron star into a quark star

The conversion of a hadronic neutron star into a quark star, modeled as a combustion, is the topic of this section. After an introduction we will discuss the aspects of combustion applied to this subject. Then we will present our simulation setup and the results of the simulations. Finally we will describe our results regarding the gravitational wave signal of the conversion process.

Large parts of this chapter were published before (Herzog and Röpke, 2011). In the following, we will adopt substantial parts of this publication literally or with minor modifications. A considerable amount of new material was added to the original work, in particular Sections 4.4.6 to 4.4.8 and Section 4.5.

### 4.1. Introduction

Based on earlier work by Bodmer (1971) and Itoh (1970), Witten (1984) suggested that a mixture of about the same number of u-, d- and s-quarks, called strange quark matter (SQM), was the true ground state of matter, whereas ordinary nuclear matter is only a metastable, yet usually extremely long-lived state. This conjecture, known today as *strange matter hypothesis*, was discussed lively ever since, but no final verdict about its correctness could be made because the equation of state (EoS) of cold dense matter is still largely unknown. Matter in this extreme state is inaccessible to laboratory experiments; compact stars, however, offer a possibility to test the strange matter hypothesis. Shortly after Witten's work also Haensel et al. (1986) and Alcock et al. (1986) proposed *strange stars*, compact stars consisting entirely of strange quark matter. Alcock et al. (1986) based their work on the idea that compact stars are not born as strange stars, but as hadronic neutron stars, which later are converted into strange stars or *hybrid stars* – compact stars consisting of a quark core and hadronic outer layers.

Hadronic matter does not decay into strange quark matter spontaneously, even though it would be energetically favorable, because this process would require a large amount of simultaneous weak reactions – the probability for this to happen is vanishingly low. But if some strange quark matter already exists inside a neutron star, the diffusion of s-quarks from this seed into the surrounding hadronic matter would convert it into strange quark matter. This conversion process should take place in a confined region and on length-scales small compared to the size of the star. It is expected to occur only if the conversion releases energy, that is, if it is an exothermic process. The described situation is therefore similar to the propagation

of a chemical flame, or even more similar to the thermonuclear burning inside a white dwarf during a Type Ia supernova. Thus, it is natural to think of the conversion of hadronic matter into strange quark matter as a “combustion”. In the spirit of this analogy, we will sometimes refer to the conversion as “burning” and to the conversion front as “flame front”. Alcock et al. (1986) were the first to suggest that a strange star may originate from a combustion of an ordinary neutron star. They also considered how a strange quark matter seed which subsequently triggers the conversion into a strange star may come about and described various possibilities by either internal nucleation or external seeding. Subsequently the idea of a combustion was discussed in more detail by various authors (Horvath and Benvenuto, 1988; Olesen and Madsen, 1991; Cho et al., 1994; Lugones et al., 1994; Lugones and Benvenuto, 1995; Tokareva and Nusser, 2006; Drago et al., 2007; Niebergal et al., 2010).

The laminar conversion velocity was first estimated by Olinto (1987), and, with similar results, by Heiselberg et al. (1991). Based on their results, Olesen and Madsen (1991) calculated the burning of a neutron star using a one-dimensional model with laminar burning and obtained conversion timescales from  $10^{-1}$  s to  $10^2$  s. Horvath and Benvenuto (1988) suggested that the combustion should be turbulent due to various instabilities of the conversion front and therefore the conversion velocity should be enhanced considerably (see Horvath (2010) for a recent update). Lugones et al. (1994) and Lugones and Benvenuto (1995) pointed out the importance of the conditions for an exothermic combustion. The combustion mode was discussed from a hydrodynamic point of view also by Cho et al. (1994), Tokareva and Nusser (2006) and Drago et al. (2007), where the latter expected the burning to be subsonic, although accelerated by turbulence. New ideas concerning the initial seeding were recently published by Perez-Garcia et al. (2010). They suggested that the self-annihilation of weakly interacting dark matter particles (WIMPs) inside a neutron star may provide a strange quark matter seed. Recently, hydrodynamic simulations of the combustion front were presented by Niebergal et al. (2010). Their results of the laminar conversion velocity differed strongly from earlier estimates. On the observational side Leahy and Ouyed (2008), extended in Ouyed et al. (2012), examined the supernova SN 2006gy and suggested that this extremely luminous event can be explained by a “quark nova” – the transition of the newly formed neutron star to a strange quark star shortly after a core-collapse supernova of a very massive star.

Here we study the dynamical behavior of the conversion inside a neutron star. We model the conversion as a combustion, particularly as a subsonic deflagration. As mentioned above, it is widely assumed that the conversion process turns turbulent (e.g. Drago et al., 2007; Horvath and Benvenuto, 1988; Horvath, 2010), but dynamical, multi-dimensional simulations have never been performed. Thus, our main focus will be to explore if and how turbulent motion occurs during the conversion process and to which consequences for the final state of the neutron star this may lead.

For our investigations we attempt to conduct hydrodynamic simulations. Numerical methods to model the thermonuclear burning in white dwarfs are available to us; we introduced them in Section 3. Our concept is now to draw an analogy between the conversion from hadronic into strange quark matter and the thermonuclear burning of carbon and oxygen. In

the next section we describe how and to what extent we can transfer the existing numerical methods to the new physical environment.

## 4.2. Modeling the conversion process as a combustion

We model the conversion from hadronic matter into strange quark matter as a combustion, initiated by a seeding of strange quark matter which we assume to occur in the center of the star. We do not specify the origin of the initial strange quark matter seed (see Alcock et al. (1986) for various possibilities, or Perez-Garcia et al. (2010) for new ideas). The flame front, initially consisting of the boundary surface of some central seed, propagates outwards and converts hadronic matter into strange quark matter, provided this reaction is exothermic. If this is the case, the difference in the energy per baryon is released into internal energy and therefore the temperature increases. The combustion process takes place on length scales of the micro-physical reactions, which can be estimated as follows: The disintegration of a nucleon into quarks happens on time scales of the strong interaction,  $\sim 10^{-24}$  s, corresponding to a length scale of  $\sim 10^{-13}$  cm. The conversion of a d-quark into an s-quark due to the weak interaction takes place in  $\sim 10^{-8}$  s. Since the weak processes are much slower, they determine the time scale of the burning, leading to a width of the reaction zone,  $l_{\text{burn}}$ , not exceeding  $10^2$  cm, whereas realistic calculations yield  $l_{\text{burn}} \sim 10$  cm (Niebergal et al., 2010). These length scales are much smaller than the resolution we can achieve in our simulations ( $l_{\text{resolved}} > 10^3$  cm) and therefore we cannot resolve the reaction zone.

Instead, we apply the concepts described in Section 2.4.1 and model the conversion front as a discontinuity which separates the “unburnt” (hadronic) matter from the “burnt” (strange quark) matter and have to take the propagation velocity of the conversion front with respect to the fluid flow as an input parameter, since this velocity is not determined by the hydrodynamic equations but by micro-physical processes on scales of the internal structure of the conversion front.

A combustion can take place either as a supersonic detonation driven by a shock wave, or as a subsonic deflagration driven by diffusion processes (cf. Section 2.4.1). Since we cannot resolve the internal structure of the flame we have to decide before starting our computations whether to model the conversion as a deflagration or as a detonation. Drago et al. (2007) examine the conversion of hadronic matter into quark matter based on the hydrodynamic jump conditions. They assume the combustion to start as a deflagration and conclude that the process should stay subsonic. Also Niebergal et al. (2010) and Horvath (2010) assume the conversion to be subsonic. Based on these recent publications we decided to choose a deflagration as combustion mode, though we do not exclude the detonation mode and might consider it in future work.

The relevant input velocity for a deflagration is the laminar burning velocity  $v_{\text{lam}}$ , which is only very poorly known for the burning of hadronic matter into strange quark matter. The first attempts to determine it were made by Olinto (1987), who estimates  $v_{\text{lam}}$  based on the

diffusion of strange quarks and the equilibration of the strange quark matter via weak interactions. The resulting velocities are generally rather low but strongly temperature dependent and would lead to a wide range of neutron star conversion timescales from milliseconds up to several minutes. Recently, Niebergal et al. (2010) conducted one-dimensional hydrodynamic simulations of the combustion flame, including neutrino emission and strange quark diffusion. They found laminar burning velocities much higher than in earlier work. Because the methods of Niebergal et al. (2010) are more sophisticated than in previous publications, we adopt a weakly density-dependent laminar burning velocity based on a linear fit to their results:

$$v_{\text{lam}} = \left( 0.87 \left( \frac{e}{10^7 \text{ g cm}^{-3}} \right) + 1.3 \times 10^7 \right) \text{ cm s}^{-1}, \quad (4.1)$$

where  $e$  is the total energy density in units of  $[\text{g cm}^{-3}]$ . This leads to  $v_{\text{lam}} = 1 \times 10^8 \text{ cm s}^{-1}$  in the center of the initial neutron star at densities of  $e = 1 \times 10^{15} \text{ g cm}^{-3}$ . If the burning velocity is strongly enhanced by turbulence, the importance to know the exact value of  $v_{\text{lam}}$  is subordinate (see below).

In chemical flames, as well as during the thermonuclear burning of carbon and oxygen in the center of a white dwarf, the large amount of energy released during the burning process leads to a sharp increase in temperature. In chemical flames a strong increase of pressure, or a strong decrease in density at constant pressure, is the natural result and therefore is usually taken for granted in qualitative considerations. Similarly, in thermonuclear supernovae the degeneracy of the matter is partially lifted, therefore the density decreases also in this case, albeit not as strongly as in chemical flames. Moreover, in these cases, although the chemical abundances change during the burning process, the EoS does not change dramatically. In the case of the burning in white dwarfs at densities  $\lesssim 7$  to  $8 \times 10^9 \text{ g cm}^{-3}$  this leads to an inverse density stratification, instabilities and turbulence (e.g. Timmes and Woosley, 1992). However, because of the strongly degenerate state of matter in neutron stars and the fundamentally different EoS before and after the conversion process it cannot be taken for granted that the neutron star matter behaves in the same way as described above. The state of the fluid behind the conversion front is determined by the change of the EoS and the hydrodynamic jump conditions (see e.g. Drago et al., 2007) which result from the conservation of the baryon flux density and the energy-momentum tensor across the flame surface and has to be computed in hydrodynamic simulations. To explore if in the vicinity of the propagation front the density of the strange quark matter is lower than the density of the hadronic phase for our choice of EoS is therefore one aim of this part of the thesis.

We described in Section 2.4.2 that when an inverse density stratification appears, the burning can become turbulent if some conditions are fulfilled. It is another central aim of this thesis to explore whether the conversion of hadronic matter into strange quark matter in the interior of neutron stars becomes turbulent; and, connected to that, to test if the turbulent burning velocity becomes independent of the poorly known laminar burning velocity. In order to do that, we need a model to treat turbulent burning in our hydrodynamic simulations.

We found a Gibson scale of  $l_G = 10^2$  cm in Section 2.4.3 for a typical case of a rising Rayleigh-Taylor bubble of strange quark matter. We discussed above that the scale of the flame is  $l_{\text{burn}} \sim 10$  cm (Niebergal et al., 2010). Our resolution is  $l_{\text{resolved}} > 10^3$  cm, as we will see in Section 4.4.1. Therefore, condition (2.39),  $l_{\text{burn}} < l_G < l_{\text{resolved}}$ , holds; it is therefore justified to conduct large eddy simulations and apply the numerical techniques developed for thermonuclear burning in white dwarfs (cf. Section 3.1.6) also to the new physical environment.

### 4.3. Conditions for exothermic combustion

As described in Section 2.4.4, the thermonuclear burning in white dwarfs is always exothermic. Concerning the conversion of hadronic matter into strange quark matter, the condition for exothermic burning (2.40) is not fulfilled automatically, as we will see in the following.

Since we describe the conversion of hadronic matter into strange quark matter as a combustion, and a combustion has to be, by definition, exothermic (Anile (1989); cf. Section 2.4.4), we can use condition (2.40) to specify the following necessary condition for the conversion to take place: The total energy density of the quark phase  $e_q$  in a thermodynamic state  $(P, X)$  has to be lower than the energy for the hadronic matter  $e_h$  in the same state,

$$e_h(P, X) > e_q(P, X), \quad (4.2)$$

where  $P$  is the pressure,  $X$  is the generalized volume,  $X = (e + P)/n_B^2$ , and  $n_B$  is the baryon density. In the case of our analytic EoS for strange quark matter (2.11), this can be rewritten as a simple condition for the energy density of the hadronic phase (Barz et al., 1985; Lugones et al., 1994) :

$$e_h(P) > 3P + 4B. \quad (4.3)$$

From this relation it becomes clear that for each given total energy density  $e_h$  and temperature  $T_h$  the corresponding pressure of the hadronic phase  $P$  and the value of  $B$  determine whether the conversion can proceed in form of a combustion wave. Thus, after choosing the EoS and assuming a fixed  $T_h$  we can calculate for each  $e_h$  a critical bag constant,  $B_{\text{crit}}(e_h)$ , which is the largest possible bag constant for an exothermic combustion. The results of these calculations using both the LS EoS with  $K = 180$  MeV and the Shen EoS are shown in Figure 4.1 (a). Here the results are plotted for two different cases: In the first case we assume a constant temperature of the unburnt hadronic matter of  $T_h = 100$  keV and a constant electron fraction of  $Y_e = 0.2$ . We adopt these assumptions for our numerical simulations presented in Section 2.4. In the second case we assume  $\beta$ -equilibrium and zero temperature. As visible in Figure 4.1 (a), the differences between the two cases are rather small and thus negligible for the qualitative treatment in this work. Also apparent from this figure is that for bag constants larger than the theoretical lower limit,  $B^{1/4} > 145$  MeV, and temperatures found in the interior of cold

#### 4. Combustion of a hadronic neutron star into a quark star

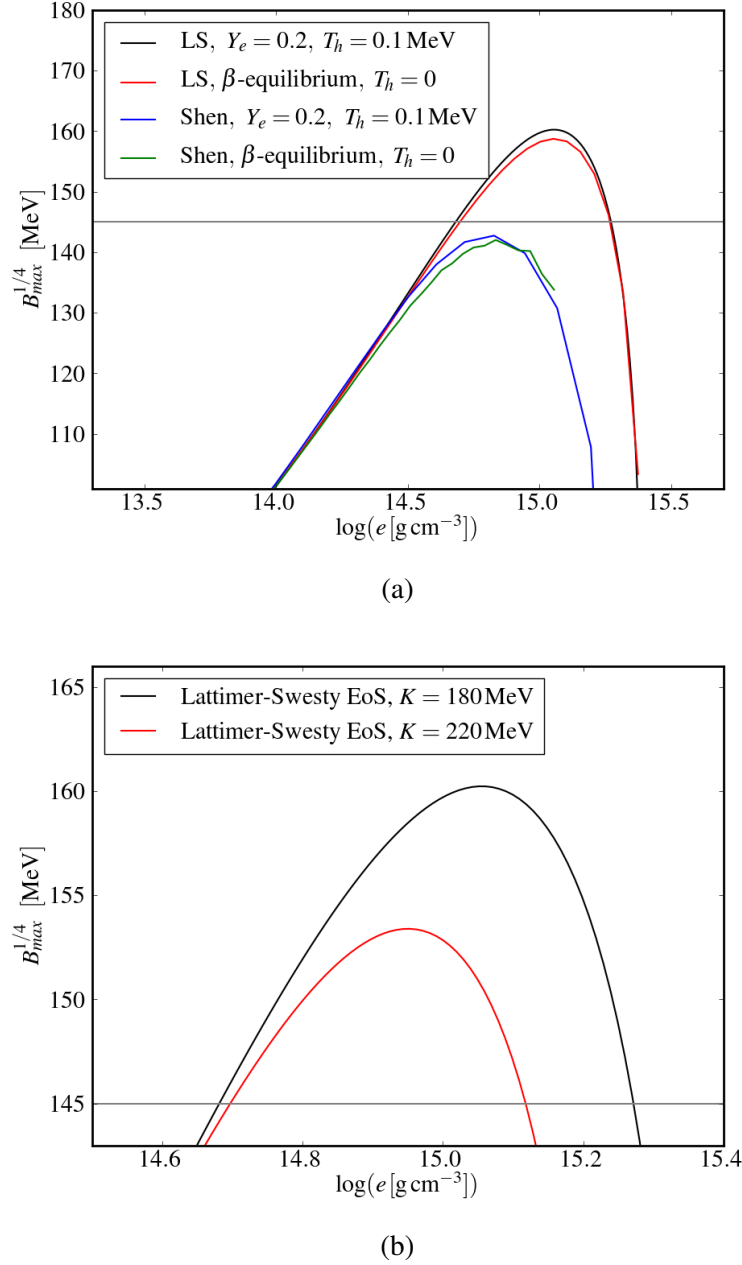


**Figure 4.1.:** Maximum bag constant  $B$  allowing an exothermic combustion as function of the total energy density  $e$ . (a) Two different hadronic EoS (Lattimer-Swesty with  $K = 180 \text{ MeV}$  and Shen); for each EoS, two cases are plotted: in the first case temperature  $T_h$  and electron fraction  $Y_e$  are kept constant, in the second case the matter is in  $\beta$ -equilibrium at zero temperature. (b) LS EoS with two different incompressibility moduli  $K$ . The gray horizontal line indicates the theoretical lower limit of  $B$  in (a) and (b).

neutron stars, hadronic matter described by the Shen EoS cannot be burned into strange quark matter in an exothermic combustion, regardless of the density. In contrast, matter described by the LS EoS can be converted into strange quark matter in an exothermic way at densities occurring in the center of neutron stars. The difference between the two hadronic EoS can be explained as follows. The Shen EoS is rather stiff, much stiffer than the LS EoS, that is at the same density the pressure is much higher. According to equation (4.3) this leads to a higher energy threshold for a given density. Based on these results we have to refrain from using the Shen EoS in our hydrodynamic simulations.

As mentioned in Section 2.1.2, the maximum mass of a neutron star described by the LS180 EoS is incompatible with observations. We nevertheless use the LS180 EoS in this work, because we see the simulations conducted in this section as a first step into this so far mostly unexplored field; we do not claim to conduct realistic simulations.

An alternative would be to change the incompressibility modulus of the LS EoS to  $K = 220 \text{ MeV}$ , which leads to a maximum mass compatible with the observations. We compare these two versions of the LS EoS in Figure 4.1 (b). For low bag constants ( $B^{1/4} \sim 145 \text{ MeV}$ ) the higher stiffness of the EoS with higher  $K$  affects the lower density limit only slightly, but for  $B^{1/4} \gtrsim 152 \text{ MeV}$  the range in which exothermic combustion is possible becomes very narrow. Since our goal is to conduct simulations with higher bag constants to be able to compare the results for a wide range in the amount of released energy, we use in our simulations only the LS EoS with  $K = 180 \text{ MeV}$ .

In Figure 4.2 we concentrate on this case. Here we plot the minimum total energy density of the hadronic phase,  $e_{\min}(B)$ , as a function of  $B$  and for different fixed temperatures. Since below this density threshold no combustion is possible, it plays an important role in our simulations. The green line in Figure 4.2 shows the case with  $T_h = 100 \text{ keV}$ , the temperature we adopt for the cold neutron star in our simulations. In addition we explore the effects of several higher temperatures. For temperatures up to  $T_h = 1 \text{ MeV}$  only slight differences would be visible due to the strong degeneracy of the matter. In proto-neutron stars considerably higher temperatures occur, therefore also results for  $T_h = 10, 20, \text{ and } 30 \text{ MeV}$  are shown in the figure. These temperatures have a noticeable effect on the density threshold, as visible in Figure 4.2. In general, higher temperatures move the density threshold to higher densities.

## 4.4. Simulations

We conducted simulations of the conversion of a hadronic neutron star into a quark star by means of the numerical methods introduced in Section 3, in particular using the LEAFS hydrodynamics code with the modifications described in Section 3.2. We will first explain the setup we use as initial condition, then investigate the onset of turbulence, followed by several sections in which we discuss the results and the influence of different numerical and physical parameters on them.

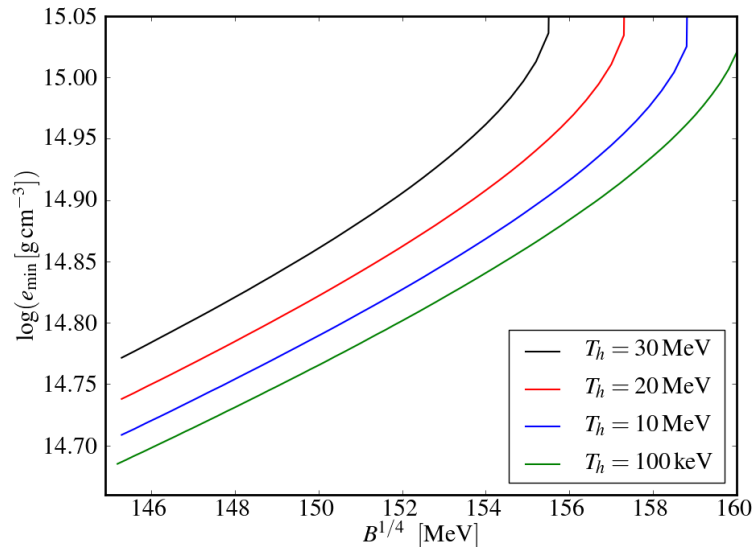


**Figure 4.2.:** Minimum total energy density  $e$  for an exothermic combustion as function of the bag constant  $B$  and for different temperatures  $T_h$ , using the Lattimer-Swesty EoS with  $K = 180\text{MeV}$ .

#### 4.4.1. Neutron star setup

In the simulations presented in this section, we set up one octant of the neutron star on a three-dimensional Cartesian grid with 128 or 192 grid cells in each dimension. In the simulations that we conduct to calculate the gravitational wave signal, presented in Section 4.5, we set up the full neutron star on a three-dimensional Cartesian grid with 256 grid cells per dimension.

We use a moving hybrid grid as described in Section 3.1.3 with the minor modification explained in Section 3.2.5. This way we achieve in our three-dimensional neutron star simulations an initial resolution in the center of the star of

$$l_{\text{resolved}} = 2.6 \times 10^3 \text{ cm} \times (\text{grid cells per dimension}/128)^{-1}, \quad (4.4)$$

if our grid covers one octant of the star. A factor of 2 has to be included on the right-hand side in the case of the full-star simulations of Section 4.5.

Burning is initialized in the following way: At the center of the star we construct a small sphere with a radius of  $r_{\text{seed}} = 10^5 \text{ cm}$  on which a sinusoidal perturbation with an amplitude of  $2 \times 10^4 \text{ cm}$  is superimposed. The initial seed is shown in the close-up of Figure 4.6 (a). When starting the simulation, the matter inside this small volume is converted instantly and constitutes the initial strange quark matter seed.

Since both the size and the geometric shape of the initial seed are not known, we choose

this configuration for numerical reasons: The size of the perturbations is similar to the minimum length scale for turbulent burning  $\lambda_{\min}$  (cf. Sections 2.4.2 and 4.4.2), therefore the front is expected to develop Rayleigh-Taylor instabilities soon after the start of the simulations. Smaller initial perturbations would need some time to grow before Rayleigh-Taylor instabilities become possible. But since in the end the core is converted completely, the results should change only slightly, whereas the computational costs would be considerably higher.

As described in Section 2.4, we assume the combustion to be a deflagration and ignite the burning accordingly. Although we do not expect different initial configurations to alter our results considerably, possible effects of different initial geometries and different ways of ignition should be subject to future work.

For simplicity we assume for all our neutron star simulations a constant low electron fraction  $Y_e$ . Variations of its value, particularly assuming  $\beta$ -equilibrium, do not lead to a significant change of our results, as is shown exemplary in Section 4.3. In the same section we explained that for physical reasons it turns out that it is impossible to use the Shen EoS, thus we perform all our hydrodynamic simulations of neutron stars using the LS EoS.

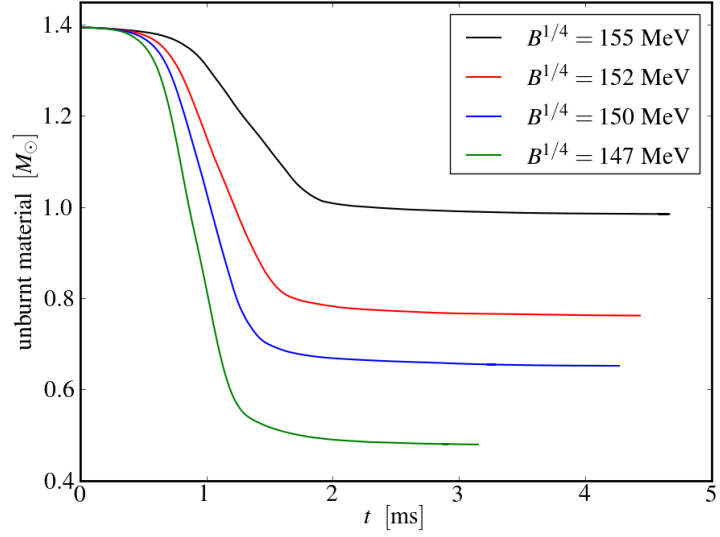
We conduct several runs with varying bag constant  $B$ . Since only some constraints on  $B$  are known, we can use it as a parameter to change the EoS for strange quark matter and are thus able to control the amount of released energy from very high to rather low values, according to equation (2.12). We vary  $B$  in a subset of the theoretically admissible range between a lower limit of  $B_{\text{low}}^{1/4} = 147 \text{ MeV}$  and an upper limit of  $B_{\text{high}}^{1/4} = 155 \text{ MeV}$ . At even higher  $B$ , the combustion would be restricted to the very innermost region of the neutron star or would not be possible at all, see Figure 4.1 (a) and equation (4.2). We use  $B^{1/4} > 155 \text{ MeV}$  only to test if instabilities grow at the beginning of the burning; results are presented in Section 4.4.2. In alternative units our chosen limits are roughly  $B_{\text{low}} = 60 \text{ MeV}/\text{fm}^3$  and  $B_{\text{high}} = 80 \text{ MeV}/\text{fm}^3$  – values also used as lower and upper limits in the literature (e.g. Bauswein et al., 2010).

We start our computations with a nonrotating, cold, isothermal “standard neutron star” in hydrostatic equilibrium, which has an initial central total energy density of  $e_c = 1.0 \times 10^{15} \text{ g cm}^{-3}$ , a gravitational mass of  $M = 1.4 M_{\odot}$ , a radius of  $R = 11 \text{ km}$ , an electron fraction of  $Y_e = 0.2$ , and a temperature of  $T = 100 \text{ keV}$ . We conducted four runs with a resolution of 128 grid cells per dimension and bag constants of  $B^{1/4} = 147, 150, 152$  and  $155 \text{ MeV}$ , respectively. Table 4.1 shows an overview of the models presented here. In Figure 4.3 the temporal evolution of the conversion for different  $B$  is shown, represented by the gravitational mass of the remaining unburnt hadronic material.

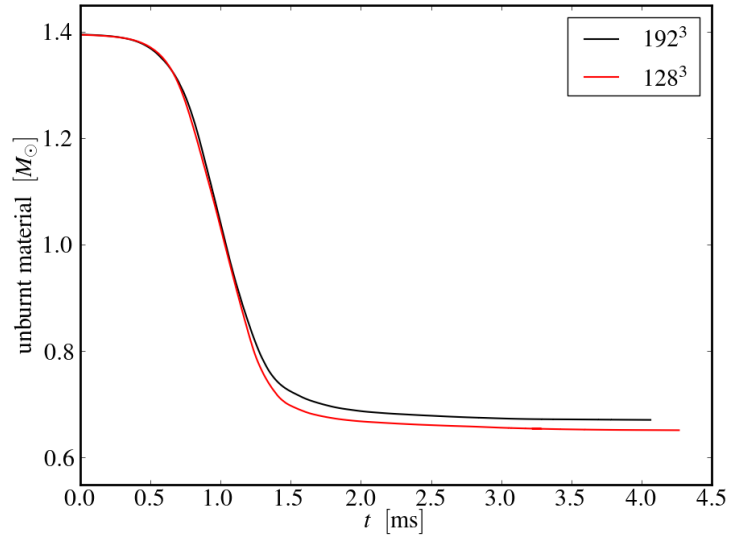
In addition, we conducted one run with a higher resolution, 192 grid cells per dimension, using an intermediate bag constant of  $B^{1/4} = 150 \text{ MeV}$  (model B150\_192). To study the effects of different resolutions, we compare in Figure 4.3 (b) the two models B150\_128 and B150\_192, which differ only in the resolution ( $128^3$  and  $192^3$ , respectively). Apparently there are only slight differences between the two models. In particular the slopes in the phase of rapid burning, which are determined by the conversion rate, which in turn depends on the turbulent burning velocity, agree very well. The different resolutions only become noticeable

#### 4. Combustion of a hadronic neutron star into a quark star

---



(a)



(b)

**Figure 4.3.:** Gravitational mass of unburnt (hadronic) material in the three-dimensional simulations as a function of time: (a) for different bag constants  $B$  (models B155\_128, B152\_128, B150\_128 and B147\_128); (b) Resolution study, two models with  $B^{1/4} = 150$  MeV which differ only in resolution (models B150\_192 and B150\_128)

Model	Resolution	$B^{1/4}/\text{MeV}$	$M_{\text{unburnt}}/M_{\odot}$
B147_128	$128^3$	147	0.48
B150_128	$128^3$	150	0.66
B150_192	$192^3$	150	0.67
B152_128	$128^3$	152	0.77
B155_128	$128^3$	155	0.99

**Table 4.1.:** Overview of the different models.  $M_{\text{unburnt}}$  is the gravitational mass of the remaining hadronic outer layer at  $t = 3.0$  ms, when the combustion can be considered as complete in all cases.

$B^{1/4}/\text{MeV}$	145	147	150	152	155	157
$At$	0.11	0.091	0.067	0.051	0.027	0.010
$\lambda_{\text{min}}/10^4 \text{ cm}$	3.6	4.4	6.2	8.5	16	45

**Table 4.2.:** Atwood number  $At$  and minimal length scale for turbulent burning  $\lambda_{\text{min}}$  for different bag constants  $B$  at time  $t = 0.1$  ms, determined in three-dimensional simulations.

in the representation of the exact position of the density threshold for exothermic combustion – hence the slight discrepancy in the amount of unburnt matter at later times. Therefore we consider our simulations converged in the sense that the effects caused by resolution are smaller than uncertainties caused by other sources. Thus, we regard a resolution of 128 cells per dimension to be sufficient for our quantitative analysis.

After addressing the question of whether burning is turbulent, the results of the simulation with the highest resolution, model B150\_192, are discussed in some detail below. In the subsequent sections we will briefly discuss differences in the two extreme cases (models B147\_128 and B155\_128). In the last three sections 4.4.6 to 4.4.8 we present results of simulations that have a setup differing from the standard setup described above.

#### 4.4.2. Onset of turbulence

We calculate the minimum length scale for turbulent burning  $\lambda_{\text{min}}$  according to equation (2.34), see Section 2.4.2. To ensure comparability, we use the same three-dimensional setup for all  $B$ , as described above, and the same resolution of 128 grid cells in each dimension.

In Figure 4.4 we compare  $\lambda_{\text{min}}$  at the beginning of the conversion process for different bag constants  $B$  and points in time. The density contrast is quantified by the *Atwood number*  $At = (e_h - e_q)/(e_h + e_q)$ . Table 4.2 lists  $At$  and  $\lambda_{\text{min}}$  for different  $B$ . The values were determined at  $t = 0.1$  ms. As visible in Table 4.2 and Figure 4.4,  $\lambda_{\text{min}}$  depends strongly on  $B$ , and becomes very large for high  $B$ . For the highest examined bag constant,  $B^{1/4} = 157 \text{ MeV}$ ,  $\lambda_{\text{min}}$  is comparable to the size of the system and no growth of Rayleigh-Taylor instabilities is expected. Bag constants starting at  $B^{1/4} = 152 \text{ MeV}$  down to the lowest  $B$  lead to smaller  $\lambda_{\text{min}}$

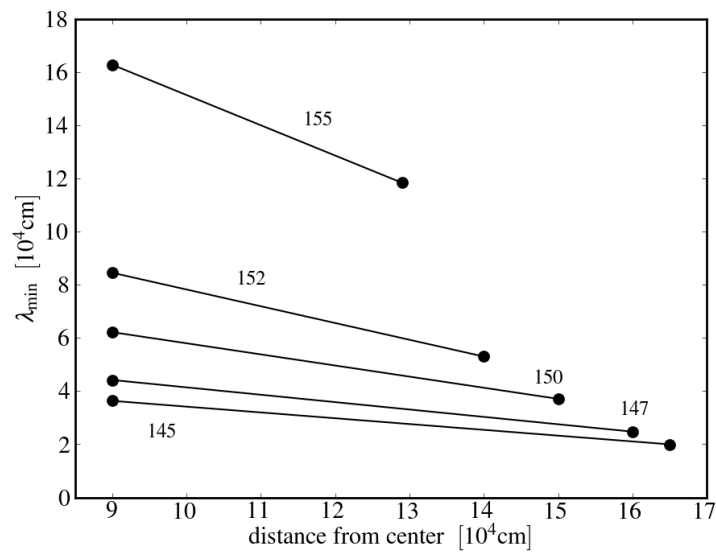


**Figure 4.4.:** Comparison of the minimal length scale for turbulent burning  $\lambda_{\min}$  in the early phase of the conversion process for different bag constants  $B$  and points in time, determined in three-dimensional simulations. The number on each line indicates  $B^{1/4}$  in MeV. For each  $B$  the first and second point correspond to time  $t_1 = 0.1$  ms and  $t_2 = 0.2$  ms, respectively. On the abscissa the average position of the conversion front at  $t_1$  and  $t_2$  is shown.

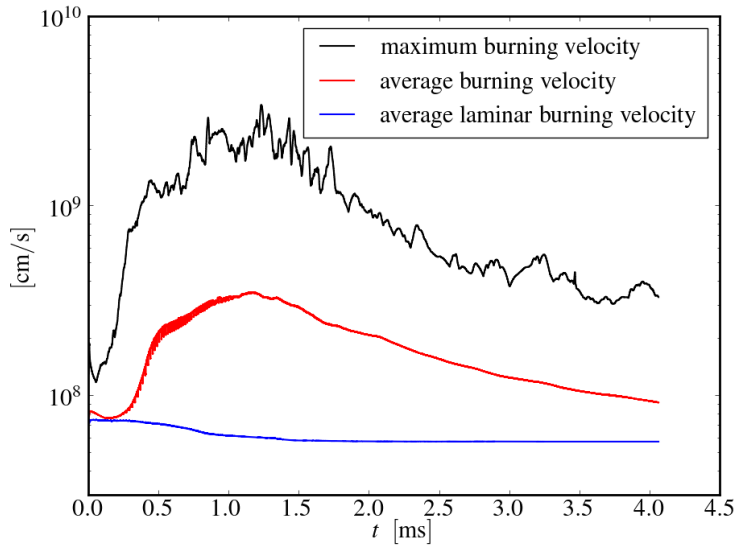


**Figure 4.5.:** Burning velocity: Comparison at each timestep of maximum burning velocity, average burning velocity, and the underlying average laminar burning velocity. The averages were done over all cells in which burning occurs. Data from the high resolution run with  $B^{1/4} = 150 \text{ MeV}$  (model B150\_192).

which are comparable to or smaller than the size of the initial perturbations – thus instabilities can grow. In the simulation with  $B^{1/4} = 155 \text{ MeV}$  this is not the case at  $t = 0.1 \text{ ms}$  but already at some slightly later time, since  $\lambda_{\min}$  decreases with time as the gravitational acceleration becomes stronger, see equation (2.34) and Figure 4.4. Our simulations confirm this: in all runs except for  $B^{1/4} \gtrsim 157 \text{ MeV}$  we see Rayleigh-Taylor instabilities forming. Thus the burning of a hadronic neutron star into a quark star becomes turbulent in most cases, given our choice of EoS.

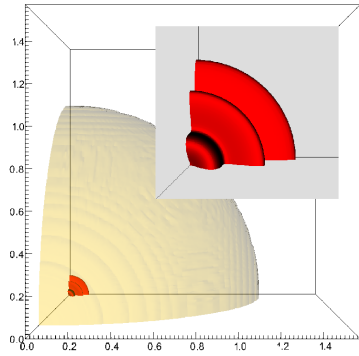
We note that the quantitative results of this analysis apply only for neutron stars with masses of  $M = 1.4 M_{\odot}$ . Neutron stars of higher masses have higher central densities; therefore, in these cases exothermic burning is possible also with higher bag constants (cf. Section 4.3). The above stated upper limit for the onset of Rayleigh-Taylor instabilities ( $B^{1/4} \sim 155 \text{ MeV}$ ) shifts to higher bag constants as well. Examples are presented in Section 4.4.8.

#### 4.4.3. Intermediate case: $B^{1/4} = 150 \text{ MeV}$

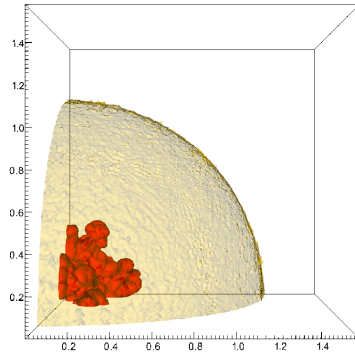
In this section we present a detailed discussion of the results of the simulation with a resolution of 192 grid cells per dimension and an intermediate bag constant,  $B^{1/4} = 150 \text{ MeV}$  (model B150\_192). According to equation (2.12) the energy per baryon in this case is  $E/A =$

#### 4. Combustion of a hadronic neutron star into a quark star

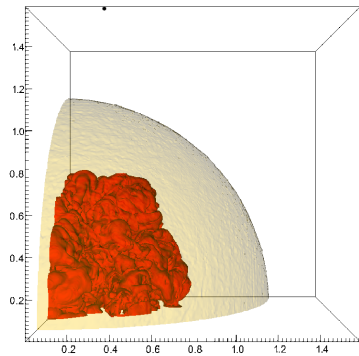
---



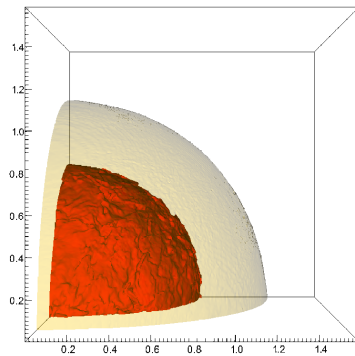
(a)  $t = 0$



(b)  $t = 0.7$  ms



(c)  $t = 1.2$  ms



(d)  $t = 4.0$  ms

**Figure 4.6.:** Model B150\_192: Conversion front (red) and surface of the neutron star (yellow) at different times  $t$ . In (a) a close-up of the central region is added. Spatial units  $10^6$  cm.

858 MeV, corresponding to a difference of  $\sim 70$  MeV per baryon with respect to the energy of nuclear matter.

In Figure 4.6 (a) the initial configuration including the strange quark matter seed in the center can be seen. The shape of the seed as described in Section 4.4.1 is shown additionally in the close-up in this figure. After ignition the conversion front propagates into the hadronic matter, at first in a laminar way until initial perturbations of the conversion front become unstable due to Rayleigh-Taylor instabilities. Until turbulence has fully developed, the conversion process stays in a short phase of nearly laminar burning while the instabilities grow, see Figure 4.3 (a) which shows the amount of unburnt (hadronic) matter as a function of time, and Figure 4.5, where we compare the average laminar burning velocity, the average burning velocity and the maximum burning velocity at each timestep. The averaging was done over all cells in which burning occurs.

As the instabilities grow, typical mushroom-shaped structures, rising plumes of strange quark matter, are forming and hadronic matter is falling down in between. These structures can be seen in Figure 4.6 (b), where the conversion surface is shown at  $t = 0.7$  ms. Starting at  $t \sim 0.5$  ms strong turbulence develops and rapid burning takes place until  $t \sim 1.5$  ms, as visible in Figure 4.3 (a). The structure of the conversion front near the end of this phase of rapid burning can be seen in Figure 4.6 (c). The plumes grow until the conversion front reaches densities where the condition for exothermic combustion (4.2) is no longer fulfilled. They continue to grow laterally, until they eventually merge, leaving bubbles of hadronic matter in between. Turbulence then weakens and the flame slows down. The remaining pockets filled with hadronic material shrink until they eventually vanish completely. Now all matter inside the volume confined by the above mentioned density threshold is burned and the star consists of an inner sphere of strange quark matter containing about half of the mass and an outer layer of unburnt hadronic matter (cf. Figure 4.6 (d)). This outer layer has a mass of about  $0.67 M_{\odot}$  and densities lower than the threshold (4.2) but mostly still super-nuclear (applying LS180 EoS and  $B^{1/4} = 150$  MeV, the density threshold in cold matter is at about  $1.8 \rho_{\text{nuclear}}$ , see Figure 4.2).

Turbulent motions lead to burning velocities considerably higher than the laminar burning velocities, the amplification factor is at maximum as high as about 50 and on average between 2 and 20, as displayed in Figure 4.5. This figure also clearly shows that the turbulent burning velocity and thus the strength of turbulence increases rapidly until it reaches a maximum at  $t \sim 1.0$  ms. At that point a steady but slower decrease starts. The maximum Mach numbers reached were about 0.2. This means that the combustion was clearly subsonic. As we do not include any kind of cooling, the large amount of energy released in the burning process is turned into thermal energy and the inner strange quark matter region is heated to temperatures of about 50 MeV in the center of the star.

We stopped this simulation at  $t = 4.0$  ms. By then the conversion rate has dropped to a very low value and seems to approach zero asymptotically. Since at that time the system is approximately in hydrostatic equilibrium (the dynamical time scale of a neutron star is  $\tau_{\text{dyn}} \sim 5 \times 10^{-2}$  ms) we do not expect any further conversion of a significant amount of mass.

#### 4. Combustion of a hadronic neutron star into a quark star

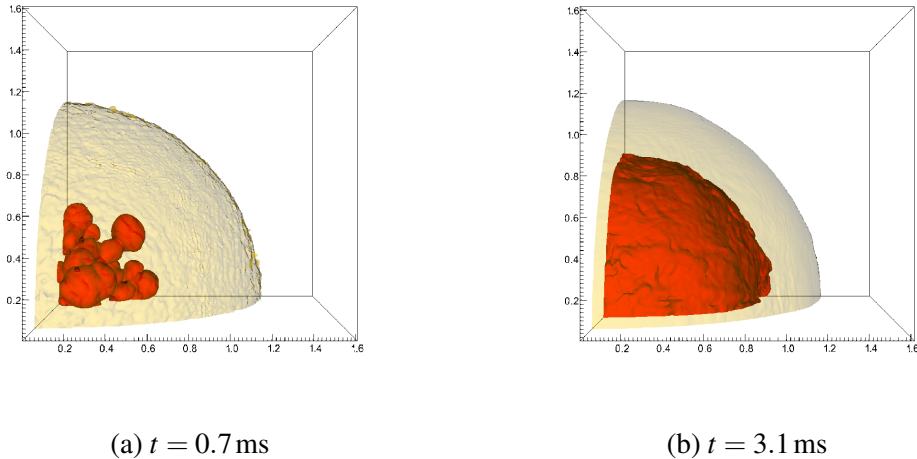


**Figure 4.7.:** Model B147\_128: Conversion front (red) and surface of the neutron star (yellow) at different times  $t$ . Spatial units  $10^6$  cm.

Therefore the structure of the remnant should not change if the simulation would have been carried on for longer timescales – at least in our model without cooling processes and in the approximation of a hydrodynamic combustion.

#### 4.4.4. Lower limit: $B_{\text{low}}^{1/4} = 147$ MeV

Now we briefly discuss the simulation with 128 grid cells per dimension and with our lower limit for the bag constant,  $B_{\text{low}}^{1/4} = 147$  MeV (model B147\_128). This corresponds to the largest difference in energy per baryon compared to nuclear matter,  $E/A = 90$  MeV.

Qualitatively, the conversion process evolves in the same way as in the case described above (model B150\_192), but there are some quantitative differences: The energy release is higher than in the intermediate case, therefore the burning leads to a stronger inverse density stratification, resulting in a faster growth of instabilities and stronger turbulence. The rising plumes of strange quark matter can be seen in Figure 4.7 (a) as typical “mushrooms”, like in the previous case. Comparing Figure 4.7 (a) and Figure 4.6 (b), both showing the conversion surface at  $t = 0.7$  ms, clarifies that the conversion process takes place considerably faster for the lower  $B$ . Figure 4.3 (a) shows that after a short phase of slow burning, rapid burning occurs from  $t \sim 0.4$  ms until  $t \sim 1.5$  ms. Then the burning slows down and the conversion rate approaches zero. At  $t = 5$  ms, the remnant has an inner strange quark matter core with a radius of  $\sim 9$  km, see Figure 4.7 (b), surrounded by a hadronic outer layer with a mass of  $0.48 M_{\odot}$ , the least massive outer layer in all our simulations. Central temperatures of the core reach 53 MeV, somewhat higher than in the previous case due to the higher energy release.

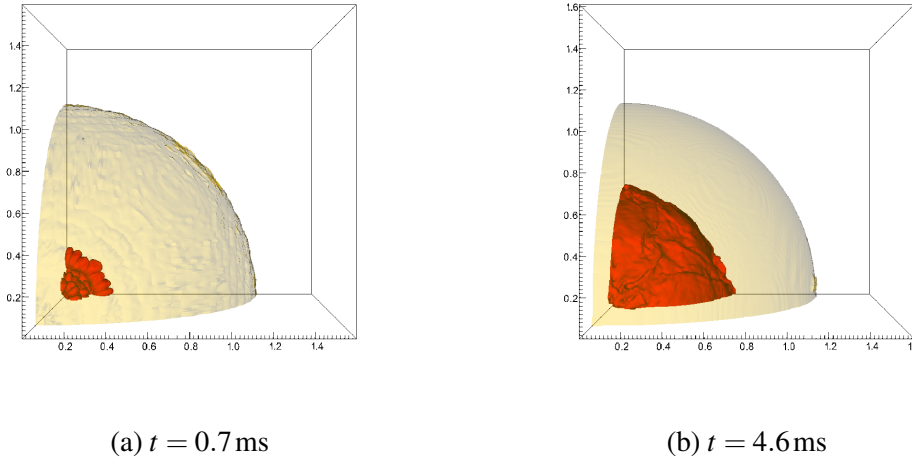


**Figure 4.8.:** Model B155\_128: Conversion front (red) and surface of the neutron star (yellow) at different times  $t$ . Spatial units  $10^6$  cm.

#### 4.4.5. Upper limit: $B_{\text{high}}^{1/4} = 155$ MeV

Next we present the simulation with 128 grid cells per dimension and our highest bag constant,  $B_{\text{high}}^{1/4} = 155$  MeV (model B155\_128). Here the difference in energy per baryon,  $E/A \sim 40$  MeV, is considerably lower than in the cases B147\_128 and B150\_128. Figures 4.8 (a) and 4.8 (b) show the conversion front at  $t = 0.7$  ms and at the point when we stopped our simulation, at  $t = 4.6$  ms. From the figures the similar evolution compared to the above described cases with lower  $B$  are visible. The lower  $E/A$  and the higher density threshold for exothermic burning (cf. Figure 4.2) lead to a slower and less violent burning, which ceases at higher densities compared to the models previously shown. Consequently, at the end of the simulation the resulting strange matter core is smaller and is surrounded by a hadronic outer layer of  $0.98 M_{\odot}$ . Temperatures of around 45 MeV are reached in the center. Figure 4.3 (a) shows that the conversion rate, represented by the slope of the curves, is lower than in the other cases and the combustion takes longer although less material is burnt.

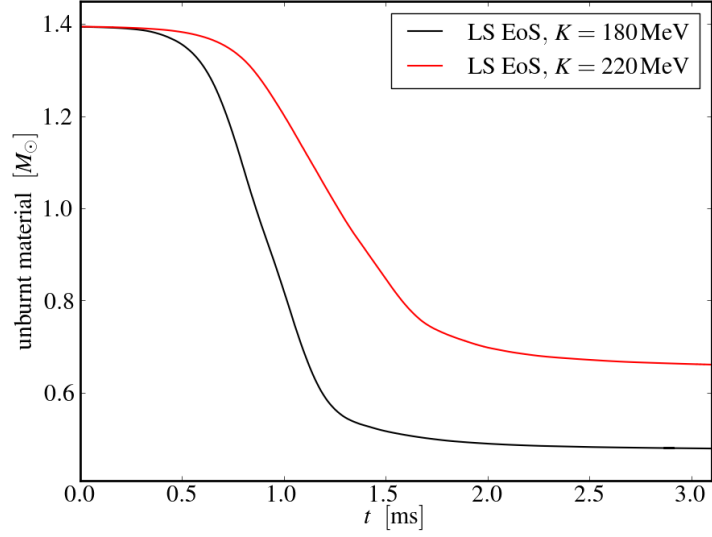
#### 4.4.6. Lattimer-Swesty equation of state: different incompressibility moduli $K$

In this and the following two sections we vary the standard setup described in Section 4.4.1. At first, we change the properties of the hadronic EoS.

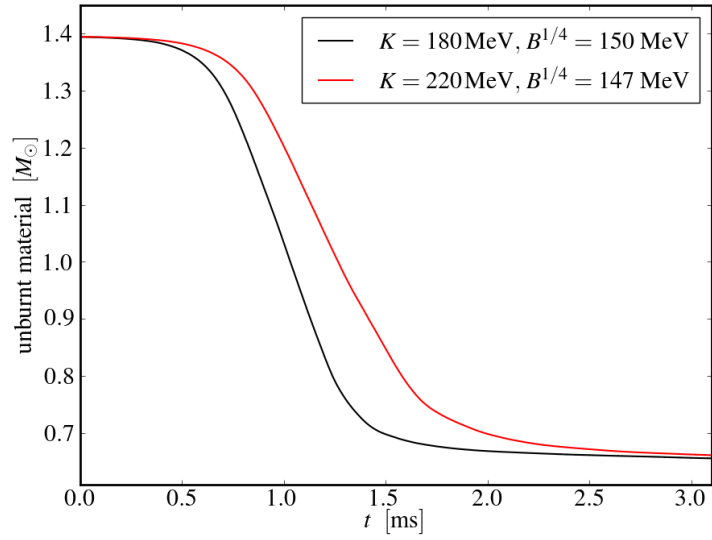
In Figure 4.9 (a) we compare two realizations of model B147\_128 using the same initial conditions, including bag constant  $B^{1/4} = 147$  MeV, but different versions of the Lattimer-Swesty (LS) EoS (cf. Section 2.1.2). The black line represents our standard case in which we

#### 4. Combustion of a hadronic neutron star into a quark star

---



(a)



(b)

**Figure 4.9.:** Gravitational mass of unburnt (hadronic) material as a function of time: (a) model B147.128 using two different versions of the LS EoS with different incompressibility modulus  $K$ ; (b) model B147.128 with LS220 compared to model B150.128 with LS180.

choose an incompressibility modulus of  $K = 180\text{MeV}$  (LS180), the red line is the result of the simulation in which  $K = 220\text{MeV}$  is applied (LS220).

In the latter case the burning proceeds slower, and the mass of the remaining hadronic outer layer is higher,  $0.66M_{\odot}$  compared to  $0.48M_{\odot}$  in the former case. This is due to the lower amount of released binding energy in the case with higher  $K$ , which is connected to a higher threshold for exothermic conversion, as discussed in Section 4.3 and shown in Figure 4.1 (b). An increase in  $K$  of the hadronic EoS has qualitatively the same effect as an increase in the bag constant  $B$  of the strange quark EoS. For example, the above shown model B147\_128 and LS220 leads to nearly the same amount of unburnt mass at the end of the simulation ( $t = 3\text{ms}$ ) as model B150\_128 and LS180, compared in Figure 4.9 (b). However, the figure shows also that the conversion process evolves somewhat differently.

We note as an important result from these calculations that the qualitative behavior of the burning process is the same for different versions of the LS EoS.

#### 4.4.7. Different subgrid scale models

To get an impression of the impact of the specific implementation of the subgrid scale (SGS) model on the results we conducted one simulation with the same initial conditions as model B150\_128 but a different implementation of the SGS model. Our standard SGS model features localized closures, whereas the alternative implementation is based on statistical closures (Schmidt et al. (2006a,b), cf. Section 3.1.6).

In Figure 4.10 (a) the gravitational mass of the unburnt matter as a function of time is shown for both implementations. Although there are some differences in the value of the average turbulent burning velocities, the overall results agree very well and are practically indistinguishable in the first millisecond, as can be seen in Figure 4.10 (a). This shows that the outcome of our simulations depends only slightly on the implementation of the SGS model.

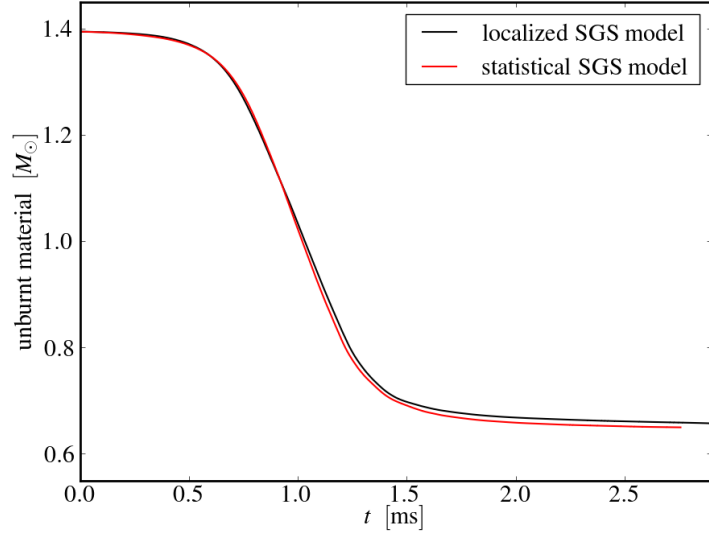
#### 4.4.8. Neutron stars with different masses

Another interesting parameter that can be varied is the mass  $M$  of the neutron star. A “standard neutron star” of  $M = 1.4M_{\odot}$  constitutes the initial setup for all simulations of the preceding sections, but now we explore the effect of different masses of the neutron star while keeping the bag constant and everything else constant. In Figure 4.10 (b) we present the results of four models with masses in the range  $1.15$  to  $1.65M_{\odot}$ . The plot shows clearly that a higher mass leads to faster, more violent conversion, and that the mass of the unburnt outer layers is the lower the higher the mass of the neutron star is. The reason for this behavior is due to the more compact configuration of the higher mass neutron stars. Much more mass is concentrated inside of the radius where the threshold density for exothermic combustion is located as in neutron stars with lower mass, whose density profile is flatter.

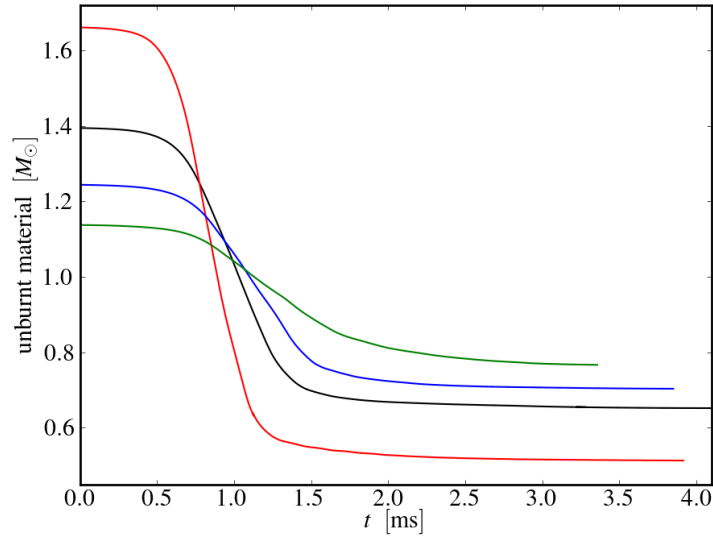
The higher densities in the center of the high-mass neutron stars allow for exothermic burning also with bag constants for which no combustion is possible in our standard setup with

#### 4. Combustion of a hadronic neutron star into a quark star

---



(a)



(b)

**Figure 4.10.:** Gravitational mass of unburnt (hadronic) material as a function of time. In all models the same bag constant is used ( $B^{1/4} = 150 \text{ MeV}$ ). (a) model B150\_128 using two different subgrid scale models applying either localized or statistical closures; (b) Four models with different masses of the neutron star.

$M = 1.4M_{\odot}$ . As an example, we conducted one simulation of the conversion in a neutron star of  $M = 1.65M_{\odot}$  and applied  $B^{1/4} = 160\text{MeV}$ . The conversion becomes turbulent in this case as well, although only a small fraction of the neutron star is converted into strange quark matter.

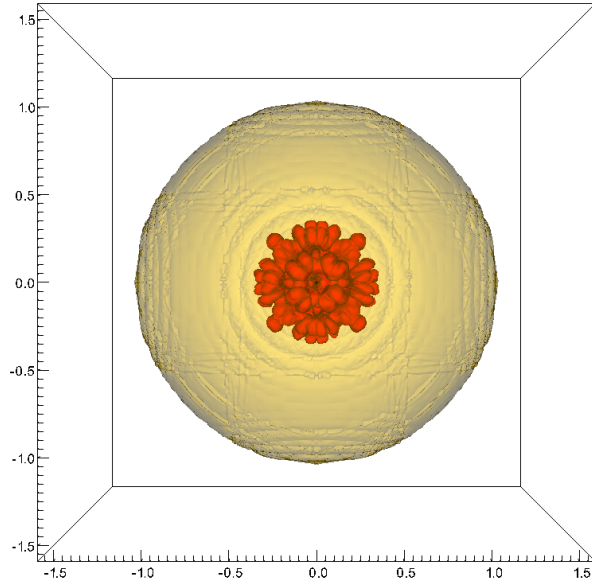
## 4.5. Gravitational wave signal

We presented in the preceding sections simulations of the conversion of a hadronic neutron star into a quark star. The results carry considerable uncertainties, in particular concerning the EoS for hadronic as well as strange quark matter. It would be helpful to derive observable quantities from our calculations to observationally constrain the parameter space. According to our simulations the conversion process is probably unobservable with devices relying on electromagnetic radiation. An alternative will be, in the near future, the detection of gravitational waves. An introduction into the concepts of gravitational waves was given in Section 2.5, we will present our attempts to calculate the gravitational wave signal of the conversion of a hadronic neutron star into a quark star in the following. At first we will describe our numerical setup and show the results of the computations. As we will see, these results are meaningful only to a limited extent. Hence, we will make an attempt to correct and interpret them in order to get an order-of-magnitude estimate. After having discussed the energy spectra of the signals we will discuss their detectability and compare different numerical methods.

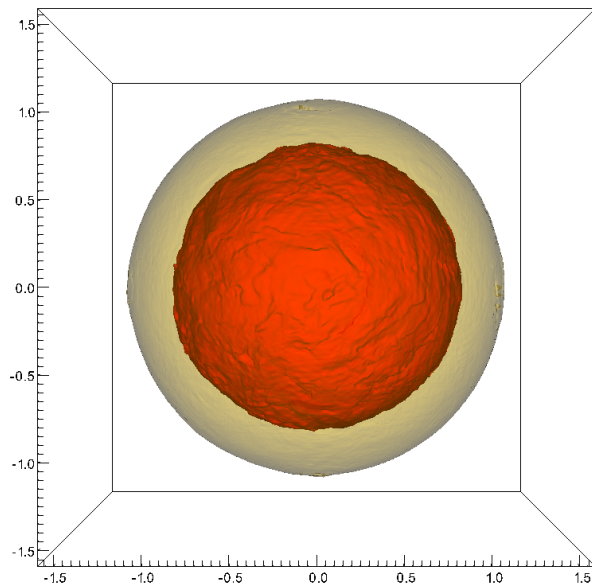
### 4.5.1. Simulations

Because the generation of gravitational waves is an inherently three-dimensional process in which the variations of the mass quadrupole moment are the most important sources, we refrain from applying any symmetry assumption and conduct simulations of the whole star (solid angle of  $4\pi$ ), not just of one octant as in the previously presented simulations, to calculate the gravitational wave signal. To achieve the same resolution as in the standard setup of the preceding sections, we double the number of grid cells per dimension from 128 to 256. Every other property of the standard initial setup remains unaltered (cf. Section 4.4.1). For consistency, we compared the dynamical behavior of the conversion in the full-star simulations to the corresponding octant model; the results are the same with only minor deviations, which gives us a justification of the use of octant simulations in the preceding sections.

We calculate the gravitational wave amplitudes, energy release, and energy spectra using the methods described in Section 3.4. Due to the considerably high numerical costs we conducted only a small number of full-star simulations; we present in the following two models, B147\_4 $\pi$  and B150\_4 $\pi$ , that differ only in the bag constant of the strange quark matter EoS. We choose  $B^{1/4} = 147\text{MeV}$  and  $B^{1/4} = 150\text{MeV}$ , respectively. Snapshots of the simulation B147\_4 $\pi$  are shown in Figure 4.11, at  $t = 0.5\text{ms}$  in (a) and  $t = 5.1\text{ms}$  in (b). The conversion front is marked in red, the surface of the neutron star in yellow. These snapshots show the great similarities



(a)  $t = 0.5$  ms



(b)  $t = 5.1$  ms

**Figure 4.11.:** Model B147\_4 $\pi$ : Conversion front (red) and surface of the neutron star (yellow) at different times  $t$ . Spatial units  $10^6$  cm.

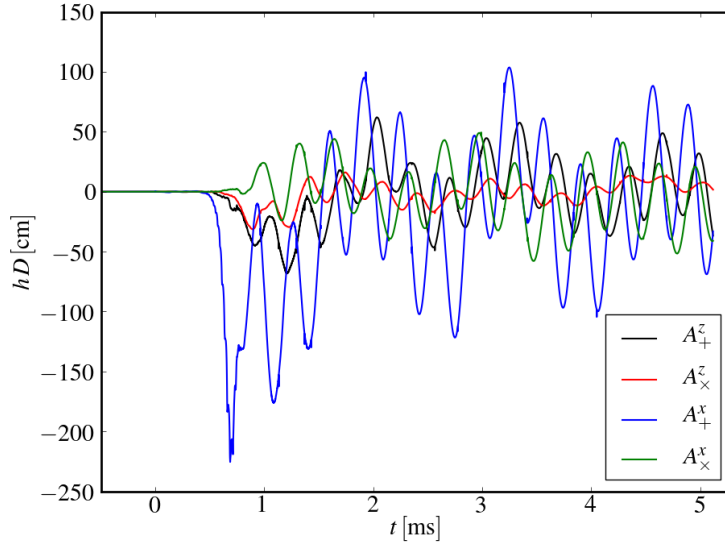


**Figure 4.12.:** Four gravitational wave amplitudes as a function of time for model B147.4 $\pi$ . The conversion process was started at  $t = 0$ .

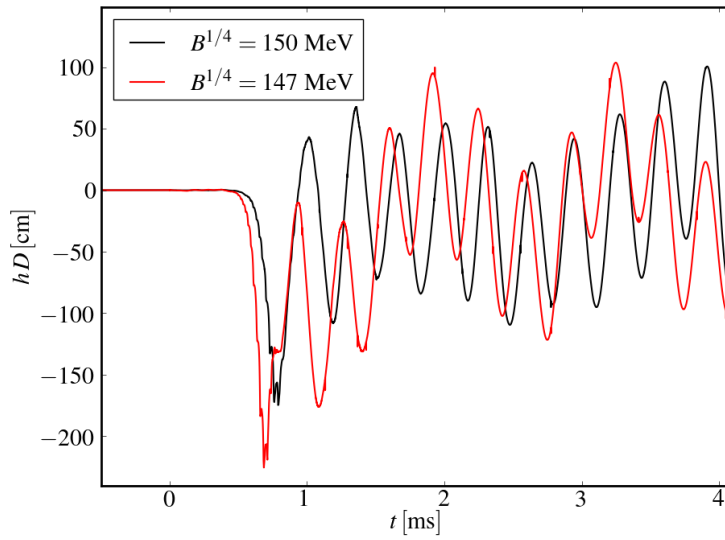


**Figure 4.13.:** Comparison of gravitational wave amplitude  $A_+^x$  as a function of time for different bag constants (models B147.4 $\pi$  and B150.4 $\pi$ ). The conversion process was started at  $t = 0$ .

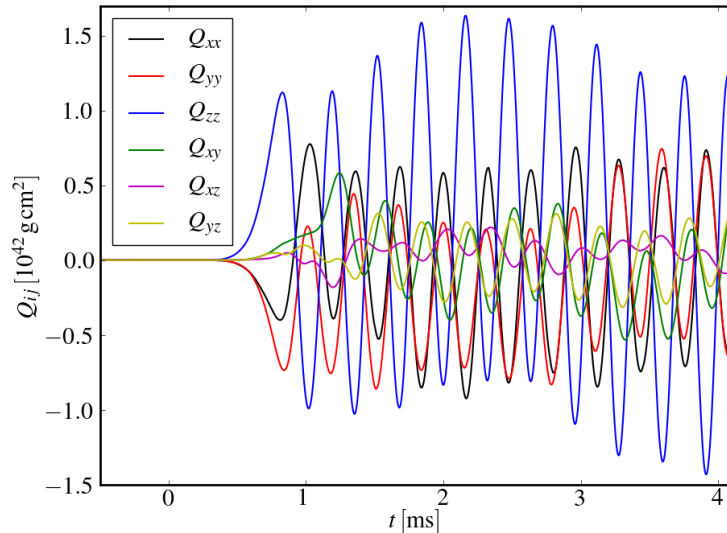


**Figure 4.14.:** Temporal evolution of the six components of the mass quadrupole moment  $\mathbf{Q}$  for model B150.4 $\pi$ .

compared to the octant simulations presented in the preceding sections (e.g. Figure 4.6); see there for a detailed description of the conversion process.

As explained in Section 3.4, we compute in each time step four different amplitudes; two lines of sight ( $x$ - and  $z$ -direction) with, in each case, two polarization modes (“+” and “ $\times$ ”). In Figure 4.12 we show the four gravitational wave amplitudes as a function of time for model B147.4 $\pi$ . The star was adapted to the grid by means of our relaxation method (cf. Section 3.2.4) from  $t = -0.5$  ms to  $t = 0$ ; at  $t = 0$  the conversion was started. We see in Figure 4.12 that in the first phase no signal is generated. When at  $t \sim 0.5$  ms the turbulent phase of the conversion starts we see a steep increase of the amplitudes – the rising strange quark matter plumes, massive and rapidly flowing parts of the fluid, become noticeable as a change in the quadrupole moment of the star. The differences in  $x$ - and  $z$ -direction show that the conversion evolves not in a spherically symmetric fashion.

In Figure 4.13 we compare the two simulations with different bag constants,  $B^{1/4} = 147$  MeV and  $B^{1/4} = 150$  MeV, respectively, by means of the amplitude  $A_+^x$ . The lower bag constant that yields more violent conversions as described in the preceding sections also leads to an on average slightly higher gravitational wave amplitude. The shapes of the two signals are very similar.

After the phase of rapid conversion ends at  $t \sim 2$  ms we expected the neutron star to enter a quasi-hydrostatic regime. In this phase, the quadrupole moment should not change significantly and the gravitational wave signal should cease. However, in Figure 4.12 it is visible

that this is not the case in our simulations; instead, the amplitudes display oscillations of high amplitude. The period of the main component of the oscillations is  $p \sim 0.3$  ms, corresponding to a frequency of  $f \sim 3$  kHz. Higher order oscillations of the star on the computational grid lead to a periodically changing quadrupole moment that in turn generates the oscillations of the gravitational wave amplitude.

We presume that the oscillation of the quadrupole moment  $\mathbf{Q}$  – the components of  $\mathbf{Q}$  are shown in Figure 4.14 as a function of time – is not of physical origin but an artifact caused by our numerical methods. Albeit various attempts to eliminate this drawback were made, we did not find a solution to this problem. Hence we are not able to calculate the gravitational wave signal of the conversion of a hadronic neutron star into a quark star properly.

It is yet unclear to us what causes this oscillations. A hint might be that that no oscillations or other numerical problems occur when we calculate the gravitational wave signal of thermonuclear supernovae. We will present an example of such a calculation in Appendix A. Therefore, a likely explanation might be a possible disagreement of the Newtonian dynamics with the effective relativistic gravitational potential, which is also the likely cause of unphysical oscillations in another quasi-hydrostatic setup as discussed in Section 3.2.4. The methods applied in that case cannot be applied here, because they would influence the outcome of the simulations. A test run without the relaxation procedure shows that this procedure does not cause the oscillations.

Another explanation of the oscillatory behavior might be that a Cartesian grid and a spherical mass arrangement such as a compact star cannot agree very well and this combination will lead inevitably to numerical errors. The implementation of a spherical grid into our code would give rise to a number of difficulties; for instance it would necessitate a complete re-implementation of the level-set method and the subgrid scale model.

The oscillations may as well not be caused by numerical shortcomings of the code, but be excited by fluid motions during the conversion process in connection with the rather soft equation of state of the quark core. The symmetric setup possibly contributes to that effect. A future study should investigate the effect of a different grid resolution and a less symmetric initial setup on the computed gravitational wave signal. Due to the time-consuming nature of these simulations it is not possible to include them into this work.

For now we cannot provide better results; therefore, we try to make the best of our results and will give some estimates based on them in the next section.

#### 4.5.2. Order-of-magnitude estimation

In order to be able to conduct at least an order-of-magnitude estimate, we looked for a way to extract some useful information from the results of the simulations. To this end, we assume that the genuine gravitational wave signal ceases when the turbulent conversion processes are completed at  $t \sim 2$  ms. Therefore, we consider the signal that we get after  $t = 2$  ms as numerical “noise” that we intend to remove. We assume further that the noise signal is a periodic function of time. We thus fit a superposition of sine waves to it. The fit is subtracted

#### 4. Combustion of a hadronic neutron star into a quark star

---

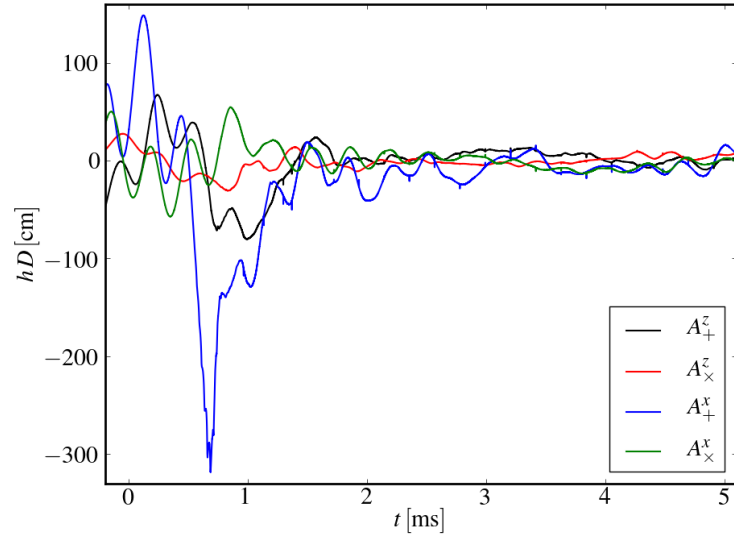


**Figure 4.15.:** Four gravitational wave amplitudes as in Figure 4.12, but here the fitted “noise” was subtracted.

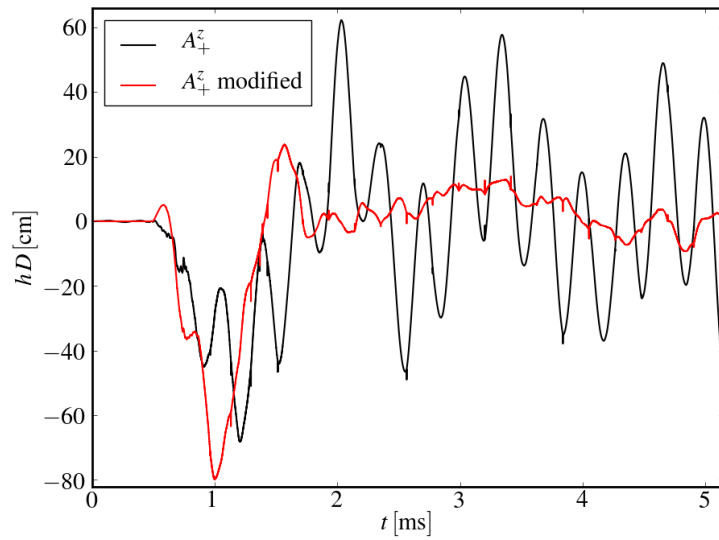


**Figure 4.16.:** Gravitational wave amplitude  $A_+^z$  of model B147.4 $\pi$  as a function of time; original data and modified data, where fitted and filtered “noise” signal was subtracted, see text for details.

from the data to get the “real” signal. The result of this procedure is shown in Figure 4.15, where we plotted the same data as in Figure 4.12, but with the fitted noise signal subtracted. Of course, this procedure in turn leads to artificial oscillating amplitudes in the first  $t \sim 1$  ms, where initially no signal was seen.

To get rid of the artificial signal in the first 1 ms we multiplied the noise fit with a filter which is zero for  $t < 0.5$  ms and then rises linearly with time up to a value of 1 at  $t = 1.0$  ms. This filter is certainly somewhat arbitrary, but we think it is sufficient for our purpose. We compare the original and modified data, and show the amplitude  $A_+^z$  as an example in Figure 4.16. The result looks quite nice and we think we can estimate from this result the typical maximum order of magnitude of a gravitational wave amplitude originating from the conversion of a hadronic neutron star into a quark star to be  $h_{\max} D \sim 10^2$  cm. This is comparable to the signal generated by moving matter in core-collapse supernovae (Marek and Janka, 2009; Müller et al., 2012).

The total energy radiated in gravitational waves  $E_{\text{gw}}$  is, calculated using the original data by means of equation (3.27),  $3.5 \times 10^{40}$  erg for model B147\_4 $\pi$ , and  $1.5 \times 10^{40}$  erg for model B150\_4 $\pi$ . Due to the unphysical oscillations, which contribute to the gravitational wave energy, these values have to be taken as upper limits. However, this upper limit of  $E_{\text{gw}}$  is many orders of magnitude lower than any other form of energy – kinetic, potential or internal – in the system.

### 4.5.3. Energy spectra

Using the method described in Section 3.4, we calculated the energy spectrum for model B150\_4 $\pi$ , and both the original and the modified signal of model B147\_4 $\pi$ , by applying equation (3.30). The energy spectra are plotted in Figure 4.17. Because of the unphysical oscillations in the original signal and the rather rough correction procedure applied to it, these results have to be taken with great caution and should again be considered only as an order-of-magnitude estimate.

In the original data we see a pronounced peak at  $f \sim 3$  kHz (black and blue lines in Figure 4.17). It corresponds to the frequency of the main oscillation component estimated from Figure 4.12. Another peak is visible at  $f \sim 0.7$  kHz, which is also visible in the energy spectrum of the corrected signal (red line in Figure 4.17), although shifted towards somewhat higher frequencies. As intended, the peak at  $f \sim 3$  kHz is lower in the corrected data, although it does not vanish completely. From these results we conclude that we can attribute the first maximum in the range 0.5 to 1.5 kHz to the physical frequency range of signals generated by the conversion of a hadronic neutron star into a quark star. Frequencies around 1 kHz could be expected because the relevant dynamical processes last  $\sim 1$  ms. Frequencies higher than  $\sim 2$  kHz are most likely due to numerical artifacts and noise, although we cannot exclude a physical source of frequencies in this range.

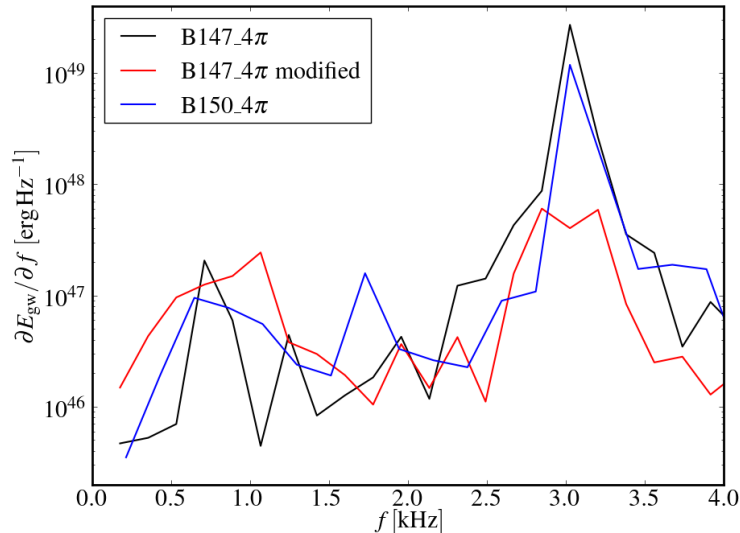


**Figure 4.17.:** Energy spectrum of model B147\_4 $\pi$  (black line), the modified version of model B147\_4 $\pi$  (red line, see text for details), and model B150\_4 $\pi$  (blue line).

#### 4.5.4. Detectability

An interesting question is whether the gravitational wave signal of the conversion of a hadronic neutron star located in our galaxy into a quark star is detectable. To determine at which distances the gravitational wave signal can be detected, we have to divide the estimated maximum amplitude of  $h_{\max}D \sim 10^2$  cm by the distance  $D$  and compare it to the sensitivity of gravitational wave detectors in the respective frequency range (cf. Section 2.5.2).

The anticipated sensitivity at  $f \sim 1$  kHz of the currently assembled ground based detector *advanced LIGO* is  $\gtrsim 5 \times 10^{-23}$  (Waldman, 2011). That means that advanced LIGO is able to detect a signal of  $hD \sim 10^2$  cm at  $f = 1$  kHz throughout our galaxy. However, the very short length of the signal, of order 1 ms, will make the detection of the gravitational wave signal of the conversion of a hadronic neutron star into a quark star extremely challenging.

#### 4.5.5. Comparison of numerical methods

We explained in Section 3.4 the advantages of calculating the gravitational wave amplitudes using a different version of the quadrupole formula, equation (3.17), that does not contain second time derivatives (e.g. Müller and Janka, 1997). For comparison we calculated the gravitational wave amplitude of some models directly, applying equation (3.16) and using simple numerical time derivatives.

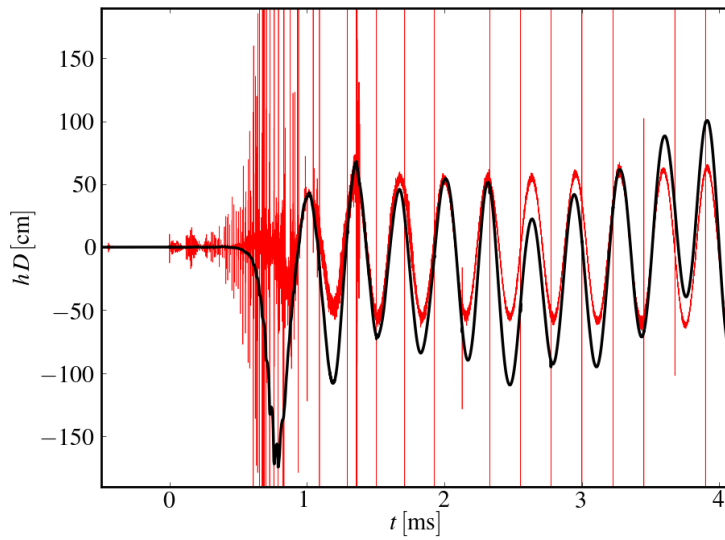


**Figure 4.18.:** Comparison of gravitational wave amplitude  $A_+^x$  of the model B150\_4 $\pi$ , calculated using different methods: applying the method described by Müller and Janka (1997) (equation (3.17), black line), and using the second time derivatives of the quadrupole directly (equation (3.16), red line).

As an example, we compare in Figure 4.18 the amplitude  $A_{\pm}^x$  of model B150.4 $\pi$ , calculated with both methods. Our standard method (equation 3.17) yields the black line, while the direct calculation (equation 3.16) yields the red line. This comparison shows clearly that the direct method leads to a very noisy result that is useless for any quantitative analysis. However, the figure suggests strongly that the red line is a noisy version of the black line – in particular visible towards later times – and the underlying physics are the same. This serves as a validation of our numerical method; the problems that we encounter (cf. Section 4.5.1) are not caused by the particular numerical implementation of the computation of gravitational waves.

## 4.6. Conclusions

We presented three-dimensional hydrodynamic simulations of the conversion of a hadronic neutron star into a quark star assuming different bag constants  $B$  for describing strange quark matter. We explored a large space of physical and numerical parameters. In all cases we observe growing Rayleigh-Taylor instabilities of the conversion front. The resulting turbulent motion enhances the conversion velocity strongly, leading to conversion timescales of  $\tau_{\text{burn}} \sim 2$  ms for all  $B$ . However, recent suggestions (Niebergal et al., 2010; Horvath, 2010) that the turbulence enhances the burning speed to sonic or even supersonic velocities could not be confirmed, which came as no surprise since in the analogous case of thermonuclear supernovae such a transition is not possible either as long as burning proceeds in the flamelet regime (Niemeyer and Woosley, 1997).

We varied numerical parameters such as the numerical resolution, the size of the physical domain, and the subgrid scale turbulence model. We explored the influence of changes in the strange quark and hadronic equation of state by varying the bag constant and the incompressibility modulus, respectively. Furthermore, we conducted simulations with different masses of the neutron star. In all cases we observe at the end of our simulations a spherical strange quark matter interior surrounded by an outer layer of hadronic matter. This outer layer exists because in our hydrodynamic approximation the combustion stops when the conversion front reaches conditions under which exothermic burning is no longer possible. Since this condition depends on density and is fulfilled for sufficiently high densities only, it can roughly be described as a density threshold which forms a boundary that separates the high density (burnt) strange quark matter and the low density (unburnt) hadronic matter. In our approximation we can make no statement on whether the conversion process proceeds further beyond this boundary by processes that cannot be described as a combustion. Possibly free neutrons diffuse into the quark matter and are converted subsequently (Olinto, 1987), a process that probably is exothermic, as Lugones et al. (1994) already pointed out. Free neutrons are abundant in hadronic matter at densities higher than the neutron drip density,  $e_{\text{drip}} \sim 4 \times 10^{11} \text{ g cm}^{-3}$ . However we expect these additional processes to happen on much longer timescales than the combustion described in this work.

The obvious consequence of an at least temporary existence of an outer layer of unburnt hadronic matter is that the resulting quark star could support a rather thick crust, unlike bare strange stars, which can presumably support only a tiny crust. This would allow for pulsar glitches, if the time between the end of the combustion process and a potentially complete conversion into a strange star is large enough.

Some authors suggested that the conversion of a hadronic neutron star into a strange star may eject neutron-rich material from the surface, and that in these ejecta the nucleosynthesis of heavy neutron-rich nuclei via the r-process may occur (Jaikumar et al., 2007). However, our results suggest that ejection of matter from the star is rather unlikely since the violent burning ceases before reaching the surface. Any subsequent continuation of the conversion by processes not describable by a combustion is expected to be much slower, and to take place in a much less violent way. But given our ignorance about these processes more detailed work on this subject may lead to differing conclusions.

We attempted to calculate the gravitational wave signal of the conversion of a hadronic neutron star into a quark star. Because, according to our results, the conversion process is unlikely to be observable by detection of electromagnetic radiation, the detection of gravitational wave signals would give valuable possibilities to constrain the models. However, since the calculation of the gravitational wave signal is hindered by numerical problems, we are only able to conduct order-of-magnitude estimates resulting in a maximum amplitude of  $h_{\max}D \sim 10^2$  cm at frequencies of  $f \sim 1$  kHz. Variations of the bag constant do not change these results within our accuracy. According to these estimates, the signal of a galactic event is in principle detectable with ground-based instruments such as *advanced LIGO*, but the short duration of the signal might prevent a detection.

The existence and size of the hadronic outer layers, or the possibility of exothermic combustion even in the center of neutron stars, depends (like many other properties) strongly on the EoS used for the hadronic as well as for the quark phases. Hence any firm prediction needs a more realistic treatment. Furthermore, the maximum mass configuration of nonrotating stars of both the LS180 EoS and our bag model EoS (for all but the lowest allowed bag constants) have  $M_{\max} < 2M_{\odot}$  and therefore conflict with observations (Demorest et al., 2010). As mentioned before, we nevertheless use those EoS in this work because we consider them as sufficient for our first attempts; moreover, computations using the LS220 EoS that is compatible with the observations show no qualitative differences.

Future work should aim to improve on this by means of applying more realistic EoS. Regarding the quark phase, finite strange quark masses and QCD-interactions can be included into the bag model. Strange quark matter bag model EoS which contain these corrections can support a  $2M_{\odot}$  neutron star, as was shown by Weissenborn et al. (2011). Recently also the choice of micro-physical finite-temperature EoS for nuclear matter has become larger (e.g. Hempel and Schaffner-Bielich, 2010; Typel et al., 2010), so we can consider additional hadronic EoS apart from the LS and Shen EoS which we used in this work. Another possibility is to consider the use of modern zero-temperature micro-physical EoS together with an ideal gas component to account for temperature effects, whose reliability has been tested in Bauswein

#### *4. Combustion of a hadronic neutron star into a quark star*

---

et al. (2010). Further improvement would be achieved by adding neutrino cooling, which could be relevant since rather high temperatures are reached in the quark core. Until now we use an initial model resembling an old isolated neutron star; the same calculations could be done with a young (proto)neutron star and in connection with a core-collapse supernova.

## 5. Deflagrations in high-density carbon-oxygen white dwarfs

We will now leave the discussion of neutron stars and turn to the other family of compact stars, white dwarfs. But we consider those white dwarfs which are, in a sense, closest to neutron stars: the most compact of them with the highest central densities. We will call them *high-density white dwarfs*, and examine in particular those that are made of carbon and oxygen. Our focus will be on *deflagration processes* in those objects. We start with an introduction into this second main topic of the thesis.

### 5.1. Introduction

In the following section, we will present an overview of the physical processes that influence the fate of high-density white dwarfs. We will give the corresponding references and a general review of the literature of this research field in Section 5.1.2. In Section 5.1.3 we will explain the objectives of this part of the thesis.

#### 5.1.1. The fate of high-density white dwarfs

Mass-accreting white dwarfs are expected to become unstable when they approach the limiting Chandrasekhar mass (cf. Section 2.2.2). The increasing pressure in the center of the star may ignite degenerate carbon burning in the interior, which can lead to an explosion of the white dwarf. This is one possible physical explanation of supernovae of Type Ia (cf. Section 1.3) and is called the *Chandrasekhar-mass explosion model*. Alternative progenitor systems are discussed in Section 1.3.2.

However, the central density in cold white dwarfs that accrete at a very low rate, or at a very high rate in some exotic models, might rise to very high values before the carbon ignites. It is expected that if the central density of the white dwarf exceeds some critical value  $\rho_{\text{crit}}$  the star does not explode, but instead collapses to a neutron star when approaching the Chandrasekhar limit. The reason for the collapse is a rapid decrease of the electron degeneracy pressure in the center of the white dwarf because of decreasing electron fraction  $Y_e$  caused by neutronization due to electron capture processes on free protons and protons in nuclei (reaction 2.56). Such an event is called *electron capture induced collapse*, or, since the growth of the central density of the white dwarf is caused by mass accretion, *accretion-induced collapse (AIC)* (see next section for references).

This mechanism was suggested to be one possible way to create neutron stars in low mass X-ray binaries (LMXBs) and is physically similar to the collapse of the core of a single intermediate mass star at the beginning of a core-collapse supernova, which is presumably the most common way to form a neutron star.

Depending on the mass of the progenitor main sequence star, stellar evolution theory predicts different chemical compositions of white dwarfs. With growing mass of the progenitor the main constituents of the white dwarf are carbon and oxygen (C+O white dwarfs), or oxygen, neon, and smaller fractions of magnesium and sodium (O+Ne white dwarfs) (cf. Section 1.2). White dwarfs with helium cores (He white dwarfs), which can be formed in binaries by envelope stripping, have too little mass to be candidates for AICs. In this work we will concentrate on C+O white dwarfs, the most numerous white dwarfs and the progenitors of Type Ia supernovae (cf. Section 1.3.2). Nevertheless, we will now give a short overview of high-density O+Ne white dwarfs to emphasize the differences compared to high-density C+O white dwarfs.

Electron captures on  $^{20}\text{Ne}$  start at  $\rho_{\text{ec,Ne}} = 6.2 \times 10^9 \text{ g cm}^{-3}$  and on  $^{24}\text{Mg}$  already at  $\rho_{\text{ec,Mg}} = 3.2 \times 10^9 \text{ g cm}^{-3}$  (Shapiro and Teukolsky, 1983). Central densities similar to these values should be reached easily in the interior of accreting O+Ne white dwarfs, therefore it is very likely that they undergo an electron capture induced collapse to neutron stars. A similar scenario is expected if in a C+O white dwarf thermonuclear burning is ignited in the outer layers. This may be possible if the white dwarf is accreting at a very high rate (Nomoto and Iben, 1985). At the low densities far from the center the carbon and oxygen is burnt into oxygen and neon. Subsequently, electron captures start onto the hot ashes, which leads to pressure reduction and collapse. The same scenario is suggested in some cases shortly after the merger of two unequal-mass C+O white dwarfs, if the metastable merged C+O object ignites in areas of low density (Saio and Nomoto, 2004). Elaborate simulations of the AIC of an O+Ne white dwarf were conducted by Dessart et al. (2006) and Abdikamalov et al. (2010).

As mentioned above, we will focus in this work on C+O white dwarfs, which form when helium burning in the center of low mass stars ( $M \lesssim 8M_{\odot}$ ) ceases (cf. Section 1.2). Here the situation is fundamentally different: We showed in Section 2.6 that no electrons can be captured by the unburnt matter,  $^{12}\text{C}$  and  $^{16}\text{O}$ ; electron capture reactions are only possible in the ashes of the thermonuclear burning. Therefore, accreting C+O white dwarfs are stable objects as long as no thermonuclear combustion occurs in their interior.

When the carbon burning ignites, the fate of a C+O white dwarf with high central density cannot be predicted easily – either it explodes in a thermonuclear supernova, or it collapses into a neutron star. Whether the white dwarf collapses is – to first order – a competition between pressure rise by the energy release due to nuclear burning and pressure decrease by neutronization due to electron captures. At low central densities the pressure increase is certainly faster, leading to a thermonuclear supernova. But since the electron capture rates increase strongly with increasing density, it is expected that at some critical central density the reverse happens: the white dwarf collapses. “Standard” C+O white dwarfs with central densities up to  $\rho_c \sim 3.0 \times 10^9 \text{ g cm}^{-3}$  never collapse but usually explode if ignited centrally, as

was shown in various hydrodynamic simulations. Only for white dwarfs with central densities considerably higher than this value, a collapse cannot be excluded from the start. In this case, the strength of the competing physical processes decide which one of the two possibilities occurs in nature, depending on the properties of the white dwarf. Parameters which influence the strength of the respective processes are:

- **Burning velocity:** The higher the burning velocity, the higher is the rate of energy release of the nuclear burning and the less likely is a collapse. The burning velocity can be enhanced by turbulence due to growing flamefront instabilities (cf. Section 2.4.2). This can only be examined properly in multidimensional computations.
- **Electron capture rates:** Higher electron capture rates lead to faster neutronization and faster pressure decrease and therefore to a higher probability of collapse.
- **Central density:** The higher the central density, the more effective is the neutronization, that is the electron capture rates are higher.
- **Carbon fraction:** If the ratio of carbon to oxygen is lower, less energy per mass is released in the nuclear burning, which leads to a lower pressure increase. This would enhance the probability of collapse. On the other hand, lower energy production per mass yields lower temperatures, which in turn lead to a slower neutronization, since the electron capture rates are also strongly temperature dependent. Therefore, the net effect of a change in the carbon fraction is not easy to predict and is an interesting question that we will address in our numerical simulations.

We have seen that a gravitational collapse can only occur in C+O white dwarfs in which nuclear burning has already been ignited; furthermore, we stated that the lower the burning velocity the likelier is a collapse. Consequently, the scenario in which the probability of a collapse is highest is when the nuclear burning proceeds as a slow, subsonic *deflagration*, as opposed to faster *detonations* or *delayed detonations* (cf. Section 2.4).

### 5.1.2. Current state of research

Shortly after the existence of two observationally different types of supernovae became apparent in the 1940s, the explosions of white dwarfs were connected to supernovae of Type I (e.g. Mestel, 1952), see also the detailed discussion in Section 1. Hoyle and Fowler (1960) suggested that the thermonuclear combustion of a degenerate core of a low-mass star leads to Type Ia supernovae. Soon the alternative fate of white dwarfs was discussed as well: Schatzman (1963) mentioned the possibility of a gravitational collapse of the white dwarf into a neutron star due to pressure decrease by electron captures on nuclei.

The first who examined in detail the collapse of a C+O white dwarf were Canal and Schatzman (1976), who suggested this process as a formation mechanism for neutron stars in X-ray binaries (XRBs). They considered an explosive origin of the neutron star as unlikely because

this would lead to large eccentricities of the orbits in the binary systems, whereas observed orbits are mostly circular. Moreover, according to Canal and Schatzman (1976) the observational pulsar birth rate exceeds the core-collapse supernova rate. They estimated the possibility of a collapse of the white dwarf by comparing the timescales of inverse  $\beta$ -decays and pycnonuclear reaction rates; however, they considered cold white dwarfs with extremely high central densities of  $\rho_c > 2 \times 10^{10} \text{ g cm}^{-3}$ ; that is well in the regime where electron captures on  $^{16}\text{O}$  take place.

In their important work on *carbon deflagration supernovae*, Nomoto et al. (1976) presented the first hydrodynamic computations of deflagrations in C+O white dwarfs, as an alternative to the at that time predominantly assumed detonation model. In their work they did not yet mention the possibility of a collapse of the white dwarf.

Canal and Isern (1979) extended their earlier work and stated that in a cold C+O white dwarf accreting at the Eddington rate, thermonuclear runaway starts at about  $\rho_c \sim 1 \times 10^{10} \text{ g cm}^{-3}$ . According to them, this should lead to the collapse of the star.

Soon afterwards, Canal et al. (1980) applied an idea of Stevenson (1980) and assumed a separation of carbon and oxygen at high densities and low temperatures – the oxygen accumulates and crystallizes in the center, whereas the carbon is pushed to outer layers. They concluded that explosive carbon burning begins when the neutronization of oxygen has already started; the central densities are thus very high,  $\rho_c > 2 \times 10^{10} \text{ g cm}^{-3}$ . Also in this scenario a collapse of the white dwarf is most likely. We will take up the idea of separation of carbon and oxygen in Section 5.2.6.

A detailed analysis of the evolution of accreting white dwarfs before a possible collapse was presented by Isern et al. (1983). They found that the outcome does not depend strongly on the accretion rate but on the chemical composition of the white dwarf; in particular, whether the carbon and oxygen is completely mixed or separated. However, in all cases the central density at the start of the thermonuclear runaway is larger than  $\rho_c \gtrsim 1 \times 10^{10} \text{ g cm}^{-3}$ . It has to be mentioned that they started the accretion process at very high initial white dwarf masses of  $M_{\text{ini}} = 1.37 M_{\odot}$ .

Nomoto et al. (1984) also presented models of accreting white dwarfs and discussed the nucleosynthesis results of their hydrodynamic carbon deflagration simulations. They considered accretion rates of  $\dot{M} = 10^{-7}$  to  $10^{-9} M_{\odot} \text{ yr}^{-1}$ , which are quite high but much lower and probably more realistic than the near-Eddington rates of Canal and Isern (1979) and comparable to the highest accretion rates considered in Isern et al. (1983). They found central ignition densities in the range  $\rho_c \sim 2$  to  $5 \times 10^9 \text{ g cm}^{-3}$ , depending on the accretion rate. These values are considerably lower than the ones obtained by Isern et al. (1983). Nomoto et al. (1984) stated that typical white dwarfs whose explosions constitute the majority of thermonuclear supernovae have a central ignition density of  $\rho_c \sim 3 \times 10^9 \text{ g cm}^{-3}$ . Since then this value, which was confirmed in later work (e.g. Lesaffre et al., 2006), has been used as a standard value for many simulations of Chandrasekhar-mass models of thermonuclear supernovae (e.g. Reinecke et al., 1999a, 2002a; Röpke and Niemeyer, 2007; Kasen et al., 2009; Röpke et al., 2012). Furthermore, Nomoto et al. (1984) calculated the neutrino luminosity and the impact of the

energy released by neutrinos on the explosion dynamics, and found that it was negligible at the considered densities.

The first hydrodynamic calculations of the collapse of an accreting C+O white dwarf due to electron captures behind a deflagration front were presented by Baron et al. (1987). They used a white dwarf model from Nomoto (1986) with initial mass of  $M_{\text{ini}} = 1.1 M_{\odot}$  and an extremely low accretion rate of  $\dot{M} = 2.5 \times 10^{-10} M_{\odot} \text{yr}^{-1}$ . In this model they obtained a central ignition density of  $\rho_c = 1 \times 10^{10} \text{g cm}^{-3}$  and found that the white dwarf collapses into a neutron star, regardless of the burning velocity.

The evolution of cold accreting white dwarfs was discussed in Hernanz et al. (1988). They considered a large parameter space in accretion rate and initial mass of the white dwarf, and two different phase diagrams for carbon-oxygen mixtures at high densities. Their calculations resulted in central ignition densities in the range  $\rho_c \sim 6 \times 10^9$  to  $1.2 \times 10^{10} \text{g cm}^{-3}$  which lead to a collapse of the white dwarf for low initial temperatures, high initial masses, and very high or very low accretion rates.

In their important review, Canal et al. (1990a) discussed the origin of neutron stars in binaries and, connected to that, the collapse of C+O white dwarfs as one possibility to form neutron stars. Summarizing earlier results of hydrodynamic simulations, they stated that the outcome of a deflagration in a C+O white dwarf depends strongly on the burning velocity – at the considered range of central ignition densities,  $\rho_c = 9.5 \times 10^9$  to  $1.5 \times 10^{10} \text{g cm}^{-3}$ , they found that both outcomes are possible for each  $\rho_c$ . For example, at a central density of  $\rho_c = 9.5 \times 10^9 \text{g cm}^{-3}$  a burning velocity of 0.5% of the sound velocity  $c_s$  lead to a collapse, whereas a burning velocity twice as high lead to an explosion of the white dwarf. Similar results were presented shortly afterwards by Canal et al. (1990b).

Also Nomoto and Kondo (1991) conducted hydrodynamic simulations of the collapse of both C+O and O+Ne white dwarfs. Regarding the former, they found a strong dependency of the results on the burning velocity, similar to the results of the aforementioned authors. They stated that at a central ignition density of  $\rho_c = 1 \times 10^{10} \text{g cm}^{-3}$  a critical burning velocity of  $0.03 c_s$  separates collapse from explosion. They assumed that the realistic burning velocity is  $0.01 c_s$ , according to this a white dwarf with  $\rho_c = 1 \times 10^{10} \text{g cm}^{-3}$  would collapse.

In their seminal work, Timmes and Woosley (1992) calculated the conductive propagation velocities for nuclear flames in degenerate C+O and O+Ne matter. These velocities became the standard input for simulations of deflagrations in white dwarfs, and are still almost exclusively used today (cf. Section 3.1.4). Timmes and Woosley (1992) applied their results also to calculate deflagrations in high-density white dwarfs and found a critical central density of  $\rho_{\text{crit}} \sim 9 \times 10^9 \text{g cm}^{-3}$  for C+O as well as for O+Ne white dwarfs. By means of a fractal dimension model they also considered in their calculations the acceleration of the flame velocity by turbulence due to Rayleigh-Taylor instabilities.

Accreting white dwarfs were examined by Bravo et al. (1996). They started their calculations with an initial C+O white dwarf with a mass of  $M = 0.8 M_{\odot}$  and discussed several accretion rates ranging from  $\dot{M} = 10^{-10} M_{\odot} \text{yr}^{-1}$  to  $\dot{M} = 5 \times 10^{-6} M_{\odot} \text{yr}^{-1}$ . The resulting maximum central ignition density is  $\rho_c = 6.3 \times 10^9 \text{g cm}^{-3}$ . However, they stopped their cal-

culations with the lowest accretion rate, the only case in which the white dwarf cools during the accretion phase, before carbon ignition. In this case considerably higher central densities might have been possible.

Woosley (1997) examined the neutron-rich nucleosynthesis in carbon deflagration supernovae. He calculated the last stages of accretion with a stellar evolution code and then simulated the combustion and explosive nucleosynthesis using a large nuclear network. He found a critical density for the collapse of C+O white dwarfs of  $\rho_{\text{crit}} \sim 9 \times 10^9 \text{ g cm}^{-3}$ . He examined the nucleosynthesis results from deflagrations in C+O white dwarfs with central densities below  $\rho_{\text{crit}}$ , in the range  $\rho_c = 2$  to  $8 \times 10^9 \text{ g cm}^{-3}$ . After comparing the nucleosynthesis yields with solar isotopical abundances he concluded that most thermonuclear supernovae should ignite at low densities of about  $\rho \sim 2 \times 10^9 \text{ g cm}^{-3}$ . But a small fraction ( $\sim 2\%$ ) of the total thermonuclear supernovae should be explosions of high-density C+O white dwarfs in order to explain the solar abundance of nuclei such as  $^{48}\text{Ca}$ , because no other production site of these nuclei is known. In Section 5.3 we will compare our nucleosynthesis results to his results and discuss this issue in detail.

García-Senz et al. (1998) presented a smoothed-particle hydrodynamics (SPH) code for deflagrations in white dwarfs and applied it to simulations of thermonuclear supernovae and AICs. They found that a C+O white dwarf with  $\rho_c = 8.5 \times 10^9 \text{ g cm}^{-3}$  collapses in three-dimensional as well as in one-dimensional simulations. In later work they included Coulomb corrections in the EoS for matter in NSE (Bravo and García-Senz, 1999). They found that the Coulomb corrections lead to a decrease in the laminar burning velocity  $v_{\text{lam}}$  of  $\sim 16\%$  as well as an increase in the neutronization rate  $\dot{Y}_e$  of  $\sim 28\%$  at high densities and temperatures. As an application of their results they again conducted simulations of thermonuclear supernovae and AICs of white dwarfs. Including the Coulomb corrections lead to a smaller  $\rho_{\text{crit}}$ , because both the higher neutronization rate and the lower burning velocity accelerate the collapse. They obtained  $\rho_{\text{crit}}^{\text{CC}} \approx 5.5 \times 10^9 \text{ g cm}^{-3}$ , whereas without Coulomb corrections they got  $\rho_{\text{crit}}^{\text{no CC}} \approx 8.5 \times 10^9 \text{ g cm}^{-3}$ , in agreement with Woosley (1997). These are the most recent simulations of deflagrations in high-density C+O white dwarfs we are aware of. We will compare our simulations to their results in Section 5.2.7.

Bravo and García-Senz (1999), Woosley (1997), and many other authors used weak interaction rates provided by Fuller et al. (1985). Langanke and Martínez-Pinedo (2000, 2001) calculated new rates including also  $pf$ -shell nuclei, as was discussed in Section 3.3.1. As stated above, the rates may have a profound influence on the value of the critical density. To our knowledge, no hydrodynamic simulations of deflagrations in high-density C+O white dwarfs were published using these new rates, although they became standard in simulations of thermonuclear supernovae (e.g. Seitenzahl et al., 2011). In our work we will mainly use the new rates.

Iwamoto et al. (1999) and Brachwitz et al. (2000) discussed in detail nucleosynthesis results and the role of electron captures in Chandrasekhar-mass models of thermonuclear supernovae. In order to do this, they applied a tracer particle method (cf. Section 3.1.7) and post-processed one-dimensional hydrodynamic simulations of thermonuclear supernovae, in which a fixed

burning velocity of  $0.015 c_s$ , and rather low central ignition densities were assumed. Brachwitz et al. (2000) compared nucleosynthesis results obtained with the old rates from Fuller et al. (1985) with the new ones from Langanke and Martínez-Pinedo (2001). They concluded that the new rates shift the range of central ignition densities for normal thermonuclear supernovae consistent with the solar abundances of nuclei towards higher densities.

Lesaffre et al. (2006) conducted detailed binary population synthesis calculations of single-degenerate progenitors of Type Ia supernovae. In their distribution of central ignition densities they observed a sharp cutoff at  $\rho_c \sim 5 \times 10^9 \text{ g cm}^{-3}$ .

Seitenzahl et al. (2011) examined the influence of the central density on the nucleosynthesis results of delayed-detonation models. Based on Lesaffre et al. (2006) they only considered central densities up to  $\rho_c = 5.5 \times 10^9 \text{ g cm}^{-3}$ . They found that higher central densities lead to higher yields of iron group elements. However, only in faint supernovae, in which the delayed-detonation models show a strong deflagration phase, the  $^{56}\text{Ni}$  yields increase with increasing central density, while the  $^{56}\text{Ni}$  yields do not change significantly at higher central densities in bright delayed detonations which have weak deflagrations. We will compare their findings to our nucleosynthesis results in Section 5.3.

To summarize this overview of the literature: Central ignition densities higher than  $\rho_c \gtrsim 6 \times 10^9 \text{ g cm}^{-3}$  tend to be disfavored in the recent publications, despite being a quite common result of earlier work. Nevertheless, the statement from Woosley (1997) that explosions of high-density white dwarfs have to occur to explain the solar abundances of neutron-rich isotopes, in particular  $^{48}\text{Ca}$ , is still unchallenged. The current generally accepted values of the critical density for electron-capture induced collapse of C+O white dwarfs seems to be  $\rho_c^{\text{crit}} \sim 9 \times 10^9 \text{ g cm}^{-3}$  (e.g. Woosley, 1997) except for Bravo and García-Senz (1999) who obtained a lower value of  $\rho_c^{\text{crit}} \sim 5.5 \times 10^9 \text{ g cm}^{-3}$  after including Coulomb corrections in their EoS for NSE matter.

### 5.1.3. Objectives of this part of the thesis

In this part of the thesis we aim to use highly resolved two-dimensional hydrodynamic simulations with up-to-date weak interaction rates to study the evolution of high-density C+O white dwarfs. As we have seen above, C+O white dwarfs are inert objects even at high central densities, unless carbon burning is ignited. We focus on the case in which the thermonuclear burning proceeds in the deflagration mode as the case in which the probability of gravitational collapse is highest. We discuss the effects of several physical and numerical parameters on the results of our simulations. In the cases in which a supernova occurs, we aim to calculate nucleosynthesis results and, following Woosley (1997), try to derive from these results statements about the frequency of those events compared to deflagrations in C+O white dwarfs with standard central density. Furthermore we will present neutrino luminosities and discuss the detectability of such signals.

This part of the thesis is organized as follows: In Section 5.2 we will present our hydrodynamic simulations, including the initial configuration (Section 5.2.1), results obtained by vari-

ation of several parameters (Sections 5.2.2–5.2.9), and neutrino luminosities (Section 5.2.10). We will discuss the results of our nucleosynthesis calculations in Section 5.3 before we will draw our conclusions in Section 5.4.

## 5.2. Hydrodynamic simulations

We present our hydrodynamic simulations of deflagrations in high-density C+O white dwarfs in this section. Our aim is to explore a large parameter space of different physical and numerical factors that may influence the way a deflagration wave in a high-density C+O white dwarf proceeds; some of them were discussed above in Section 5.1.1. In addition to variations of the central density, we discuss, with the help of illustrative examples, in the subsequent sections the effects of variations in resolution, in the shape of the ignition kernel, in chemical composition, burning velocity, and neutronization rate.

The numerical methods that we apply are described in Section 3: We employ the LEAFS-code with the minor modifications described in Section 3.3. We start with a description of our initial configurations.

### 5.2.1. Initial configurations

The arguably most important parameter of this study is  $\rho_c$ , the central density of the white dwarf. In Section 2.2.3 we showed that according to our calculations the maximum central density for hydrostatically stable C+O white dwarfs is  $\rho_c^{\max} \sim 2 \times 10^{10} \text{ g cm}^{-3}$  (visualized in Figure 2.2). However, we consider in the simulations presented in the following only C+O white dwarfs with central densities up to  $1.0 \times 10^{10} \text{ g cm}^{-3}$ . We refrain from extending our parameter space up to  $\rho_c^{\max}$  for the following reasons: Firstly, we use the laminar burning velocities  $v_{\text{lam}}$  published by Timmes and Woosley (1992). They calculated the burning velocities in C+O matter up to densities of  $1 \times 10^{10} \text{ g cm}^{-3}$  and provided analytical fit formulae to their results (cf. Section 3.1.4). At higher densities, those expressions describe the combustion probably incorrectly. Secondly, the rates of change of the electron fraction were calculated by Seitenzahl et al. (2009) based on the weak interaction rates of Langanke and Martínez-Pinedo (2001) (cf. Section 3.3.1). In these data, rates of the weak reactions are only available for densities up to  $1 \times 10^{10} \text{ g cm}^{-3}$ .

Hence, our upper limit originates mainly from a lack of input data. But it is also physically justified, because C+O white dwarfs with central densities higher than  $1 \times 10^{10} \text{ g cm}^{-3}$  are not expected to exist in nature, as discussed in the introduction (Section 5.1.2). Therefore we consider an upper limit of  $\rho_c \leq 1.0 \times 10^{10} \text{ g cm}^{-3}$  as sufficient for a comprehensive study of high-density C+O white dwarfs.

We conduct two-dimensional simulations on a grid of 1024 cells per dimension, if not indicated otherwise. We use cylindrical coordinates; our numerical domain covers one quadrant of the  $r$ - $z$ -plane including the center of the white dwarf at the origin. By applying reflecting

boundary conditions we impose rotational symmetry around the  $z$ -axis and mirror symmetry with respect to the equatorial plane.

The resolution in the center is crucial for the processes considered in this work. Due to our hybrid moving grid (cf. Section 3.1.3) we can vary the central resolution by changing the size of the *ignition kernel*, the volume in the center of the white dwarf that is burned instantly at the beginning of the simulations: Because the initial size of the inner grid is chosen to be such that it tracks the size of the ignition kernel, and the number of cells reserved for the inner grid is constant for a given total number of grid cells, a smaller size of the ignition kernel leads to higher resolution in the center.

Our models of lowest central resolution (models with prefix A) correspond to the standard setup in the LEAFS-code for simulations of centrally ignited Chandrasekhar-mass models of thermonuclear supernovae, first described as model c3\_2d in Reinecke et al. (1999b).

In most of our models, the shape of the ignition kernel is a sphere on which sinusoidal perturbations are overlaid – the same shape as the ignition kernel of model c3\_2d of Reinecke et al. (1999b). Therefore, we indicate our models featuring this ignition kernel shape by “c3”. The intention for adding a sinusoidal perturbation is to control the growth of Rayleigh-Taylor instabilities to some extent – instead of waiting for numerical perturbations to grow. The latter are uncontrollable, resolution dependent, and might lead to unphysical grid effects; therefore, it is usually preferable to include the perturbations by hand. But since these artificial perturbations might accelerate the growth of Rayleigh-Taylor instabilities and thereby influence our results concerning the question whether the white dwarf collapses, we consider also models without artificial perturbations. Such models feature a spherical ignition kernel and are indicated with “sph”.

Our initial models are hydrostatic configurations based on one-dimensional solutions of the equations of hydrostatic equilibrium (2.16–2.17) as discussed in Section 2.2.3. If not stated otherwise, the white dwarfs are made of carbon and oxygen, homogeneously distributed and in equal mass fractions. The initial white dwarfs are assumed to be cold ( $T = 5.0 \times 10^5$  K) and isothermal.

In the cases in which the white dwarf explodes we run the simulations until  $t = 10$  s. At this time, all nuclear reactions except radioactive decays have ceased and the matter is in a state of homologous expansion, in which the radial velocity is proportional to the distance from the explosion center.

In Table 5.1 we compare several of our initial configurations that have different resolution. Stated is the radius of the ignition kernel, the initial size of one grid cell in the central, uniform part of the grid, and the total number of grid cells.

### 5.2.2. Resolution

In the following we compare eleven different models with varying initial resolution of the inner grid (A,B,C, and D, see Table 5.1), shape of the ignition kernel (c3 or sph, see Section 5.2.1), and total number of grid cells to examine the influence of these parameters on

5. Deflagrations in high-density carbon-oxygen white dwarfs

Model prefix	$R_i$ [cm]	central resolution [cm]	grid cells
A	$1.5 \times 10^7$	47250	$1024 \times 1024$
B	$1.5 \times 10^6$	4725	$1024 \times 1024$
C512	$1.5 \times 10^5$	945	$512 \times 512$
C	$1.5 \times 10^5$	472.5	$1024 \times 1024$
C2048	$1.5 \times 10^5$	236.25	$2048 \times 2048$
D	$1.5 \times 10^4$	47.25	$1024 \times 1024$
u4096	$1.5 \times 10^5$	38560	$4096 \times 4096$

**Table 5.1.:** Model prefix, radius of the central ignition kernel  $R_i$ , initial size of a grid cell in the central uniform part of the grid, total number of grid cells.

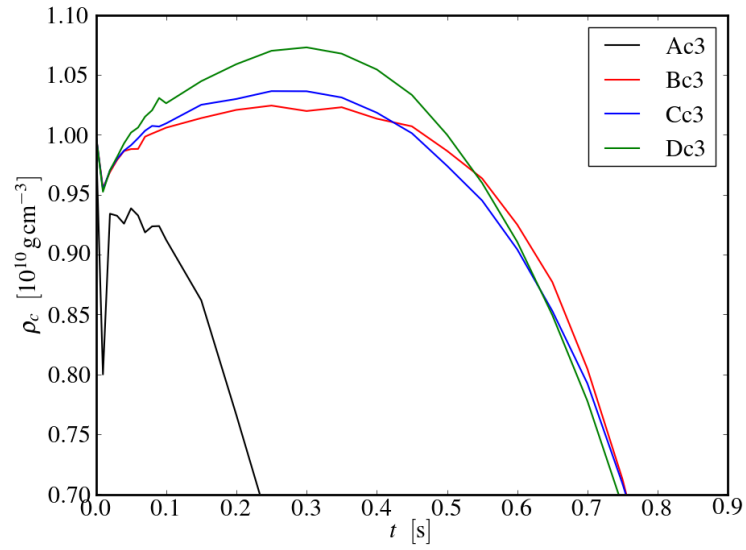


**Figure 5.1.:** Evolution of central density  $\rho_c$  for four models with ignition kernel shape c3 and different initial central resolution, cf. Table 5.2.

Model name	reso- lution	ignition kernel	$\rho_c^{\text{ini}}$ [ $10^9 \text{ g cm}^3$ ]	carbon fraction	burning velocity	$dY_e/dt$ rates
Asph	A	sph	10.0	0.5	$v_{\text{lam}}$	Seitenzahl et al. (2009)
Bsph	B	sph	10.0	0.5	$v_{\text{lam}}$	Seitenzahl et al. (2009)
Csph	C	sph	10.0	0.5	$v_{\text{lam}}$	Seitenzahl et al. (2009)
Dsph	D	sph	10.0	0.5	$v_{\text{lam}}$	Seitenzahl et al. (2009)
Ac3	A	c3	10.0	0.5	$v_{\text{lam}}$	Seitenzahl et al. (2009)
Bc3	B	c3	10.0	0.5	$v_{\text{lam}}$	Seitenzahl et al. (2009)
Cc3*	C	c3	10.0	0.5	$v_{\text{lam}}$	Seitenzahl et al. (2009)
C512c3	C512	c3	10.0	0.5	$v_{\text{lam}}$	Seitenzahl et al. (2009)
C2048c3	C2048	c3	10.0	0.5	$v_{\text{lam}}$	Seitenzahl et al. (2009)
u4096c3	u4096	c3	10.0	0.5	$v_{\text{lam}}$	Seitenzahl et al. (2009)
Dc3	D	c3	10.0	0.5	$v_{\text{lam}}$	Seitenzahl et al. (2009)
Cc3.0.8vlam	C	c3	10.0	0.5	$0.8 \times v_{\text{lam}}$	Seitenzahl et al. (2009)
Cc3.0.6vlam	C	c3	10.0	0.5	$0.6 \times v_{\text{lam}}$	Seitenzahl et al. (2009)
Cc3.0.4vlam	C	c3	10.0	0.5	$0.4 \times v_{\text{lam}}$	Seitenzahl et al. (2009)
Cc3.0.25C*	C	c3	10.0	0.25	$v_{\text{lam}}$	Seitenzahl et al. (2009)
Cc3.0.75C*	C	c3	10.0	0.75	$v_{\text{lam}}$	Seitenzahl et al. (2009)
Cc3.Ocore*	C	c3	10.0	O core	$v_{\text{lam}}$	Seitenzahl et al. (2009)
Cc3.9e9_Ocore*	C	c3	10.0	O core	$v_{\text{lam}}$	Seitenzahl et al. (2009)
Cc3.8e9_Ocore*	C	c3	10.0	O core	$v_{\text{lam}}$	Seitenzahl et al. (2009)
Cc3.bravo_cc	C	c3	10.0	0.5	Eq. (5.4)	Eq. (5.3)
Cc3.bravo_nocc	C	c3	10.0	0.5	$v_{\text{lam}}$	Eq. (5.2)
Cc3.9e9*	C	c3	9.0	0.5	$v_{\text{lam}}$	Seitenzahl et al. (2009)
Cc3.8e9*	C	c3	8.0	0.5	$v_{\text{lam}}$	Seitenzahl et al. (2009)
Cc3.7e9_SGS	C	c3	7.0	0.5	$v_{\text{turb}}$	Seitenzahl et al. (2009)
Cc3.6e9_SGS	C	c3	7.0	0.5	$v_{\text{turb}}$	Seitenzahl et al. (2009)
Cc3.5e9_SGS	C	c3	7.0	0.5	$v_{\text{turb}}$	Seitenzahl et al. (2009)
Cc3.4e9_SGS	C	c3	7.0	0.5	$v_{\text{turb}}$	Seitenzahl et al. (2009)
Cc3.2.9e9*	C	c3	2.9	0.5	$v_{\text{lam}}$	Seitenzahl et al. (2009)

**Table 5.2.:** Overview of different models discussed in this work: model name, resolution according to Table 5.1, shape of ignition kernel, initial central density, initial carbon fraction, burning velocity, and source of rates that describe the change of the electron fraction; see text for details. Models indicated with an asterisk (\*) have been additionally calculated as turbulent deflagrations. In the text, for these models a suffix (“\_SGS”) will be added if the run with SGS model is meant.

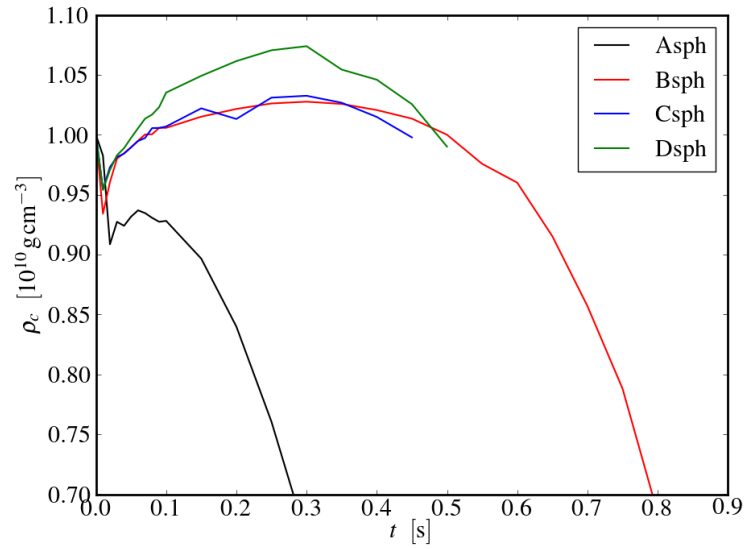


**Figure 5.2.:** Evolution of central density  $\rho_c$  for four models with spherical ignition kernel and different initial central resolution, cf. Table 5.2.

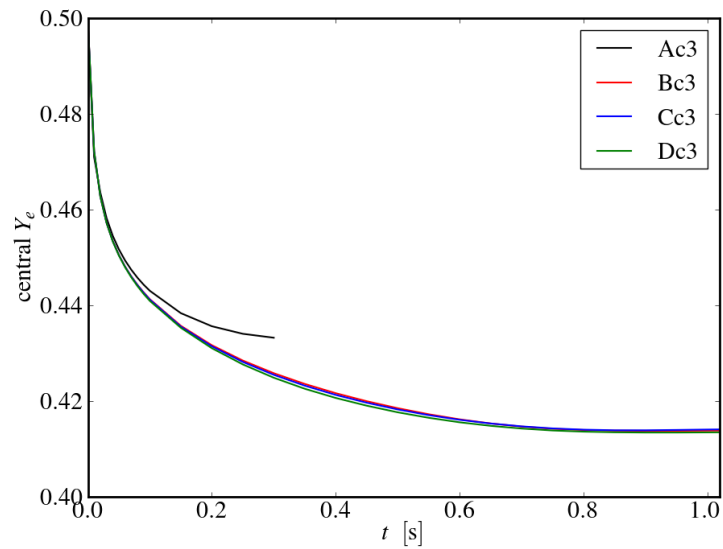


**Figure 5.3.:** Evolution of central electron fraction  $Y_e$  for four models with ignition kernel shape c3 and different initial central resolution, cf. Table 5.2.

the results of the simulations. An overview of those configurations and of all further models, which we will discuss in the following sections, can be found in Table 5.2.

In all models discussed in this resolution study the burning velocity is the laminar burning velocity  $v_{\text{lam}}$  according to Timmes and Woosley (1992). We conduct the resolution tests, and the simulations presented in the following Sections 5.2.3–5.2.7, without subgrid scale (SGS) turbulence model (cf. Sections 2.4.2 and 3.1.6). Therefore, these calculations represent the extreme case in which no acceleration of the burning velocity due to turbulent motions is taken into account. This is done with the aim to simulate configurations in which a gravitational collapse of the white dwarf is most probable. A drawback to this approach is that, without SGS model, in principle no convergence of the resolution study can be expected, because the turbulent motion on unresolved scales is neglected, and the extent of these unresolved scales depends, of course, on the resolution. However, the influence of the SGS model on the dynamics of the first burning stage is very minor, as we will show in Section 5.2.9.

In Figure 5.1 the time evolution of the central density  $\rho_c$  is shown for four models with ignition kernel shape c3 and resolution A, B, C, and D, respectively; in Figure 5.2 the same can be seen for the four corresponding models with spherical ignition kernel. The main result here is that the white dwarf does not collapse, independent of the resolution. However, the maximum value of  $\rho_c$  increases with resolution regardless of the shape of the ignition kernel.

In models A, which adopt the standard setup of our code, the central density does not even reach its initial value and soon, at  $t \sim 0.1$  s, drops rapidly. At this time, the minimal length scale of turbulent burning  $\lambda_{\text{min}}$  (see Section 2.4.2 and equation (2.34)) has already decreased<sup>1</sup> to about  $1 \times 10^6$  cm, which is considerably smaller than the size of the initial perturbations ( $3.0 \times 10^6$  cm). Therefore, the perturbations grow rapidly and the burning features strong turbulence. This leads to a fast density decrease and to the explosion of the white dwarf.

Hence, setup A is certainly not suited for our studies. In the models with next higher resolution, models B, the quantitative results are clearly different: The central density rises slightly above its initial value and drops rapidly after  $t \sim 0.5$  s. At this time,  $\lambda_{\text{min}}$  is still about a factor of  $\sim 2$  larger than the initial perturbations of setup B; thus, the perturbations do not grow. The differences between models B and both C and D, as well as between C and D, are much less pronounced than the differences between A and B. The central density increase is the highest in models D, but the rapid decrease starts at  $t \sim 0.5$  s as well and the general shape of the central density evolution is very similar to models B and C. During the first  $\sim 0.5$  s of the simulations of models C and D,  $\lambda_{\text{min}}$  is always much larger than the initial perturbations; therefore, the perturbations in those models do not grow during this period as well. This explains the similarities in the central density evolution of models Bc3, Cc3, and Dc3, in contrast to model Ac3, in which the perturbations are soon larger than  $\lambda_{\text{min}}$ .

Simulations with resolution D are expensive – in the first stages the numerical time step is restricted to  $\Delta t \approx 10^{-8}$  s. Extended studies of different parameters with this or even higher res-

<sup>1</sup>The value of  $\lambda_{\text{min}}$  decreases with time as the flame propagates away from the center of the white dwarf, mainly because the gravitational acceleration becomes stronger (cf. equation (2.34), see also Section 4.4.2).

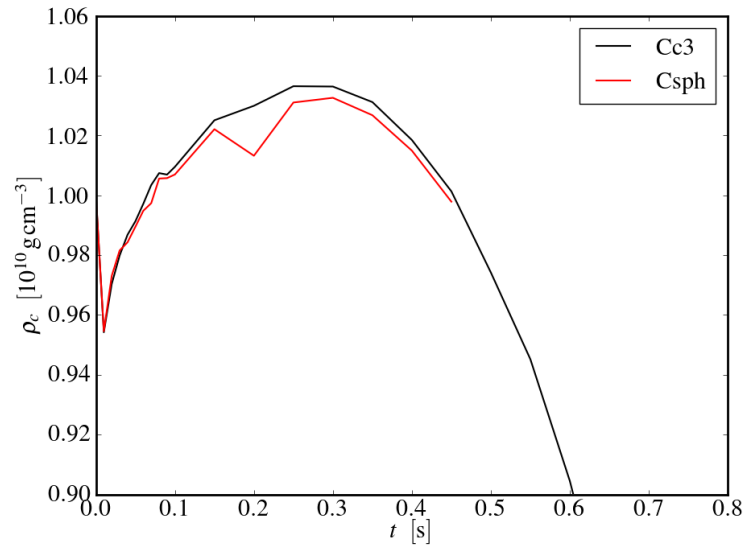


**Figure 5.4.:** Evolution of central density for two models with resolution C and a different shape of the ignition kernel, cf. Table 5.2.

olution are not feasible for us due to limited computational resources. We however think that higher resolution does not lead to fundamentally different results. This argument is supported by the temporal evolution of the central electron fraction  $Y_e$ , plotted in Figure 5.3 for the same four models with ignition kernel shape c3 and varying central resolution as in Figure 5.1. We discussed in Section 5.1.1 that the central electron fraction is a key quantity because it directly affects the pressure in the center. As can be seen from Figure 5.3, the minimum of the  $Y_e$ -value agrees well for all but the lowest resolved model A. The difference in the minimum  $Y_e$  between models C and D is only about  $5 \times 10^{-4}$ . All other important quantities that we tested (e.g. the neutrino luminosity, see Section 5.2.10) are quite insensitive to changes of the resolution from C to D, too.

Therefore, in order to find a compromise between optimal resolution and the possibility to calculate a large number of models to examine the influence of different parameters, we decided to use resolution C in the following simulations as our standard configuration. This choice still provides a satisfactory resolution in the center, and we obtain the possibility to conduct simulations exploring several different parameters at reasonable computational costs.

The variation in the results between simulations that differ only in the shape of the ignition kernel is negligible, as is visualized in Figure 5.4 where we show as an example the central density evolution of two models with resolution C and different ignition kernels. One reason for this is that the initial perturbations in model Cc3 remain smaller than  $\lambda_{\min}$  for a long time, as described above. Because in the simulations that start with a spherical ignition kernel

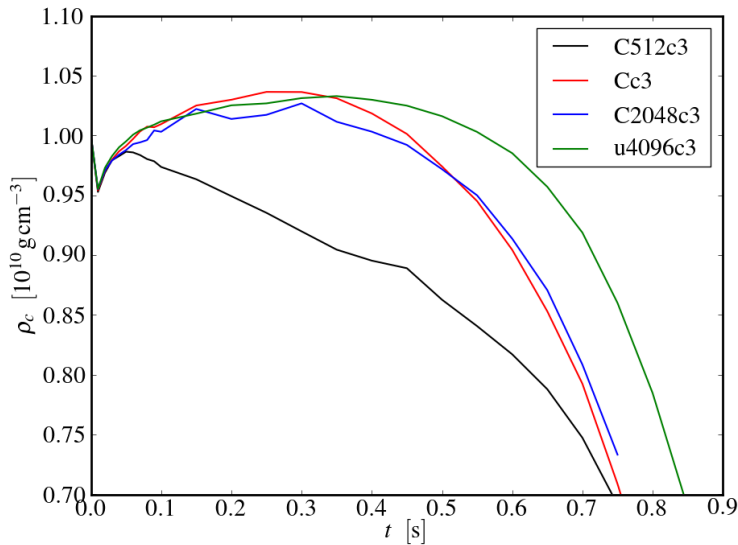


**Figure 5.5.:** Evolution of central density for four models with ignition kernel Cc3 and a different grid size and geometry, cf. Table 5.2.

without perturbations instabilities tend to grow at the edges of the grid and may thus contribute to grid effects and other numerical artifacts, we will use in all following simulations an ignition kernel of shape c3.

In a last point of this resolution study we compare the influence of the total number of grid cells while keeping the shape and size of the ignition kernel, and thereby the physical extent of the inner grid, constant. Results are presented in Figures 5.5 and 5.6, in which we compare models with initial configuration Cc3 and grid sizes of  $512^2$ ,  $1024^2$ , and  $2048^2$  cells; again we make the comparison based on the evolution of the central density and electron fraction. No clear connection between the grid size and the highest increase in central density can be seen, in particular the step from  $1024^2$  to  $2048^2$  grid cells does not follow the trend that exists in the case of increasing resolution in the center (Figure 5.1). However, the computational costs rise dramatically and we are not able to conduct extensive studies using a grid size of  $2048^2$  cells to explain this behavior.

Comparable to the results of the preceding paragraphs, the evolution of the central electron fraction is very similar in all simulations with different grid sizes except for the model with the smallest grid ( $512^2$  cells). This provides further support to our decision to declare setup C with  $1024^2$  grid cells to be our standard configuration.

In addition to the resolution study, we checked exemplary the influence of the grid geometry on the results of our simulations. The construction method of the hybrid grid (cf. Section 3.1.3) implies that the outermost cells become quite large if the resolution in the center is as high

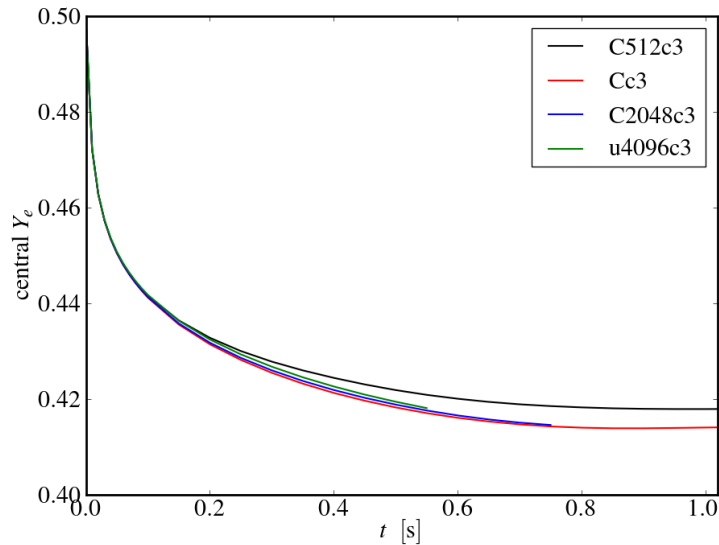


**Figure 5.6.:** Evolution of central electron fraction  $Y_e$  for four models with ignition kernel Cc3 and a different grid size and geometry, cf. Table 5.2.

as in our cases C and D. To dispel the suspicion that this fact might affect the stability of the star and distort the results, we conducted one simulation with a uniform grid. To achieve a comparably high resolution as in the standard configurations C, we chose a very large grid size of  $4096^2$  grid cells. The size and shape of the ignition kernel is the same as in model Cc3. The results of this model (called “u4096c3”) are also plotted in Figures 5.5 and 5.6 and show that this change of the grid geometry does not affect the results significantly. The rapid decrease of central density is shifted slightly to later times ( $t \sim 0.6$ s), whereas no difference in the evolution of the central electron fraction is visible. Because the computations that apply a large uniform grid are expensive, we conduct no further tests with this configuration.

As a consequence of this comparison of initial configurations and grid sizes we decide, taking the above stated feasibility arguments into account, to use setup Cc3 and a moving hybrid grid with a size of  $1024^2$  cells (cf. Table 5.1) as the initial configuration best suited for the following studies. We will use it as a standard case on which further discussion will be based.

The simulations in this section were conducted with older versions of some parts of the code. Subsequent changes in these parts of the code (e.g. slightly different treatment of neutrino energy losses) lead to small changes in the results of the simulations, in particular of model Cc3 that is used as reference in the discussions of the following chapters, but have no impact on the conclusions drawn from this resolution study. Therefore we refrain from repeating this study, on which a considerable amount of computing time was spent.

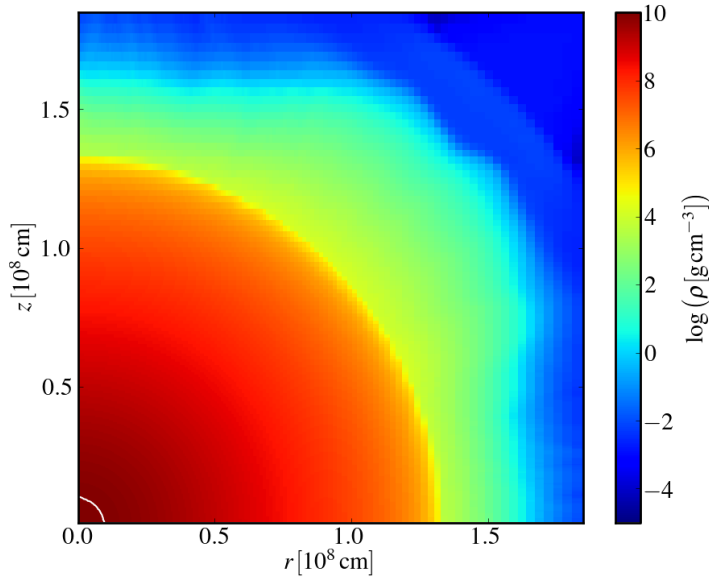


**Figure 5.7.:** Density at  $t = 0.3$  s (model Cc3). The white line indicates the position of the flame front.

### 5.2.3. Discussion of standard model Cc3

We explained in the preceding section the reasons why we chose model Cc3 (cf. Table 5.2) to be our standard model. In this section we look in some detail into the results of the simulation of this model.

As briefly mentioned above, a key result is the fact that no electron capture induced collapse occurs in a configuration that features an initial central density that is higher than the value of the critical density above which a C+O white dwarf is assumed to collapse according to earlier work (cf. Section 5.1.2).

The black curve in Figure 5.4 shows the evolution of the central density of the white dwarf as a function of time. After an initial dip, the central density rises until  $t \sim 0.3$  s, when its value is  $\sim 4\%$  higher than its initial value. A snapshot at this time is shown in Figure 5.7 in which the logarithm of the density is color coded and the white line shows the position of the flame front, numerically represented by the zero level set. The very small initial perturbations did not yet grow and are not visible in this figure. This changes in the next tenths of a second: The perturbations start to grow due to the onset of Rayleigh-Taylor instabilities. At  $t \sim 0.65$  s (Figure 5.8) the flamefront is not smooth anymore, the growing instabilities are now clearly recognizable. After that, the instabilities grow rapidly and form the typical mushrooms-shaped structures, clearly visible in the third snapshot at  $t \sim 1.15$  s (Figure 5.9). Also the expansion of the white dwarf is already evident – the radius of the star nearly doubled. The enlarged

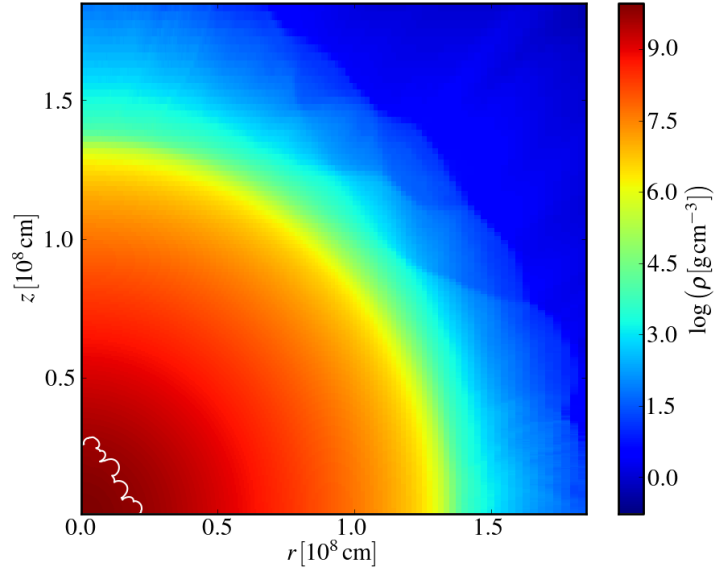


**Figure 5.8.:** Density at  $t = 0.65$  s (model Cc3). The white line indicates the position of the flame front.

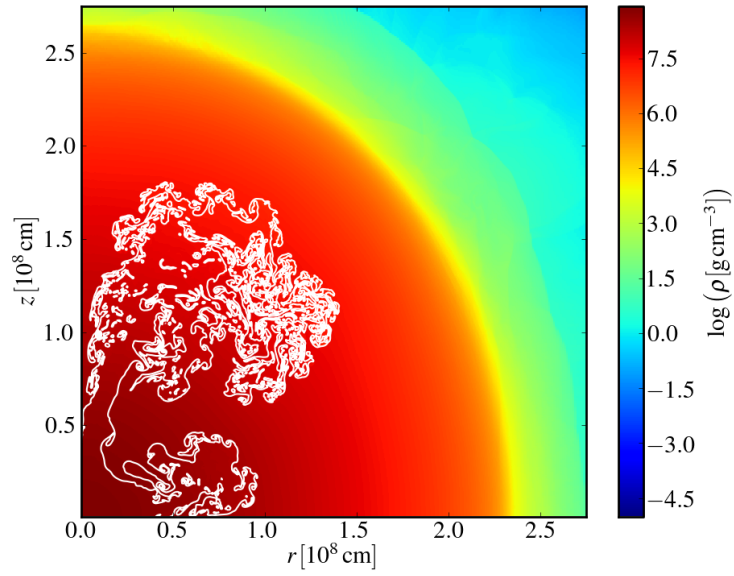


**Figure 5.9.:** Density at  $t = 1.15$  s (model Cc3). The white line indicates the position of the flame front.

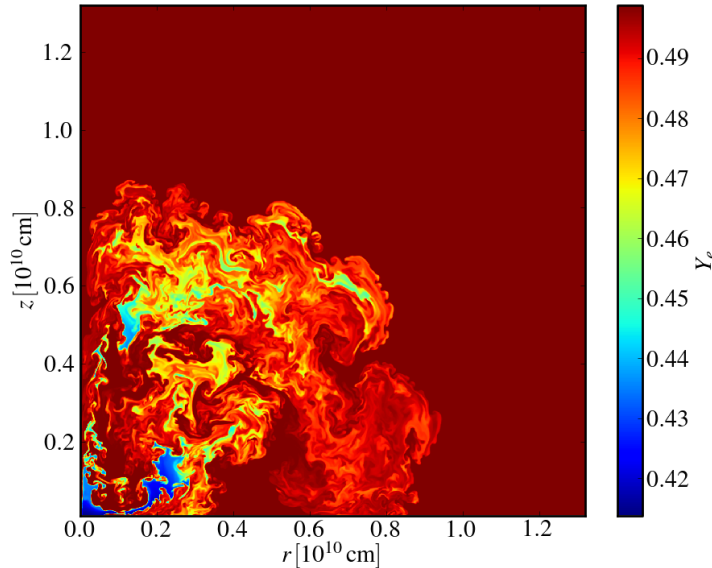


**Figure 5.10.:** Electron fraction  $Y_e$  at  $t = 10$  s (model Cc3).

flame surface leads to high fuel consumption; the star expands further and thus the central density decreases rapidly (Figure 5.4): The white dwarf explodes, forming a thermonuclear supernova, and the matter that comprised the white dwarf is ejected into space, leaving no remnant star behind.

Figure 5.10 shows the spatial distribution of the electron fraction  $Y_e$  of model Cc3 at the time when we stop the simulation ( $t = 10$  s). At that time the ejecta cover already an extended area with a radius of  $\sim 10^{10}$  cm, and the density in the center is about  $10^5 \text{ g cm}^{-3}$ . We see in Figure 5.10 that the material of lowest  $Y_e$  is concentrated in confined areas in the innermost part of the ejecta, but there is also matter of relative low  $Y_e$  in the outer parts, showing the characteristic mixing of a deflagration. The minimum  $Y_e$  reached in the simulation is 0.4120 at  $t = 0.95$  s after ignition; at the end of the simulation we obtain a minimum of  $Y_e = 0.4127$ , the slight rise compared to the absolute minimum is caused by  $\beta$ -decays.

Due to the combustion in the high-density environment, the fraction of the C+O matter that is burned into iron group elements (IGEs, cf. Section 5.3.2) is relatively large for a pure deflagration<sup>2</sup>; consequently, the abundance of intermediate mass elements (IMEs) is low and a large amount of nuclear binding energy is released. This leads to a high kinetic energy of the ejecta after the burning ceases.

<sup>2</sup>We use the term *pure deflagration* to distinguish our models from models that feature a deflagration-to-detonation transition.

$a$	1	0.8	0.6	0.4
$Y_e^{\min}$	0.4120	0.4091	0.4056	0.4037
$t (Y_e = Y_e^{\min})$	0.95 s	1.05 s	1.15 s	1.40 s

**Table 5.3.:** Minimum electron fraction  $Y_e^{\min}$ , and time  $t$  after ignition when this minimum is reached, for the models in which the burning velocity is multiplied by a factor  $a$ , compared to our standard model ( $a = 1$ ).

Another consequence of the burning at high densities is the subsequent fast neutronization, resulting in a low  $Y_e$  in the ashes, as discussed above and shown in Figure 5.10. Thus, the fraction of  $^{56}\text{Ni}$  in the total IGEs has to be rather low, because  $Z(^{56}\text{Ni})/A(^{56}\text{Ni}) = 0.5$ . The radioactive decay of  $^{56}\text{Ni}$  powers the lightcurve of a supernova; compared to other models, a deflagration of a high-density C+O white dwarf would therefore be rather faint.

Furthermore, a large amount of carbon and oxygen remains unburnt, which is a typical consequence of a pure deflagration. A quantitative analysis of the  $^{56}\text{Ni}$ -abundance, further nucleosynthesis yields, and comparisons to standard thermonuclear supernovae will be presented in Section 5.3.

#### 5.2.4. Central density

In this section we briefly discuss the influence of the initial central density  $\rho_c^{\text{ini}}$  of the white dwarf on the results of the simulations. Generally, it is expected that white dwarfs with lower central density are less likely to collapse, because lower density leads to slower neutronization. Our results confirm this, see Figures 5.11 (a) and (b), in which we compare the temporal evolution of the central density and electron fraction, respectively, of three models with different initial central densities in the range  $8 \times 10^9$  to  $1 \times 10^{10} \text{ g cm}^{-3}$  (models Cc3, Cc3\_9e9, and Cc3\_8e9; see Table 5.2). All other parameters are left unchanged.

All models show a very similar qualitative behavior. In each case, the central densities rises by a few per cent before dropping quite rapidly – the white dwarf collapses in neither case. The final central  $Y_e$  rises with decreasing initial  $\rho_c$ , as expected. The minimum value of  $Y_e$  in the three models Cc3, Cc3\_9e9, and Cc3\_8e9 is 0.412, 0.419, and 0.424, respectively. The differences regarding the nucleosynthesis yields between models with different initial central density will be discussed in Section 5.3.

#### 5.2.5. Burning velocity

Since the burning velocity is an important parameter regarding the fate of the white dwarf, we conducted several tests in which we multiplied the laminar burning velocity (taken from Timmes and Woosley (1992) as in the other simulations, cf. Section 3.1.4) with a constant

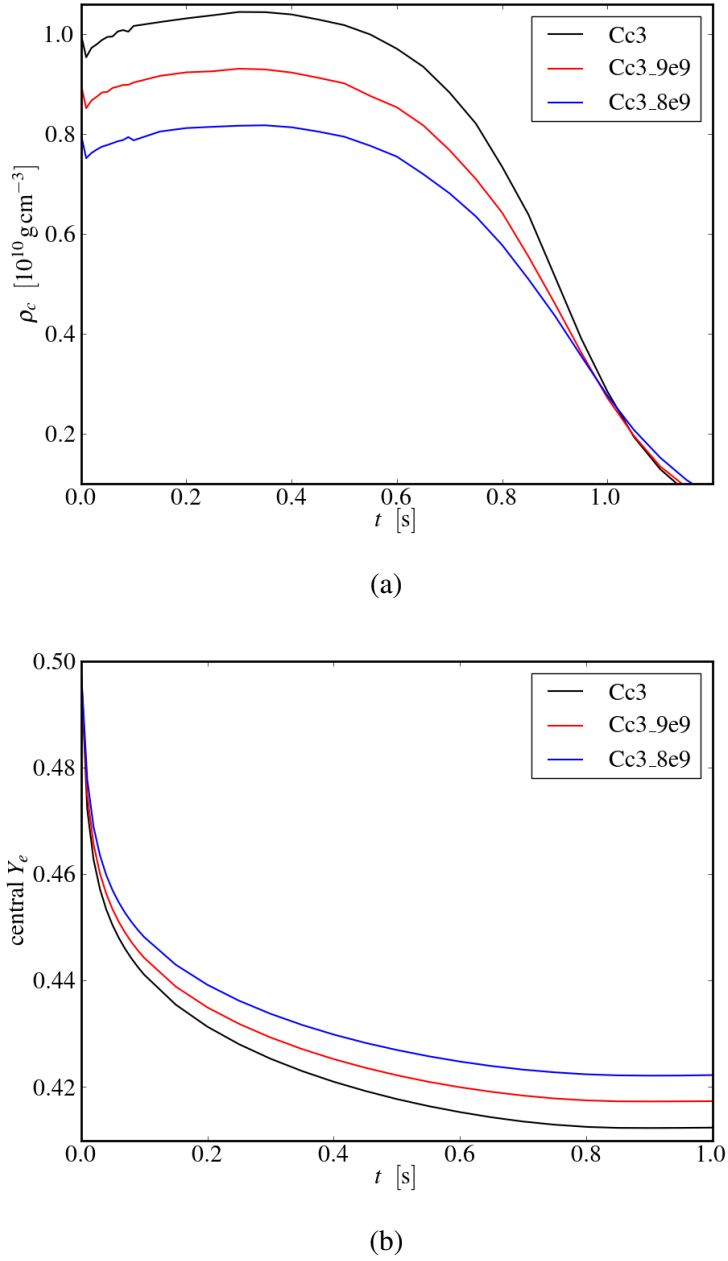


**Figure 5.11.:** Evolution of (a) central density  $\rho_c$  and (b) central electron fraction  $Y_e$  of three models with different initial central densities, cf. Table 5.2.

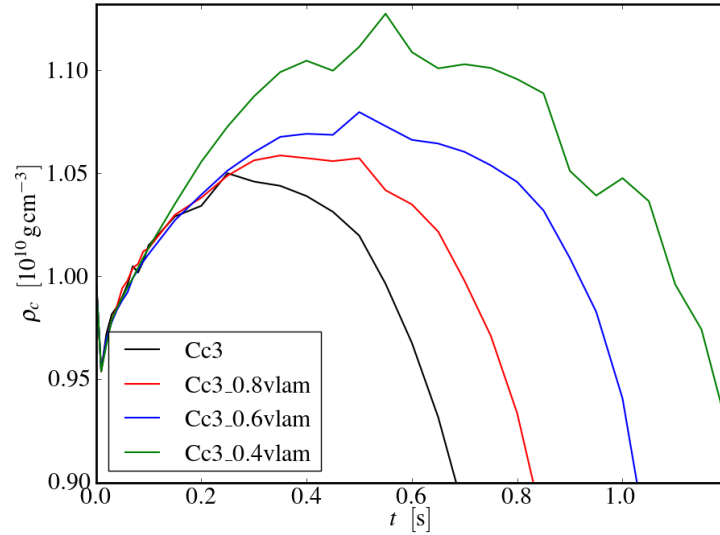


**Figure 5.12.:** Evolution of central density  $\rho_c$  of four models with different laminar burning velocity, cf. Table 5.2.

factor  $a < 1$ ,

$$v'_{\text{lam}} = a \cdot v_{\text{lam}}. \quad (5.1)$$

We considered values of  $a = 0.8, 0.6$ , and  $0.4$ . The results are plotted in Figure 5.12 in terms of the temporal evolution of the central density. We see that the increase in central density is clearly the higher the lower the burning velocity is. But even in the extreme case  $a = 0.4$ , in which the burning velocity is less than half of its standard value, the white dwarf does not collapse to a neutron star, although the central density rises by more than 10% and stays above its initial value for about 1.1 s.

The results of our simulations of this section imply that the fate of the white dwarf is not very sensitive to a reduction of the burning velocity. A qualitative explanation of this behavior is that the decrease of the electron fraction  $Y_e$  is too slow, and the time gained by the slower burning velocity is not sufficient to lead to a collapse. This is supported by the minimum  $Y_e$  values of the simulations which are given in Table 5.3. The data show that the decrease in  $Y_e^{\min}$  is not very pronounced, while the time at which this minimum is reached is shifted backwards. Therefore we conclude that models with  $\rho_c^{\text{ini}} = 1.0 \times 10^{10} \text{ g cm}^{-3}$  may only collapse if the burning velocity is reduced by more than a factor of 2. While there might be physical reasons to expect a moderate decrease of the burning velocity at high densities (see e.g. Bravo and García-Senz, 1999), there is no known physical reason to expect such a strong decrease.

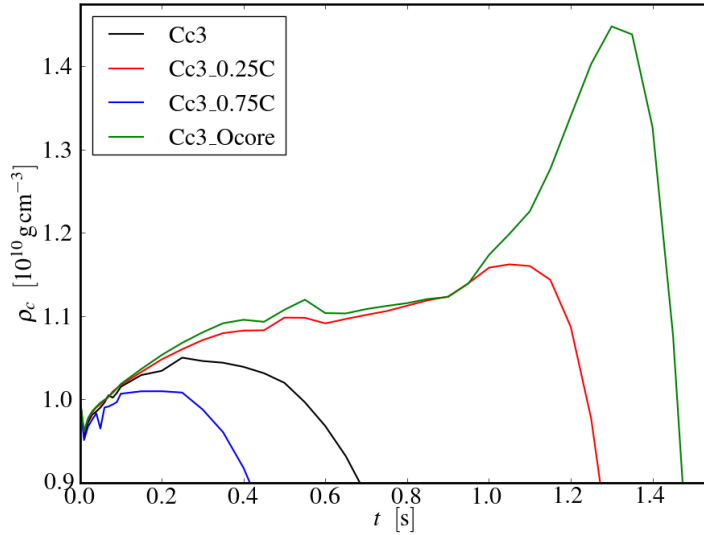


**Figure 5.13.:** Evolution of central density  $\rho_c$  of four models with different chemical composition, cf. Table 5.2.

### 5.2.6. Chemical composition

Until now, we only considered white dwarf models with an initially homogeneous composition of carbon and oxygen, each providing 50% of the total mass ( $X(C) = X(O) = 0.5$ ). We stated in Section 5.1.1 that it is unclear what the implications of a change in carbon fraction are; therefore, we examine in this section chemical compositions that differ from the standard model. In a first step we change the carbon fraction while keeping a homogeneous distribution. Exemplary we calculated two models, one with a carbon fraction of  $X(C) = 0.25$  (model Cc3\_C0.25), and one with  $X(C) = 0.75$  (model Cc3\_C0.75).

In the second step we consider a partial spatial separation of the carbon and the oxygen while keeping the total mass ratio equal ( $X(C)_{\text{total}} = 0.5$ ). In particular, we consider a composition profile with oxygen concentrated in the center, while the carbon is moved partially to the outer layers. We calculate three models with such a configuration and varying initial central density in the range  $8 \times 10^9$  to  $1 \times 10^{10} \text{ g cm}^{-3}$ : Cc3\_Ocore, Cc3\_9e9\_Ocore, and Cc3\_8e9\_Ocore (cf. Table 5.2). In these models we assume an “oxygen core” in the center of the star, defined as  $r \leq 2 \times 10^7 \text{ cm}$ , where  $r$  is the radial coordinate. In this region we set  $X(C)_{\text{core}} = 0.2$ . A linear transition zone is assumed in the range  $2 \times 10^7 \text{ cm} < r \leq 5 \times 10^7 \text{ cm}$ , in which  $X(C)$  rises linearly with  $r$ . The outer value of the carbon fraction is adjusted to guarantee equal mass fractions of carbon and oxygen integrated over the whole star. For the models Cc3\_Ocore, Cc3\_9e9\_Ocore, and Cc3\_8e9\_Ocore this leads to  $X(C)_{\text{out}} = 0.66, 0.643,$

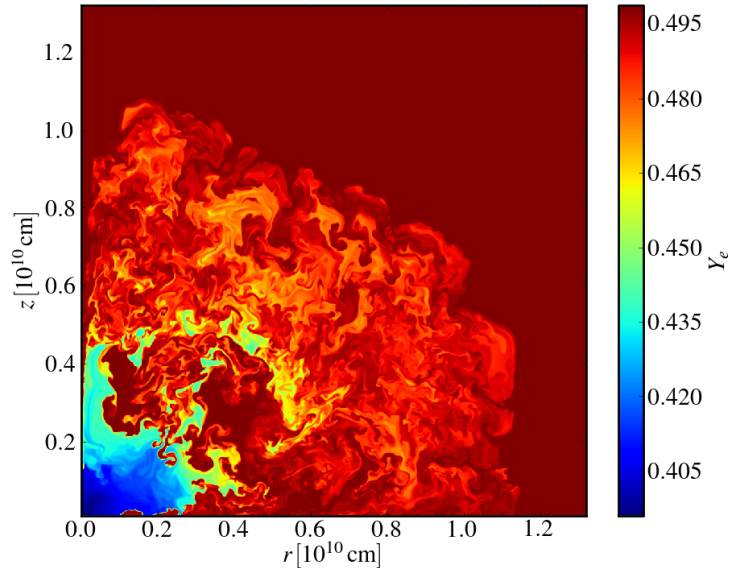


**Figure 5.14.:** Electron fraction  $Y_e$  at  $t = 10$ s (model Cc3\_Ocore, cf. Table 5.2).

and 0.629, respectively. The lower values in the models with lower initial central density are due to the larger radius of the white dwarf in those less compact models.

This setup is physically motivated by the possible separation of carbon and oxygen in cold massive white dwarfs. Accreting white dwarfs are normally assumed to be convectively completely mixed. However, they have to accrete at a very low rate to reach the high central densities considered in this work. That slow accretion process might allow for the cooling of the white dwarf, resulting in the possibility that sedimentation and phase separation sets in (Stevenson, 1980; Canal et al., 1980).

In Section 3.1.5 we explained that for incomplete burning at low densities the composition in terms of the five representative species is tabulated. When those tables were compiled, the standard carbon fraction  $X(C) = 0.5$  was assumed. For different carbon fractions, new tables should be calculated to treat incomplete burning correctly. For simplicity we did not calculate new composition tables for incomplete burning but used the existing tables. This approach introduces only a minor error concerning the energy release in the hydrodynamics, because in our simulations of high-density white dwarfs the combustion occurs to a large extent at high densities, especially in the crucial early phases, and most of the matter is burned to nuclear statistical equilibrium. The change in carbon fraction has no impact on matter in NSE because in this case the composition depends only on density, temperature, and electron fraction – all three quantities are unaffected when the carbon fraction is altered. However, we

have to keep this issue in mind when we calculate the nucleosynthesis results of those models in Section 5.3.

We conducted simulations of the five models described above and compared the results to our standard case with the same resolution. Also in the models with altered chemical composition the white dwarfs do not collapse but form a supernova. The evolution of the central density of the highest-density models is plotted in Figure 5.13. We see, in both models that have a lower carbon fraction in the center, a rise of the central density that is considerably stronger than in model Cc3.

In model Cc3\_C0.25, the white dwarf does not collapse, although the density rises by 15% and stays above its initial value for more than a second. Because the globally lower carbon abundance means a lower energy content of the fuel, one might expect that less kinetic energy will be released than in the standard model. But this is not the case, because of an effect that is similar to the mechanism that works in our standard model Cc3, as discussed in Section 5.2.3, and leads to higher explosion energies compared to normal Chandrasekhar-mass deflagration models. Here the effect is even stronger: Since the burning velocity as derived by Timmes and Woosley (1992) is directly proportional to the carbon fraction at the position of the flame (see equation 3.6), a reduction of the carbon fraction is always connected to a reduction of the laminar burning velocity<sup>3</sup>. This fact, and the initially slower energy release, leads to a slowdown of the expansion of the star; therefore, more matter is burned at higher densities compared to model Cc3. The burning at high densities leads to more complete burning; this overcompensates the lower energy content of the fuel and hence the final kinetic energy of the ejecta is larger than in model Cc3 ( $0.66$  vs.  $0.55 \times 10^{51}$  erg). Also the energy carried away by neutrinos (see Section 5.2.10) is considerably larger in the model with lower carbon fraction. The minimum electron fraction of model Cc3\_C0.25 is somewhat higher than in the corresponding model with oxygen core (see below) but lower than in the standard model. We obtain  $Y_e^{\min} = 0.403$  at  $t = 1.35$  s, at  $t = 10$  s we have  $Y_e^{\min} = 0.404$ .

As expected, the high amount of released nuclear energy in the model with very high carbon fraction (model Cc3\_C0.75) quickly leads to an explosion. The kinetic energy at  $t = 10$  s is only  $0.38 \times 10^{51}$  erg. This confirms the trend that we observed above – higher carbon fractions lead to lower explosion energies in pure deflagrations in high-density white dwarfs. Also not surprising is that the minimum electron fraction reached in model Cc3\_C0.75 is the highest of all models with  $\rho_c^{\text{ini}} = 1.0 \times 10^{10} \text{ g cm}^{-3}$ :  $Y_e^{\min} = 0.417$  at  $t = 0.75$  s, and at the end of the simulation at  $t = 10$  s we obtain  $Y_e^{\min} = 0.418$ .

The central density increases by nearly 50% in model Cc3\_Ocore (Figure 5.13). But a collapse does not occur either – we observe a rapid decline after the density peak. This fast decrease in central density corresponds to a very violent explosion of the star. The behavior of this model is qualitatively very similar to that of model Cc3\_C0.25: Due to the fact that

<sup>3</sup>We have to note that the laminar burning velocity calculated by Timmes and Woosley (1992) as given in equation (3.6) might not be accurate if the carbon fraction  $X(C)$  deviates from 0.5, as was pointed out by Röpke (2003).

in the models with carbon depletion in the core the white dwarf does not expand in the first  $\sim 1$  s, the density in the burning region stays high. Unlike in usual pure deflagrations, a large amount of matter is burned completely; therefore, the kinetic energy is extremely high for a pure deflagration. This trend is most pronounced in model Cc3\_Ocore, in which  $E_{\text{kin}} = 1.00 \times 10^{51}$  erg at the end of the simulation.

For this model, Figure 5.14 shows the spatial distribution of the electron fraction  $Y_e$  at  $t = 10$  s after ignition, when we stopped the simulation. At that time, we find an extended region in the center of the white dwarf where  $Y_e$  is very low, down to  $Y_e^{\text{min}} = 0.397$ . Compared to Figure 5.10, which shows the spatial distribution of  $Y_e$  of the standard model Cc3 at the same time and scale, the larger extension of the ejecta shows the considerably larger kinetic energy in the model with oxygen core.

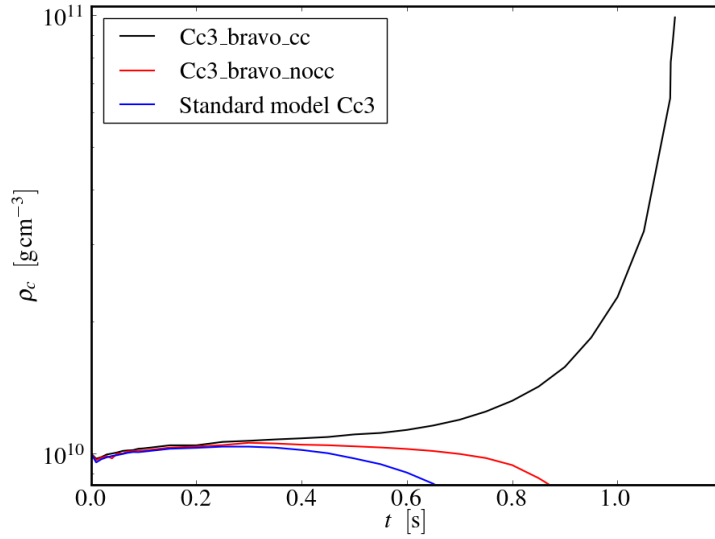
Qualitatively similar results were obtained in the models with lower initial central density, Cc3\_9e9\_Ocore and Cc3\_8e9\_Ocore. But the rise in central density is less pronounced than in the model of highest central density, Cc3\_Ocore, and the results are much more similar compared to the respective models with homogeneous chemical composition. This applies also to the nucleosynthesis yields, as discussed in Section 5.3.

To summarize the results of this section: Also a change of the chemical composition does not lead to a collapse of the white dwarf. In the models in which the carbon fraction is lower than usual the explosion becomes much more violent, and the neutronization is stronger. This leads to interesting consequences for the nucleosynthesis, as we will explore in Section 5.3. Figure 5.13 suggests that an even lower carbon fraction in the center might lead to a collapse, because the difference between the red line ( $X(C)_{\text{core}} = 0.25$ ) and the green line ( $X(C)_{\text{core}} = 0.2$ ) is dramatic at  $t \sim 1.3$  s. But our numerical methods are not suited to model such a case to satisfying accuracy. However, we do not consider a central carbon fraction below  $\sim 0.2$  as a realistic scenario because up-to-date stellar evolution theory does not provide according models (e.g. Siess, 2008).

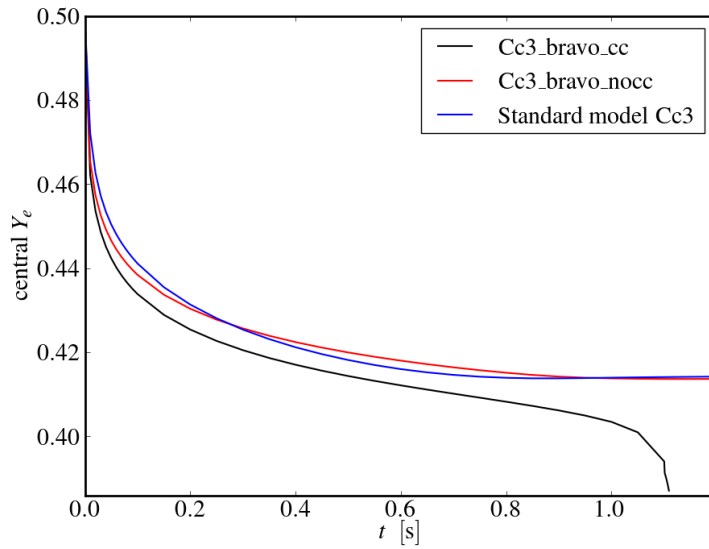
### 5.2.7. Comparison with calculations of Bravo and García-Senz (1999)

In this section we compare the results of our simulations of deflagrations in high-density C+O white dwarfs with calculations done by Bravo and García-Senz (1999) – the most recent corresponding work we are aware of. They included Coulomb corrections in their equation of state for NSE matter and found rather low critical densities of  $\rho_{\text{crit}}^{\text{CC}} \approx 5.5 \times 10^9 \text{ g cm}^{-3}$  in their simulations in which Coulomb corrections were included, and  $\rho_{\text{crit}}^{\text{noCC}} \approx 8.5 \times 10^9 \text{ g cm}^{-3}$  in the same simulations without Coulomb corrections, as was mentioned in Section 5.1.2.

We note that Seitenzahl et al. (2009) as well included Coulomb corrections in the NSE matter EoS into their neutronization rates, which we use in our simulations. The main difference is that the neutronization rates of Seitenzahl et al. (2009) are based on the newer weak interaction rates by Langanke and Martínez-Pinedo (2000, 2001), whereas the rates of Bravo and García-Senz (1999) are based on those of Fuller et al. (1985). We discussed this subject in detail in Section 3.3.1.



(a)



(b)

**Figure 5.15.:** Evolution of (a) central density  $\rho_c$  and (b) central electron fraction  $Y_e$  for two models in which the description of the neutronization rate and burning velocity given by Bravo and García-Senz (1999) was applied, with and without Coulomb corrections, respectively; in comparison with our standard model Cc3 (cf. Table 5.2).

## 5. Deflagrations in high-density carbon-oxygen white dwarfs

---

Although the input data that Bravo and García-Senz (1999) used, in particular the neutronization rates and burning velocities, are not entirely available to us, we can apply the following fitting formulae that they give in their work. For the case without Coulomb corrections they obtained a neutronization rate of

$$\dot{Y}_e^{\text{noCC}} = -0.27 \left( \frac{\rho}{10^9 \text{ g cm}^{-3}} \right)^{1.90} \left( \frac{Y_e}{0.5} \right)^{39.9}; \quad (5.2)$$

including Coulomb corrections resulted in

$$\dot{Y}_e^{\text{CC}} = -0.29 \left( \frac{\rho}{10^9 \text{ g cm}^{-3}} \right)^{1.95} \left( \frac{Y_e}{0.5} \right)^{38.1}. \quad (5.3)$$

In this case also the laminar burning velocity changes to

$$v_{\text{lam}}^{\text{CC}} = \left( 0.894 - 0.0316 \ln \left( \frac{\rho}{10^9 \text{ g cm}^{-3}} \right) \right) v_{\text{TW92}}, \quad (5.4)$$

where  $v_{\text{TW92}}$  is the burning velocity according to Timmes and Woosley (1992), as used in most of the other simulations in this work (cf. Section 3.1.4). According to Bravo and García-Senz (1999), equations (5.2) and (5.3) are valid for  $\rho \sim 10^9 \text{ g cm}^{-3}$  and in the range  $0.45 \leq Y_e \leq 0.5$ , whereas equation (5.4) is valid in the range  $5 \times 10^7 \leq \rho \leq 10^{10} \text{ g cm}^{-3}$ . To avoid any misunderstandings: Bravo and García-Senz (1999) did not apply those fitting formulae in their simulations, but the original data on which the fits are based.

We conducted two simulations using their formulae, one with and one without Coulomb corrections. The first is model Cc3.bravo.nocc (cf. Table 5.2) with unchanged burning velocity and neutronization rate  $\dot{Y}_e^{\text{noCC}}$  from equation (5.2). In the second model, Cc3.bravo.cc, we apply  $\dot{Y}_e^{\text{CC}}$  according to equation (5.3) and  $v_{\text{lam}}^{\text{CC}}$  according to equation (5.4).

For various reasons these calculations can only be considered as a numerical experiment and the results have to be taken with great caution. We use the formulae beyond the ranges where Bravo and García-Senz (1999) considered them valid because we have no other information about their input data. Furthermore, we do not have according neutrino energy loss rates available. Therefore we estimate them by scaling the neutrino energy loss rates from Seitenzahl et al. (2009) with the ratio of the  $\dot{Y}_e$ -rates of Seitenzahl et al. (2009) and the ones given in the above formulae. Despite these caveats we regard the following comparison insightful.

Figure 5.15 (a) shows the central density evolution for the two models described above, compared to our standard model Cc3. Figure 5.15 (b) shows the evolution of the central electron fraction for the same models. In our simulation of model Cc3.bravo.nocc, no collapse of the white dwarf occurs. It is visible that applying equation (5.2) instead of our tabulated rates leads to a similar result compared to our standard case, both in the evolution of the central density and the evolution of the central  $Y_e$ . In a corresponding model with the same initial central density of the white dwarf, Bravo and García-Senz (1999) saw a collapse, both in models with and without Coulomb corrections.

The reasons for this differing behavior are not entirely clear to us. One likely factor could be that the parametrization according to equation (5.2) underestimates the neutronization rate at low electron fractions or high densities and thus prevents a collapse in our simulations. Another explanation might be found in the differences of the numerical codes – we employ an Eulerian grid code, whereas Bravo and García-Senz (1999) applied a Lagrangian SPH code. But it remains unclear if and how these differences influence the results. Maybe additional reasons are rooted in some other dissimilarity of the numerical methods; further work is required to gain more insight into this issue.

The simulation of our second model, Cc3\_bravo\_cc, resulted in a different outcome: As shown in Figure 5.15 (a), applying equations (5.3) and (5.4) leads to a collapse of the white dwarf after  $\sim 1$  s. For numerical reasons the simulation was stopped when  $\rho_c$  reached  $\sim 1 \times 10^{11} \text{ g cm}^{-3}$ , but at that point a collapse is inevitable. Since the reduction of the burning velocity by 10 to 20% due to equation (5.4) has no dramatic effect on the central density evolution, as we found out in Section 5.2.5, the main reason for the collapse has to be the faster neutronization rate due to equation (5.3). The more rapid decrease of  $Y_e$  compared to our standard model Cc3 can be seen clearly in Figure 5.15 (b).

Even with the above mentioned caveats in mind, this result is very important in the sense that it shows that the fact that the white dwarf does not collapse in our previous simulations is not a shortcoming of our numerical methods. Otherwise one would be inclined to think that some obscure numerical reason would generally prevent a collapse of the white dwarf when our numerical methods are applied.

### 5.2.8. General relativistic corrections

Although the densities in the interior of the white dwarfs that we consider in this work,  $\rho \leq 1 \times 10^{10} \text{ g cm}^{-3}$ , are extremely high for white dwarfs (a typical isolated C+O white dwarf of  $M = 0.65 M_\odot$  has  $\rho_c = 4 \times 10^6 \text{ g cm}^{-3}$ ), they are still a factor of  $\sim 10^5$  lower than the densities in the core of neutron stars. The compactness,  $GM/Rc^2$ , is a good indicator of the magnitude of relativistic effects. High-density white dwarfs and neutron stars have a compactness of  $GM/Rc^2 \sim 10^{-3}$  and  $GM/Rc^2 \sim 10^{-1}$ , respectively. Therefore, we estimate that the relativistic effects in neutron stars contribute at a 10%-level, whereas in white dwarfs we expect the corrections to be of the order  $\sim 10^{-3}$ . To confirm this, we applied the effective relativistic gravitational potential based on the Tolman-Oppenheimer-Volkov equations that we implemented for our neutron star simulations (introduced in Section 3.2.3) to our high-density white dwarf simulations and tested the strength of the relativistic corrections on the gravitational potential. We found that in our most compact model (Cc3) these corrections are at most  $\sim 4 \times 10^{-3}$ . We thus consider the influence of such a correction on the dynamics of one individual model – in contrast to the series of hydrostatic configurations presented in Section 2.2.3 – negligible, and prefer a purely Newtonian potential which is consistent with the Newtonian dynamics. By this decision we also avoid the numerical difficulties that likely arise with the coupling of the Newtonian dynamics to the relativistic potential, such as those

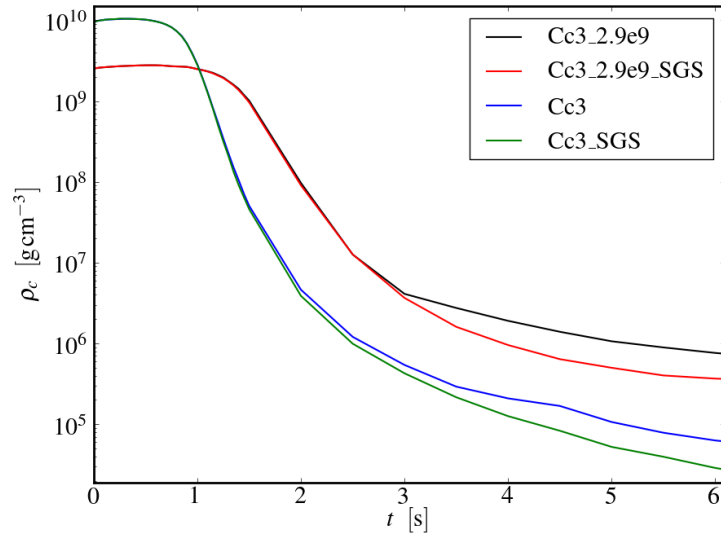


**Figure 5.16.:** Evolution of central density  $\rho_c$  for models Cc3 and Cc3\_2.9e9 with and without SGS model, respectively.

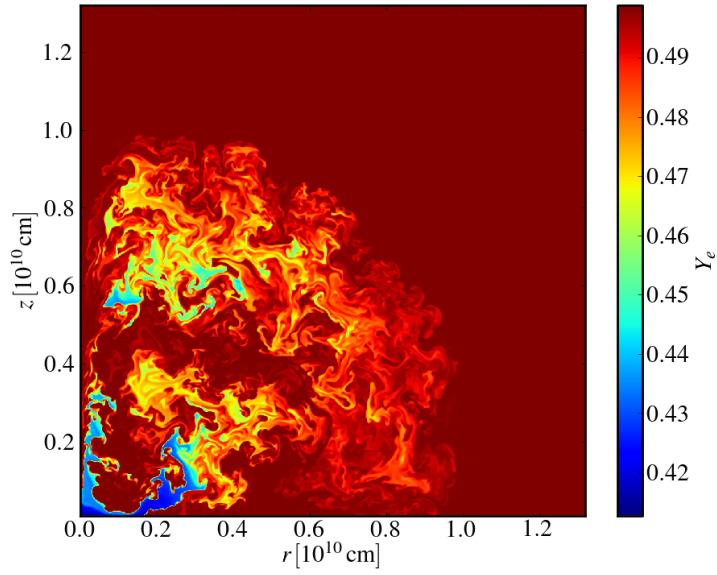
that we encounter in our neutron star simulations, discussed in Section 3.2.4.

### 5.2.9. Subgrid scale turbulence model

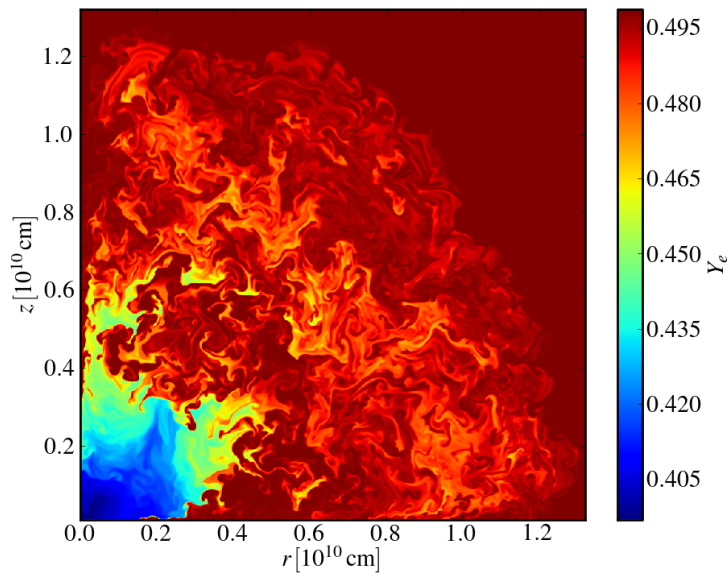
As a last parameter, we investigate the influence of turbulent burning on the dynamical behavior of deflagrations in high-density C+O white dwarfs. To this end we consider several models with different initial central densities. In each case we conduct one run with our subgrid scale (SGS) turbulence model (introduced in Section 3.1.6) switched on and compare the respective results to the simulations that we discussed above, in which we applied only laminar burning velocities. The initial conditions and all other parameters are kept constant (see Table 5.2).

To be clear we note that the models in the previous sections were calculated without SGS model in order to test the extreme case of purely laminar burning, in which the probability of a gravitational collapse is the highest.

Results from the models with highest and lowest central density (models Cc3 and Cc3\_2.9e9) are presented in Figure 5.16 in terms of the evolution of the central density. The plot shows that the application of the SGS model has only very minor consequences for the dynamics in the center of the star in those particular configurations. Only in the late phases, after  $\sim 1.5$  s, the faster decline of the central density in the models including the subgrid scale model shows the higher burning velocities due to turbulence that is taken account of in the SGS model. The minimum value of the electron fraction,  $Y_e^{\min}$ , differs between the two models with the highest



(a)



(b)

**Figure 5.17.:** Spatial distribution of electron fraction  $Y_e$  (color-coded) at  $t = 10$  s: (a) model Cc3\_SGS, (b) model Cc3\_Ocore\_SGS, cf. Table 5.2.

central density by only  $4 \times 10^{-6}$ , although  $\beta$ -equilibrium is reached only at a considerably lower value of  $Y_e$  (cf. Figure 3.2). Also the difference in the amount of energy emitted by neutrinos (cf. Section 5.2.10) between models Cc3 and Cc3\_SGS is very small. That shows that deflagrations in white dwarfs with very high central densities, ignited in the way described in Sections 5.2.1 and 5.2.2, stay in a laminar regime for a long time, a result that could be expected because also  $\lambda_{\min}$  is larger than the perturbations of the flame for a long time (see Section 5.2.2). However, in the later phases of the explosion and in the regions relatively far from the center, turbulent motion becomes important. In those regions, the inclusion of the SGS model enhances the burning velocity significantly and has a noticeable influence on the amount of matter that is burned and thus on the total released nuclear energy. The largest effect is seen in the increase in kinetic energy of the expanding ejecta: At the end of the simulation, the kinetic energy in model Cc3\_SGS is about 37% higher than in the case without SGS model.

If the initial central density is lower, this effect will become more pronounced. In the models Cc3\_2.9e9 and Cc3\_2.9e9\_SGS that have the standard initial central density for Chandrasekhar-mass thermonuclear supernovae models,  $\rho_c^{\text{ini}} = 2.9 \times 10^9 \text{ g cm}^{-3}$ , the amount of kinetic energy more than doubles when the SGS model is switched on. But also in this case, the evolution of the central density, central electron fraction, and the minimum value of  $Y_e$  is hardly affected by the inclusion of the SGS model ( $Y_e^{\min}$  differs by 0.1%). It has, however, a large influence on the nucleosynthesis yields that will be discussed in Section 5.3. Therefore, all cited abundances of synthesized nuclides usually originate from simulations that we re-calculated including the SGS model, because we consider this the more realistic way to model a deflagration. Some of the main quantitative results of important models that we presented in Sections 5.2.3–5.2.6 and re-calculated using the SGS model can be found in Table 5.4.

Figures 5.17 (a) and (b) show the spatial distribution of the electron fraction of models Cc3\_SGS and Cc3\_Ocore\_SGS, respectively, at the time when we stop the simulation ( $t = 10\text{s}$ ). Hence, Figure 5.17 (a) corresponds exactly to Figure 5.10, while Figure 5.17 (b) corresponds to Figure 5.14 – the only difference is the application of the SGS model in the calculations that are shown in Figures 5.17 (a) and (b). When we compare the corresponding pairs of figures, we see that the ejecta in the models including the SGS model are more extended, indicating the larger kinetic energy, and that generally more matter is burned in those models. However, the structure of the low- $Y_e$  matter in the center looks very similar in both variants.

### 5.2.10. Energy loss due to neutrinos

After having investigated the influence of various numerical and physical parameters in the preceding sections, we will now present our results concerning the energy emitted by neutrinos, and discuss its relevance. This subject is nonstandard regarding the research of thermonuclear supernovae, because neutrinos do not play an important role during the nuclear burning in white dwarfs of standard central densities. However, in deflagrations in high-density white

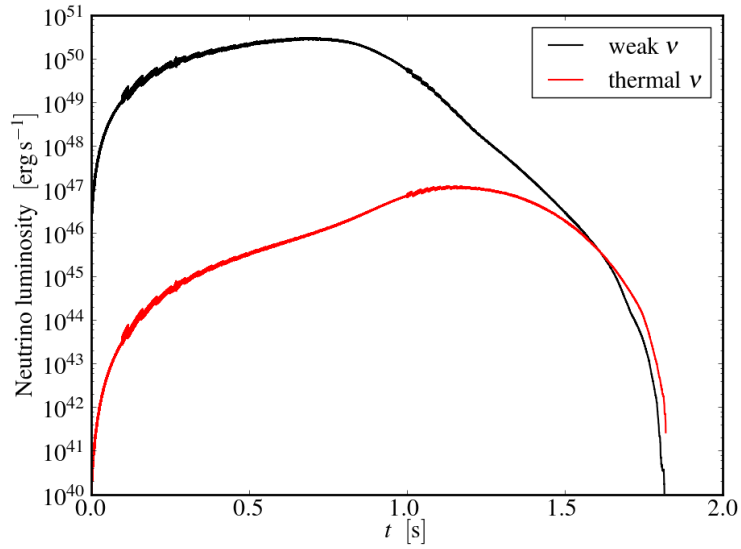


**Figure 5.18.:** Neutrino luminosity as a function of time, originating from weak and thermal neutrinos, respectively (model Cc3, cf. Table 5.2).

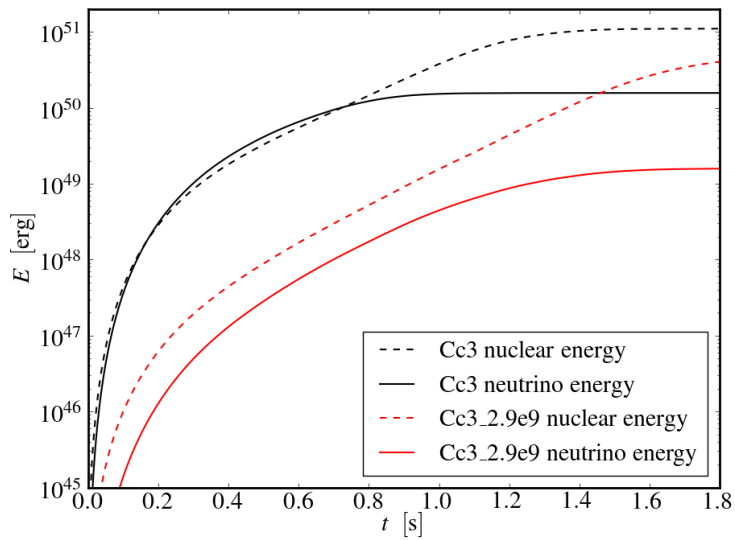


**Figure 5.19.:** Temporal evolution of the total energy carried away by neutrinos compared to the released nuclear energy (models Cc3 and Cc3.2.9e9, cf. Table 5.2).

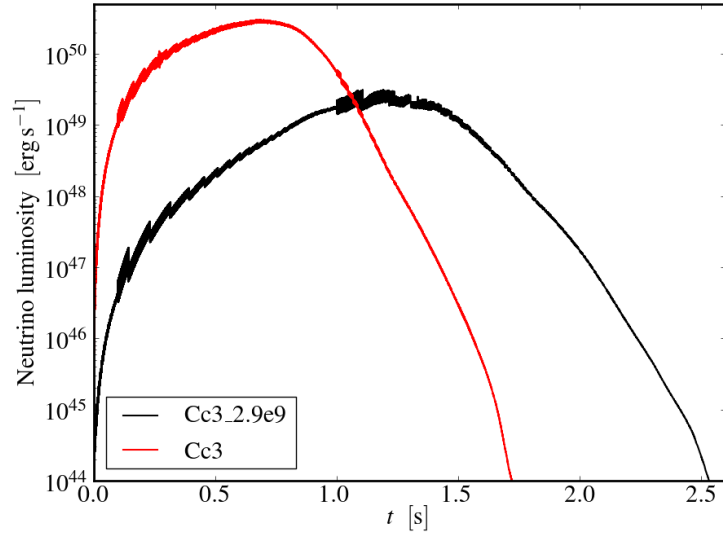


**Figure 5.20.:** Weak neutrino luminosity as a function of time (models Cc3 and Cc3\_2.9e9, respectively, cf. Table 5.2).

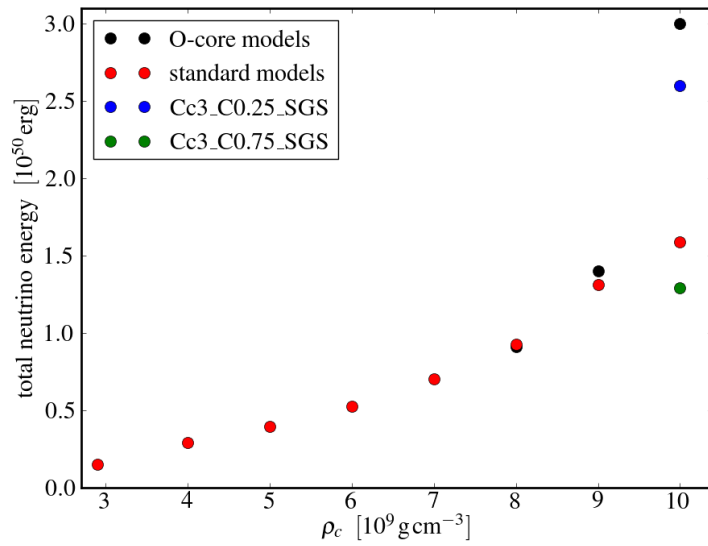


**Figure 5.21.:** Total neutrino energy as a function of central density for different models, see text and Table 5.2 for details.

dwarfs the situation is different, as we will see. The theoretical background relevant to the following was explained in Section 2.7; in Section 3.3.2 we presented our numerical methods to calculate the neutrino energy loss.

In those sections we explained that we discriminate between neutrinos originating from nuclear reactions involving the weak interaction (*weak neutrinos*) and those generated by thermal plasma processes (*thermal neutrinos*). In Figure 5.18 the neutrino luminosity originating from those two sources is compared with the help of the results of our standard model Cc3 (cf. Table 5.2). As visible from the figure, in the crucial phases of the explosion the luminosity from thermal neutrinos<sup>4</sup> is many orders of magnitude lower than the luminosity due to weak neutrinos and therefore their impact on the dynamical behavior of the system is negligible. Only  $\sim 1.5$  s after ignition the two contributions become comparable, but at a low level. In model Cc3, the total amount of energy carried away by weak neutrinos is  $1.5 \times 10^{50}$  erg, and  $5.3 \times 10^{46}$  erg is emitted in thermal neutrinos. The maximum luminosities are  $3.0 \times 10^{50}$  erg s<sup>-1</sup> in weak and  $1.2 \times 10^{47}$  erg s<sup>-1</sup> in thermal neutrinos, at  $t = 0.7$  s and  $t = 1.2$  s, respectively.

Figure 5.20 shows the luminosity from weak neutrinos as a function of time, a comparison of the results from our standard model Cc3 and the model with the central density common in Chandrasekhar-mass scenarios (model Cc3\_2.9e9, cf. Table 5.2) is made. The two curves feature significant differences: In the low-density model, the peak luminosity is lower by about one order of magnitude, whereas the maximum is shifted towards later times by about 0.5 s. The neutrino burst has a total duration of  $\sim 2.5$  s, compared to  $\sim 1.7$  s in the high-density case. The total amount of energy released in weak neutrinos in model Cc3\_2.9e9 is  $\sim 1.6 \times 10^{49}$  erg, again about an order of magnitude less than the result from model Cc3. These differences originate from the strong density dependence of the neutronization reactions, which are the main source of the neutrinos.

We compare in Figure 5.19 the amount of energy carried away by neutrinos to the energy released by nuclear burning; both values were integrated since  $t = 0$ . During the first  $\sim 0.7$  s of the simulation of our standard model Cc3, the neutrino energy has the same order of magnitude as the nuclear energy. Around  $t \sim 0.55$  s the energy lost by neutrinos is even about 20% higher than the energy gained by nuclear energy production. This shows that the neutrino energy loss is indeed dynamically important for simulations of deflagrations in high-density white dwarfs – the omission of the neutrino energies would lead to substantially wrong results. After  $t \sim 0.7$  s the neutrino luminosity drops dramatically due to the rapid density decrease, while the nuclear reactions continue for about another second. Therefore, when the neutrino emission processes as well as the nuclear reactions have ceased at  $t \sim 2$  s, the released nuclear energy exceeds the energy lost by neutrinos by a factor of  $\sim 7$ .

The results of model Cc3\_2.9e9, however, are quite different: Here the neutrino energy

<sup>4</sup>The code from Timmes, F. X. (2011) allows us to calculate the energy loss from five different thermal neutrino-creating processes separately (cf. Section 3.3.2). Due to the unimportance compared to the energy loss from weak neutrinos we refrain from a detailed discussion of the particular contributions but refer to Itoh et al. (1996) and Odrzywolek and Plewa (2011).

loss is always at least a factor of a few lower than the energy produced in nuclear reactions, see Figure 5.19 (red lines); at  $t = 10$  s the difference amounts to more than a factor of 30. Therefore, the neutrino energy loss is arguably negligible in models in which the initial central density of the white dwarf is  $2.9 \times 10^9 \text{ g cm}^{-3}$  or lower.

The total energy emitted by neutrinos as a function of initial central density is displayed in Figure 5.21. All results in this figure are taken from simulations in which we included the subgrid scale turbulence model for a more realistic modeling of the deflagrations, especially of those in which the initial central density is low. In addition to our standard models (Cc3\_2.9e9\_SGS, Cc3\_4e9\_SGS, . . . , Cc3\_9e9\_SGS, Cc3\_SGS; cf. Table 5.2) we also plot the results of our simulations in which the chemical composition of the white dwarf was altered: the models that have an oxygen core (models Cc3\_8e9\_Ocore\_SGS, Cc3\_9e9\_Ocore\_SGS, and Cc3\_Ocore\_SGS) as well as two of the models with globally altered carbon fraction (models Cc3\_C0.25\_SGS and Cc3\_C0.75\_SGS), see Section 5.2.6 and Table 5.2 for details.

It is clearly visible in Figure 5.21 that the total neutrino energy loss rises with increasing central density. This trend holds for the oxygen core models as well. The differences between the models with and without oxygen core are only pronounced at the highest central densities; at  $\rho_c^{\text{ini}} = 8 \times 10^9 \text{ g cm}^{-3}$  the two values are hardly distinguishable. The points at  $\rho_c^{\text{ini}} = 1 \times 10^{10} \text{ g cm}^{-3}$  show clearly that the total neutrino energy loss rises strongly with decreasing carbon fraction in the core. The reason for this is mainly that the amount of energy lost to the star by neutrino emission is a strong function of density; in the simulations with lower carbon fraction the density in the center remains higher for a longer period, leading to a higher energy loss due to neutrinos.

It would be interesting to know if this neutrino signal can be detected in neutrino detectors. Kunugise and Iwamoto (2007) stated that a detection is not probable today in a detector such as *SuperKamiokande*, but maybe possible for next generation detectors. Odrzywolek and Plewa (2011) made detailed calculations to estimate the number of events for proposed and planned detectors. The results indicate that with these future detectors it will be possible to measure a neutrino signal only from very near thermonuclear supernovae at distances not higher than 1 kpc – that is essentially only the solar neighborhood, far from reaching to the galactic center.

Since we calculate just the total neutrino luminosity and neither the spectral energy distribution nor the contribution of the individual neutrino species, it is difficult for us to make any statement whether the neutrino signal generated in our models is detectable. Because the peak luminosity and the total released energy of the models with the highest initial central density are only a factor of 2 to 4 higher than in the models considered in Kunugise and Iwamoto (2007) and Odrzywolek and Plewa (2011), our conclusions concerning the detectability of the signal have to be similar to the ones made in the above mentioned publications. However, it can be stated that deflagrations in high-density white dwarfs should have the highest detection probability compared to all other proposed Type Ia supernovae scenarios, because in this case the neutronization as main contributor to the neutrino luminosity is the most advanced.

Model	$Y_e^{\min}$	$E_{\text{kin}}$ [ $10^{50}$ erg]	$E_{\text{neutrino}}$ [ $10^{50}$ erg]	$M(^{56}\text{Ni})$ [ $M_{\odot}$ ]	$M(^{12}\text{C})$ [ $M_{\odot}$ ]	$M(^{16}\text{O})$ [ $M_{\odot}$ ]
Cc3_SGS	0.413	5.5	1.6	0.28	0.29	0.33
Cc3_9e9_SGS	0.418	5.9	1.3	0.31	0.28	0.33
Cc3_8e9_SGS	0.423	4.3	0.92	0.26	0.35	0.39
Cc3_2.9e9_SGS	0.469	1.8	0.15	0.21	0.46	0.51
Cc3_Ocore_SGS	0.397	10	3.0	0.37	0.13	0.17
Cc3_Ocore_9e9_SGS	0.412	6.1	1.4	0.30	0.29	0.34
Cc3_Ocore_8e9_SGS	0.419	4.9	0.91	0.28	0.34	0.38
Cc3_C0.25_SGS	0.401	6.6	2.6	0.34	0.17	0.22

**Table 5.4.:** Overview of the results of some selected models (cf. Table 5.2): minimum electron fraction  $Y_e^{\min}$ , kinetic energy  $E_{\text{kin}}$ , neutrino energy  $E_{\text{neutrino}}$ , masses  $M$  of the isotopes  $^{56}\text{Ni}$ ,  $^{12}\text{C}$ , and  $^{16}\text{O}$ . All quantities were determined at  $t = 10\text{s}$  after ignition, the abundances are results of the nucleosynthesis calculations.

## 5.3. Nucleosynthesis

During the nuclear burning in white dwarfs a wide range of nuclides are synthesized from the initial fuel of carbon and oxygen (*nucleosynthesis*). Thermonuclear supernovae are an important site for nucleosynthesis and a main contributor of many elements heavier than lithium in our solar system. The abundances of these nuclides are important quantities that help us to constrain models of thermonuclear supernovae by comparing them to observations of light curves and spectra, and to the isotopical abundances in the solar system.

In this section we study the influence of high initial central densities on the nucleosynthesis yields in our models of deflagrations in C+O white dwarfs. At first, we will give an overview on the numerical specifications applied in our analysis; then we will discuss general nucleosynthesis results in Section 5.3.2. In Section 5.3.3 we will focus on the results regarding neutron-rich isotopes.

### 5.3.1. Numerical specifications

We apply a tracer particle method to calculate the nucleosynthesis yields. Thereby we include passive tracer particles into the fluid and record the thermodynamic history of those particles. The thermodynamic trajectories of all tracers are evaluated in detailed nucleosynthesis calculations in a post-processing step. This method is described in detail in Section 3.1.7; we apply the small modifications discussed in Section 3.3.3.

All nucleosynthesis results presented in the following sections (5.3.2 and 5.3.3) are based on models in which turbulent deflagrations were simulated by means of an application of our subgrid scale turbulence model. This method is explained in Section 3.1.6; the results of the hydrodynamic simulations of the respective models are described in Section 5.2.9 and listed

in Table 5.4.

We decided on this approach in order to get results that are as realistic as possible, in particular to be able to make valid comparisons to deflagrations in white dwarfs of lower initial central density, in which the enhancement of the burning velocity by turbulent combustion has a large effect. As briefly discussed in Section 5.2.9, also in high-density white dwarfs the amount of burnt matter is underestimated if the burning velocity increase due to turbulence is not taken into account. For example, the amount of  $^{56}\text{Ni}$  differs by  $\sim 25\%$  between models Cc3 and Cc3\_SGS.

We explained in Section 1.2 that in carbon-oxygen white dwarfs originating from progenitors of nonzero metallicity, all elements involved in the hydrogen-burning CNO-cycle end up as neon ( $^{22}\text{Ne}$ ) after completion of the helium burning stage. In simulations, adding a small amount of neon to the carbon and oxygen of the initial white dwarf matter is thus a legitimate way to take account of the metallicity of the progenitor star. The ratio of atomic number to mass number,  $Z/A$ , of  $^{22}\text{Ne}$  is

$$\frac{Z(^{22}\text{Ne})}{A(^{22}\text{Ne})} = \frac{10}{22} \approx 0.45. \quad (5.5)$$

It is commonly assumed (e.g. Nomoto et al., 1984; Travaglio et al., 2004; Maeda et al., 2010) that a neon fraction of  $X(^{22}\text{Ne}) = 0.025$  resembles the amount of CNO-cycle elements in a star of solar metallicity. If 2.5% of the mass consists of  $^{22}\text{Ne}$  and the rest consists of  $^{12}\text{C}$  and  $^{16}\text{O}$ , the total electron fraction  $Y_e$  is

$$Y_e = X(^{22}\text{Ne}) \frac{Z(^{22}\text{Ne})}{A(^{22}\text{Ne})} + X(^{12}\text{C}) \frac{Z(^{12}\text{C})}{A(^{12}\text{C})} + X(^{16}\text{O}) \frac{Z(^{16}\text{O})}{A(^{16}\text{O})} \quad (5.6)$$

$$= 0.025 \frac{10}{22} + 0.975 \cdot 0.5 \approx 0.498864. \quad (5.7)$$

We assume solar metallicity in our calculations of the nucleosynthesis results presented in the following sections, if not mentioned otherwise. Numerically, this is arranged by changing 2.5% of the initial white dwarf mass from carbon to neon before starting the post-processing. We do not change the composition in the initial setup of the hydrodynamic simulations since the influence on the dynamics would be very minor. This is a common approach that was also adopted by, for example, Iwamoto et al. (1999) and Travaglio et al. (2004).

We included in total about 20000 tracer particles into the initial white dwarf configuration (cf. Section 5.2.1). This is equivalent to  $\sim 140$  tracer particles per spatial dimension – Seitenzahl et al. (2010) asserted that this amount of tracer particles is sufficient to reach a satisfactory degree of convergence for all nuclides of major abundance. The tracer particles have variable masses to assure an optimum spatial resolution and are distributed according to the procedure introduced by Seitenzahl et al. (2010).

All nucleosynthesis yields presented in the following are calculated at  $t = 10\text{s}$  after ignition, the moment when we stopped our hydrodynamic simulations. At this time nuclear burning

has already ceased for several seconds and the only ongoing nuclear reactions are radioactive decays. Therefore no further significant changes in the abundances occur, as we verified exemplary for one model for which we did not stop the hydrodynamic simulation before  $t = 100$ s. Subsequently we compared the respective nucleosynthesis yields determined at  $t = 10$ s and  $t = 100$ s and found no significant differences.

As described in Section 3.3.3, the nuclear reaction network in our post-processing code consists of 458 nuclides from protons and neutrons up to  $^{98}\text{Zr}$ ; similar to the *alternate n-rich network* employed by Woosley (1997).

### 5.3.2. General results

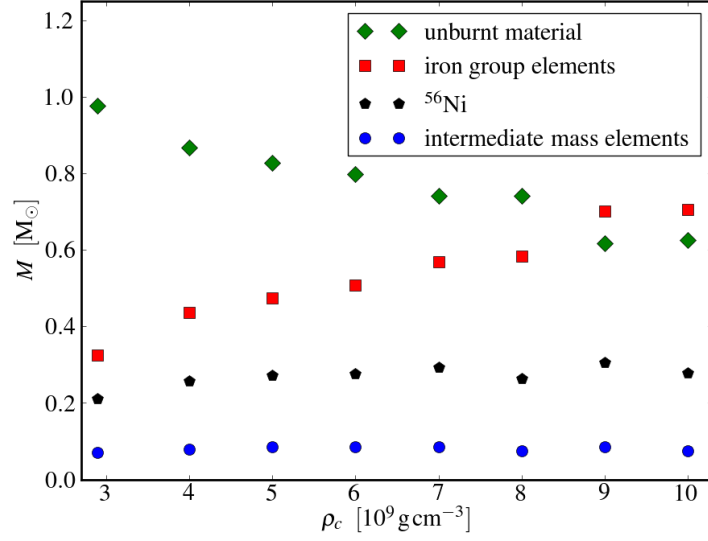
In this section we concentrate on the main nucleosynthesis yields of thermonuclear supernovae, including:

- **$^{56}\text{Ni}$ :** The lightcurve of supernovae is powered by the gamma rays originating from the decay of  $^{56}\text{Ni}$  to  $^{56}\text{Co}$ ; the amount of this abundant radioactive isotope with a lifetime of 6 days thus controls the brightness of a supernova (cf. Section 1.3.2).
- **Iron group elements (IGEs):** All elements from chromium to nickel. The more IGEs are produced for a given white dwarf mass, the more fuel was burned completely and hence the higher is the total kinetic energy.
- **Intermediate mass elements (IMEs):** The high abundance of elements from silicon to calcium is a characteristic property of Type Ia supernovae; the IMEs yields of the nucleosynthesis calculations are therefore important to constrain a particular explosion model by comparing it to observations.
- **Unburnt material:** The amount of carbon and oxygen that was not burned during the explosion.

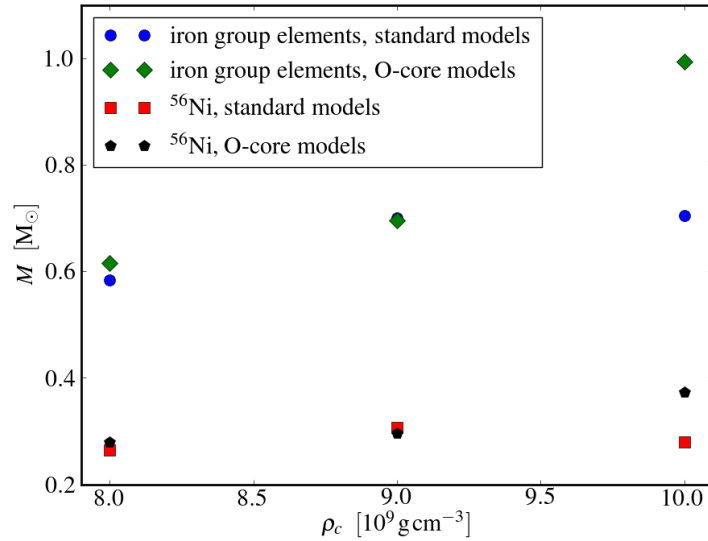
We show in Figure 5.22 (a) the dependence of the above mentioned main nucleosynthesis products on the initial central density of the white dwarf. We display the results of our standard models Cc3\_2.9e9\_SGS, Cc3\_4e9\_SGS, . . . , Cc3\_9e9\_SGS, and Cc3\_SGS (cf. Table 5.2).

In the case of delayed-detonation models, Seitenzahl et al. (2011) observed that for the same initial configuration the amount of IGEs rises with central density, but the yield of  $^{56}\text{Ni}$  stays approximately constant due to the enhanced neutronization at larger densities. As visible in Figure 5.22 (a), our results show a similar behavior<sup>5</sup>. A rise in central density leads to an increase in produced IGEs; the yields range from  $0.32M_{\odot}$  in the model of lowest initial central density (Cc3\_2.9e9\_SGS) to  $0.70M_{\odot}$  in the highest-density case (model Cc3\_SGS).

<sup>5</sup>Although our simulations, being pure deflagrations, follow a different explosion mechanism than the delayed-detonation models of Seitenzahl et al. (2011), a comparison of the results is valid to some extent because both mechanisms feature an initial deflagration phase. Nevertheless, we have to keep in mind the fact that the models differ substantially.



(a)



(b)

**Figure 5.22.:** (a) Produced  $^{56}\text{Ni}$  and total mass of iron group elements, intermediate mass elements, and unburnt material, as a function of initial central density (models Cc3\_SGS, Cc3.9e9\_SGS, Cc3.8e9\_SGS, Cc3.7e9\_SGS, Cc3.6e9\_SGS, Cc3.5e9\_SGS, Cc3.4e9\_SGS, Cc3.2.9e9\_SGS, cf. Table 5.2). (b) Produced  $^{56}\text{Ni}$  and total mass of iron group elements as a function of initial central density, for models with and without initial partial spatial separation of carbon and oxygen (standard models: Cc3\_SGS, Cc3.9e9\_SGS, Cc3.8e9\_SGS; O-core models: Cc3\_Ocore\_SGS, Cc3\_Ocore.9e9\_SGS, Cc3\_Ocore.8e9\_SGS, cf. Table 5.2).

The amount of synthesized  $^{56}\text{Ni}$ , however, increases only slightly at intermediate initial central densities and stays almost constant at higher initial central densities, though some scattering around the mean value of  $\sim 0.27 M_{\odot}$  occurs.

Also no clear trend can be seen in the absolute value of the IMEs yields; about 0.07 to  $0.08 M_{\odot}$  are produced. But compared to the total burnt material the amount of IMEs decreases with increasing initial central density: The ratio  $M_{\text{IGE}}/M_{\text{IME}}$  is  $\sim 4.6$  in the lowest-density case and  $\sim 9.3$  in the highest-density case. Naturally, the inverse relation holds for the unburnt matter; the range of unconsumed fuel stretches from  $0.98 M_{\odot}$  in model Cc3\_2.9\_SGS to  $0.61 M_{\odot}$  in model Cc3\_SGS.

In Figure 5.22 (b) we compare nucleosynthesis results from simulations of models with partial spatial separation of carbon and oxygen (*O-core models*: Cc3\_Ocore\_SGS, Cc3\_Ocore\_9e9\_SGS, and Cc3\_Ocore\_8e9\_SGS, cf. Section 5.2.6 and Table 5.2) to our models with standard chemical composition. Figure 5.22 (b) shows that the differences in the yields of  $^{56}\text{Ni}$  and IGEs are very small in the two cases with  $\rho_c^{\text{ini}} = 8 \times 10^9 \text{ g cm}^{-3}$  and  $\rho_c^{\text{ini}} = 9 \times 10^9 \text{ g cm}^{-3}$ . Only in the models with the highest densities,  $\rho_c^{\text{ini}} = 1.0 \times 10^{10} \text{ g cm}^{-3}$ , the differences are more pronounced. Here, 30 to 40% more  $^{56}\text{Ni}$  and IGEs are produced in the O-core model. We observe the same behavior regarding the neutron-rich isotopes, as we will discuss in the next section.

The main results of this section can be explained by the scenario already discussed in Sections 5.2.3 and 5.2.6: In the models with high initial central densities, the deflagration is initially very slow and the white dwarf expands very little, which leads to complete burning of large amounts of fuel into IGEs. Also the density of the burnt matter is high for a long time, resulting in strong neutronization and hence comparatively low  $^{56}\text{Ni}$  yields. This effect is enhanced if the carbon fraction in the center is decreased, which decelerates the burning further. At lower central densities, the white dwarf expands faster, and the amount of IMEs and  $^{56}\text{Ni}$  is proportionally larger.

### 5.3.3. Neutron-rich isotopes

Our simulations of deflagrations in high-density C+O white dwarfs show a large degree of neutronization in the central regions; therefore, we are especially interested in the abundances of neutron-rich isotopes, in particular  $^{48}\text{Ca}$ ,  $^{50}\text{Ti}$ , and  $^{54}\text{Cr}$ .

$^{48}\text{Ca}$  has the largest neutron excess of those three nuclides. It is doubly magic with closed neutron (28) and proton (20) shells, corresponding to  $Z(^{48}\text{Ca})/A(^{48}\text{Ca}) \approx 0.417$ . This value shows that the formation of  $^{48}\text{Ca}$  requires an environment in which the electron fraction is lower than in standard models of thermonuclear supernovae. Its solar abundance is extraordinarily high for a low-mass neutron-rich isotope.  $^{48}\text{Ca}$  decays in a double  $\beta$ -decay to  $^{48}\text{Ti}$ , but its lifetime is extremely long,  $\sim 4 \times 10^{19}$  years (Balysh et al., 1996). The origin of  $^{48}\text{Ca}$  is still enigmatic. Until now, the only known site where the conditions may be right to synthesize  $^{48}\text{Ca}$  are thermonuclear supernovae (Meyer et al., 1996a; Woosley, 1997; Woosley et al., 1995; Meyer et al., 1996b).

## 5. Deflagrations in high-density carbon-oxygen white dwarfs

Model	$\alpha$ ( $^{48}\text{Ca}$ )	$\alpha$ ( $^{50}\text{Ti}$ )	$\alpha$ ( $^{54}\text{Cr}$ )
Cc3_SGS	115	221	202
Cc3_9e9_SGS	60	170	164
Cc3_8e9_SGS	29	139	141
Cc3_7e9_SGS	8.7	83	98
Cc3_6e9_SGS	2.4	52	71
Cc3_5e9_SGS	0.11	20	41
Cc3_4e9_SGS	$2.6 \times 10^{-3}$	7.2	20
Cc3_2.9e9_SGS	$2.5 \times 10^{-6}$	1.2	5.0
Cc3_Ocore_SGS	277	257	230
Cc3_Ocore_9e9_SGS	88	167	157
Cc3_Ocore_8e9_SGS	30	111	120
Cc3_C0.25_SGS	249	251	229

**Table 5.5.:** Overview of the synthesized neutron-rich nuclides resulting from some selected models (cf. Table 5.2): production factors  $\alpha$  of  $^{48}\text{Ca}$ ,  $^{50}\text{Ti}$ , and  $^{54}\text{Cr}$ .

The only alternative production site discussed in the literature are the ejecta of core-collapse supernovae; in the vicinity of the protoneutron star the values of  $Y_e$  are in the right range (Woosley, 1997). However, this material has a high entropy, which leads to a destruction of the newly formed  $^{48}\text{Ca}$  before all nuclear reactions cease, as was discussed in detail by Meyer et al. (1996a). Their reasoning can be summarized as follows: While having similar temperatures of  $\sim 10^{10}$  K, the density of the ejecta of thermonuclear supernovae is much higher than the density of the wind-like ejecta of core-collapse supernovae; therefore, the entropy is low in the former and high in the latter case. In both cases, the abundance of  $^{48}\text{Ca}$  differs considerably from the abundances resulting from NSE-calculations. In the high-entropy case, a high amount of  $^{48}\text{Ca}$  is produced initially. But at the time when the triple-alpha reactions freeze out due to the temperature decrease in the expanding matter, a high abundance of alpha particles remains in the ejecta (*alpha-rich freezeout*). The result of this freezeout is a termination of the production of heavier nuclei from alpha particles and nucleons. Subsequently, the initially high abundance of  $^{48}\text{Ca}$  is reduced dramatically because the equilibrium with respect to the exchange of alpha particles (*quasi-equilibrium, QSE*) shifts towards more massive nuclei as a consequence of the high abundance of alpha particles. In the words of Meyer et al. (1996a), “one must envision [this process] as a broad abundance peak shifting to another, heavier, broad abundance peak containing the same number of nuclei.”

Because of the higher density in the low-entropy case, the abundance of alpha particles is much lower at freezeout. Contrary to matter in NSE, where the abundance of  $^{48}\text{Ca}$  would eventually drop at low temperatures, the low-entropy matter in QSE remains having a high abundance of  $^{48}\text{Ca}$ . According to this line of argument,  $^{48}\text{Ca}$  can only be produced abundantly in low-entropy matter, which can be found in the expanding ejecta of thermonuclear

supernovae.

Kratz et al. (2001) obtained somewhat different results than Meyer et al. (1996a), but they also stated that the  $^{48}\text{Ca}$  yields from core-collapse supernovae cannot explain the high solar abundance.

In the 1980s, another possibility to form  $^{48}\text{Ca}$  was discussed: the *neutron capture/ $\beta$ -decay ( $n\beta$ )-process* (Sandler et al., 1982; Kratz et al., 1987), in which the effectivity of the neutron captures and the  $\beta$ -decays are of the same size – in contrast to the *r*-process, in which the neutron captures dominate, and the *s*-process, in which the  $\beta$ -decays are more effective. The *n $\beta$* -process would allow for the production of  $^{48}\text{Ca}$  in core-collapse supernovae. But subsequent laboratory experiments could not confirm the existence of this process; see the review by Kratz et al. (2001) for details.

As mentioned above, we are further interested in the neutron-rich isotopes  $^{50}\text{Ti}$  and  $^{54}\text{Cr}$ . Their solar abundances are also quite large; but unlike  $^{48}\text{Ca}$ , these isotopes can certainly be produced in sites apart from thermonuclear supernovae. Both can be synthesized in core-collapse supernovae, whereas  $^{50}\text{Ti}$  can also be produced in massive stars (Meyer et al., 1995). The  $Y_e$  required for the formation of  $^{50}\text{Ti}$  and  $^{54}\text{Cr}$  is  $\sim 0.44$ , since  $Z(^{50}\text{Ti})/A(^{50}\text{Ti}) = 0.44$  and  $Z(^{54}\text{Cr})/A(^{54}\text{Cr}) \approx 0.444$ . Values close to that are more commonly seen in models of thermonuclear supernovae than the very low values required for the formation of  $^{48}\text{Ca}$ .

Comparing the results of nucleosynthesis calculations to the solar abundances is an important way to constrain models of thermonuclear supernovae. In this manner it is also possible to specify upper limits on the frequency of one particular explosion model, as we will see later. In order to compare the calculated nucleosynthesis yields to the solar abundances, it is common to determine the *production factor*  $\alpha(X)$  for each nuclide  $X$ . The production factor is defined as the ratio of the abundance of a nuclide  $X$  to the solar abundance, in either case relative to the abundance of  $^{56}\text{Fe}$ :

$$\alpha(X) = \frac{M(X)/M(^{56}\text{Fe})}{M(X)_\odot/M(^{56}\text{Fe})_\odot}. \quad (5.8)$$

We use Anders and Grevesse (1989) as a reference for the solar abundances. More recent compilations of the isotopical abundances of the sun, e.g. Lodders et al. (2009), show only minor differences in the nuclides that are of interest in this work; we use the older publication in order to be able to make valid comparisons of our results to the results obtained by Woosley (1997).

The masses of all radioactive isotopes such as  $^{56}\text{Ni}$ ,  $^{56}\text{Co}$ ,  $^{56}\text{Mn}$  that will decay eventually into stable iron ( $^{56}\text{Fe}$ ) and have not yet decayed at  $t = 10\text{s}$  were added to  $M(^{56}\text{Fe})$  before the calculation of the production factors.

The nucleosynthesis yields in terms of the production factor of  $^{48}\text{Ca}$ ,  $^{50}\text{Ti}$ , and  $^{54}\text{Cr}$  resulting from the post-processing of some selected models are presented in Table 5.5. The results of the models in which the initial chemical composition of the white dwarf was changed (O-core models and model Cc3\_C0.25\_SGS, cf. Table 5.2) might not be accurate, as discussed

in Section 5.2.6, because we conducted these tentative simulations without recalibrating the burning velocity and the abundance table for incomplete burning.

$5.8 \times 10^{-3} M_{\odot}$  of  $^{48}\text{Ca}$  is produced in our standard model Cc3\_SGS. The amount of stable iron is  $0.36 M_{\odot}$ ; the ratio of  $^{48}\text{Ca}$  to stable iron is 115 times larger than in the solar system. The production factor  $\alpha$  drops steeply with decreasing initial central density, in the lowest-density model Cc3\_2.9e9\_SGS only a tiny amount of  $^{48}\text{Ca}$  is produced:  $8.0 \times 10^{-11} M_{\odot}$ , corresponding to  $\alpha = 2.5 \times 10^{-6}$ . This confirms that the production of this isotope requires initial central densities significantly higher than those of standard Chandrasekhar-mass models.

The abundances of  $^{50}\text{Ti}$  and  $^{54}\text{Cr}$  are also strongly dependent on the initial central density. However, we observe an important difference compared to the  $^{48}\text{Ca}$ -yields: Even in the lowest-density models the abundances of  $^{50}\text{Ti}$  and  $^{54}\text{Cr}$  are above the solar value, more moderately so in the case of  $^{50}\text{Ti}$  than in the case of  $^{54}\text{Cr}$ .

Differences in the models with and without partial spatial separation of the carbon and oxygen are only pronounced in the model with the highest  $\rho_c^{\text{ini}}$  – not surprising if we look at the corresponding results concerning the neutrino energy loss (Section 5.2.10) and main nucleosynthesis products (Section 5.3.2). Model Cc3\_Ocore\_SGS produces  $0.018 M_{\odot}$  of  $^{48}\text{Ca}$ , more than three times as much than model Cc3\_SGS; the production factor is only about twice as high, because also 30% more stable iron is produced in the O-core model. The production factors resulting from model Cc3\_C0.25\_SGS are comparable to those resulting from model Cc3\_Ocore\_SGS.

Type Ia supernovae are less frequent than core-collapse supernovae, but produce a larger amount of heavy elements. It turns out that Type Ia supernovae account for roughly half of the iron and other heavy elements in the galaxy (Iwamoto et al., 1999). Therefore, an explosion model leading to a production factor that is much larger than  $\sim 2$  of any nuclide cannot explain the majority of Type Ia supernovae. In the case that such a model is indeed realized in nature, corresponding supernovae have to happen infrequently. That applies to various models featuring high initial central densities (Table 5.5).

On the other hand, only in the models in which the white dwarfs have high initial central densities the amount of produced  $^{48}\text{Ca}$  is large enough to explain the solar abundance. If the argument of Meyer et al. (1996a) and Woosley (1997) holds that only thermonuclear supernovae are able to produce enough  $^{48}\text{Ca}$ , supernovae resembling one of the high-density models have to occur in nature, because no other model of thermonuclear supernovae provides the required low electron fraction. However, since the production factors of some neutron-rich isotopes are very high in these models, they can only account for a very small fraction of all Type Ia supernovae and therefore have to be rare events: the highest-density models have to account for less than 1% of all Type Ia supernovae.

Our models that feature intermediate initial central densities ( $\rho_c^{\text{ini}} = 6$  to  $7 \times 10^9 \text{ g cm}^{-3}$ ) produce a reasonable amount of  $^{48}\text{Ca}$ , but about one order of magnitude more  $^{50}\text{Ti}$  and  $^{54}\text{Cr}$  (in terms of the production factor). The models of highest  $\rho_c^{\text{ini}}$  have more balanced ratios of  $\alpha(^{48}\text{Ca}) / \alpha(^{50}\text{Ti}) / \alpha(^{54}\text{Cr})$ , albeit higher absolute values. Cc3\_Ocore\_SGS is the only model in which  $\alpha(^{48}\text{Ca})$  is higher than  $\alpha(^{50}\text{Ti})$  and  $\alpha(^{54}\text{Cr})$ , which would be desirable

initial $^{22}\text{Ne}$	$M(^{56}\text{Ni}) [M_{\odot}]$	$\alpha(^{48}\text{Ca})$	$\alpha(^{50}\text{Ti})$	$\alpha(^{54}\text{Cr})$
0	0.30	109	209	191
2.5%	0.28	115	221	202
7.5%	0.24	130	250	229

**Table 5.6.:** Influence of changes in metallicity on the nucleosynthesis results of our standard model Cc3\_SGS. The three cases correspond to zero metallicity, solar, and three times solar metallicity, respectively.

considering the fact that  $^{50}\text{Ti}$  and  $^{54}\text{Cr}$  are also produced apart from thermonuclear supernovae (e.g. in core-collapse supernovae). From this point of view it seems to be more plausible that in nature events involving white dwarfs of very high  $\rho_c^{\text{ini}}$  occur, but at an extremely low rate, instead of explosions of white dwarfs of intermediate  $\rho_c^{\text{ini}}$  at a somewhat higher rate.

As mentioned above, we wish to compare our results to the ones obtained by Woosley (1997). The main differences originate from the fact that the minimum electron fraction  $Y_e^{\text{min}}$  in our simulations does not drop to values as low as those resulting from the computations of Woosley (1997). The reason for this is most likely due to our application of the new weak interaction data from Langanke and Martínez-Pinedo (2001) that have lower electron capture rates than the old rates from Fuller et al. (1985), as discussed in Section 3.3.1. Comparisons are thus rather difficult. Simulations of our model Cc3\_SGS, in which the initial central density of the white dwarf is highest ( $\rho_c^{\text{ini}} = 1.0 \times 10^{10} \text{ g cm}^{-3}$ ), result in  $Y_e^{\text{min}} = 0.412$ . The nearest equivalent to this model is the slow deflagration model NCD6A of Woosley (1997) that has the properties  $\rho_c^{\text{ini}} = 6.0 \times 10^9 \text{ g cm}^{-3}$  and  $Y_e^{\text{min}} = 0.414$ . In this model,  $\alpha(^{48}\text{Ca})$  is about 25% smaller than in our model Cc3\_SGS. The values of  $\alpha(^{50}\text{Ti})$  and  $\alpha(^{54}\text{Cr})$  are about half as high as in our simulations. Noticeably our study lacks models in which  $\alpha(^{48}\text{Ca})$  is much higher than  $\alpha(^{50}\text{Ti})$  and  $\alpha(^{54}\text{Cr})$ , see the preceding paragraph. In contrast, Woosley (1997) obtained according results in his models NCD7A and NCD8A that feature  $\rho_c^{\text{ini}} = 7.0 \times 10^9 \text{ g cm}^{-3}$  and  $\rho_c^{\text{ini}} = 8.0 \times 10^9 \text{ g cm}^{-3}$ , respectively. One might draw an analogy and speculate that we would obtain comparable results if we proceed to even higher  $\rho_c^{\text{ini}}$  than  $1.0 \times 10^{10} \text{ g cm}^{-3}$  due to the apparent shift in the  $\rho_c^{\text{ini}}-Y_e^{\text{min}}$  relation of our work compared to Woosley (1997).

As a final point of this nucleosynthesis study, we test the influence of a change in the initial metallicity of the white dwarf on the results of the nucleosynthesis calculations. To this end we post-process our standard model Cc3\_SGS (cf. Table 5.2) with three different initial  $^{22}\text{Ne}$  fractions – with no neon (representing zero metallicity), 2.5% neon (solar metallicity, as was adopted in all previous calculations, see Section 5.3.1), and 7.5% neon (three times solar metallicity). The results are listed in Table 5.6. Not surprisingly, an initially higher abundance of  $^{22}\text{Ne}$  that is connected to more available neutrons leads to the production of a larger amount of neutron-rich isotopes, at the expense of nuclides such as  $^{56}\text{Ni}$  that have an equal number of protons and neutrons. However, the differences in the results of the nucleosynthesis calcu-

lations that are caused by this large variation in metallicity are rather minor, the change from zero to three times solar metallicity leads to an increase in  $\alpha$  ( $^{48}\text{Ca}$ ) by 19%, while the mass of  $^{56}\text{Ni}$  drops by 20%.

## 5.4. Conclusions

We conduct two-dimensional hydrodynamic simulations of deflagrations in carbon-oxygen white dwarfs that have initial central densities considerably higher than white dwarfs in standard Chandrasekhar-mass scenarios of thermonuclear supernovae. Based on our results and assuming standard input physics, we conclude that C+O white dwarfs do not collapse to neutron stars for initial central densities up to  $\rho_c^{\text{ini}} = 1.0 \times 10^{10} \text{ g cm}^{-3}$  – the largest central density that we consider – but instead explode, forming a thermonuclear supernova.

This conclusion is contradictory to the results of previous work, in particular that of Woosley (1997) and Bravo and García-Senz (1999), who found that the critical central density, above which a deflagration leads to the collapse of C+O white dwarfs, is located in the range from  $5 \times 10^9 \text{ g cm}^{-3}$  to  $9 \times 10^9 \text{ g cm}^{-3}$ . However, our results of the simulations seem to be robust: Variations in numerical parameters such as resolution, grid geometry, and shape of the ignition kernel do not lead to a collapse or any indication thereof. As a caveat we have to state that we cannot exclude that much higher resolution might change this result, although we see no sign for such a change in behavior in our resolution study. Limits in computational resources prevent us from conducting simulations with significantly higher resolution.

We vary also several physical parameters of our simulation setup. A decrease in the laminar burning velocity  $v_{\text{lam}}$  (in purely laminar deflagrations) leads to a stronger increase in the central density, and a shift of the explosion towards a slightly later time, than in our standard case; but the white dwarf does not collapse in the range of initial central densities considered by us, even in the case in which  $v_{\text{lam}}$  is reduced to 40% of its original value. The general reason for this outcome is most likely rooted in the electron capture rates, which become very low at  $Y_e \sim 0.4$ , although  $\beta$ -equilibrium is not yet reached. Therefore, the pressure decrease in the center is too slow to prevent the white dwarf from exploding.

The picture is similar when we reduce the central carbon fraction: the central density rises a few per cent in the first second, but no collapse occurs in the explored parameter space. In contrast to the simulations in which  $v_{\text{lam}}$  is reduced, we see some indications that a further decrease in the central carbon fraction would lead to a collapse of the white dwarf. However, such simulations would be doubtful for numerical reasons and in contradiction to predictions of stellar evolution theory.

In the context of a comparison of our work to simulations conducted by Bravo and García-Senz (1999), we apply different neutronization rates by means of an analytical description. This change leads, in connection with a moderate decrease in the burning velocity, to a collapse of the white dwarf in the model in which  $\rho_c^{\text{ini}} = 1.0 \times 10^{10} \text{ g cm}^{-3}$ .

These results indicate that the application of different neutronization rates is the main cause

of our deviating results compared to earlier work; the rates applied in our work are based on Langanke and Martínez-Pinedo (2001), whereas Woosley (1997) and Bravo and García-Senz (1999) applied the older rates of Fuller et al. (1985) that are known to lead to faster neutronization. There is one caveat to this implication: When using an alternative analytical description of the neutronization rate, we again see no collapse of a white dwarf of  $\rho_c^{\text{ini}} = 1.0 \times 10^{10} \text{ g cm}^{-3}$ , contrary to the results of Bravo and García-Senz (1999). However, there are likely convincing explanations for that behavior, explicated in Section 5.2.6.

The second main difference between our study and previous work lies in the applied numerical methods. We conduct two-dimensional simulations employing a Eulerian grid code. The faster rise of inherently multi-dimensional flame instabilities might be one distinctive feature of our simulations compared to the calculations conducted by Woosley (1997) who applied a one-dimensional Lagrangian code. Less clear to us are the consequences of the differences between our code and the three-dimensional SPH code applied by Bravo and García-Senz (1999). This issue requires further investigations.

Because the high-density white dwarfs do not collapse in most of our simulations, we are able to analyze the results of their explosion, in particular the composition of the ejecta and the released nuclear energy. In models in which the white dwarf has an initial central density of  $\rho_c^{\text{ini}} = 1.0 \times 10^{10} \text{ g cm}^{-3}$ , the resulting kinetic energy of the ejecta is very high compared to deflagrations in Chandrasekhar-mass white dwarfs of standard central density. The reason for the large energy release is that because of the slow expansion of the star a comparatively large fraction of the fuel is burned at high densities into iron group elements (complete burning), releasing a large amount of nuclear energy. We show that this effect is yet enhanced when the carbon fraction in the core of the white dwarf is decreased; however, in simulations of white dwarfs of lower  $\rho_c^{\text{ini}}$  the differences between the low-carbon-fraction models and our standard models are much less pronounced.

We furthermore calculate the neutrino energy loss of deflagrations in C+O white dwarfs and find that, in the highest-density model ( $\rho_c^{\text{ini}} = 1.0 \times 10^{10} \text{ g cm}^{-3}$ ), the energy carried away by neutrinos constitutes a considerable fraction of the kinetic energy of the ejecta. In the first phases of the explosion the neutrino energy loss is comparable or even slightly higher than the energy released by nuclear reactions. Taking account of the energy emitted by neutrinos is thus important in order to achieve correct results of the dynamics of the fluid. The situation is different concerning deflagrations in low-density white dwarfs: Here the neutrino energy loss is continuously lower than the released nuclear energy, by at least a factor of a few. Consequently, neglecting the neutrino energy is justifiable if  $\rho_c^{\text{ini}} \lesssim 3.0 \times 10^9 \text{ g cm}^{-3}$ . A detection of the neutrino signal of thermonuclear supernovae by planned detectors is only possible for very close events and therefore unlikely.

To complete our analysis we present the results of detailed nucleosynthesis calculations that were obtained by post-processing the hydrodynamic simulations by means of a tracer particle method. We see that the amount of produced iron group elements increases towards higher initial central densities, as indicated above. However, the amount of synthesized  $^{56}\text{Ni}$  does not follow this trend: Due to the enhanced neutronization at higher densities, the  $^{56}\text{Ni}$ -yields

do not change significantly when the initial central density is increased. These findings are similar to the results of Seitenzahl et al. (2011).

According to our simulations of deflagrations in high-density white dwarfs, the electron fraction in the inner part of the ejecta is unusually low compared to common models of thermonuclear supernovae. Therefore we focus our attention on the results regarding the amount of synthesized neutron-rich isotopes such as  $^{48}\text{Ca}$ ,  $^{50}\text{Ti}$ , and  $^{54}\text{Cr}$ . We find that  $^{50}\text{Ti}$  and  $^{54}\text{Cr}$  are abundantly produced in all our models, which cover a range from  $\rho_c^{\text{ini}} = 2.9 \times 10^9 \text{ g cm}^{-3}$  to  $\rho_c^{\text{ini}} = 1.0 \times 10^{10} \text{ g cm}^{-3}$ , whereas  $^{48}\text{Ca}$  is practically non-existent in our low-density models but shows a high abundance in high-density models.

Meyer et al. (1996a) and Woosley (1997) argued that only in thermonuclear supernovae  $^{48}\text{Ca}$  can be produced in quantities that are large enough to explain the solar abundances. If this is true, our results show that deflagrations in high-density C+O white dwarfs have to occur in nature. However, these events have to be infrequent and hence cannot explain the majority of Type Ia supernovae, because the synthesized neutron-rich isotopes are much more abundant – normalized to stable iron – than what we measure in the solar system. In addition, we see some indications that deflagrations in very high-density white dwarfs ( $\rho_c^{\text{ini}} \sim 1.0 \times 10^{10} \text{ g cm}^{-3}$ ) might match the solar abundance pattern of neutron-rich isotopes better than deflagrations in white dwarfs with intermediate central densities ( $\rho_c^{\text{ini}} \sim 5 \text{ to } 8 \times 10^9 \text{ g cm}^{-3}$ ).

A change in initial metallicity of the white dwarfs has no dramatic effect on our nucleosynthesis results and does not alter our conclusions.

The outcome of this study is partially quite surprising and in contradiction to earlier publications; therefore, our results should be confirmed in future work. One important approach would be to apply neutronization rates based on the weak interaction rates by Fuller et al. (1985) to check our assumption that the neutronization rate is the crucial physical parameter concerning the question whether the white dwarf collapses or not.

On the numerical side, detailed comparisons between different computer codes might further elucidate the reasons for the dissenting results. Moreover, applying our code to conduct simulations with higher resolution would be desirable, in order to dispel any concerns that our results are an artifact of too low resolution; although, judging from our resolution study, we do not expect that higher resolution will change the results significantly, as mentioned above.

According to the literature, no consensus is reached regarding the maximum central density of accreting C+O white dwarfs. We hope that the conclusions from our work might trigger new investigations if and how C+O white dwarfs that have central densities as high as  $\rho_c^{\text{ini}} \sim 1.0 \times 10^{10} \text{ g cm}^{-3}$  can be formed by accretion processes in binary systems.

Concerning the nucleosynthesis of neutron-rich nuclides, it would be interesting to explore whether our models can explain unusual ratios of several neutron-rich isotopes (*Ca-Ti-Cr anomalies*; e.g. high  $\alpha(^{48}\text{Ca})/\alpha(^{46}\text{Ca})$  ratios) that are found in some meteorites, in particular the *Allende meteorite*, and are not yet explained in a satisfying way (e.g. Sandler et al., 1982; Kratz et al., 2001).

## 6. Epilogue

Under the title *hydrodynamic simulations of combustion processes at high densities in compact stars*, we combine two topics into this thesis:

In Section 4, we present three-dimensional numerical simulations of turbulent combustion converting a neutron star into a quark star. Hadronic matter, described by a micro-physical finite-temperature equation of state, is converted into strange quark matter. We assume this phase, represented by a bag-model equation of state, to be absolutely stable. Following the example of thermonuclear burning in white dwarfs leading to Type Ia supernovae, we treat the conversion process as a potentially turbulent deflagration. Solving the non-relativistic Euler equations using established numerical methods we conduct large eddy simulations including an elaborate subgrid scale turbulence model, while the propagation of the conversion front is modeled with a level-set method. Our results show that for large parts of the parameter space the conversion becomes turbulent and therefore significantly faster than in the laminar case. Despite assuming absolutely stable strange quark matter, in our hydrodynamic approximation an outer layer remains in the hadronic phase, because the conversion front stops when it reaches conditions under which the combustion is no longer exothermic. In our attempts to calculate the gravitational wave signal we encounter serious numerical difficulties. Nevertheless, we are able to conduct an order-of-magnitude estimate and conclude that the gravitational wave amplitude of a galactic event is inside of the sensitivity range of advanced LIGO, but the short duration of the signal will make a detection very challenging.

The subjects of Section 5 are high-density carbon-oxygen white dwarfs. Here we focus as well on deflagration processes: We perform two-dimensional hydrodynamic simulations of deflagrations in carbon-oxygen white dwarfs with high initial central densities, up to  $1.0 \times 10^{10} \text{ g cm}^{-3}$ , and find that these white dwarfs do not collapse in the explored parameter space if we assume standard input physics. Variations in resolution, flame velocity, and chemical composition do not change this result, whereas a considerable increase in the neutronization rates leads to a collapse of the highest-density white dwarfs. Furthermore, we calculate the neutrino energy emitted during the deflagration and see that a significant part of the released nuclear energy is carried away by neutrinos in the highest-density models. For some selected models we follow the explosion up to homologous expansion and achieve detailed nucleosynthesis results by post-processing the hydrodynamic simulations. We find that, in the highest-density models, the abundances of the produced neutron-rich isotopes such as  $^{48}\text{Ca}$ ,  $^{50}\text{Ti}$ , and  $^{54}\text{Cr}$  are significantly higher than the solar abundances; therefore, those events have to be rare. However, this confirms that  $^{48}\text{Ca}$ , an isotope of high solar abundance but obscure origin, can be produced in Type Ia supernovae – but only if high-density white dwarfs

are involved.

The physical environment, the numerical key aspects, and the objectives of the results of both parts of this thesis are very distinct at first glance; but both topics have, remarkably, a lot in common. First, the two scenarios occur in compact stars, which “just” differ in the applied equation of state of the fluid. Therefore, we can describe both kinds of compact stars by applying the same fundamental concepts, in particular similar hydrostatic initial configurations and a description of the fluid dynamics by means of the Euler equations. These considerations are presented in Section 2.

Further similarities are most notably rooted in the modeling approaches, as discussed in detail in Section 3: The Euler equations are solved using the same numerical scheme; and the concepts of combustion are implemented in the same way – the thermonuclear burning front in white dwarfs as well as the conversion front in neutron stars are described as deflagration waves, numerically presented by the zero level set. In both cases, the turbulent burning is described by a subgrid scale turbulence model. The burning starts slowly in both scenarios, the respective compact star stays in a quasi-hydrostatic state for a comparably long time. Caused by this fact, we encounter in both cases similar numerical problems, which were solved by reducing the time steps by means of a decrease in the CFL-factor.

In both cases the combustion processes occur at very high densities, between  $\sim 10^7 \text{ g cm}^{-3}$  and  $\sim 10^{15} \text{ g cm}^{-3}$ . The highest central densities in our white dwarf models are a factor of  $10^5$  lower than in our neutron star models; however, the employed densities are extreme for white dwarfs but only average for neutron stars. Anyway, except for the inaccessible black holes and shortly after the Big Bang, there is no place in the Universe that features densities as high as in the interior of compact stars.

Also common to both topics, and connected to the high densities, is the thematic connection to nuclear physics. These ties are, however, established to completely different fields of nuclear physics – the equation of state of dense matter in the first case, the synthesis of nuclei in the second case. Due to the experimental inaccessibility and the theoretically very difficult nature of matter at densities above nuclear saturation density, the first question is a fundamental one because we do not even know the basic properties of such matter, for example whether it comprises hadronic or quark matter. In contrast, the second question is more down-to-earth in an almost literal sense: the synthesis of elements which are essential constituents of the solar system, including Earth. Our work is intended to adjust details of an in general well understood problem; but as we have seen, surprising results can be found in this case as well.

There are further fundamental differences between the two main topics of this work. Most prominently, it is pretty straightforward to compare the combustion of white dwarf matter to premixed chemical combustion, for which the applied combustion theory was developed: Heat conduction leads to the propagation of the flame, chemical fuel is burned into ash by chemical reactions, chemical binding energy is released – *chemical* is just replaced by *nuclear* in those notions. The analogy between chemical flames and the conversion of hadronic matter into strange quark matter is more far-fetched: The diffusion of s-quarks replaces the heat conduction, and the energy is released not by a change in composition but by a transition to a

---

totally different equation of state; the process is comparable to a phase transition. Therefore, the term *combustion-like* might be a more appropriate description of this process; however, we have seen that the description of the conversion process as a combustion is well motivated and successful.

Naturally, also the numerical modeling of the burning process itself differs considerably. The conversion of hadronic matter into strange quark matter is conceptually easier in the sense that the burnt matter just consists of strange quark matter; in the thermonuclear case we have to consider the correct final composition of the ashes to get the energy release right. Numerically, this is implemented by means of five representative species. However, in the neutron star conversion case, the fact that we have to switch from one equation of state to another complicates the modeling significantly; in particular the question arises whether the burning is exothermic – it turns out that this is a crucial issue. In the thermonuclear case this question is trivial, because the combustion is always exothermic by construction.

In addition to the equation of state, there is another important difference between neutron stars and white dwarfs: We have seen that in neutron star simulations a purely Newtonian approach regarding the gravitational potential is not appropriate, although the applied general relativistic gravitational potential gives rise to a number of numerical problems. In contrast, according to our estimation even the most compact white dwarfs can be described to good approximation by a Newtonian potential.

To summarize, we successfully applied very similar fundamental concepts as well as numerical methods to two distinct physical environments. We achieved interesting qualitative results in the yet unexplored field of dynamical simulations of conversion processes in neutron stars; and interesting qualitative as well as quantitative results in the established field of thermonuclear supernovae simulations, in particular simulations of deflagrations in high-density carbon-oxygen white dwarfs. Both topics are important examples of nuclear astrophysics.

Being confronted with the similarities as well as the differences between the two main topics of this thesis lead to a deeper understanding of the physical and numerical aspects of combustion processes in compact stars. The opportunity to apply the same physical and numerical concepts to two disjunct physical environments is one factor that helped the author to experience this work as a fulfilling journey into the fascinating world of computational nuclear astrophysics.



## A. Gravitational wave signal of a typical thermonuclear supernova

In this section we present our computations of the gravitational wave signal of thermonuclear supernovae. We show one example of a particular model that provides a good match to the observational properties of a typical Type Ia supernovae.

This section is not included into the main part of this thesis because the discussed thermonuclear supernova scenario is thematically quite different from the two main topics of the thesis, which treat pure deflagrations in neutron stars and in high-density white dwarfs. However, we have already implemented a numerical technique to calculate gravitational wave signals into the LEAFS-code, as we described in Section 3.4. The underlying theoretical considerations are introduced in Section 2.5. This technique, without any modification, can also be applied to calculate the gravitational wave signal of thermonuclear supernovae. The results might be of general interest; therefore we append this section.

### A.1. Introduction

Research on gravitational wave signals of thermonuclear supernovae is a largely unexplored field. Pioneering work has been done recently by Falta et al. (2011) and Falta and Fisher (2011), who calculated the gravitational wave signal of *gravitationally-confined detonation* (GCD) models of thermonuclear supernovae (cf. Section 1.3.3). In these models, an off-center ignited deflagration bubble rises due to buoyancy forces until it reaches the surface of the white dwarf; the deflagration does not unbind the star but triggers a subsequent detonation that ignites opposite to the point where the deflagration bubble reaches the surface. This scenario leads to asymmetric explosions and thus to relatively strong gravitational wave signals, which are discussed in detail in Falta et al. (2011). In Section A.3 we will compare our results to their work.

Based on their earlier results, Falta and Fisher (2011) analyzed the stochastic gravitational wave background originating from thermonuclear supernovae. They found that it might pose a considerable source of noise – in the frequency range between 0.1 Hz and 10 Hz – for future gravitational wave detectors such as BBO and DECIGO (see Section 2.5.2) that are assigned to detect the gravitational wave signal of cosmological inflation.

Dan et al. (2011) calculated the gravitational wave signal of a close binary system of two white dwarfs in the ringdown phase until the start of the merger, but they did not model the following thermonuclear burning which may lead to a supernova.

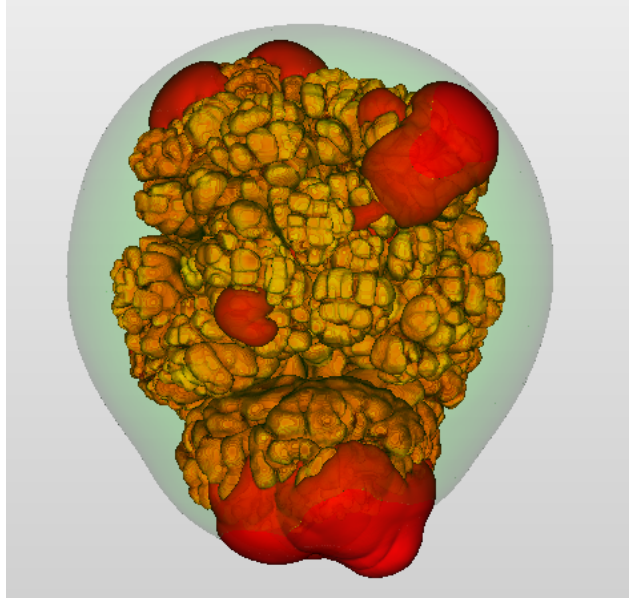


**Figure A.1.:** Model N0100 shortly after the ignition of the detonation. The density isosurface at  $\rho = 5 \times 10^5 \text{ g cm}^{-3}$  is plotted in green. The detonation flame front is marked in red, the deflagration front in yellow. Figure provided by Ivo Seitenzahl.

In the following section we will discuss the model that we apply: a delayed-deflagration model in the Chandrasekhar-mass scenario. After that, we will present the results of our hydrodynamic simulation. In the last section, we will discuss our results and give an outlook to future work.

## A.2. Delayed-detonation model N0100

The *delayed-detonation model* of thermonuclear supernovae is similar to the pure-deflagration model as described in Section 5: The thermonuclear burning in the interior of a Chandrasekhar-mass carbon-oxygen white dwarf starts in a deflagration mode, but later a *deflagration-to-detonation transition (DDT)* occurs at some points; a detonation is triggered that burns a large fraction of the remaining fuel. These points in time and space are determined by a *DDT criterion*, which is often assumed to be just a density threshold. In our model, however, a physical DDT criterion that is based on determining the strength of the turbulent velocity fluctuations on the subgrid scale is applied (Seitenzahl et al. (2011); Ciaraldi-Schoolmann (2012); Ciaraldi-Schoolmann and Röpke, in preparation).

Considering all models of the Chandrasekhar-mass scenario, delayed-detonation models currently provide the best match to observations, see Kasen et al. (2009), Röpke et al. (2012), and Section 1.3.3. Delayed-detonation models are, like GCD models, inherently asymmetric

and should therefore yield a comparably strong gravitational wave signal. For these two reasons we chose a delayed-detonation model as a suitable example to calculate the gravitational wave signal of a typical thermonuclear supernova.

In our delayed-detonation model, in contrast to the pure-deflagration model presented in Section 5, the white dwarf is not ignited in the center but by means of a number of spherical ignition kernels that are placed around the center; their positions resemble a truncated Gaussian distribution. The carbon-oxygen white dwarf has a standard initial central density of  $\rho_c = 2.9 \times 10^9 \text{ g cm}^{-3}$ . We conducted a three-dimensional simulation on a Cartesian grid of 512 cells per dimension and applied the subgrid scale turbulence model with localized closure (Schmidt et al. (2006a,b); cf. Section 3.1.6). Apart from that, the same initial configuration (Section 5.2.1) and numerical methods (Section 3) were applied as in our simulations of deflagrations in high-density white dwarfs (Section 5).

In this model, the strength of the deflagration phase, parametrized by the number of ignition kernels, controls the brightness of the supernova: a large number of ignition kernels results in a strong deflagration phase, which leads to a strong pre-expansion of the white dwarf. The subsequent detonation occurs at lower densities; consequently, little  $^{56}\text{Ni}$  is produced and the supernova is comparably faint. Conversely, a small number of ignition kernels leads to a weak deflagration phase, a detonation at high densities, and a bright supernova.

The particular model that we discuss in the following, called N0100, is part of a series of models of three-dimensional high-resolution delayed-detonation models with varying number of ignition kernels (Seitenzahl et al. 2012, in preparation). Its deflagration phase, ignited by means of 100 ignition kernels, is of intermediate strength. Röpke et al. (2012) chose it as a standard model because it provides a reasonable match to the observational properties of SN 2011fe. The simulation of model N0100 yields  $0.60 M_\odot$  of  $^{56}\text{Ni}$ ,  $0.84 M_\odot$  of iron group elements, and a kinetic energy of the ejecta of  $1.45 \times 10^{51}$  erg. More detailed results are given in Röpke et al. (2012). Figure A.1 shows a snapshot of the simulation shortly after the DDT occurred at  $\sim 1$  s after ignition; the yellow and red contours indicate the position of the deflagration and detonation front, respectively. The density isosurface at  $\rho = 5 \times 10^5 \text{ g cm}^{-3}$  is marked in green.

## A.3. Results

In the following we will present the results from the simulation of model N0100 that we introduced above; we start with a presentation of the gravitational wave amplitudes.

### A.3.1. Gravitational wave amplitudes

In Figure A.2 we plot four different gravitational wave amplitudes that arise from two different lines of sight ( $x$ - and  $z$ -direction), each with two polarization states ( $\times$  and  $+$ ), see Section 3.4 for a detailed explanation. In the first  $\sim 0.4$  s no signal is visible; after that the absolute values

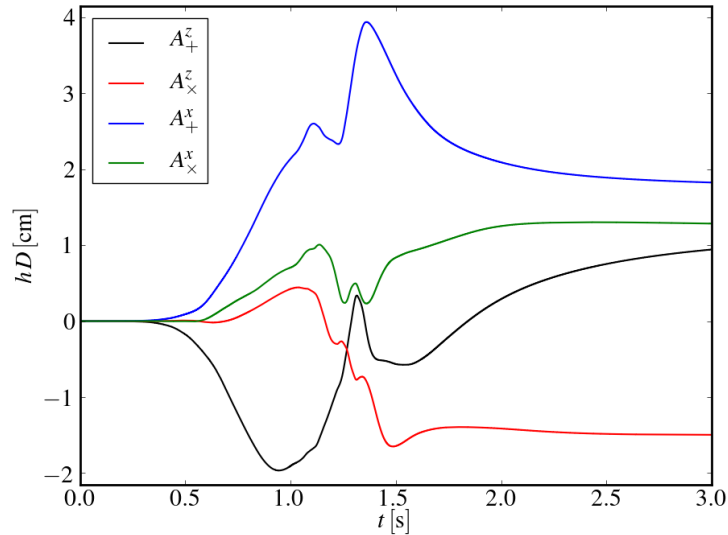


**Figure A.2.:** Time evolution of four gravitational wave amplitudes of delayed-detonation model N0100, see text for details.

of all amplitudes rise in a steady, monotonic way. The ignition of the detonation at  $t \sim 1$  s has a visible effect on the signal: in three cases the direction of the slope of the respective amplitude is reversed, whereas in the fourth case ( $A_+^x$ , blue line in Figure A.2) a small bump occurs in the evolution of the amplitude. In this case, the signal reaches a maximum value of  $hD \sim 4$  cm at  $t \sim 1.5$  s, about a factor of 3 less than the maximum amplitude obtained by Falta et al. (2011) in their GCD model. The homologous expansion of the supernova ejecta after  $\sim 3$  s generates a signal that is constant in time up to  $t = 100$  s, when the simulation was stopped.

Note that we do not encounter numerical problems such as unphysical oscillations of the quadrupole moment that occur in our calculations of the gravitational wave signal of the conversion of a hadronic neutron star into a quark star (cf. Section 4.5). Most likely this is because of the fact that the white dwarf explodes – the fluid expands continuously and does not stay in a numerically challenging quasi-hydrostatic state like the neutron star after the conversion process has ceased.

### A.3.2. Gravitational wave energy

The energy emitted in gravitational waves is another important quantity that we are able to determine, by means of equation (3.27). The gravitational wave luminosity as a function of time is plotted in Figure A.3. Clearly visible is a two-peaked structure; the first peak

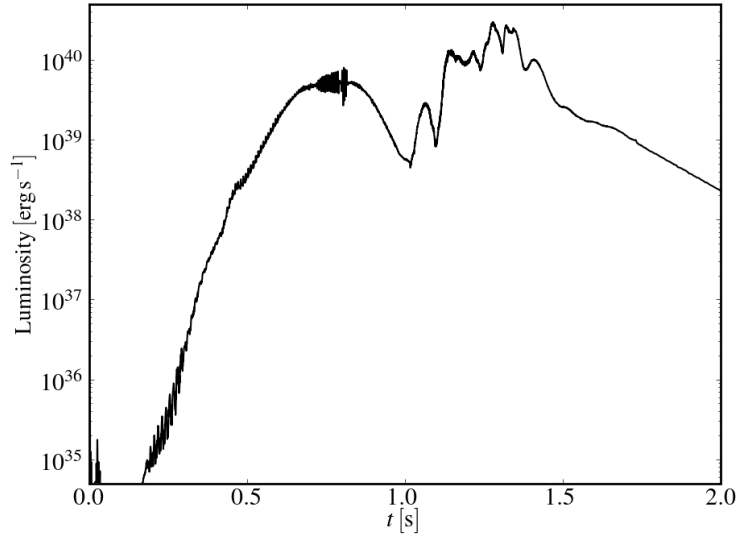


**Figure A.3.:** Gravitational wave luminosity as a function of time of delayed-detonation model N0100.

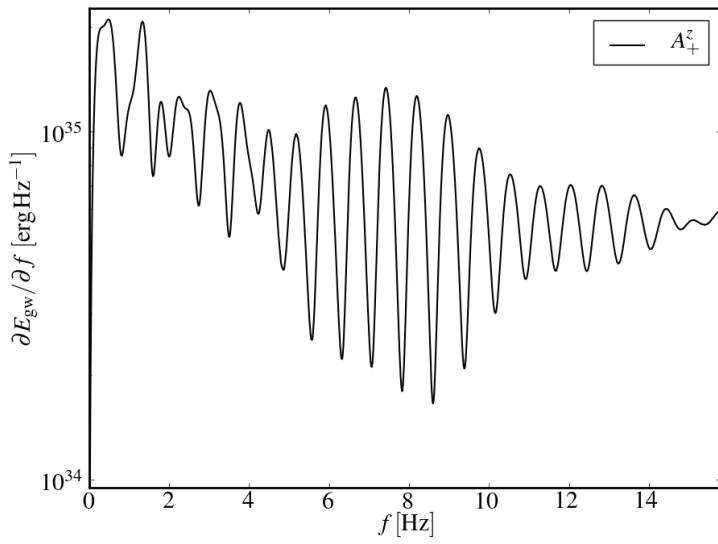


**Figure A.4.:** Energy spectrum of delayed-detonation model N0100.

corresponds to the deflagration phase and features a maximum luminosity of  $8 \times 10^{39} \text{ erg s}^{-1}$  at  $t \sim 0.8 \text{ s}$ , while the second, considerably higher, peak can be attributed to the detonation phase. Here the maximum luminosity is  $3 \times 10^{40} \text{ erg s}^{-1}$  at  $t \sim 1.3 \text{ s}$ . In contrast, the GCD model of Falta et al. (2011) yielded significantly higher luminosities during the deflagration phase than during the detonation phase.

The total energy amounts to  $6.9 \times 10^{39} \text{ erg}$ , about an order of magnitude less than the total energy resulting from the simulation of Falta et al. (2011) – this is consistent to the results shown in Section A.3.1, because the calculated amplitudes differ by a factor of  $\sim 3$  between our delayed-detonation model and their GCD model, and the energy is proportional to the square of the amplitudes. By the way, these values also show that the gravitational wave energy is much smaller than any other important form of energy in the system, such as internal, kinetic, nuclear, or even neutrino loss energy (which we determine to be  $E_{\nu}^{\text{total}} = 2.0 \times 10^{49} \text{ erg}$ ) and is therefore dynamically unimportant.

Figure A.4 shows the energy spectrum of the gravitational wave signal, calculated by means of equation (3.30), see Section 3.4. Besides the first peaks at  $\sim 0.5 \text{ Hz}$  and  $\sim 1.5 \text{ Hz}$  we see a range of peaks around  $\sim 8 \text{ Hz}$ . The energy spectrum calculated by Falta et al. (2011) features a single peak at  $\sim 2 \text{ Hz}$ .

## A.4. Discussion and outlook

We present the gravitational wave signal of a typical thermonuclear supernova in terms of different amplitudes, the energy spectrum, and the luminosity as a function of time. As an example we chose a delayed-detonation model that provides a reasonable match to the observations of SN 2011fe.

The results show that the detection of gravitational wave signals of Type Ia supernovae provides a way to differentiate between different explosion models, if future instruments are able to detect those signals. Signals as presented above show signs of a deflagration-to-detonation transition; gravitational waves generated by mergers of white dwarfs would feature the characteristic signal of the ringdown phase – according to Dan et al. (2011), the gravitational wave signal in the ringdown phase is of the same magnitude as the signal of the supernova in the above discussed scenarios:  $hD = 2 \text{ cm}$  to  $20 \text{ cm}$ , depending on the masses of the white dwarfs. GCD models show a sharp single peak in the time evolution of the amplitude (Figure 2 in Falta et al. (2011)). However, the low frequency range of the signals prevents a detection by second-generation instruments comparable to advanced LIGO; but according to Falta et al. (2011) third-generation detectors like BBO or DECIGO that cover a lower frequency range should be able to detect the gravitational wave signal of at least all galactic Type Ia supernovae.

The gravitational wave frequencies that we obtain are consistent with the results of Falta et al. (2011) and Falta and Fisher (2011). Our results indicate that also thermonuclear supernovae modeled as delayed detonations contribute to the stochastic gravitational wave background in the frequency range between  $0.1 \text{ Hz}$  and  $10 \text{ Hz}$  and thus pose a source of noise that

might obscure the gravitational wave signal that originates from the era of inflation shortly after the Big Bang; the measurement of this signal is a central goal of the planned detectors BBO and DECIGO.

Falta and Fisher (2011) considered only gravitationally-confined detonation models in order to estimate the stochastic gravitational wave background from Type Ia supernovae. In future work we plan to improve on that by calculating the gravitational wave signal from other thermonuclear supernova scenarios as well, in particular from sub-Chandrasekhar-mass models and models of mergers of two white dwarfs, in addition to the signals from delayed-detonation models presented here. Those signals should be weighted with appropriate Type Ia supernovae event rates, taken for example from binary population synthesis studies (e.g. Ruiter et al., 2010), in order to achieve a realistic estimate of the stochastic gravitational wave background originating from all Type Ia supernovae.



## Bibliography

- E. B. Abdikamalov, C. D. Ott, L. Rezzolla, L. Dessart, H. Dimmelmeier, A. Marek, and H.-T. Janka. Axisymmetric general relativistic simulations of the accretion-induced collapse of white dwarfs. *Phys. Rev. D*, 81(4):044012–+, Feb. 2010.
- W. S. Adams. The Spectrum of the Companion of Sirius. *PASP*, 27:236, Dec. 1915.
- C. Alcock, E. Farhi, and A. Olinto. Strange stars. *ApJ*, 310:261–272, Nov. 1986.
- P. Amaro-Seoane, S. Aoudia, S. Babak, P. Binétruy, E. Berti, A. Bohé, C. Caprini, M. Colpi, N. J. Cornish, K. Danzmann, J.-F. Dufaux, J. Gair, O. Jennrich, P. Jetzer, A. Klein, R. N. Lang, A. Lobo, T. Littenberg, S. T. McWilliams, G. Nelemans, A. Petiteau, E. K. Porter, B. F. Schutz, A. Sesana, R. Stebbins, T. Sumner, M. Vallisneri, S. Vitale, M. Volonteri, and H. Ward. Low-frequency gravitational-wave science with eLISA/NGO. *Classical and Quantum Gravity*, 29(12):124016, June 2012.
- E. Anders and N. Grevesse. Abundances of the elements - Meteoritic and solar. *Geochim. Cosmochim. Acta*, 53:197–214, Jan. 1989.
- A. M. Anile. *Relativistic fluids and magneto-fluids: With applications in astrophysics and plasma physics*. Cambridge and New York, Cambridge University Press, 1989.
- A. Arcones, G. Martínez-Pinedo, L. F. Roberts, and S. E. Woosley. Electron fraction constraints based on nuclear statistical equilibrium with beta equilibrium. *A&A*, 522:A25+, Nov. 2010.
- W. D. Arnett. On the theory of Type I supernovae. *ApJ*, 230:L37–L40, May 1979.
- Australia Telescope National Facility. ATNF Pulsar Catalogue. <http://www.atnf.csiro.au/research/pulsar/psrcat/>, 2012. Accessed May 2012.
- W. Baade and F. Zwicky. On Super-novae. *Contributions from the Mount Wilson Observatory*, vol. 3, pp.73-78, 3:73–78, 1927.
- W. Baade and F. Zwicky. Remarks on super-novae and cosmic rays. *Physical Review*, 46: 76–77, July 1934a.
- W. Baade and F. Zwicky. Cosmic Rays from Super-novae. *Proceedings of the National Academy of Science*, 20:259–263, May 1934b.

## BIBLIOGRAPHY

---

- A. Balysh, A. de Silva, V. I. Lebedev, K. Lou, M. K. Moe, M. A. Nelson, A. Piepke, A. Pronskiy, M. A. Vient, and P. Vogel. Double Beta Decay of  $^{48}\text{Ca}$ . *Physical Review Letters*, 77: 5186–5189, Dec. 1996.
- E. Baron, J. Cooperstein, S. Kahana, and K. Nomoto. Collapsing white dwarfs. *ApJ*, 320: 304–307, Sept. 1987.
- H. W. Barz, L. P. Csernai, B. Kampfer, and B. Lukács. Stability of detonation fronts leading to quark-gluon plasma. *Phys. Rev. D*, 32:115–122, July 1985.
- A. Bauswein, H.-T. Janka, and R. Oechslin. Testing approximations of thermal effects in neutron star merger simulations. *Phys. Rev. D*, 82(8):084043, Oct 2010.
- A. Bauswein, R. Oechslin, and H. Janka. Discriminating strange star mergers from neutron star mergers by gravitational-wave measurements. *Phys. Rev. D*, 81(2):024012–+, Jan. 2010.
- O. G. Benvenuto and M. A. De Vito. The formation of helium white dwarfs in close binary systems - II. *MNRAS*, 362:891–905, Sept. 2005.
- H. A. Bethe. Supernova mechanisms. *Reviews of Modern Physics*, 62:801–866, Oct. 1990.
- L. Blanchet, T. Damour, and G. Schafer. Post-Newtonian hydrodynamics and post-Newtonian gravitational wave generation for numerical relativity. *MNRAS*, 242:289–305, Jan. 1990.
- D. Blaschke, H. Grigorian, D. N. Voskresensky, and F. Weber. Cooling of the neutron star in Cassiopeia A. *Phys. Rev. C*, 85(2):022802, Feb. 2012.
- A. R. Bodmer. Collapsed Nuclei. *Phys. Rev. D*, 4:1601–1606, Sept. 1971.
- F. Brachwitz, D. J. Dean, W. R. Hix, K. Iwamoto, K. Langanke, G. Martínez-Pinedo, K. Nomoto, M. R. Strayer, F.-K. Thielemann, and H. Umeda. The role of electron captures in Chandrasekhar-mass models for type Ia supernovae. *ApJ*, 536:934–947, June 2000.
- T. Brahe. *De nova et nullius aevi memoria prius visa stella, iam pridem á nato Christo 1572, mense Novembri primum conspecta, contemplatio mathematica*. Laurentius Benedictus, Kopenhagen, 1573.
- E. Bravo and D. García-Senz. Coulomb corrections to the equation of state of nuclear statistical equilibrium matter: implications for SNIa nucleosynthesis and the accretion-induced collapse of white dwarfs. *MNRAS*, 307:984–992, Aug. 1999.
- E. Bravo, A. Tornambe, I. Dominguez, and J. Isern. Clues to Type Ia SN progenitors from degenerate carbon ignition models. *A&A*, 306:811–822, Feb. 1996.

- M. Camenzind. *Compact objects in astrophysics: white dwarfs, neutron stars, and black holes*. Springer-Verlag Berlin, 2007.
- R. Canal and J. Isern. Collapse of white dwarfs in close binary systems. In H. M. van Horn and V. Weidemann, editors, *IAU Colloq. 53: White Dwarfs and Variable Degenerate Stars*, pages 52–55, 1979.
- R. Canal and E. Schatzman. Non explosive collapse of white dwarfs. *A&A*, 46:229–235, Jan. 1976.
- R. Canal, J. Isern, and J. Labay. The collapse of carbon-oxygen white dwarfs. *ApJ*, 241: L33–L36, Oct. 1980.
- R. Canal, D. Garcia, J. Isern, and J. Labay. Can C+O white dwarfs form neutron stars? *ApJ*, 356:L51–L53, June 1990a.
- R. Canal, J. Isern, and J. Labay. The origin of neutron stars in binary systems. *ARA&A*, 28: 183–214, 1990b.
- J. Chadwick. The Existence of a Neutron. *Royal Society of London Proceedings Series A*, 136:692–708, June 1932.
- I. Chakrabarty. Gravitational Waves: An Introduction. *ArXiv Physics e-prints*, Aug. 1999.
- S. Chandrasekhar. The maximum mass of ideal white dwarfs. *ApJ*, 74:81–82, July 1931.
- H. T. Cho, K. Ng, and A. D. Speliotopoulos. A hydrodynamical analysis of the burning of a neutron star. *Physics Letters B*, 326:111–117, Apr. 1994.
- A. Chodos, R. L. Jaffe, K. Johnson, C. B. Thorn, and V. F. Weisskopf. New extended model of hadrons. *Phys. Rev. D*, 9:3471–3495, June 1974.
- F. Ciaraldi-Schoolmann. *Modeling delayed detonations of Chandrasekhar-mass white dwarfs*. PhD thesis, Technische Universität München, 2012.
- F. Ciaraldi-Schoolmann, W. Schmidt, J. C. Niemeyer, F. K. Röpke, and W. Hillebrandt. Turbulence in a three-dimensional deflagration model for Type Ia supernovae. I. Scaling properties. *ApJ*, 696:1491–1497, May 2009.
- J. Cleymans, R. V. Gavai, and E. Suhonen. Quarks and gluons at high temperatures and densities. *Phys. Rep.*, 130:217–292, Jan. 1986.
- P. Colella. Multidimensional upwind methods for hyperbolic conservation laws. *Journal of Computational Physics*, 87:171–200, Mar. 1990.
- P. Colella and H. M. Glaz. Efficient solution algorithms for the riemann problem for real gases. *Journal of Computational Physics*, 59:264–289, June 1985.

## BIBLIOGRAPHY

---

- P. Colella and P. R. Woodward. The Piecewise Parabolic Method (PPM) for gas-dynamical simulations. *Journal of Computational Physics*, 54:174–201, Sept. 1984.
- S. A. Colgate and C. McKee. Early supernova luminosity. *ApJ*, 157:623–643, Aug. 1969.
- G. B. Cook, S. L. Shapiro, and S. A. Teukolsky. Spin-up of a rapidly rotating star by angular momentum loss - Effects of general relativity. *ApJ*, 398:203–223, Oct. 1992.
- R. Courant, K. O. Friedrichs, and H. Lewy. Über die partiellen Differentialgleichungen der mathematischen Physik. *Math. Ann.*, 100:32–74, 1928.
- M. Dan, S. Rosswog, J. Guillochon, and E. Ramirez-Ruiz. Prelude to A Double Degenerate Merger: The Onset of Mass Transfer and Its Impact on Gravitational Waves and Surface Detonations. *ApJ*, 737:89, Aug. 2011.
- M. Davis, R. Ruffini, W. H. Press, and R. H. Price. Gravitational Radiation from a Particle Falling Radially into a Schwarzschild Black Hole. *Physical Review Letters*, 27:1466–1469, Nov. 1971.
- P. B. Demorest, T. Pennucci, S. M. Ransom, M. S. E. Roberts, and J. W. T. Hessels. A two-solar-mass neutron star measured using Shapiro delay. *Nature*, 467:1081–1083, Oct. 2010.
- L. Dessart, A. Burrows, C. D. Ott, E. Livne, S.-C. Yoon, and N. Langer. Multidimensional Simulations of the Accretion-induced Collapse of White Dwarfs to Neutron Stars. *ApJ*, 644:1063–1084, June 2006.
- A. Drago, A. Lavagno, and I. Parenti. Burning of a hadronic star into a quark or a hybrid star. *ApJ*, 659:1519–1535, Apr. 2007.
- A. S. Eddington. On the relation between the masses and luminosities of the stars. *MNRAS*, 84:308–332, Mar. 1924.
- A. S. Eddington. *The Internal Constitution of the Stars*. Cambridge University Press, Cambridge, 1926.
- J. H. Elias, K. Matthews, G. Neugebauer, and S. E. Persson. Type I supernovae in the infrared and their use as distance indicators. *ApJ*, 296:379–389, Sept. 1985.
- D. Falta and R. Fisher. Stochastic gravitational wave background from the single-degenerate channel of type Ia supernovae. *Phys. Rev. D*, 84(12):124062, Dec. 2011.
- D. Falta, R. Fisher, and G. Khanna. Gravitational Wave Emission from the Single-Degenerate Channel of Type Ia Supernovae. *Physical Review Letters*, 106(20):201103, May 2011.
- E. Farhi and R. L. Jaffe. Strange matter. *Phys. Rev. D*, 30:2379–2390, Dec. 1984.

- M. Fink, W. Hillebrandt, and F. K. Röpke. Double-detonation supernovae of sub-Chandrasekhar mass white dwarfs. *A&A*, 476:1133–1143, Dec. 2007.
- M. Fink, F. K. Röpke, W. Hillebrandt, I. R. Seitenzahl, S. A. Sim, and M. Kromer. Double-detonation sub-Chandrasekhar supernovae: can minimum helium shell masses detonate the core? *A&A*, 514:A53, May 2010.
- M. A. Fink. *Modeling detonations in Type Ia supernovae*. PhD thesis, Technische Universität München, 2010.
- R. H. Fowler. On dense matter. *MNRAS*, 87:114–122, Dec. 1926.
- J. L. Friedman, J. R. Ipser, and R. D. Sorkin. Turning-point method for axisymmetric stability of rotating relativistic stars. *ApJ*, 325:722–724, Feb. 1988.
- B. A. Fryxell, E. Müller, and W. D. Arnett. Unpublished, 1989.
- G. M. Fuller, W. A. Fowler, and M. J. Newman. Stellar weak interaction rates for intermediate-mass nuclei. IV - Interpolation procedures for rapidly varying lepton capture rates using effective log (ft)-values. *ApJ*, 293:1–16, June 1985.
- D. García-Senz, E. Bravo, and N. Serichol. A particle code for deflagrations in white dwarfs. I. Numerical techniques. *ApJS*, 115:119–139, Mar. 1998.
- S. K. Godunov. Finite difference method for numerical computation of discontinuous solution of the equations of fluid dynamics. *Matematicheskii Sbornik*, 47:271, 1959.
- D. A. Green and F. R. Stephenson. Historical supernovae. In K. W. Weiler, editor, *Supernovae and Gamma-Ray Bursters*, volume 598 of *Lecture Notes in Physics*, pages 7–19, Berlin Heidelberg New York, 2003. Springer-Verlag.
- P. Haensel, J. L. Zdunik, and R. Schaefer. Strange quark stars. *A&A*, 160:121–128, May 1986.
- C. O. Heinke, G. B. Rybicki, R. Narayan, and J. E. Grindlay. A Hydrogen Atmosphere Spectral Model Applied to the Neutron Star X7 in the Globular Cluster 47 Tucanae. *ApJ*, 644:1090–1103, June 2006.
- H. Heiselberg, G. Baym, and C. J. Pethick. Burning of strange quark matter and transport properties of QCD plasmas. *Nuclear Physics B Proceedings Supplements*, 24:144–147, Dec. 1991.
- M. Hempel and J. Schaffner-Bielich. A statistical model for a complete supernova equation of state. *Nuclear Physics A*, 837:210–254, June 2010.
- M. Hernanz, J. Isern, R. Canal, J. Labay, and R. Mochkovitch. The final stages of evolution of cold, mass-accreting white dwarfs. *ApJ*, 324:331–344, Jan. 1988.

## BIBLIOGRAPHY

---

- M. Herzog and F. K. Röpke. Three-dimensional hydrodynamic simulations of the combustion of a neutron star into a quark star. *Phys. Rev. D*, 84(8):083002, Oct. 2011.
- A. Hewish, S. J. Bell, J. D. H. Pilkington, P. F. Scott, and R. A. Collins. Observation of a Rapidly Pulsating Radio Source. *Nature*, 217:709–713, Feb. 1968.
- S. Hild, M. Abernathy, F. Acernese, P. Amaro-Seoane, N. Andersson, K. Arun, F. Barone, B. Barr, M. Barsuglia, M. Beker, and others. Sensitivity studies for third-generation gravitational wave observatories. *Classical and Quantum Gravity*, 28(9):094013, May 2011.
- W. Hillebrandt and J. C. Niemeyer. Type Ia supernova explosion models. *ARA&A*, 38:191–230, 2000.
- G. Hobbs, A. Archibald, Z. Arzoumanian, D. Backer, M. Bailes, N. D. R. Bhat, M. Burgay, S. Burke-Spolaor, D. Champion, and others. The International Pulsar Timing Array project: using pulsars as a gravitational wave detector. *Classical and Quantum Gravity*, 27(8):084013, Apr. 2010.
- J. E. Horvath. The birth of strange stars: kinetics, hydrodynamics and phenomenology of supernovae and GRBs. *International Journal of Modern Physics D*, 19:523–538, 2010.
- J. E. Horvath and O. G. Benvenuto. On the stability of slow neutron combustion in astrophysical objects. *Physics Letters B*, 213:516–520, Nov. 1988.
- F. Hoyle and W. A. Fowler. Nucleosynthesis in supernovae. *ApJ*, 132:565–590, Nov. 1960.
- J. Isern, J. Labay, M. Hernanz, and R. Canal. Collapse and explosion of white dwarfs. I - Precollapse evolution. *ApJ*, 273:320–329, Oct. 1983.
- N. Itoh. Hydrostatic Equilibrium of Hypothetical Quark Stars. *Progress of Theoretical Physics*, 44:291–292, July 1970.
- N. Itoh, H. Hayashi, A. Nishikawa, and Y. Kohyama. Neutrino Energy Loss in Stellar Interiors. VII. Pair, Photo-, Plasma, Bremsstrahlung, and Recombination Neutrino Processes. *ApJS*, 102:411, Feb. 1996.
- K. Iwamoto, F. Brachwitz, K. Nomoto, N. Kishimoto, H. Umeda, W. R. Hix, and F.-K. Thielemann. Nucleosynthesis in Chandrasekhar Mass Models for Type Ia Supernovae and Constraints on Progenitor Systems and Burning-Front Propagation. *ApJS*, 125:439–462, Dec. 1999.
- P. Jaikumar, B. S. Meyer, K. Otsuki, and R. Ouyed. Nucleosynthesis in neutron-rich ejecta from quark-novae. *A&A*, 471:227–236, Aug. 2007.
- H.-T. Janka. Explosion Mechanisms of Core-Collapse Supernovae. *ArXiv e-prints*, June 2012.

- H.-T. Janka, K. Langanke, A. Marek, G. Martínez-Pinedo, and B. Müller. Theory of core-collapse supernovae. *Phys. Rep.*, 442:38–74, Apr. 2007.
- D. Kasen, F. K. Röpke, and S. E. Woosley. The diversity of type Ia supernovae from broken symmetries. *Nature*, 460:869–872, Aug. 2009.
- A. M. Khokhlov. Delayed detonation model for type Ia supernovae. *A&A*, 245:114–128, May 1991.
- A. N. Kolmogorov. The local structure of turbulence in incompressible viscous fluid for very large reynolds numbers. *Dokl. Akad. Nauk SSSR*, 30:299–303, 1941. In Russian.
- K.-L. Kratz, P. Möller, W. Hillebrandt, W. Ziegert, V. Harms, A. Wöhr, and F.-K. Thielemann. Nuclear structure effects far from stability and their consequences on rapid-neutron-capture processes. In *American Institute of Physics Conference Series*, volume 164 of *American Institute of Physics Conference Series*, pages 558–567, Dec. 1987.
- K.-L. Kratz, W. Böhmer, C. Freiburghaus, P. Möller, B. Pfeiffer, T. Rauscher, and F.-K. Thielemann. On the origin of the Ca-Ti-Cr isotopic anomalies in the inclusion EK-1-4-1 of the Allende-meteorite. *Mem. Soc. Astron. Italiana*, 72:453–466, 2001.
- O. Krause, M. Tanaka, T. Usuda, T. Hattori, M. Goto, S. Birkmann, and K. Nomoto. Tycho Brahe’s 1572 supernova as a standard type Ia as revealed by its light-echo spectrum. *Nature*, 456:617–619, Dec. 2008.
- M. Kromer and S. A. Sim. Time-dependent three-dimensional spectrum synthesis for Type Ia supernovae. *MNRAS*, 398:1809–1826, Aug. 2009.
- M. Kromer, S. A. Sim, M. Fink, F. K. Röpke, I. R. Seitenzahl, and W. Hillebrandt. Double-detonation Sub-Chandrasekhar Supernovae: Synthetic Observables for Minimum Helium Shell Mass Models. *ApJ*, 719:1067–1082, Aug. 2010.
- T. Kunugise and K. Iwamoto. Neutrino Emission from Type Ia Supernovae. *PASJ*, 59:L57+, Dec. 2007.
- L. D. Landau and E. M. Lifshitz. *Fluid Mechanics, Second Edition: Volume 6 (Course of Theoretical Physics)*. Butterworth-Heinemann, 2 edition, January 1987.
- K. Langanke and G. Martínez-Pinedo. Shell-model calculations of stellar weak interaction rates. II. Weak rates for nuclei in the mass range  $A = 45$ – $65$  in supernovae environments. *Nuclear Physics A*, 673:481–508, June 2000.
- K. Langanke and G. Martínez-Pinedo. Rate Tables for the Weak Processes of pf-SHELL Nuclei in Stellar Environments. *Atomic Data and Nuclear Data Tables*, 79:1–46, Sept. 2001.

## BIBLIOGRAPHY

---

- K. Langanke, G. Martínez-Pinedo, J. M. Sampaio, D. J. Dean, W. R. Hix, O. E. Messer, A. Mezzacappa, M. Liebendörfer, H.-T. Janka, and M. Rampp. Electron Capture Rates on Nuclei and Implications for Stellar Core Collapse. *Physical Review Letters*, 90(24): 241102–+, June 2003.
- J. M. Lattimer and M. Prakash. The Physics of Neutron Stars. *Science*, 304:536–542, Apr. 2004.
- J. M. Lattimer and M. Prakash. Neutron star observations: Prognosis for equation of state constraints. *Phys. Rep.*, 442:109–165, Apr. 2007.
- J. M. Lattimer and F. D. Swesty. A generalized equation of state for hot, dense matter. *Nuclear Physics A*, 535:331–376, Dec. 1991.
- D. Leahy and R. Ouyed. Supernova SN2006gy as a first ever Quark Nova? *MNRAS*, 387: 1193–1198, July 2008.
- P. Lesaffre, Z. Han, C. A. Tout, P. Podsiadlowski, and R. G. Martin. The C flash and the ignition conditions of Type Ia supernovae. *MNRAS*, 368:187–195, May 2006.
- R. J. LeVeque. Nonlinear conservation laws and finite volume methods. In O. Steiner and A. Gautschi, editors, *Computational Methods for Astrophysical Flows*, Saas-Fee Advanced Course 27, pages 1–159. Springer, Berlin Heidelberg New York, 1998.
- B.-A. Li, L.-W. Chen, C. M. Ko, P. G. Krastev, D.-H. Wen, A. Worley, Z. Xiao, J. Xu, G.-C. Yong, and M. Zhang. Constraining the EOS of Neutron-Rich Nuclear Matter and Properties of Neutron Stars with Heavy-Ion Reactions. In P. Danielewicz, editor, *American Institute of Physics Conference Series*, volume 1128 of *American Institute of Physics Conference Series*, pages 131–143, May 2009.
- W. Li, J. Leaman, R. Chornock, A. V. Filippenko, D. Poznanski, M. Ganeshalingam, X. Wang, M. Modjaz, S. Jha, R. J. Foley, and N. Smith. Nearby supernova rates from the Lick Observatory Supernova Search - II. The observed luminosity functions and fractions of supernovae in a complete sample. *MNRAS*, 412(3):1441–1472, Mar. 2011.
- M. Liebendörfer, U.-L. Pen, and C. Thompson. Efficient approximations of neutrino physics for three-dimensional simulations of stellar core collapse. In *International Symposium on Nuclear Astrophysics - Nuclei in the Cosmos*, 2006.
- LIGO Scientific Collaboration. Advanced LIGO. <https://www.advancedligo.mit.edu/>, 2012. Accessed April 2012.
- K. Lodders, H. Palme, and H.-P. Gail. 4.4 Abundances of the elements in the Solar System. In J. E. Trümper, editor, *Solar System, Landolt-Börnstein - Group VI Astronomy and Astrophysics, Volume 4B*. Springer-Verlag Berlin Heidelberg, page 712, 2009.

- G. Lugones and O. G. Benvenuto. Strange matter equation of state and the combustion of nuclear matter into strange matter in the quark mass-density-dependent model at  $T > 0$ . *Phys. Rev. D*, 52:1276–1280, July 1995.
- G. Lugones, O. G. Benvenuto, and H. Vucetich. Combustion of nuclear matter into strange matter. *Phys. Rev. D*, 50:6100–6109, Nov. 1994.
- J. Madsen. Physics and Astrophysics of Strange Quark Matter. In J. Cleymans, H. B. Geyer, & F. G. Scholtz, editor, *Hadrons in Dense Matter and Hadrosynthesis*, volume 516 of *Lecture Notes in Physics*, Berlin Springer Verlag, pages 162–203, 1999.
- K. Maeda, F. K. Röpkke, M. Fink, W. Hillebrandt, C. Travaglio, and F. Thielemann. Nucleosynthesis in two-dimensional delayed detonation models of Type Ia supernova explosions. *ApJ*, 712:624–638, Mar. 2010.
- A. Marek and H. Janka. Delayed neutrino-driven supernova explosions aided by the standing accretion-shock instability. *ApJ*, 694:664–696, Mar. 2009.
- A. Marek, H. Dimmelmeier, H. Janka, E. Müller, and R. Buras. Exploring the relativistic regime with Newtonian hydrodynamics: an improved effective gravitational potential for supernova simulations. *A&A*, 445:273–289, Jan. 2006.
- L. Mestel. On the theory of white dwarf stars. II. The accretion of interstellar matter by white dwarfs. *MNRAS*, 112:598–+, 1952.
- B. S. Meyer, T. A. Weaver, and S. E. Woosley. Isotope source table for a 25 Msun supernova. *Meteoritics*, 30:325, May 1995.
- B. S. Meyer, T. D. Krishnan, and D. D. Clayton.  $^{48}\text{Ca}$  Production in Matter Expanding from High Temperature and Density. *ApJ*, 462:825, May 1996a.
- B. S. Meyer, L.-S. The, and M. F. El Eid. On the Nucleosynthesis of  $^{48}\text{Ca}$  and  $^{50}\text{Ti}$ . In *Lunar and Planetary Institute Science Conference Abstracts*, volume 27, page 875, Mar. 1996b.
- R. Minkowski. The spectra of the supernovae in IC 4182 and in NGC 1003. *ApJ*, 89:156–217, Mar. 1939.
- R. Minkowski. Spectra of supernovae. *PASP*, 53:224–225, Aug. 1941.
- C. W. Misner, K. S. Thorne, and J. A. Wheeler. *Gravitation*. San Francisco: W.H. Freeman and Co., 1973.
- R. Mönchmeyer, G. Schäfer, E. Müller, and R. E. Kates. Gravitational waves from the collapse of rotating stellar cores. *A&A*, 246:417–440, June 1991.

## BIBLIOGRAPHY

---

- E. Müller. Gravitational radiation from collapsing rotating stellar cores. *A&A*, 114:53–59, Oct. 1982.
- E. Müller and H.-T. Janka. Gravitational radiation from convective instabilities in Type II supernova explosions. *A&A*, 317:140–163, Jan. 1997.
- E. Müller and M. Steinmetz. Simulating self-gravitating hydrodynamic flows. *Computer Physics Communications*, 89:45–58, Aug. 1995.
- E. Müller, H.-T. Janka, and A. Wongwathanarat. Parametrized 3D models of neutrino-driven supernova explosions. Neutrino emission asymmetries and gravitational-wave signals. *A&A*, 537:A63, Jan. 2012.
- T. Nakamura and K.-I. Oohara. *Methods in 3 D numerical relativity*, pages 254–280. Evans, C. R., Finn, L. S., & Hobill, D. W., 1989.
- B. Niebergal, R. Ouyed, and P. Jaikumar. Numerical simulation of the hydrodynamical combustion to strange quark matter. *Phys. Rev. C*, 82(6):062801–+, Dec. 2010.
- J. C. Niemeyer and W. Hillebrandt. Turbulent nuclear flames in type Ia supernovae. *ApJ*, 452:769–778, Oct. 1995.
- J. C. Niemeyer and A. R. Kerstein. Burning regimes of nuclear flames in SN Ia explosions. *New Astronomy*, 2:239–244, Aug. 1997.
- J. C. Niemeyer and S. E. Woosley. The thermonuclear explosion of Chandrasekhar mass white dwarfs. *ApJ*, 475:740–753, Feb. 1997.
- K. Nomoto. Evolution of supernova progenitors and supernova models. *Annals of the New York Academy of Sciences*, 470:294–319, 1986.
- K. Nomoto and I. Iben, Jr. Carbon ignition in a rapidly accreting degenerate dwarf—A clue to the nature of the merging process in close binaries. *ApJ*, 297:531–537, Oct. 1985.
- K. Nomoto and Y. Kondo. Conditions for accretion-induced collapse of white dwarfs. *ApJ*, 367:L19–L22, Jan. 1991.
- K. Nomoto, D. Sugimoto, and S. Neo. Carbon deflagration supernova, an alternative to carbon detonation. *Ap&SS*, 39:L37–L42, Feb. 1976.
- K. Nomoto, F.-K. Thielemann, and K. Yokoi. Accreting white dwarf models of Type I supernovae. III. Carbon deflagration supernovae. *ApJ*, 286:644–658, Nov. 1984.
- P. E. Nugent, M. Sullivan, S. B. Cenko, R. C. Thomas, D. Kasen, D. A. Howell, D. Bersier, J. S. Bloom, S. R. Kulkarni, M. T. Kandrashoff, A. V. Filippenko, J. M. Silverman, G. W. Marcy, A. W. Howard, H. T. Isaacson, K. Maguire, N. Suzuki, J. E. Tarlton, Y.-C. Pan,

- L. Bildsten, B. J. Fulton, J. T. Parrent, D. Sand, P. Podsiadlowski, F. B. Bianco, B. Dilday, M. L. Graham, J. Lyman, P. James, M. M. Kasliwal, N. M. Law, R. M. Quimby, I. M. Hook, E. S. Walker, P. Mazzali, E. Pian, E. O. Ofek, A. Gal-Yam, and D. Poznanski. Supernova SN 2011fe from an exploding carbon-oxygen white dwarf star. *Nature*, 480:344–347, Dec. 2011.
- A. Odrzywolek and T. Plewa. Probing thermonuclear supernova explosions with neutrinos. *A&A*, 529:A156, May 2011.
- M. L. Olesen and J. Madsen. Burning a neutron star into a strange star. *Nuclear Physics B Proceedings Supplements*, 24:170–174, Dec. 1991.
- A. V. Olinto. On the conversion of neutron stars into strange stars. *Physics Letters B*, 192: 71–75, June 1987.
- J. R. Oppenheimer and G. M. Volkoff. On Massive Neutron Cores. *Physical Review*, 55: 374–381, Feb. 1939.
- S. Osher and J. A. Sethian. Fronts propagating with curvature-dependent speed: Algorithms based on Hamilton–Jacobi formulations. *Journal of Computational Physics*, 79:12–49, Nov. 1988.
- R. Ouyed, M. Kostka, N. Koning, D. A. Leahy, and W. Steffen. Quark nova imprint in the extreme supernova explosion SN 2006gy. *MNRAS*, 423:1652–1662, June 2012.
- R. Pakmor, M. Kromer, F. K. Röpkke, S. A. Sim, A. J. Ruiter, and W. Hillebrandt. Sub-luminous type Ia supernovae from the mergers of equal-mass white dwarfs with mass  $\sim 0.9M_{\odot}$ . *Nature*, 463:61–64, Jan. 2010.
- R. Pakmor, M. Kromer, S. Taubenberger, S. A. Sim, F. K. Röpkke, and W. Hillebrandt. Normal Type Ia Supernovae from Violent Mergers of White Dwarf Binaries. *ApJ*, 747:L10, Mar. 2012.
- M. A. Perez-Garcia, J. Silk, and J. R. Stone. Dark Matter, Neutron Stars, and Strange Quark Matter. *Physical Review Letters*, 105(14):141101–+, Oct. 2010.
- S. Perlmutter, G. Aldering, G. Goldhaber, R. A. Knop, P. Nugent, P. G. Castro, S. Deustua, S. Fabbro, A. Goobar, D. E. Groom, I. M. Hook, A. G. Kim, M. Y. Kim, J. C. Lee, N. J. Nunes, R. Pain, C. R. Pennypacker, R. Quimby, C. Lidman, R. S. Ellis, M. Irwin, R. G. McMahon, P. Ruiz-Lapuente, N. Walton, B. Schaefer, B. J. Boyle, A. V. Filippenko, T. Matheson, A. S. Fruchter, N. Panagia, H. J. M. Newberg, W. J. Couch, and The Supernova Cosmology Project. Measurements of Omega and Lambda from 42 high-redshift supernovae. *ApJ*, 517:565–586, June 1999.
- N. Peters. *Turbulent Combustion*. Cambridge University Press, Cambridge, 2000.

## BIBLIOGRAPHY

---

- M. M. Phillips. The absolute magnitudes of Type Ia supernovae. *ApJ*, 413:L105–L108, Aug. 1993.
- T. Plewa, A. C. Calder, and D. Q. Lamb. Type Ia supernova explosion: Gravitationally confined detonation. *ApJ*, 612:L37–L40, Sept. 2004.
- T. Rauscher and F.-K. Thielemann. Astrophysical reaction rates from statistical model calculations. *Atomic Data and Nuclear Data Tables*, 75:1–2, May 2000.
- M. Reinecke, W. Hillebrandt, and J. C. Niemeyer. Thermonuclear explosions of Chandrasekhar-mass C+O white dwarfs. *A&A*, 347:739–747, July 1999a.
- M. Reinecke, W. Hillebrandt, J. C. Niemeyer, R. Klein, and A. Gröbl. A new model for deflagration fronts in reactive fluids. *A&A*, 347:724–733, July 1999b.
- M. Reinecke, W. Hillebrandt, and J. C. Niemeyer. Refined numerical models for multidimensional type Ia supernova simulations. *A&A*, 386:936–943, May 2002a.
- M. Reinecke, W. Hillebrandt, and J. C. Niemeyer. Three-dimensional simulations of type Ia supernovae. *A&A*, 391:1167–1172, Sept. 2002b.
- M. A. Reinecke. *Modeling and simulation of turbulent combustion in Type Ia supernovae*. PhD thesis, Technische Universität München, 2001.
- C. E. Rhoades and R. Ruffini. Maximum Mass of a Neutron Star. *Physical Review Letters*, 32:324–327, Feb. 1974.
- L. F. Richardson. *Weather prediction by numerical process*. Cambridge University Press, Cambridge, 1922. Republished Dover 1965.
- A. G. Riess, A. V. Filippenko, P. Challis, A. Clocchiatti, A. Diercks, P. M. Garnavich, R. L. Gilliland, C. J. Hogan, S. Jha, R. P. Kirshner, B. Leibundgut, M. M. Phillips, D. Reiss, B. P. Schmidt, R. A. Schommer, R. C. Smith, J. Spyromilio, C. Stubbs, N. B. Suntzeff, and J. Tonry. Observational evidence from supernovae for an accelerating universe and a cosmological constant. *AJ*, 116:1009–1038, Sept. 1998.
- F. K. Röpke. *On the Stability of Thermonuclear Flames in Type Ia Supernova Explosions*. PhD thesis, Technische Universität München, 2003.
- F. K. Röpke. Following multi-dimensional type Ia supernova explosion models to homologous expansion. *A&A*, 432:969–983, Mar. 2005.
- F. K. Röpke and W. Hillebrandt. Full-star type Ia supernova explosion models. *A&A*, 431: 635–645, Feb. 2005.

- F. K. Röpke and J. C. Niemeyer. Delayed detonations in full-star models of type Ia supernova explosions. *A&A*, 464:683–686, Mar. 2007.
- F. K. Röpke, M. Gieseler, M. Reinecke, C. Travaglio, and W. Hillebrandt. Type Ia supernova diversity in three-dimensional models. *A&A*, 453:203–217, July 2006a.
- F. K. Röpke, W. Hillebrandt, J. C. Niemeyer, and S. E. Woosley. Multi-spot ignition in type Ia supernova models. *A&A*, 448:1–14, Mar. 2006b.
- F. K. Röpke, M. Kromer, I. R. Seitenzahl, R. Pakmor, S. A. Sim, S. Taubenberger, F. Ciaraldi-Schoolmann, W. Hillebrandt, G. Aldering, P. Antilogus, C. Baltay, S. Benitez-Herrera, S. Bongard, C. Buton, A. Canto, F. Cellier-Holzem, M. Childress, N. Chotard, Y. Copin, H. K. Fakhouri, M. Fink, D. Fouchez, E. Gangler, J. Guy, S. Hachinger, E. Y. Hsiao, J. Chen, M. Kerschhaggl, M. Kowalski, P. Nugent, K. Paech, R. Pain, E. Pecontal, R. Pereira, S. Perlmutter, D. Rabinowitz, M. Rigault, K. Runge, C. Saunders, G. Smadja, N. Suzuki, C. Tao, R. C. Thomas, A. Tilquin, and C. Wu. Constraining Type Ia Supernova Models: SN 2011fe as a Test Case. *ApJ*, 750:L19, May 2012.
- A. J. Ruiter, K. Belczynski, S. A. Sim, W. Hillebrandt, M. Fink, and M. Kromer. Type Ia Supernovae and Accretion Induced Collapse. In V. Kologera and M. van der Sluys, editors, *American Institute of Physics Conference Series*, volume 1314, pages 233–238, Dec. 2010.
- A. J. Ruiter, K. Belczynski, S. A. Sim, W. Hillebrandt, C. L. Fryer, M. Fink, and M. Kromer. Delay times and rates for Type Ia supernovae and thermonuclear explosions from double-detonation sub-Chandrasekhar mass models. *MNRAS*, 417:408–419, Oct. 2011.
- H. Saio and K. Nomoto. Off-Center Carbon Ignition in Rapidly Rotating, Accreting Carbon-Oxygen White Dwarfs. *ApJ*, 615:444–449, Nov. 2004.
- J. Saltzman. An Unsplit 3D Upwind Method for Hyperbolic Conservation Laws. *Journal of Computational Physics*, 115:153–168, Nov. 1994.
- D. G. Sandler, S. E. Koonin, and W. A. Fowler. Ca-Ti-Cr anomalies in an Allende inclusion and the n-beta-process. *ApJ*, 259:908–919, Aug. 1982.
- S. Sato, S. Kawamura, M. Ando, T. Nakamura, K. Tsubono, A. Araya, I. Funaki, K. Ioka, and others. DECIGO: The Japanese space gravitational wave antenna. *Journal of Physics Conference Series*, 154(1):012040, Mar. 2009.
- E. Schatzman. White dwarfs and type I supernovae. In L. Gratton, editor, *Star Evolution*, pages 389–+, 1963.
- W. Schmidt, J. C. Niemeyer, and W. Hillebrandt. A localised subgrid scale model for fluid dynamical simulations in astrophysics. I. Theory and numerical tests. *A&A*, 450:265–281, Apr. 2006a.

## BIBLIOGRAPHY

---

- W. Schmidt, J. C. Niemeyer, W. Hillebrandt, and F. K. Röpke. A localised subgrid scale model for fluid dynamical simulations in astrophysics. II. Application to type Ia supernovae. *A&A*, 450:283–294, Apr. 2006b.
- I. R. Seitenzahl, D. M. Townsley, F. Peng, and J. W. Truran. Nuclear statistical equilibrium for Type Ia supernova simulations. *Atomic Data and Nuclear Data Tables*, 95:96–114, Jan. 2009.
- I. R. Seitenzahl, F. K. Röpke, M. Fink, and R. Pakmor. Nucleosynthesis in thermonuclear supernovae with tracers: convergence and variable mass particles. *MNRAS*, 407:2297–2304, Oct. 2010.
- I. R. Seitenzahl, F. Ciaraldi-Schoolmann, and F. K. Röpke. Type Ia supernova diversity: white dwarf central density as a secondary parameter in three-dimensional delayed detonation models. *MNRAS*, 414:2709–2715, July 2011.
- S. L. Shapiro and S. A. Teukolsky. *Black Holes, White Dwarfs, and Neutron Stars*. John Wiley & Sons, New York, 1983.
- H. Shen, H. Toki, K. Oyamatsu, and K. Sumiyoshi. Relativistic Equation of State of Nuclear Matter for Supernova Explosion. *Progress of Theoretical Physics*, 100:1013–1031, Nov. 1998.
- L. Siess. Structural and chemical evolution of low- and intermediate-mass stars. In C. Charbonnel and J.-P. Zahn, editors, *EAS Publications Series*, volume 32, pages 131–171, Nov. 2008.
- S. A. Sim. Multidimensional simulations of radiative transfer in Type Ia supernovae. *MNRAS*, 375:154–162, Feb. 2007.
- A. W. Steiner, J. M. Lattimer, and E. F. Brown. The Equation of State from Observed Masses and Radii of Neutron Stars. *ApJ*, 722:33–54, Oct. 2010.
- D. J. Stevenson. A eutectic in carbon-oxygen white dwarfs. *Journal de Physique*, 41:C2–61 to C2–64, Mar. 1980.
- O. Straniero, I. Domínguez, G. Imbriani, and L. Piersanti. The Chemical Composition of White Dwarfs as a Test of Convective Efficiency during Core Helium Burning. *ApJ*, 583:878–884, Feb. 2003.
- The LIGO Scientific Collaboration and The Virgo Collaboration. Sensitivity Achieved by the LIGO and Virgo Gravitational Wave Detectors during LIGO’s Sixth and Virgo’s Second and Third Science Runs. *ArXiv e-prints*, Mar. 2012.

- F.-K. Thielemann, M.-A. Hashimoto, and K. Nomoto. Explosive nucleosynthesis in SN 1987A. II - Composition, radioactivities, and the neutron star mass. *ApJ*, 349:222–240, Jan. 1990.
- F.-K. Thielemann, K. Nomoto, and M.-A. Hashimoto. Core-Collapse Supernovae and Their Ejecta. *ApJ*, 460:408–436, Mar. 1996.
- F. X. Timmes and D. Arnett. The Accuracy, Consistency, and Speed of Five Equations of State for Stellar Hydrodynamics. *ApJS*, 125:277–294, Nov. 1999.
- F. X. Timmes and S. E. Woosley. The conductive propagation of nuclear flames. I. Degenerate C+O and O+Ne+Mg white dwarfs. *ApJ*, 396:649–667, Sept. 1992.
- Timmes, F. X. Stellar neutrino loss rates. [http://cococubed.asu.edu/code\\_pages/nuloss.shtml](http://cococubed.asu.edu/code_pages/nuloss.shtml), 2011. Accessed November 2011.
- I. Tokareva and A. Nusser. On the possibility of combustion of neutrons into strange quark matter. *Physics Letters B*, 639:232–236, Aug. 2006.
- R. C. Tolman. Static Solutions of Einstein’s Field Equations for Spheres of Fluid. *Physical Review*, 55:364–373, Feb. 1939.
- E. F. Toro. *Riemann solvers and numerical methods for fluid dynamics: a practical introduction*. Springer-Verlag, Berlin Heidelberg, 1997.
- C. Travaglio, W. Hillebrandt, M. Reinecke, and F.-K. Thielemann. Nucleosynthesis in multi-dimensional SN Ia explosions. *A&A*, 425:1029–1040, Oct. 2004.
- J. W. Truran, W. D. Arnett, and A. G. W. Cameron. Nucleosynthesis in supernova shock waves. *Canadian Journal of Physics*, 45:2315–2332, 1967.
- S. Typel, G. Röpke, T. Klähn, D. Blaschke, and H. H. Wolter. Composition and thermodynamics of nuclear matter with light clusters. *Phys. Rev. C*, 81(1):015803–+, Jan. 2010.
- S. J. Waldman. The Advanced LIGO Gravitational Wave Detector. *ArXiv e-prints*, Mar. 2011.
- F. Weber. Strange quark matter and compact stars. *Progress in Particle and Nuclear Physics*, 54:193–288, Mar. 2005.
- J. M. Weisberg, D. J. Nice, and J. H. Taylor. Timing Measurements of the Relativistic Binary Pulsar PSR B1913+16. *ApJ*, 722:1030–1034, Oct. 2010.
- S. Weissenborn, I. Sagert, G. Pagliara, M. Hempel, and J. Schaffner-Bielich. Quark Matter in Massive Compact Stars. *ApJ*, 740:L14, Oct. 2011.
- E. Witten. Cosmic separation of phases. *Phys. Rev. D*, 30:272–285, July 1984.

## BIBLIOGRAPHY

---

- S. E. Woosley. Neutron-rich nucleosynthesis in carbon deflagration supernovae. *ApJ*, 476: 801–810, Feb. 1997.
- S. E. Woosley, T. A. Weaver, and R. D. Hoffman. Rare Neutron-Rich Nucleosynthesis in Type IA Supernovae. In C. M. R. M. Busso and R. Gallino, editors, *Nuclei in the Cosmos III*, volume 327 of *American Institute of Physics Conference Series*, page 463, 1995.
- M. Zingale, S. E. Woosley, C. A. Rendleman, M. S. Day, and J. B. Bell. Three-dimensional numerical simulations of Rayleigh-Taylor unstable flames in Type Ia supernovae. *ApJ*, 632: 1021–1034, Oct. 2005.

# Danksagung

Ich möchte mich bei Fritz Röpke zum einen für die gute Betreuung bedanken, die auch nach seinem Umzug nach Würzburg problemlos abgelaufen ist, zum anderen auch für das gute soziale Klima in seiner Gruppe, unter anderem ausgedrückt durch die alljährlichen Weihnachtsfeiern mit seiner hervorragenden Feuerzangenbowle.

Bedanken will ich mich auch bei Michi Fink, der mich geduldig in die Geheimnisse des Post-Processing-Codes eingeweiht hat, bei Ivo Seitenzahl für seinen Rat in kernphysikalischen Fragen und die Durchführung der N0100-Simulationen, außerdem bei allen anderen Kollegen, die mir mit guten Ratschlägen, vor allem in Computerfragen, zur Seite gestanden sind, besonderes bei Philipp Edelman, Bernhard Müller, Franco Ciaraldi-Schoolmann, Fabian Miczek, Rüdiger Pakmor und Uli Nöbauer.

Meinen ehemaligen und aktuellen Bürokollegen Bernhard Müller, Stefan „Hätschi“ Hachinger, Fabian Miczek, Janina von Groote, Philipp Edelman, Uli Nöbauer und Michi Klauser danke ich für die schöne Zeit – besonders die Bürokollegen aus 009 haben keine Langeweile aufkommen lassen und ganz nebenbei habe ich einiges dazugelernt.

Weiter möchte ich mich bei Wolfgang Hillebrandt und Ewald Müller bedanken, die mir die Promotion am MPA ermöglicht haben und die schönen Workshops in Ringberg veranstaltet haben; dem Compstar Network für die Organisation und Finanzierung zweier schöner Sommerschulen und Workshops; dem Rechenzentrum Garching, das mir die Arbeit auf den Clustern OPA und VIP ermöglicht hat; und bei Maria Depner, Cornelia Rickl und allen anderen hilfsbereiten MPA-Mitarbeitern.

Auch meinen Eltern will ich ganz herzlich für die unverminderte Unterstützung danken.

Schließlich möchte ich mich bei meiner lieben Hedi bedanken, durch sie sind die letzten dreieinhalb Jahre zu einer ganz besonderen Zeit geworden.

